Design, Synthesis and Evaluation of Multimodal Paramagnetic Lipids for Liposomal Fluorescence and Magnetic Resonance Imaging

Nazila Kamaly

Imperial College London

Department of Chemistry

A thesis submitted for the degree of

Doctor of Philosophy of Imperial College London

and for the

Diploma of Membership of Imperial College London

November 2007

Declaration

I hereby declare that the work described within this thesis is entirely my own, except where specifically acknowledged in the text.

Nazila Kamaly – Thesis submitted November 2007

Abstract

Molecular imaging techniques have revolutionised our understanding of disease states and the underlying processes causing their occurrence. Such a feat would not have been accomplished without the utilisation of the imaging probes central to the field of molecular imaging. The work undertaken in this thesis describes the synthesis and biological evaluation of lipidic contrast agent probes, designed for effective cellular entry and solid tumour imaging.

A gadolinium (Gd) based paramagnetic lipid (Gd.DOTA.DSA) was synthesised and liposome formulations containing this lipid were optimised for maximum cellular labelling. MRI signal enhancing properties of bimodal paramagnetic-fluorescent liposomes utilising Gd.DOTA.DSA was shown both *in vitro* and *in vivo*. Tumour MRI results revealed these liposomes to benefit from a prolonged *in vivo* circulation time and excellent tumour accumulation properties as co-validated by both MRI and fluorescence microscopy of tumour sections. Here, the enhanced permeation and retention (EPR) effect of tumour tissue was exploited, whereby nanoparticles such as the paramagnetic liposomes described, are able to accumulate in tumour tissue due to leaky endothelial layers of damaged blood vessels.

A further bimodal fluorescent and paramagnetic lipid (Gd.DOTA.Rhoda.DSA) was designed and synthesised and was shown to label cancer cells *in vitro* and effectively enhance tumour MRI signal *in vivo*. These results were also analysed by MRI and fluorescence modalities.

Work towards a trimodal fluorescent, ^{1}H and ^{19}F MRI agent was undertaken and prospective routes for its final synthesis purposed.

Table of Contents

1. Introduction **22**

1.1 Biological Imaging 23
1.1.1 Molecular Imaging 23
1.1.2 Targets for Molecular Imaging 24
1.1.3 Molecular Imaging of Gene Expression 25
1.1.4 Molecular Imaging of Molecular Markers 28
1.1.5 Molecular Imaging of Cancer 30
1.1.6 Molecular Imaging in Drug Discovery and Development 31

1.2 Cellular Imaging 33
1.2.1 Cellular Labelling and MRI 34
1.2.2 Iron Based MR Cellular Labelling Agents 35
1.2.3 Gadolinium Based Cell Labelling Agents 38
1.2.4 Fluorine Based Cellular Labelling Agents 39
1.2.5 Manganese Based Cellular Imaging agents 40
1.2.6 Stem Cell Imaging With MRI 41
1.2.7 Cellular Labelling with Other Imaging Modalities 42

1.3 Tumour Imaging 43
1.3.1 Angiogenesis Imaging 43
1.3.2 Further Tumour Imaging Methods 44
1.3.3 Nanotechnology and Tumour Imaging 45

1.4 Imaging Modalities 46
1.4.1 X-Ray and CT imaging 48
1.4.2 PET Imaging 48
1.4.3 SPECT Imaging 49
1.4.4 Magnetic resonance imaging (MRI) 50
1.4.5 Optical Imaging 50
1.4.6 Ultrasound Imaging 51

1.5 Magnetic Resonance Imaging (MRI) – Background and Principles 52

1.6 Fluorescence Imaging – Background and Principles 61

1.7 MRI Contrast Agents 64
1.7.1 Gadolinium Contrast Agents (T_1 Agents). 64
1.7.2 Small Molecular Weight Gadolinium Contrast Agents 68
1.7.3 Large Molecular Weight Contrast Agents 70

1.7.4 Polymeric and Dendrimeric Contrast Agents 70
1.7.5 CEST and LIPOCEST Contrast Agents 71
1.7.6 Superparamagnetic Contrast Agents (T_2 agents) 72
1.7.7 Nanoparticle Contrast Agents 73

1.8 Paramagnetic Liposomes and MR Imaging 75
1.8.1 Paramagnetic Liposomes by Contrast Agent Encapsulation 77
1.8.2 Paramagnetic Liposomes by Gd Lipid Incorporation 78
1.8.3 Targeted Gd Liposomes for MRI 79
1.8.4 Further Applications of Paramagnetic Liposomes 80

1.9 Thesis Synopsis 83

2. Synthesis and MRI Analysis of First Generation Gadolinium Lipid - Gd.DOTA.DSA 84

2.1 Paramagnetic Gd Lipids 85

2.2 Synthesis of Gd.DOTA.DSA 86
2.2.1 Synthesis of Protected DOTA Ligand 89
2.2.2 Coupling of Protected DOTA and Lipidic Amine 91
2.2.3 Synthesis of Lipidic Amine Tail 94
2.2.4 Synthesis of Control Paramagnetic Lipid Gd.DTPA.BSA 95

2.3 MRI Analysis of Paramagnetic Lipids Gd.DOTA.DSA and Gd.DTPA.BSA 97
2.3.1 Chapter Summary 101

3. In Vitro and In Vivo Biological Evaluations of Gd.DOTA.DSA 102

3.1 In Vitro Evaluation of Gadolinium Liposomes 103
3.1.1 Gadolinium Liposome Formulation optimisation 103
3.1.2 MTT Cell Viability Assay with Gadolinium Liposomes 111
3.1.3 Lactate Dehydrogenase Cytotoxicity Assay with Gadolinium Liposomes 113
3.1.4 ICP-Mass Spectrometry of Gadolinium Liposomes 115
3.1.5 MRI Visualisation of Gadolinium Liposome Labelled Cells 116
3.1.6 Fluorescence Microscopy of Gadolinium Labelled Cells 117
3.1.7 Plasmid DNA Transfection with Gadolinium Liposomes 119
3.1.8 In Vitro Evaluation of Gd.DOTA.DSA: Conclusions 121

3.2 In Vivo Evaluation of Gadolinium Liposomes 122
3.2.1 In Vivo Considerations of Liposome Size 122
3.2.2 Liposome Surface Charge 124

3.2.3 Liposome Tumour Specificity 125
3.2.4 Preliminary In Vivo Evaluation of Gd.DOTA.DSA 125
3.2.5 Serum Aggregation Study with Gadolinium Liposomes 127
3.2.6 Cryo-Transmission Electron Microscopy (Cryo-TEM) 132
3.2.7 Relaxivity of PEGylated Gadolinium Liposomes 133

3.3 In Vivo Tumour Imaging with Gadolinium Liposomes 134
3.3.1 Laser Ablation – ICP Mass Spectrometry of Tumour Sections. 138
3.3.2 Targeted Tumour Imaging with PEGylated Folate Gadolinium Liposomes 140
3.3.3 Immunohistochemistry Analysis of Ovarian Carcinoma Cell Lines 141
3.3.4 Folate Targeted Gadolinium Liposomes for Tumour Imaging 143

3.4 Chapter Summary 150

4. Synthesis of Second Generation Bimodal Gadolinium Lipid - Gd.DOTA.Rhoda.DSA 151

4.1.1 Bimodal Fluorescent and MRI Probes 152
4.1.2 Synthesis of the Novel Bimodal Lipid: Gd.DOTA.Rhoda.DSA 154
4.1.3 MRI Analysis of Bimodal Gd.DOTA.Rhoda.DSA 171

4.2 Chapter Summary 174

5. In Vitro and In Vivo Biological Evaluations of Bimodal Gadolinium Lipid - Gd.DOTA.Rhoda.DSA 175

5.1 In Vitro Cell Labelling with Gd.DOTA.Rhoda.DSA 176

5.2 In Vivo Solid Tumour Imaging with Gd.DOTA.Rhoda.DSA Liposomes 178

5.2.1 Chapter Summary 182

6. Work Towards Trimodal Gadolinium Lipids 183

6.1 ^{19}F MRI Agents 184
6.1.1 Towards Trimodal ^{19}F Paramagnetic and Fluorescent Lipids 185

7. Conclusions and Future Directions 190

7.1 Conclusion 191

8. Experimental 194

8.1 General Information 195
8.1.1 Materials 195

8.1.2 General Procedures 195
8.1.3 Chemical Synthesis 196
8.1.4 Synthesis of Gd.DOTA.DSA 196
8.1.5 Synthesis of Gd.DTPA.BSA 201
8.1.6 Synthesis of Gd.DOTA.Rhoda.DSA 203
8.1.7 Towards the Synthesis of Trimodal Gadolinium Lipids 212
8.1.8 Xylenol Orange Test 215
8.1.9 Chloroanil Test 215
8.1.10 MRI Analysis of Gd.DOTA.DSA and Gd.DTPA.BSA 215
8.1.11 Liposome Preparations 216
8.1.12 In Vitro Fluorescent Cell Uptake Assay with Gd.DOTA.DSA Liposomes 216
8.1.13 MTT Cell Viability Assay with Gd.DOTA.DSA Liposomes 217
8.1.14 Lactate Dehydrogenase Toxicity Assay with Gd.DOTA.DSA Liposomes 218
8.1.15 MRI Analysis of Cells Labelled with Gd.DOTA.DSA Liposomes 218
8.1.16 Fluorescence Microscopy of Cells Labelled with Gd Liposomes 219
8.1.17 DNA Transfection with Gadolinium Lipoplexes formed with Gd.DOTA.DSA 220
8.1.18 ICP-Mass Spectrometry Analysis of Cell Lysates 220
8.1.19 Preliminary Intramuscular Injections of Gd.DOTA.DSA Liposomes 221
8.1.20 Serum Aggregation Analysis of PEGylated Gd Liposomes 221
8.1.21 Zeta Potential Measurements of PEGylated Gd Liposomes 222
8.1.22 Cryo-TEM of PEGylated Gd.DOTA.DSA Liposomes 222
8.1.23 Relaxivity Measurement of PEGylated Gd.DOTA.DSA Liposomes 222
8.1.24 Mouse Tumour Model 223
8.1.25 Laser Ablation – ICP Mass Spectrometry of Tumour Sections 223
8.1.26 Immunohistochemistry and FACS Analysis of Folate Receptor Expression 223
8.1.27 MRI Analysis of Gd.DOTA.Rhoda.DSA 225
8.1.28 IGROV-1 Cell Labelling with Gd.DOTA.Rhoda.DSA Liposomes 225
8.1.29 MRI of IGROV-1 Cells Labelled with Gd.DOTA.Rhoda.DSA Liposomes 225
8.1.30 Histology Experiments 226

9. References 227

Figures

Figure 1. Example of targets for molecular imaging 25
Figure 2. MRI for visualising gene expression 27
Figure 3. A smart activatable MRI probe 27
Figure 4. Cell entry mechanisms 35
Figure 5. MRI of a single contrast agent labelled cell 37
Figure 6. Hydrogen nuclei and their spin 52
Figure 7. Precession and the Larmour frequency 53
Figure 8. Establishing a magnetisation vector 53
Figure 9. Application of an RF pulse to a magnetisation vector 54
Figure 10. T_1 and T_2 relaxation processes 55
Figure 11. Graph showing T_1 and T_2 relaxation parameters 56
Figure 12. Generating a 3D image in MRI 57
Figure 13. MRI image acquisition: a summary 58
Figure 14. Time of echo (TE) 59
Figure 15. A spin-echo sequence 59
Figure 16. Three different orientations in which slices are obtained in MR imaging 60
Figure 17. Jablonski diagram of the electronic states in fluorescence emission 61
Figure 18. General example of a fluorescence detection system 62
Figure 19. Fluorescence emission spectrum of two fluorophores 62
Figure 20. Gadolinium based clinical contrast agents approved by the FDA. 64
Figure 21. The crystal structures of Gd.DOTA and Gd.DTPA 65
Figure 22. Gd relaxation mechanism and parameters 66
Figure 23. Examples of some targeted contrast agents from the literature 69
Figure 24. A core type PAMAM dendrimer, n = generation 71
Figure 25. T_2 weighted MR image of cell pellets labelled with iron nanoparticles. 73
Figure 26. Liposome formation from amphipathic lipids. 75
Figure 27. Gd.DTPA.BSA 79
Figure 28. A cartoon of a prototype NMR spectrum of a LIPOCEST system 81
Figure 29. Examples of paramagnetic lipids with various hydrophobic tails 85
Figure 30. MCO-I-68/Gd complex 86
Figure 31. Gd.DOTA.Chol, a T_1 lipidic contrast agent component of MAGfect 86
Figure 32. Paramagnetic gadolinium lipid target, Gd.DOTA.DSA 87
Figure 33. Cyclen macrocycles 89
Figure 34. Characterisation of Gd.DOTA.DSA 93
Figure 35. Characterisation of Gd.DTPA.BSA 96

Figure 36. R_1 relaxivity measurement for Gd.DOTA.DSA liposomes 99
Figure 37. The r_1 relaxivities for aqueous solutions of the paramagnetic lipids 99
Figure 38. Cartoon of liposomal relaxivity 100
Figure 39. Lipids used in Gd Liposome formulations 105
Figure 40. Fluorescence uptake assay used for liposome uptake assessment 107
Figure 41. Fluorescence emission of HeLa cell lysate post incubation 108
Figure 42. Calculated mass of Gd.DOTA.DSA lipid taken up into cells 110
Figure 43. Reduction of MTT to Formazan 111
Figure 44. MTT cell viability assay 112
Figure 45. General chemical reactions for the LDH cytotoxicity assay 113
Figure 46. LDH assay results 114
Figure 47. T_1 weighted images obtained of labelled cells 116
Figure 48. Fluorescence microscopy images of labelled cells 117
Figure 49. Confocal microscopy of gadolinium labelled cells 118
Figure 50. Gadolinium lipoplex transfections 120
Figure 51. LDH assay of lipoplexes used in luciferase transfection assay 120
Figure 52. The EPR effect 123
Figure 53. T_1-weighted MR images of IM injections with gadolinium liposomes 126
Figure 54. Influence of cholesterol lipid on liposome bilayers 128
Figure 55. Size and polydispersity of PEGylated liposomes 129
Figure 56. Size and polydispersity of non-Gd PEGylated liposomes 131
Figure 57. Cryo-transmission image of PEGylated gadolinium liposomes 132
Figure 58. Relaxivity of PEGylated gadolinium liposomes 134
Figure 59. Tumour MRI with PEGylated gadolinium liposomes 135
Figure 60. Fluorescence microscopy of tumour tissue sections 137
Figure 61. Peripheral tumour sections 138
Figure 62. Laser-ablation ICP MS of tumour sections 139
Figure 63. Immunohistochemistry of three cell lines 141
Figure 64. FACS analysis of four cell lines for α-FR expression levels. 142
Figure 65. Folate-targeted gadolinium liposomes 143
Figure 66. MRI of IGROV-1 tumour bearing Balb/C nude mice 144
Figure 67. Tumour enhancement post folate-targeted gadolinium liposomes 145
Figure 68. Fluorescence microscopy images of IGROV-1 sectioned tumours 146
Figure 69. Fluorescence microscopy of liver sections 148
Figure 70. Two bimodal polymeric contrast agents 153
Figure 71. An angiogenesis specific bimodal probe 153
Figure 72. Structures of two commonly utilised fluorescent lipids 154

Figure 73. PTIR267: a bimodal agent 155
Figure 74. R_1 relaxivity for PEGylated neutral Gd.DOTA.Rhoda.DSA liposomes 172
Figure 75. 3D model of Gd.DOTA.Rhoda.DSA 173
Figure 76. Photograph of cells labelled with Gd.DOTA.Rhoda.DSA liposomes 177
Figure 77. Fluorescence microscopy of IGROV-1 cells post liposome labelling 177
Figure 78. Tumour bearing Balb/c nude mice post liposome injection 178
Figure 79. Tumour T_1 post injection of Gd.DOTA.Rhoda.DSA liposomes 179
Figure 80. T_1-weighted tumour images of Balb/c mice injected with liposomes 180
Figure 81. Fluorescence microscopy images of sectioned tumours 180
Figure 82. A trimodal probe 185
Figure 83. Mechanism for the Staudinger Reduction of an azide to an amine 187
Figure 84. A NIR dye; Cy5.5 193

Schemes

Scheme 1. Bioluminescence reaction catalysed by firefly luciferase 51
Scheme 2. Retrosynthetic analysis of Gd.DOTA.DSA lipid 88
Scheme 3. Solid phase synthesis of Boc protected DOTA 90
Scheme 4. Amide coupling of DOTA.DSA lipid 91
Scheme 5. t-Butyl removal of protected DOTA.DSA lipid 92
Scheme 6. DSA lipid tail synthesis 94
Scheme 7. DTPA.BSA synthesis 95
Scheme 8. Gadolinium complexation 96
Scheme 9. Retrosynthetic analysis of Gd.DOTA.Rhoda.DSA 156
Scheme 10. A retrosynthetic analysis of Gd.DOTA.Rhoda.DSA precursors 158
Scheme 11. A restrosynthetic analysis of orthogonally protected lipid 34 159
Scheme 12. Rhodamine isothiocyanate coupling 160
Scheme 13. Gadolinium complexation and hydrogenation reactions 162
Scheme 14. TAMRA amide coupling 164
Scheme 15. FAM amide coupling 165
Scheme 16. FITC amide coupling 166
Scheme 17. Synthesis of orthogonally protected lipid linker precursor 167
Scheme 18. Gd.DOTA.Rhoda.DSA precursor synthesis 168
Scheme 19. Rhodamine sulfonyl chloride coupling to give Gd.DOTA.Rhoda.DSA 170
Scheme 20. Synthesis of tetrakis-trifluorobenzyl-lysine linker 54 186
Scheme 21. Proposed scheme towards the synthesis of tri-protected precursor 188
Scheme 22. Proposed scheme towards the synthesis of trimodal head group 189

Tables

Table 1. Summary of imaging modalities 47
Table 2. T_1 values and images of Gd.DOTA.DSA 97
Table 3. Gadolinium liposomes for r_1 relaxivity measurements 98
Table 4. Liposome formulations prepared for the labelling of HeLa cells 106
Table 5. T_1 values for cells labelled with gadolinium liposomes 116
Table 6. Sterically stabilised gadolinium liposomes 128
Table 7. Sterically stabilised Gd free liposomes 130
Table 8. PEGylated gadolinium liposomes used to calculate r_1 relaxivity 133
Table 9. Reaction conditions employed for Gd.DOTA.Rhoda.DSA coupling 161
Table 10. Hydrogenation conditions employed for CBz removal 163
Table 11. T_1 images and values for Gd.DOTA.Rhoda.DSA 171
Table 12. Liposomes for r_1 relaxivity measurement of Gd.DOTA.Rhoda.DSA 172

Acknowledgments

I would like to thank Professor Andrew Miller for taking me on board in his group and giving me the opportunity to work in the GTC on a very interesting and multidisciplinary project. I am grateful to him for giving me free reign with the project, and enabling me to implement my ideas. I am also grateful for his constant enthusiasm and encouragement. I'd like to thank Professor Jimmy Bell for being a second supervisor to me and offering his advice. The opportunities I was given to present my work at all the various conferences and meetings is also much appreciated.

Many have given their help and support towards this project whom I'd like to thank chronologically. Firstly, I am thankful to Dr. Michael Jorgensen who supervised the work initially, his critical eye, insight and ideas helped me a lot, and his training will remain with me. I'd like to thank Dr. Morag Oliver whom I took the project over from, and to whom I am grateful for the initial support. I was introduced to the world of *in vitro* cell culture by Dr. Ayesha Ahmad whom I thank sincerely. I'd like to thank a very nice and constantly helpful MR physicist lady, Dr. Amy Herlihy (Hammersmith campus) for all her help, training and assistance with the MRI machine, thank you Amy for the sequences and teaching me to be hands on! From the Hammersmith crew, I'd like to particularly thank Dr. Tammy Kalber. Many thanks are extended to her for her help with the *in vivo* tumour models, and all her other advice and assistance throughout the project. I'd also like to thank Dr. Po-wah So and Dr. Ian McNeish for the IGROV-1 cell line and Dr. Yu-Ting Kuo for the IM work.

I'd like to express my gratitude to Dr. Maya Thanou, a resilient and brilliant lady who has been a constant source of ideas and encouragement. I thank her for all the insightful comments, brainstorming and advice throughout the last year in particular. Maya you are the nanoparticle Queen!

Many thanks are extended to Ms. Lorraine Lewis (Imperial) for her assistance with the tissue cryo-sectioning, Dr. Sarah Stokes (University of Sheffield) for running the Laser-ablation ICP-MS experiment, Dr. Sarah James (Natural History Museum, London) for the ICP-MS experiments and Dr.Tillmann Pape for the cryo-TEM images (Imperial). I'd also like to sincerely thank Dr. Piers Gaffney and Dr. Steven Fletcher for their advice with the synthesis.

I’d like the proof readers; Dr. Michael Wright, Dr. Maya Thanou and Joe Kaplinsky, thank you for your kindness.

The last three years of my life at Imperial College would not have been as colourful, fun, interesting and eventful without my lovely colleagues at the GTC, there are so many of you to thank and remember, I’d be writing too long a list of names if I were to name you all individually! Thank you guys for all your support, encouragement, banter and entertainment over the years! However, special thanks go to Ming Wang and Nimisha Walji, you are super troopers! Thank you for being great friends and making GTC life all that more memorable ;)

I’d also like to thank the Bell group at Hammersmith for including me in their group activities and being so pleasant and helpful at all times.

Last but by no means least, I’d like to thank my family and friends; you have all been so supportive throughout the years, thank you so much! I am truly and earnestly grateful for all your support, encouragement, love and praise. I’d like to particularly thank my brother Johnny for all the computer and diagram rescue assistance! And mum, you are the best…

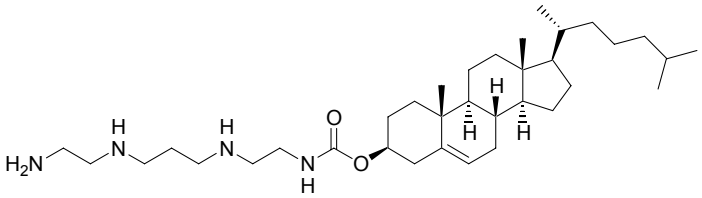
Publications

Kamaly N, Kalber T, Ahmad A, Oliver MH, So PW, Herlihy AH, Bell JD, Jorgensen MR, Miller AD. “Bimodal Paramagnetic and Fluorescent Liposomes for Cellular and Tumour Magnetic Resonance Imaging”, *Bioconj. Chem*. **2008**, Jan 16; 19(1):118-129. Epub 2007 Nov 7.

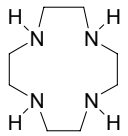
Oliver M, Ahmad A, Kamaly N, Perouzel E, Caussin A, Keller M, Herlihy A, Bell J, Miller AD, Jorgensen MR. “MAGfect: a novel liposome formulation for MRI labelling and visualisation of cells”. *Org. Biomol. Chem*. **2006**, Sep 21; 4 (18): 3489-97.

Abbreviations

aq.	Aqueous
A*β*	Amyloid-β
ATP	adenosine triphosphate
BCA	bicinchoninic acid
Br	bromine
BLI	bioluminescence imaging
BFP	blue fluorescent protein
Bn	benzyl
br	broad
Boc	*tert*-butyloxycarbonyl
BOA	acid-bis-oleate
BSA	bovine serum albumin
CBz	carboxybenzyl
CDAN	N^1-cholesteryloxycarbonyl-3,7-diaza-1,9-diaminonane

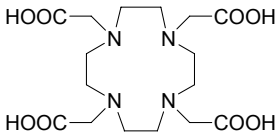


Chol	cholesterol (cholest-5-β-ol)
CCD	charged-coupled device
Cyclen	1,4,7,10-tetrazacyclododecane

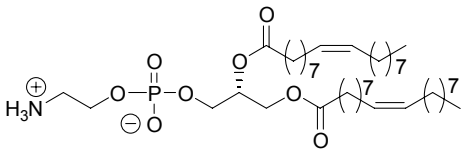


CT	computed tomography
CA	contrast agent
CAT	computer axial tomography
CEST	chemical-exchange saturation transfer
CLIO	cross-linked superparamagnetic iron oxide
CE	perfluoro-15-crown-5-ethers
Cu	copper

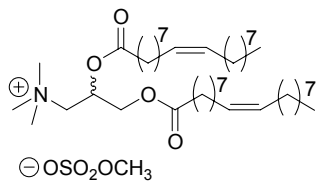
^{64}Cu-PTSM	copper-64-pyruvaldehyde-bis(N^4-methylthiosemicarbazone)
Co	cobalt
d	doublet
DCE-MRI	dynamic contrast-enhanced magnetic resonance imaging
DMAP	*N*,*N*-dimethylaminopyridine
DMPE	dimyristoylphosphoethanolamine
DMPC	dimyristoylphosphatidylcholine
DMF	*N*,*N*-dimethylformamide
DMSO	dimethyl sulfoxide
DNA	deoxyribonucleic acid
DOTA	1,4,7,10-tetraazacyclododecane-1,4,7,10-tetraacetic acid



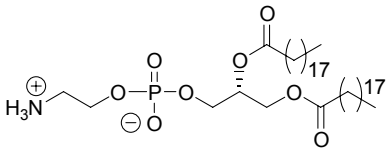
DOPE	dioleoylphosphatidylethanolamine



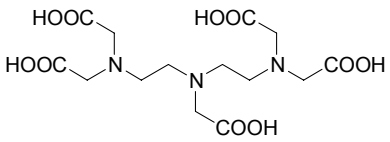
DOTAP	dioleoyloxy-3-(trimethylamonio)propane



DSPE	distearoylphosphatidylethanolamine



DTPA	diethylenetriaminepentaacetic acid



DSPC	distearoylphosphoethanolamine
DW-MRI	diffusion-weighted magnetic resonance imaging
eq.	equivalents
EG	encoding gradient
EPR	enhanced permeation and retention
ESI-MS	electrospray mass spectrometry
Et	ethyl
EtOH	ethanol
EtOAc	ethyl acetate
ETR	engineered transferrin receptor
Fe	Iron
FAB	fast atomic bombardment
FAM	carboxyfluorescein
FACS	fluorescence activated cell sorting
FDG	fluorine-18-labelled fluorodeoxyglucose
FHBG	9-[4-[^{18}F]fluoro-3-(hydroxymethyl)butyl]guanine
FIAU	5-[^{131}I-2'-fluoro-1-β-$_D$-arabinofuranosyl]uracil
FIAU-MP	5-[^{131}I-2'-fluoro-1-β-$_D$-arabinofuranosyl]uracil-monophosphate
^{18}F-FDG	fluorodeoxyglucose
FID	free induction decay
FITC	fluorescein isothiocyanate
FDA	food and drug administration
fMRI	functional magnetic resonance imaging
FRET	fluorescence resonance energy transfer
FT	Fourier Transform
FR	folate receptor
Ga	gallium
Gd	gadolinium
GFP	green fluorescent protein
GRID	gadolinium rhodamine dextran
h	hour(s)
HBTU	*O*-benzytriazol-1-*N*,*N*,*N*',*N*'-tetramethyluronium hexafluorophoshate

HE	hematoxylin and eosion
HeLa	human ovarian carcinoma
HEPES	hydroxyethylpiperazine ethane sulfonic acid
HUVEC	human umbilical vein endothelium cells
HOBt	1-hydroxybenzotriazole
HPLC	high performance liquid chromatography
HSV	herpes simplex virus
HSV1-*tk*	herpes simplex virus1- thymidine kinase
HRMS	high resolution mass spectrometry
hTfR	human transferrin receptor
IR	infra-red
IGROV-1	human ovarian carcinoma
ICP-AE	inductively-coupled plasma atomic emission
ICP-MS	inductively coupled plasma mass spectrometry
In	indium
J	coupling constant
kDa	kilodaltons
LA-ICP MS	laser ablation-inductively coupled plasma mass spectrometry
LD	liposome: DNA
LIPOCEST	liposome chemical exchange saturation transfer
LDH	lactate dehydrogenase
LS 174T	human colorectal carcinoma
LUV	large unilamellar vesicle
MACS	magnetically activated cell sorter
MeCN	acetonitrile
MPAP	myristoylated polyarginine peptide
MSCs	mesenchymal stem cells
m	multiplet
Me	methyl
Mg	magnesium
MEMRI	manganese enhanced magnetic resonance imaging
MeOH	methanol
min	minute(s)
MLV	multi lamellar vesicle
Mn	manganese
MT	magnetisation transfer
MTT	[3-(4,5-dimethylthiazol-2-yl)-2,5-diphenyltetrazolium bromide]

MR	magnetic resonance
mRNA	messenger ribonucleic acid
MRI	magnetic resonance imaging
MRS	magnetic resonance spectroscopy
mMRI	molecular magnetic resonance imaging
MION	monocrystalline iron oxide nanoparticles
MPIO	micro-metre sized paramagnetic iron oxide nanoparticles
m/z	mass-to-charge ratio
MS	mass spectrometry
NIR	near infrared
NIH 3T3	mouse embryonic fibroblast cell line
NIRF	near infrared fluorescence imaging
NGF	nerve growth factor
NEt_3	triethylamine
NBD	*N*-(7-nitro-2-1,3-benzoxadiazol-4-yl)
NADH	nicotinamide adenine dinucleotide (reduced)
NADPH	nicotinamide adenine dinucleotide phosphate (reduced)
NHS	*N*-hydroxysuccinimidyl ester
nm	nanometre (10^{-9} m)
NMR	nuclear magnetic resonance
NMRD	nuclear magnetic resonance dispersion
OVCAR-3	human ovarian carcinoma
PI	polydispersity index
PBS	phosphate buffered saline
PAMAM	polyamidoamine
pDNA	plasmid DNA
PEG	polyethylene glycol
PC	phosphocholine
PFOB	perfluoroctylbromide cores
PET	positron emission tomography
PFPE	perfluoropolyether
Ph	phenyl
PS	phosphatidylserine
RLU	relative light units
RES	reticuloendothelial system
RT	room temperature
RF	radio frequency

RGD	arginine-glycine-aspartic acid
RAD	arginine-alanine-aspartic acid
RFP	red fluorescent protein
ROI	region of interest
s	singlet
siRNA	small interfering ribonucleic acid
secs	seconds
SUV	small unilamellar vesicle
SPIO	superparamagnetic iron oxide
SPECT	single photon emission computed tomography
SKBR-3	human breast carcinoma
t	triplet
T	tesla
Tat	transactivator
Tat-CLIO	transactivator-cross-linked superparamagnetic iron oxide
Tc	technitium
TE	time of echo
TEM	transmission electron microscopy
Tf-R	transferrin receptor
Tf-MION	transferrin-monocrystalline iron oxide nanoparticles
TR	time of repetition
TFA	trifluoroacetic acid
THF	tetrahydrofuran
TLC	thin layer chromatography
UV	ultraviolet
USPIO	ultrasmall superparamagnetic iron oxide
US	ultrasonography
UTR	untranslated region
VSPIO	very small paramagnetic iron oxide
VEGF	vascular endothelial growth factor
VEGFR	vascular endothelial growth factor receptor
Y	yttrium
YFP	yellow fluorescent protein
Zn	zinc

1. Introduction

1.1 Biological Imaging

In 1665 physicist Robert Hooke looked at a sliver of cork through a microscope lens and noticed pore-like structures. It was from this observation that the idea of a cellular unit was envisaged. Since then tremendous discoveries have been made through the lens of a microscope and microscopy itself has become the definitive tool in aiding researchers "see" biological processes at the cellular and molecular level. Biological imaging encompasses the visualisation and detection of complex biomolecular assemblies, at all levels of biology including cells, tissues and organs. This "seeing" or "sensing" is realised with various imaging techniques which exploit the fluorescence, acoustic wave, radioactive and paramagnetic phenomenon.

Perhaps the most important application of biological imaging has arisen due to the need to image aberrant biology where and when it occurs. The study of disease states and the need for effective diagnosis and treatment has led to the establishment of well defined biological imaging techniques. As well as the ability to image anatomical detail, it is now possible to extend biological imaging to the "molecular" or "cellular" levels where molecules and sub-cellular components can be studied and pictured in real-time. Advancement in terms of both spatial and temporal resolution aids in the visualisation and detection of disease, and helps treatment efficacy, these developments are certain to play an important role within "theranostics". Theranostics describes the use of diagnostic testing to diagnose disease, identify the correct treatment protocol and in addition, monitor patient response to therapy. Theranostics is set to create unique opportunities which will bring together both the pharmaceutical and diagnostic industries and will offer a more holistic approach where disease detection, diagnosis and treatment may be achieved concurrently.

1.1.1 Molecular Imaging

Molecular imaging has been defined by the Commission on Molecular Imaging of the American College of Radiology as: "The spatially localized and/or temporally resolved sensing of molecular and cellular processes *in vivo*".[1]

This multidisciplinary field implements the visual portrayal, characterisation and quantification of complex biological processes at the molecular level. This "sensing" of molecular and cellular processes is realised by imaging modalities which allow the visualisation of the signal transmission from a tagged component within a targeted

area, for example a fluorescent probe inside a cell. As such, molecular imaging modalities are designed to detect signals from a range of relevant chemical entities termed probes. These can be radiopharmaceuticals, incorporating radionuclides which are used in nuclear imaging techniques such as positron emission tomography (PET) or single photon emission computed tomography (SPECT), they can also be paramagnetic contrast agents utilised in magnetic resonance imaging (MRI) or fluorescent agents used in optical imaging.

Molecular imaging aided by probes and the very techniques dedicated to it, has played a vital role in the progression of the study of gross anatomy to a more molecular approach, downscaling our attention to metabolic and physiological processes. For most part, molecular imaging has been applied to the study of molecular and cell biology of gene expression, since the sequencing of the human genome and other genomes, has made available a large amount of deoxyribonucleic acid (DNA) sequence data. As such, the imaging of reporter gene expression has been widespread in molecular imaging.[2] Nevertheless, the imaging of specific molecules involved in disease pathways in living systems has also been studied.

In summary, molecular imaging is a multidisciplinary research field which is concerned with the development of novel probes, reagents and techniques to image specific biological pathways both *in vitro* and *in vivo* with an emphasis on the imaging of key components of disease manifestations and processes. Probes designed and synthesised in this project have been applied to the labelling of cells *in vitro* and the imaging of tumours *in vivo*. This has been made possible through the imaging of such particles by MRI and fluorescence microscopy.

1.1.2 Targets for Molecular Imaging

Any biological component or system that can attract and retain an exogenous probe, imaging agent, or ligand, through either covalent or non-covalent molecular interactions can act as a target in molecular imaging. Imaging targets may involve cells, organelles, proteins, organ systems, or the whole organism. Advances within molecular imaging have been made possible as a result of the close interface of biology and chemistry, whereby custom-made molecules have been designed and synthesised for specific biological target-recognition processes. The diagram in **Figure 1** represents some cellular targets for which specific probes may be designed and probe-target interactions studied through molecular imaging.

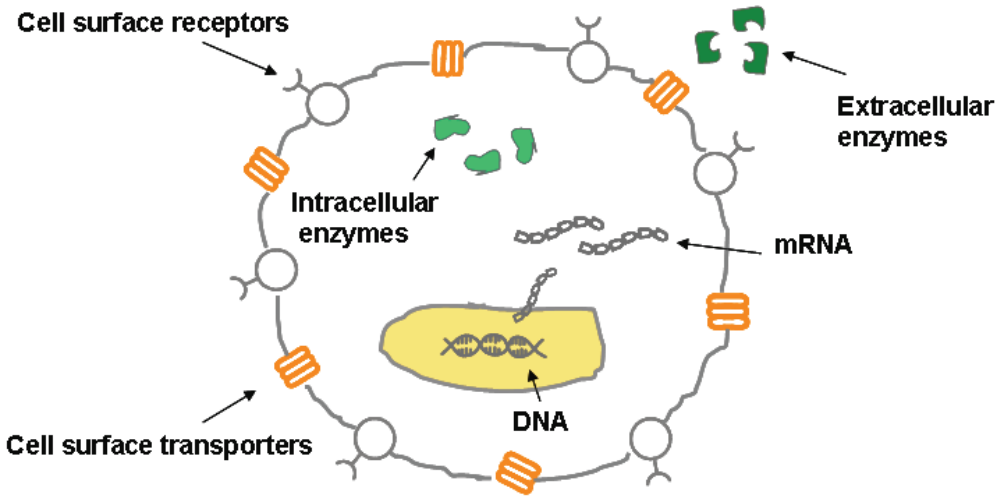


Figure 1. Example of targets for molecular imaging.

Molecular imaging techniques have been mostly applied to the imaging of processes that are relevant *in vivo*; and are mainly; the imaging of gene expression (see **1.1.3**) and molecular markers (**1.1.4**); where disease states can be identified, the progression or regression of cancer (**1.1.5**), drug treatment (**1.1.6**) and cell tracking where graft treatments like stem cell therapy can be visualised (**1.1.7***)*.

1.1.3 Molecular Imaging of Gene Expression

Molecular imaging techniques have been utilised to monitor gene expression using MRI, optical imaging, and nuclear imaging with PET and SPECT.[3] Studying gene expression has been valuable in assessing the role of particular genes in organisms and has helped shed light on the complex interplay of gene expression processes, and the link with their expression products, such as enzymes and cell receptors.[4-7] The imaging of reporter gene expression has proved valuable in gene therapy where, by coupling the reporter gene to a therapeutic gene, the level of expression of the therapeutic gene is also established and quantitated.[8-11]

Gene therapy aims to cure disease using the correct version of the functional gene that has become mutated or is absent within the host. Another level at which imaging probes may play a role is their interaction with the products of gene expression.[12] For example, specific genes can encode products such as intracellular enzymes, cell surface receptors or peptides that exogenous imaging probes can interact with, thereby allowing for a unique signature resulting from their interaction.

The herpes simplex virus thymidine kinase (HSV1-*tk*) reporter gene which is the gene that produces the thymidine kinase enzyme has been widely used in gene expression studies.[13-16] This enzyme has broad substrate specificity and once produced a range of radiolabelled ligands can be used as the enzyme's substrate. These probes can be transported across the cell membrane via an active transport mechanism. Once inside the cell the radiolabelled substrates are phosphorylated by the viral enzyme (thymidine kinase, which is not naturally expressed from the host) and become trapped in the cell as signalled by the cell's acquired radioactivity.[17] This system has been studied in PET imaging most extensively and utilised in cancer therapy.[18] For instance, the radiolabelled tracer; 5,[^{131}I-2'-fluoro-1-β-$_{D}$-arabinofuranosyl-uracil (FIAU) is administered and crosses the cell membrane by diffusion and facilitated transport (thymidine kinase transporters). It is then phosphorylated by the HSV1-*tk* enzyme from FIAU to FIAU monophosphate (FIAU-MP) which cannot escape cell membranes and hence accumulates inside the cells. Therefore, FIAU's inherent radioactivity accumulates in cancer cells.[19] This type of approach enables the monitoring of cancer gene therapy in patients.

The transferrin receptor (Tf-R) is also an attractive target for molecular imaging since it is over-expressed in various tumour cells and as such has been a target for drug transport.[20] Tf-R has also been used as a potential transporter for accumulation of probes in cells. Weissleder *et al.* have demonstrated the triggerable enhancement of signal from a sample by deliberately over-expressing the Tf-R in mice and then administering transferrin bound iron probe particles (Tf-MIONS, see **Figure 2**).[21,22] This type of biological signal amplification is a good means of studying the interaction of contrast agents attached to target receptors and also provides for a reliable method of quantitating gene expression, itself a challenging area in genetic therapy.

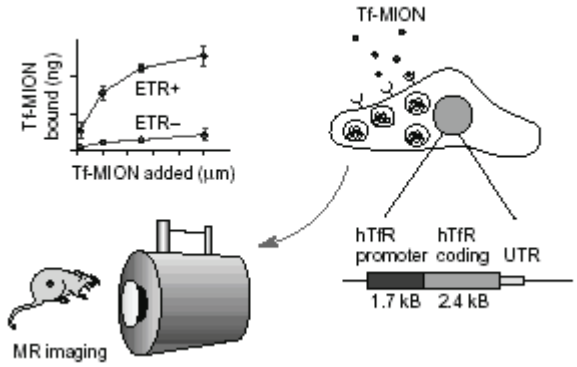


Figure 2. This diagram illustrates the use of MRI to visualise gene expression, receptor over-expression, and the use of paramagnetic probes. ETR = engineered transferrin receptor, hTfR = human transferrin receptor, mRNA = messenger RNA, Tf-MION = transferrin-monocrystalline iron oxide nanoparticles, UTR = untranslated region.[22]

In MRI, contrast agents are often used to further enhance images, commonly gadolinium (Gd) is incorporated in MRI contrast agents since it is highly paramagnetic and capable of perturbing many water hydrogen nuclei. This in turn leads to a signal enhancement and subsequent localisation of the contrast agent (refer to **section 1.5** for more detail). One of the most elegant uses of molecular imaging for studying gene-expression is the use of "smart" activatable molecular probes in MRI. Here high affinity crowded chelators have been attached to Gd, acting like a "cap" and preventing water molecules from making contact, thus suppressing the MRI signal at first (**Figure 3**). However, upon cleavage of the probe by a galactosidase enzyme (the expression of which is induced), access by water molecules to the Gd is restored as indicated by an increase in image brightness.[23,24]

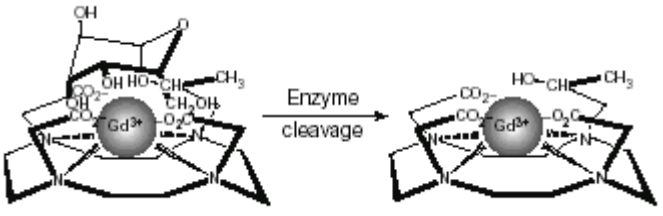


Figure 3. The enzymatic cleavage of a macromolecular Gd contrast agent, the enzyme here is β-galactosidase which is a product of gene expression. In state **a** there is no MR signal, in state **b**, upon cleavage of the sugar moiety, the MR signal appears.[23]

In the same study, experiments in *Xenopus* embryo models showed areas of intense MR signal which correlated with the regions expressing β-galactosidase, demonstrating the ability of MRI to detect gene expression *in vivo*.

Various molecular imaging methods and probes have been applied to the study of gene expression as described above.[25-28] However, an ideal *in vivo* gene expression system must be minimally invasive and clinically translatable. Much effort is currently dedicated to designing reporter systems bearing such qualities. In addition, multimodality imaging is also increasing in popularity for studying gene expression, where the partnership of PET, MRI or optical imaging techniques could be used to develop a single reporter construct with a gene product that can be analysed by scintillography, fluorescence, bioluminescence, and nuclear or magnetic resonance imaging technologies.[29] Here, the use of two signatures, such as fluorescence and MRI on the same probe is commonly referred to as bimodal or multimodal systems.

Molecular imaging of gene delivery and expression is set to be of great value in the spatial and temporal analysis of gene therapy in patients and can help shed light on many aspects of gene therapy. These can include information on whether the genes have been delivered to the target site, the kinetics of gene expression and the correlation of this data with the actual therapy observed.[30]

1.1.4 Molecular Imaging of Molecular Markers

Specificity has become an important mark of recent classes of therapeutics. Paul Ehrlich's notion of the "magic bullet" is of continuing relevance within the field of molecular imaging today, with molecular markers fitting this description well.[30] Molecular markers are chemical entities which are capable of specifically binding to targets of interest; their role can be relevant only to an imaging platform, or may extend to one of concurrent imaging and therapy, achieved through an additional attachment of a diagnostic or therapeutic moiety (theranostics). A common requirement for these agents is that they posses a targeting component which signals their localisation and a component that enables their detection by namely, MRI, optical or nuclear imaging (optical imaging techniques are mainly fluorescence or bioluminescence based, and nuclear imaging is a collective term for techniques such as PET or SPECT that image radionuclides). The molecular interactions responsible for localisation of the agent can be its binding to the targeted molecule, its local accumulation by means of molecular or cellular activity of the target, or its

modification to a detectable form through enzymatic activity of the target under investigation.

An effective demonstration of molecular imaging using molecular markers is realised with the targeted contrast agent prepared by Poduslo *et al.* for *in vivo* targeting of amyloid plaques in Alzheimer's disease.[31] A derivative of human amyloid-*β* (A*β*) peptide was designed, synthesised, and covalently attached to an MRI contrast agent. This novel molecular marker was shown to selectively target individual amyloid plaques in the brain of Alzheimer's disease transgenic mice. This engineered molecular maker was able to cross the blood-brain barrier due to the inclusion of Asp/Glu amino acids in the peptide sequence. This type of system is envisaged to enable the *in vivo* MR imaging of even single amyloid plaques within the brains of Alzheimer's sufferers, and may be used to diagnose the disease at an onset stage, contributing to the assessment of anti-amyloid therapies that currently exist.

Apoptosis (programmed cell death) is an area that has attracted a multitude of molecular markers designed to target the main apoptosis marker, annexin V. Unbalanced regulation of apoptosis is in fact a major cause of disease onset, applicable to cardiovascular, cancer and neurodegenerative diseases.[32] Once cells enter apoptosis, the composition of phospholipids in their cell membranes changes. The start of apoptosis is marked by the expression of phosphatidylserine (PS). This lipid is presented on the outside of the cell membrane and therefore annexin V is capable of binding to PS during apoptosis.[33]
Annexin V has also been radiolabelled using ^{99m}Tc, ^{18}F, as well as with various radioactive isotopes of Iodine (for example ^{124}I), and imaged using PET.[33,34,35] As a result, radioactively tagged annexin is a useful marker for assessing the efficacy of cancer treatments, given that many cancer therapies lead to eventual cell death by apoptosis.

Molecular markers in the form of antibodies have also been coupled to contrast agents and their potential as immunocontrast agents demonstrated. Muller *et al.* have shown the effectiveness of immunocontrast agents for MR imaging of human colorectal carcinoma (LS 174T) grafted in nude mice.[36] Their results showed tumour uptake of the Gd-labelled immunoconjugates of up to 20% compared to control mice as evaluated by MRI.

A large number of molecular markers have been developed to date. Each has been successful in addressing the visualisation or marking of a particular disease state or condition. The aforementioned examples are merely a small selection from the entire plethora of developed molecular markers for molecular imaging. Molecular marker development is a proliferating field that continues to flourish and generate more uniquely targeted imaging agents, with the eventual goal of facile clinical translation, disease detection, and diagnosis.

1.1.5 Molecular Imaging of Cancer

Molecular imaging technologies can be used to study both the structure and function of processes associated with cancer. Computer tomography (CT), MRI, and ultrasonography (US) are standard imaging techniques used in oncological imaging. Serial imaging using these techniques can reveal morphological features of lesions and changes over time.[37] These techniques, in addition to PET, SPECT and optical imaging have been used to image perfusion in order to improve detection and characterisation of tumours, and to monitor therapeutic response. Perfusion can be defined as the blood flow through a tissue of interest per unit volume.

MRI has been applied to the study of tumour perfusion through the use of dynamic contrast-enhanced MRI (DCE-MRI). DCE-MRI is a fast imaging technique which allows for images to be acquired prior, during and after intravenous administration of Gd contrast agents. This type of imaging has made possible the assessment of tumour microvascularity, microvessel density, metastatic tendency, and tumour recurrence information.[38] At present CT imaging is the most frequently used imaging tool for the clinical analysis of structural features of cancer.[37] Another interesting area of cancer imaging is diffusion imaging, whereby the diffusion of water molecules can be quantitatively measured with diffusion-weighted MRI (DW-MRI). This technique yields information about tissue structure and water content and hence can be used to estimate tumour cellularity and to detect early therapeutic effects.[39] It is believed that an increase in tumour cellularity leads to a restricted motion of water molecules by diffusion because of the reduction in the extracellular area, which, under normal conditions allows water diffusion more readily.

A significant area in cancer imaging is the imaging of angiogenesis, the process of new blood vessel formation. Angiogenesis has been the targeting component of many therapeutic approaches, in particular the targeting of $\alpha_v\beta_3$ integrins which are presented on activated endothelial cells that are undergoing angiogenesis.[40] The

molecular imaging of receptors that are over-expressed in various cancers is also contributing to the development of cancer therapeutics. For instance, the HER-2/neu receptor is over-expressed in numerous cancers, and antibodies targeted against this receptor have been investigated for anticancer therapy in clinical trials.[41]

1.1.6 Molecular Imaging in Drug Discovery and Development

The drug discovery and development process requires substantial time and resources since only a handful of compounds from thousands of candidates actually make it through to even a pre-clinical testing stage.[42] As such, drug discovery can benefit from an extensive application of molecular imaging for both pre-clinical small animal and human studies, aiding the acceleration of the drug development process. Molecular imaging techniques such as ultrasound, micro-computed tomography (micro-CT), MRI, PET, SPECT, bioluminescence (BLI) and near infrared fluorescence imaging (NIRF) have been used in drug research and discovery. However, the nuclear imaging techniques, PET and SPECT have had foremost use due to their excellent sensitivities. PET and SPECT both use radionuclides, where the isotopes used are unstable and decay by emitting radiation to achieve a stable non-radioactive state, this radiation is then detected and translated into an image. These techniques posses the level of sensitivity that is required to study and monitor drug distribution, pharmacokinetics and pharmacodynamics. In PET imaging many drugs can be labelled with ^{11}C or with ^{18}F and since only a single radioisotope atom is required per molecule for an effective signal, labelling of the drug, only minimally affects its overall physicochemical properties. For example, Fluconazole which is a fluorine containing anti-fungal agent has been successfully labelled and its kinetics and biodistribution studied quantitatively in various tissues, including its distribution in the human brain.[43]

With respect to molecular imaging agents, fluorodeoxyglucose (^{18}F-FDG) has been most extensively studied clinically, where it is a marker of glucose transport expression in metabolism. To this end, the use of PET in clinical imaging has become pivotal. As well as its use in imaging brain function, ^{18}F-FDG has been shown to be an excellent tumour detection marker since most tumours have a higher metabolic rate for glucose than normal tissues. Additionally, ^{18}F-FDG uptake can be correlated with the type and aggressiveness level of certain tumours.[44]

Radioimmunotherapy is another area where the “magic bullet” concept has been applied using nuclear imaging; this involves the targeting of an antigen expressed on a tumour cell by a specific antibody that binds to the antigen. The antibody is usually

labelled by a γ emitter (for example, ^{111}In or ^{99m}Tc) for labelling or a β emitter (for example, ^{131}I or ^{90}Y) which can be used for cancer treatment.[45] In most of these studies, the γ emitting agent is administered initially to establish the antibody targeting efficacy (dosimetry) and successive therapy is achieved by administering the β emitter.

In recent years the development of biomarkers has led to the pharmaceutical industry's avid use of molecular imaging techniques. The term biomarker or biological marker is defined by the Food and Drug Administration (FDA) as "a characteristic that is objectively measured and evaluated as an indicator of normal biologic processes, pathogenic processes, or pharmacologic responses to therapeutic intervention".[46] The appropriate tagging of biomarkers allows for their detection and localisation in relevant biological models and aids in the prioritisation of drug discovery resources providing early proof-of-concept studies for novel therapeutic targets. Biomarker research has been applied to the identification of plaques vulnerable to rupture in the primary prevention efforts for coronary heart disease where MRI has been used to study heart function and structure, and to assess plaque composition.[47] In addition to cardiology biomarker imaging, molecular imaging has also been used to study imaging-based biomarkers for neurodegenerative diseases such as Alzheimer's disease, these comprise the use of magnetic resonance spectroscopy (MRS), FDG-PET, SPECT and volumetric MRI of the whole brain for studying amyloid plaques.[48,49]

1.2 Cellular Imaging

Cellular imaging by optical methods such as fluorescence microscopy is routine procedure in many biological laboratories. Fluorescence microscopy has revolutionized our understanding of biological processes in single living cells. Using fluorescence microscopy the movement of cellular components such as proteins, nucleic acids and sub-cellular structures have been studied and analysed. Cell imaging however, has moved beyond the use of staining protocols and histological analysis in order to visualise cellular components of interest. The ability to study cells has been assisted by the appropriate use of pertinent imaging techniques. Cellular imaging is a collective term for the visualisation of any type of cell and has been defined as "the visualization of specific cells in an intact animal".[50] Molecular imaging aims to visualise molecules and can be specific, whereas cellular imaging concerns the imaging of entire cells.[51] Nonetheless, both molecular and cellular imaging involves the use of molecular probes.

Cellular imaging is an important area which has facilitated the study of cell behaviour in living animals; for example, the fate of stem cells has been tracked and monitored in a serial manner over time. The labelling of cell populations serves to shed light on the *in vivo* behaviour of therapeutic transplanted cells, for example, their tracking, viability, ability to differentiate and their chromosomal stability. The labelling of cells of interest is usually achieved through the use of molecular probes or nanoparticles which are capable of effective cellular entry. Perhaps due to the stability and customisable nature of the type of probes and contrast agents used in MRI, the use of paramagnetic contrast agents for the labelling and tracking of various cells *in vivo* has gained popularity in comparison to fluorescent or nuclear imaging techniques. Fluorescent labelling is often depth restricted and imaging with PET or SPECT is limited due to short lived radioisotopes, and a poor spatial resolution. In keeping with this general trend and the use of MR imaging in this project, the following discussions will mainly focus on the use of MRI compatible cell labelling techniques.

MRI is capable of producing three dimensional images of tissues containing water with a high degree of spatial resolution. In MRI contrast agents are used to further improve the quality of an image. These agents consist of molecules which incorporate a paramagnetic metal ion, most commonly Gd or Iron (Fe). Image improvement arises due the effect of the enhancement of longitudinal (T_1) or transverse (T_2) relaxation times of the surrounding bulk water protons by the coordinated metal ion. Contrast agents incorporating Gd increase both $1/T_1$ and $1/T_2$

but are generally used in T_1-weighted imaging where their $1/T_1$ effect is greater in tissue than their $1/T_2$ enhancement. Fe containing agents, on the other hand, lead to more substantial increases in $1/T_2$ and are therefore visualised with T_2-weighted images (see section **1.5** for a more detailed discussion on MRI).[52]

1.2.1 Cellular Labelling and MRI

Magnetically labelling cell populations can help our understanding of pathogenic processes considerably, since labelled cells can be studied both under normal and atypical states. The future vision of clinical cell therapy is a promising one, since stem cells, or corrected specialist immune cells can be transferred to patients and their outcomes imaged by MRI, a pre-existing non-invasive clinical imaging modality. For cell populations to be imaged by MRI they must be distinguishable from natural background noise signal. The markers that are to be used for their labelling should be able to produce significant enhancement of either T_1 (positive, bright) or T_2 (negative, dark) relaxation. The ideal cellular label as addressed by Frangioni *et al.* should posses the following characteristics: a strong signalling effect, a biocompatible nature, non-interference with cellular genetics, ideally detect single cells, have minimal dilution effect due to cell division, remain retained only in the targeted cell population, and finally, have the ability for temporal imaging over long periods of time.[53]

The traditional cell labelling agents of choice for MRI have been paramagnetic Fe or Gd based agents. Cells of interest can be labelled with these agents *in vitro* or *ex-vivo* and then subsequently re-implanted into specific sites *in vivo*.

There are various mechanisms through which cellular labelling agents have been able to enter cells. These mechanisms can be specific or non-specific. In macrophages (white blood cells) have been shown to continuously and non-specifically phagocytose large labelling particles, this has been useful in the visualisation of local inflammation.[54] The various cell internalisation mechanisms are shown in **Figure 4.**

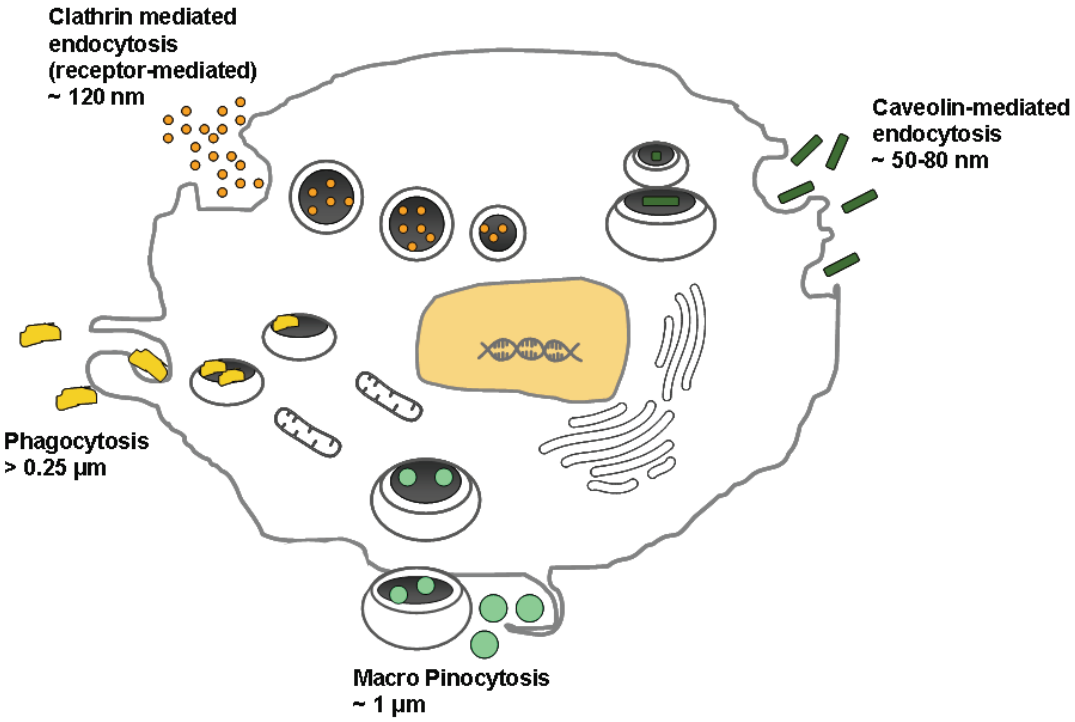


Figure 4. Cell entry mechanisms. The size of particles is shown for the various uptake mechanisms of macromolecules and particles into cells.

There are a number of pathways that particles can use to enter mammalian cells, these all fall under the general expression "endocytosis".[55] Endocytosis may include any of the following cell ingesting processes; phagocytosis, pinocytosis, clathrin-mediated endocytosis, caveolin-mediated endocytosis, and clathrin and caveolin independent endocytosis.[50] Phagocytosis is the uptake of large particles by cells and most phagocytic cells of the immune system use phagocytosis to internalise foreign bodies. These cells include neutrophils, monocytes, macrophages, and microglia. Non-phagocytic cells internalise particles using pinocytosis or fluid phase uptake and it is generally considered that any non-specific internalisation into cells is due to this mechanism. [50]

1.2.2 Iron Based MR Cellular Labelling Agents

Iron containing contrast agents have been more widely used in cellular labelling due to their biocompatible nature and strong effects on T_2* relaxation (a variation of T_2 relaxation). These Fe agents are used as part of superparamagnetic iron oxide nanoparticles. Contrast agents made of superparamagnetic iron oxides usually consist of a monocrystalline (MION) or polycrystalline magnetite (iron oxide) core, embedded within a polymer coating, such as dextran, carboxydextran, citrate or

polyethylene glycol (PEG) for effective cellular entry, solubility and immune system shielding respectively.[56] A variation in size of these iron oxide nanoparticles produces ultrasmall superparamagnetic iron oxide particles (USPIO), superparamagnetic iron oxide (SPIO) and micron metre sized iron oxide particles (MPIO). USPIOs, which are small enough in size to permeate the cellular capillary wall have been investigated in clinical trials for the MR imaging of lymph and liver tumours.[57,58] These agents generate strong T_2 and T_2* MR signal changes and have also been used in the imaging of plaques, since they are ingested by macrophages through phagocytosis.[59,60] SPIO particles have been shown to be taken up by various cells, including T lymphocytes, dendritic cells, monocytes, cancer and stem cells.[61]

The choice of polymer coating of the iron nanoparticles has been shown to be a determining factor for the route of cellular uptake. For example, Fleige *et al.* have shown particles coated with citrate, to enter macrophages via phagocytosis, whereas dextran-coated iron oxide particles were shown to be taken up by macrophages through pinocytosis.[62] Dextran-coated SPIOs were first introduced for hepatic imaging, where following intravenous injection, the particles are rapidly taken up by liver Kupffer cells, which appear hypointense (dark) in MR images.[63]

SPIO particles have been further functionalised to increase their cellular uptake ability by the incorporation of transfection agents or small peptides such as the transactivator (Tat) peptide of HIV which has been directly attached to iron oxide nanoparticles.[64] A high loading of these particles into cells was also achieved with Tat-derivatised cross-linked superparamagnetic iron oxide (Tat-CLIO) particles, where the *in vivo* tracking of haematopoietic and neural progenitor cells to the bone marrow of mice was successfully imaged.[64]

A strategy of increasing cellular uptake of particles is their surface functionalisation with a targeting ligand which can lead to the effective uptake of target cells via receptor-mediated (clathrin mediated) endocytosis. Various moieties have been used for cell surface targeting including, monoclonal antibodies, transferrin, albumin, insulin and growth factors such as vascular endothelial growth factor (VEGF).[65] It is postulated that since the receptors for these ligands are frequently over-expressed on the surface of cancer cells, they preferentially target cancer cell surfaces.[66] Suzuki *et al.* have recently tested various methods of labelling embryonic stem cells with iron oxide particles and have concluded that the use of protamine sulphate in the preparation of these particles significantly increased their intracellular uptake *in*

vitro.[67] Protamine sulphate is a small naturally occurring polycationic peptide which is an antidote to heparin anticoagulation, and also an efficient cell transfecting agent.[68]

The ability to label single cells by MRI is an exciting avenue and would be an ideal validation of cell labelling and localisation of molecular probes. Recently Zhang *et al.* have imaged single labelled living human umbilical vein endothelial cells (HUVEC) with iron oxide particles *in vitro.*[69] Uptake of SPIOs was confirmed with Prussian blue staining, electron microscopy and MACS (magnetically activated cell sorter) sorting after a 24 h incubation period (**Figure 5**). This study demonstrates the utility of cellular labelling in endothelial cell transplantation.

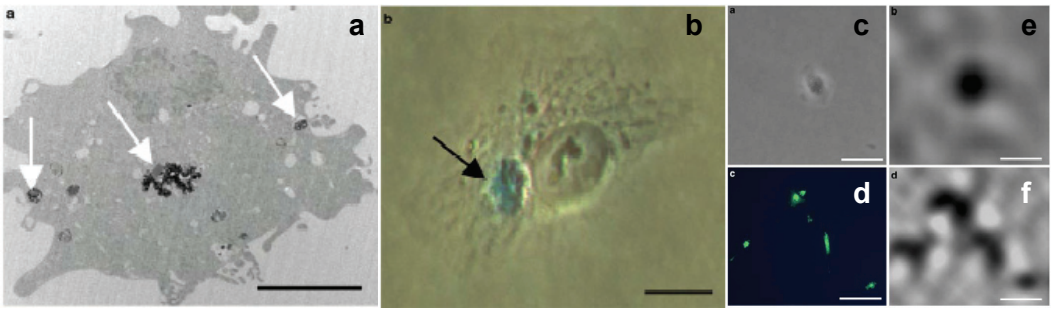


Figure 5. a: An electron-microscope image of a single labelled HUVEC (x 5600, bar: 10 μm). **b:** A Prussian blue stained HUVEC cell (x 5600, bar: 10 μm). **c-d:** Bright field and fluorescent images of different HUVEC cells 24 h post labelling and **e-f:** Corresponding MR images of **c** and **d** respectively.[69]

More recently, the *in vivo* detection of single primary mouse hepatocytes was demonstrated by Shapiro *et al*.[70] These cells were double labelled with green fluorescent iron oxide particles of 1.63 μm and a red fluorescent endosomal labelling dye. Upon labelling they were then injected into the spleens of mice and their common migration from the spleen to the liver was observed as expected, one month after administration. This result was also co-validated with histological observations and controls, in order to verify the dark contrast regions in the liver, to be that of disperse single cells. This study exhibits the viability of detecting single-cells *in vivo* by MRI and may be advantageous in the assessment of donor hepatocytes for patients with damaged livers requiring transplantation.

Cell labelling using superparamagnetic agents has been widely practiced.[71] However, there are a number of limitations that should be taken into account, such as the loss

of Fe content once labelled cells divide (valid for any cell labelling agent in general), and the fact that cells use Fe storage proteins such as apoferritin further complicates signal measurement.[72]

1.2.3 Gadolinium Based Cell Labelling Agents

From examples presented in the previous section, it can be concluded that labelling cells with various superparamagnetic iron core particles can be readily accomplished. These agents exhibit a high susceptibility effect in magnetic fields and can therefore produce very strong negative contrast enhancement in MR imaging, as demonstrated by their ability to image single cells both *in vitro* and *in vivo*. However, the high sensitivity and susceptibility effect of superparamagnetic iron oxide nanoparticles is not always advantageous as the observed signal is in fact a hyposignal (dark) and this can make the precise localisation of iron contrast agents difficult.[73] The hypersensitivity (or susceptibility) of superparamagnetic contrast agents also affects spatial resolution and leads to poor image quality (see **Figure 5**, **f**). Therefore, the need to explore Gd based cell labelling agents has arisen given that Gd based agents do not suffer from any susceptibility issues, and image enhancement is purely a consequence of the metal ion's effect on MR relaxation properties.

Sitharaman and colleagues have recently developed gadofullerenes as magnetic labels for cellular MR imaging by investigating the use of anionic $\{Gd@C_{60}[@C(COOH)_2]_{10}\}$ gadofullerene complexes.[74] Inductively-Coupled Plasma Atomic Emission (ICP-AE) spectroscopy and T_1 relaxation measurements were used to assess the cellular uptake efficiency and internalisation of gadofullerene on both NIH 3T3 (mouse embryonic fibroblast) cells and marrow stromal cells. A cell labelling efficiency of up to 100% for both cell types was reported, and it was calculated that a total of 10^{11} Gd^{3+} ions were taken up per single cell. The non-specific uptake and the high labelling efficiency of these gadofullerenes can be useful in detecting any type of labelled cell by MRI *in vivo*.

Recently a newly synthesised contrast agent system, Biotin-BSA-Gd-DTPA-FAM was used to track tumour-associated stroma by fluorescence and MR imaging.[75] Here, Granot *et al.* have demonstrated the administration of the multimodal triple-labelled albumin-based contrast agent, Biotin-BSA-Gd-DTPA-FAM which was internalised into tumour associated myofibroblasts, where it appeared to be localised in intracellular granules. This was established both *ex vivo* by incubation of cells with the contrast material, and *in vivo* by intravenous administration of the contrast material to tumour-

bearing mice. *Ex vivo* incubation of human fibroblasts derived from skin, normal breast, and breast tumour tissues with the fluorescent-conjugated contrast material confirmed the uptake of biotin-BSA-Gd-DTPA-FAM into cytoplasmic granules. The retention of labels in cultured fibroblast cells was demonstrated for up to 2 weeks and derivation of the effective relaxivity of the contrast material showed increased visibility of Gd during the first four cell cycles. Interestingly, it was concluded that, the relaxivity of the contrast material increases with cell proliferation.[71]

Previously in our group, we have demonstrated the use of paramagnetic Gd liposomal particles in the efficient cell labelling of three cell lines. Liposomes are composed of lipids that self-assemble in aqueous media to form round-bilayer membranes with an aqueous core. Oliver *et al.* have described the development and *in vitro* analysis of MAGfect, a novel liposome formulation containing a lipidic based Gd contrast agent for the labelling and MR visualisation of cells.[76] MRI analysis of cells labelled with MAGfect showed them to be highly MR active, capable of reducing T_1 relaxation to < 50% in comparison to control unlabelled cells. In addition, MAGfect was also found to be an effective vehicle for pDNA transfection of cells which demonstrated the additional gene delivery function of this molecular imaging agent.

1.2.4 Fluorine Based Cellular Labelling Agents

Recently, MR imaging of labelled immunotherapeutic cells has been achieved through the use of ^{19}F perfluoropolyether (PFPE) agents. Since background ^{19}F signal in living systems is extremely low, the detected ^{19}F signal is consequently only due to labelled cells. Ahrens and colleagues have demonstrated the labelling efficiency of these agents with dendritic cells.[77] These cells have been under investigation for cancer therapy and immunological diseases. Using both ^{19}F spectroscopy and ^{1}H MR imaging they have successfully demonstrated internalisation and quantification of the PFPE emulsions into cells *in vitro* and have also shown effective liver signal enhancement in mice *in vivo*. More recently, they have labelled diabetogenic T cells and shown their homing to the pancreas 48 hours post administration in type 1 diabetic mice.[78]

Fluorine spectroscopy has also been used to monitor fluorinated drugs and their effect on metabolism. Klomp *et al.* have shown that by using a tuneable radiofrequency coil, ^{1}H MR imaging and ^{19}F metabolite spectroscopy can be achieved simultaneously in order to detect ^{19}F drug metabolites in the human liver.[79] Using ^{19}F

spectroscopy they were able to quantitate tissue metabolite concentrations of the chemotherapeutic drug, capecitabine.

Lanza *et al.* have demonstrated the use of nanoparticle emulsions of perfluoro-15-crown-5-ethers (CE), as well as particles consisting of perfluoroctylbromide cores (PFOB), and have targeted these agents to fibrin clots *in vitro*.[80] These agents were further functionalised with biotin for targeting to avidin incubated clots, and also contained Gd (CE particles). These particles which were on average around 250 nm, were estimated to contain approximately 100,000 Gd^{3+} ions per CE particle and the PFOB particles were estimated to have a 100 M concentration of ^{19}F. Gadolinium diethylene-triamine-pentaacetic acid-bis-oleate (Gd-DTPA-BOA) was also incorporated in a 30 mol% ratio in the CE emulsions.
Both T_1-weighted images and ^{19}F spectroscopy were obtained of the fibrin clots and signals from both CE and PFOB agents were easily distinguished, allowing for the acquisition of ^{19}F MRI of the fluorine particles bound to fibrin clots. In a more clinically relevant experiment, both ^{1}H and ^{19}F images were obtained, with ^{19}F images revealing "hot spots" of bound nanoparticles in carotid artery specimens from symptomatic patients. This elegant study demonstrated the synergistic utility of both proton and fluorine MRI in clinical imaging at 1.5 Tesla (T). The utility of ^{19}F MRI in conjunction with ^{1}H MRI was also supported by work carried out by Higuchi *et al.* in their imaging of amyloid β plaques *in vivo*.[81] They were able to label brain plaques using a ^{19}F amyloidophilic contrast agent in mice.

1.2.5 Manganese Based Cellular Imaging agents

Manganese-enhanced MRI (MEMRI) has recently been established as a technique to image the movement of Mn^{2+} ions in the body, and is particularly applied to the imaging of active brain regions.[82] Manganese chloride ($MnCl_2$) is an effective MRI T_1 relaxation agent, and once injected into the body, produces Mn^{2+} ions, which are able to enter cells via voltage gated calcium channels. This movement of Mn^{2+} ions along neuronal pathways allows for the imaging of active brain regions.

Manganese has also been used in cardiac imaging, since heart muscle tissue also contains active voltage-gated calcium channels which can exchange Ca^{2+} for Mn^{2+}.[83] Aoki *et al.* have successfully shown the labelling of lymphocytes using $MnCl_2$.[84] Van der Linden *et al.* have also used $MnCl_2$ in their extensive studies of the neuronal activity of the song bird vocal control system.[85,86]

1.2.6 Stem Cell Imaging With MRI

The use of MRI in imaging cells and their biodistribution has been valuable in the monitoring of effective therapies for the treatment of cancer and conditions such as strokes. Undoubtedly, stem cell therapy presents the most distinguished use of cellular imaging to date; an elegant study by Kraitchman *et al.* has demonstrated the feasibility of MRI in this field.[87] Paramagnetically labelled stem cells were used to study mesenchymal stem cell (MSC) migration in myocardial infarcts *in vivo*. The stem cells were magnetically labelled with iron containing ferumoxides (Feridex) and imaged. This study demonstrated that local transplantation of labelled stem cells shows great promise in the treatment of many cardiovascular diseases. This recent ability to label stem cells with paramagnetic MRI visible contrast agents enables serial tracking *in vivo* with a high spatial resolution, avoiding the need to use post-mortem examinations (in animals) to determine the fate of migrating cells, and their number and location. MRI presents a non-invasive modality for the imaging of stem cell grafts. MRI cell tracking has found a range of applications in monitoring transplantation of stem cells and cell-based therapies.[88-92] The labelling of stem cells with iron oxide particles has had prevalence since they can be loaded in high amounts into cells and have excellent sensitivity.[93-95]

An area which has received most interest in the use of stem cell labelling and cell therapy, due to its limited regenerative capacity, is the central nervous system.[96-99] Modo *et al.* have labelled neuronal stem cells with a dual modality contrast agent that is both magnetically and fluorescently labelled, known as GRID (Gadolinium rhodamine dextran).[100] The cells were labelled *in vitro* and re-implanted into the brains of ischemia-damaged rats. MRI and fluorescence microscopy was used to co-validate *in vivo* MR imaging and histology observations. This study demonstrates the utility of bimodal imaging approaches for stem cell tracking and monitoring.

Bos *et al.* have studied the labelling and tracking of stem cells to the liver.[101] Rat MSC's were isolated from the bone marrow and labelled with SPIOs using a dendrimer polymer as the transfection agent. Cell labelling persisted up to 12 days and the labelled cells were shown to distribute throughout the liver. The MSCs were loaded, labelled with clinically approved SPIOs *ex vivo*, which were internalised by endocytosis in macrophages and the particles were injected intraportally into the liver. This work clearly demonstrates successful tracking of labelled MSCs with MRI. Most recently the ability to label MSCs without a transfection agent was demonstrated by

Hsiao *et al.*, who have used SPIOs coated with carboxydextran to label these cells and detect them with clinical 1.5 T scanners at the single cell level.[102]

1.2.7 Cellular Labelling with Other Imaging Modalities

PET and SPECT techniques have also been employed in the imaging of cells, Adonai *et al.* have used copper-64-pyruvaldehyde-bis(N^4-methylthiosemicarbazone) (^{64}Cu-PTSM) to radiolabel cells *ex vivo* for *in vivo* PET imaging studies of cell trafficking in mice.[103] They showed that labelling efficiency was directly proportional to ^{64}Cu-PTSM concentration and influenced negatively by serum, and that the liver was the principal organ of tracer localisation after tail-vein administration of ^{64}Cu-PTSM. However due to the limited $t_{1/2}$ of ^{64}Cu (12.7 h) experiments requiring longer time spans are not possible using this type of labelling.

Bioluminescence imaging of lymphocyte trafficking *in vivo* has been achieved by Hardy *et al.*, with the specific labelling of effector lymphocytes *in vitro* permitting localisation of these cells in animals by BLI.[104] Optical imaging is promising here, because of the ability of luciferases to emit light without external excitation and therefore, they can act as useful genetic tags. The disadvantage of this method is that an inherent genetic modification is necessary and the technique cannot be viable for clinical use in the long term. BLI also has depth detection limits and is therefore restricted to small animal studies.

Cellular MRI has benefited from a broad range of applications in biology and the concept of pre-labelling and re-implantation of cells followed by *in vivo* imaging has started in human subjects.[105] However, research is continuing to further optimise and make safe methods of cellular labelling which can become easily translatable to the clinic.

1.3 Tumour Imaging

Solid tumour imaging based on small animal models of cancer has helped our understanding of human cancer significantly. Appropriately established models are able to accurately shed light on tumour characteristics such as angiogenesis, stromal interaction, and hormone dependence.[106] Both molecular and cellular imaging techniques play an important role in analysing and studying the effects of therapy on tumour size, growth and apoptosis. This has also eliminated the need for invasive methods and post-mortem analysis. Imaging techniques such as MRI, PET and SPECT can all aid in the assessment of tumour physiology at both the molecular and cellular level, and information can be received dynamically. MRI has many advantages here, since both anatomical and functional information can be obtained systematically and dynamically over any given period of time.

1.3.1 Angiogenesis Imaging

Angiogenesis can be described as the growth of new blood vessels. This process involves the complex interplay of a range of specialised cells, growth factors, signalling molecules and regulatory elements. Molecular imaging of angiogenesis has been achieved through the use of non-invasive MRI and functional MRI (fMRI). The imaging of endothelial cell markers in angiogenesis has led to a critical understanding of angiogenic processes, an outcome which would have undoubtedly proved complex without the use of targeted contrast agents. Vascular endothelial growth factor receptors (VEGFR) that are tyrosine kinase endothelial cell-specific receptors are clinically relevant, since VEGF is known to be a predominant proangiogenic factor.[107] Once VEGF binds to various VEGFRs, a phosphorylation cascade is initiated which activates downstream receptor pathways leading to endothelial cell proliferation and angiogenesis. Various adhesion molecules have been shown to target efficiently to endothelial receptors which are themselves involved in VEGF activity. These include $\alpha_V\beta_3$, the integrin binding site for the arginine-glycine-aspartic cyclic tripeptide sequence (RGD) and E-selectin.[108]

Recently Mulder *et al.* have imaged angiogenesis by detecting the over-expression of $\alpha_v\beta_3$ integrins in tumour bearing mice using a combination of MRI and fluorescence microscopy.[109] They prepared paramagnetic and fluorescent liposomes, surface modified with the cyclic RGD amino acid sequence. These RGD functionalised liposomes were shown to target the vessel walls of cancer cells both *in vitro* and *in vivo.* Fluorescence microscopy revealed that both the control non-paramagnetic and

paramagnetic RGD liposomes targeted the vessel wall. The use of fluorescence microscopy in this study differentiated between the activity of the targeted RGD (which strongly bound to the $\alpha_v\beta_3$ receptor) and the control liposome modified with the control peptide sequence, RAD (Glycine (G) replaced by Alanine (A)), which has no affinity for the receptor.

1.3.2 Further Tumour Imaging Methods

Raatschen *et al.* have been able to use a novel contrast agent, Gd-GlyMe-DOTA-perfluorooctyl-conjugate (Gadofluorine M™), to differentiate between benign and malignant tumour lesions, in addition to evaluating the severity of the lesions and identifying necrotic areas.[110] This agent has a tendency to form micelles in aqueous media due to its molecular weight (1528 Da) and lipidic structure, and as such is able to accumulate in tumour tissue.

MRS has also been used to study tumour metabolites. Diffusion rate and vascular permeability are all indicative of diseased states such as cancer, MRS methods which measure differences in intracellular hydrogen, carbon or phosphorous atoms can be used to measure tumour pH and metabolism. MRS has been useful in detecting abnormal levels of brain chemicals associated with cancer and has shown potential to distinguish between two common brain tumours: gliomas and metastases.[111]

The conjugation of RGD in various forms to contrast agents, and labelling probes of various kinds continues to highlight the effectiveness of integrin targeting for both angiogenesis imaging and therapy. In particular, $\alpha_V\beta_3$ integrin is considered a logical target for the evaluation of angiogenesis and the pursuing of anti-angiogenic therapy. PET, SPECT and MRI have all continuously contributed to this assessment within the last few decades.[112,113] [40,114,115]

1.3.3 Nanotechnology and Tumour Imaging

The application of nanotechnology platforms to cancer imaging has opened up opportunities for the use of multifunctional nanoparticle systems in the study of cancer detection and therapy. This process has been made possible through the use of specific probes that are able to target to tumours whilst allowing simultaneous imaging, whereby the particles can be tracked, monitored and their distribution quantified. Medrova *et al.* have recently developed exactly such particles, where they demonstrated the targeting, delivery and therapy of a novel siRNA multimodal nanoparticle system.[116] The triply labelled dextran-coated superparamagnetic particle was modified with a NIR dye; Cy5.5, a cell penetrating peptide; myristoylated polyarginine peptide (MPAP) and also contained siRNA for the specific silencing of a gene that encodes for Survivin. Survivin is involved in the inhibition of apoptotic proteins. This very original study demonstrates the effective use of both MRI and optical techniques in imaging the delivery of siRNA to cancers whilst allowing for the concomitant assessment of their silencing effect.

The recent use of quantum dots has presented a sensitive method of imaging tumours.[117] Segupta *et al.* have developed unique and novel nanoscale delivery "nanocell" systems which have also been made with a quantum-dot core for fluorescence imaging.[118] These drug-loaded nanocells showed unique demonstration of temporal release of two therapeutic agents, an anti-angiogenesis agent and a chemotoxic drug.

It has been shown that macromolecular nanoparticles of 40 kDa and above are able to accumulate in tumour tissue due to the enhanced permeability and retention effect (EPR).[119] This describes tumour endothelium vasculature, which due to its "leakiness" allows the penetration of macromolecular particles through to tumours. Poor lymphatic drainage is in part a cause of this effect and it has been shown that the cut off size of leaky vasculature in peripheral human blood vessels is between 200 – 600 nm.[119] Particulate systems such as liposomes, micelles, and polymeric nanoparticles, which are capable of encapsulating drugs, nucleic acids and diagnostic imaging agents, can be used to image tumours by utilising the EPR effect. However, there is a continuing need to target cancer cells effectively so that therapeutic and imaging agents can internalise into cells efficiently, no matter what the tumour type or size.

1.4 Imaging Modalities

Molecular imaging techniques make use of modalities which cover a range of frequencies from the electromagnetic spectrum. The most commonly used techniques in molecular imaging are MRI, optical imaging and nuclear imaging (PET and SPECT).[120] PET and SPECT techniques have been most extensively used as imaging modalities, since the earliest molecular imaging agents were radiopharmaceuticals that used radionuclides such as radioactive iodide ^{131}I (diagnosis of thyroid gland disease and the assessment of thyroid gland function), and the fluorinated glucose derivative [^{18}F]-fluorodeoxyglucose ([^{18}F-FGD]) which is an analogue of glucose (once taken up into the cell it is phosphorylated and therefore trapped inside the cell indicating localisation by radioactivity).[121] Both PET and SPECT allow for the detection of radiopharmaceuticals *in vivo* and are used to study gene expression. The sensitivity of these techniques is very high and small quantities of probes can be detected in diagnostic imaging. As such, nuclear imaging modalities are applied extensively to clinical research, clinical diagnosis and drug discovery. A range of commonly used *in vivo* imaging modalities along with their characteristics are summarised in **Table 1**. Each technique has advantages and disadvantages with respect to sensitivity, resolution, tissue penetration depth, clinical viability and costs.

The imaging modality of choice is usually based on the biological process under investigation and can differ between an *in vitro* and *in vivo* setting. For example, fluorescence based techniques offer low-cost alternatives for imaging small animals in gene expression studies. BLI has minimal background noise and can be used in small animals relatively easily. The advantage of MR imaging in, for example, gene expression studies is the excellent spatial resolution of MRI. Where MRI lacks in sensitivity, PET imaging does not, since as little as 10^{-11}-10^{-12} M of tracer is detected using this nuclear imaging technique. [122]

Modality	Form of energy used	Resolution			Molecular sensitivity mol/l	Tissue penetration depth (mm)	Example reporter Agent
		Spatial (mm)	Temporal	Contrast			
PET (used for both animal and clinical imaging)	Annihilation photons	1-4 (animals) 6-10 (clinical)	Mins	Medium	10^{-11} - 10^{-12}	No limit	^{18}F ^{11}C ^{15}O ^{124}I
SPECT (used for both animal and clinical imaging)	Gamma rays	0.5-5 (animals) 7-15 (clinical)	Mins	Low	10^{-10} - 10^{-11}	No limit	^{99m}Tc ^{111}In
MRI (used for both animal and clinical imaging)	Radio-frequency waves	0.025-0.1 (animals) 0.2+ (clinical)	Min/hour	High	10^{-3} - 10^{-5}	No limit	Gd^{3+} Fe^{2+} Mn^{2+} ^{1}H ^{19}F ^{31}P ^{23}Na ^{13}C
FRI-visible (mainly small animal)	Visible to infrared light	2-10	msec	High	10^{-9} - 10^{-11}	1-20	Fluorescent proteins, photoproteins fluorochromes NIR fluorochromes
BLI (mainly small animal)	Visible to infrared	3-10	msec	High	10^{-13} - 10^{-16}	1-10	Luciferin
CT (used for both animal and clinical)	X-rays	0.03-0.4 (small animal) 0.5-1 (clinical)	Mins	High	N/A	No limit	Iodine
Ultrasound (used for both animal and clinical)	High frequency sound waves	0.05-0.5 (small animals) 0.1-1 (clinical)	Mins	Medium	N/A	No limit	Microbubbles

Table 1. Summary of imaging modalities used in molecular imaging *in vivo*.[123-125]

The above imaging modalities are useful tools in studying the biodistribution of targeted probes, gene and drug delivery vectors, and also the migration of cells *in vivo*.

1.4.1 X-Ray and CT imaging

X-Ray imaging also known as radiography is the most commonly used technique in medical imaging. X-rays are a form of electromagnetic radiation with a wavelength in the range 10 nm to 100 pm. X-rays are often used to determine the type and extent of fractured bone and are also commonly used to determine pathological changes in the lungs. Contrast agents such as barium can be employed to visualise structures in the stomach and intestine, leading to the diagnosis of cancers and disease. X-rays however are ionising radiation and repeated scanning can pose health risks to patients.

An alternative imaging technique used mainly for soft tissue imaging is CT, originally referred to as computed axial tomography (CAT), uses computer software in conjunction with X ray images to produce a 3D image. This is done by using digital geometry processing (fast algorithm generation for 3D model creation) to generate a 3D image of the interior of an object from a large series of two-dimensional X-ray images taken around a single axis of rotation. Although quite a fast imaging technique, repeated CT scanning should also be avoided due to the use of ionising radiation.[126]

1.4.2 PET Imaging

PET imaging is based on the decay of a single radioisotope which produces a single positron (positron emitters); this emitted positron then collides with an electron to produce two high energy photons that propagate in opposite directions. These propagating photons are detected by scintillography. The image is then acquired by successively summing all the detected positron emission events in either two or three dimensions. PET uses tracers which are based on a number of positron emitting radioisotopes including ^{11}C, ^{15}O, ^{13}N, ^{18}F, ^{124}I, ^{64}Cu, ^{68}Ga, ^{76}Br and ^{99m}Tc. The progression and regression of cancer is routinely studied in patients using PET to detect the decaying nuclides of ^{11}C, ^{15}O, ^{13}N, ^{18}F and ^{124}I incorporated into tumour targeted radiopharmaceuticals. PET scanners are then used to construct volumetric images of the positron-emitting probes.[8] A typical example of a molecular assay with PET imaging would involve the injection of the positron-labelled tracer followed by PET scanning which will provide measurements of the tissue concentration of the probe and its targets over a period of time. This data is then correlated with plasma probe concentrations and a compartmental model is then obtained.[127] Although a

very sensitive technique, PET suffers from low spatial resolution, making it difficult to localise original signal from biological samples.

PET-CT has evolved to be a hybrid nuclear imaging technique that has been widely used by radiologists in oncology. Combining PET with CT imaging offers advantages over using single-photon nuclear imaging alone; the advantage here is the effective anatomical correlation with computed tomography. PET-CT offers a greater sensitivity and superior spatial resolution over a large field of view and as a result small lesions can be detected more readily.[128] The combined technique does however require cyclotron access and involves the use of ionised radiation energy. Recently PET-MRI machines have also been designed and made which will allow for both imaging techniques to be applied to the same subject successively.

1.4.3 SPECT Imaging

SPECT is a nuclear imaging technique that is able to detect and quantify γ-emitting radionuclides and is frequently used in cancer imaging. The radioisotopes used for SPECT emit only one single high energy γ photon (γ emitters) and they have half lives ranging from 6 hours to 8 days, which does allow for short-time spanned experiments. The γ emitting isotopes used in SPECT are, for example, ^{67}Ga, ^{99m}Tc and ^{123}I. These isotopes produce a single photon upon decay and the photons that escape from the body are detected by large scintillation detectors placed around the subject. With SPECT imaging, due to the longer half-lives of the single photon emitters such as ^{99m}Tc, endogenous ligand interactions, as well as slow kinetic processes, and the simultaneous probing of multiple molecular pathways can be achieved.[129] The main constraint with SPECT is that only a small quantity of the γ-rays radiating from a subject can actually be detected because of the requirement for collimation, which limits its sensitivity (SPECT tracers can illuminate areas other than the target area and need co-registration with another imaging modality by computer tomography). PET imaging is more sensitive and has better resolution than SPECT because collimators are not necessary to exclude scattered photons. Reconstruction methods produce images that have a much higher sensitivity (nanomolar concentrations) with PET than those achieved with SPECT.[130] PET has disadvantages compared to SPECT, as the positron emitting radionuclides have short half-lives and instrumentation is relatively expensive. The most frequently used positron-emitting radionuclide ^{18}F has a half life of less than 2 hours. As mentioned cyclotron laboratories are necessary to generate the radionuclides (e.g. ^{11}C, ^{13}N and ^{15}O) required for PET and therefore this technique can only be used in specialist centres.

1.4.4 Magnetic resonance imaging (MRI)

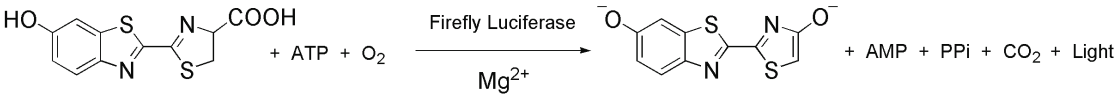
MRI has an excellent spatial resolution, clinical potential, and can consistently image structures in the millimetre range without the use of ionising radiation such as that used in X-ray, CT, PET and SPECT imaging. The fundamental nature of the MRI technique is the interaction of paramagnetic nuclei under an applied magnetic field. Contrast agents used in MRI have paramagnetic metal cations and can therefore alter the relaxation rate of nearby paramagnetic nuclei, such as the hydrogen nuclei of water molecules. The excitation of these paramagnetic nuclei by radio frequency pulses and their subsequent relaxation rate after the pulses are suspended is a tissue specific event which is characterised by the two time parameters T_1 and T_2 usually expressed in milliseconds. See section **1.5** for a more detailed discussion on MR imaging.

1.4.5 Optical Imaging

Optical imaging detects the emission of light from biological tissues and encompasses optical tomography, near infrared fluorescence imaging (NIR), fluorescence protein imaging and bioluminescence imaging (BLI). Fluorescence techniques most widely used make use of the green fluorescent protein (GFP) however; they require genetic manipulation and therefore are not suitable for human use, and may also cause immune responses, although they can be used in animal studies. NIR fluorescence imaging is a technique that is based on the absorption and emission of light (between 700-1000 nm wavelengths). NIR imaging in this range minimises the autofluorescence from non-targeted tissue and makes NIR probes the preferred choice for *in vivo* fluorescence imaging.

Near infrared imaging systems that use proteases such as Cathepsin D (detects fluorescence increase upon enzyme cleavage of imaging agent) have proven to be more valuable owing to the fact that these wavelengths can penetrate tissue further than other wavelengths used in optical imaging.[111] However, the problem with fluorescence techniques is that it is not possible to wash away unbound fluorescent agents *in vivo* so there is the issue of target-to-background noise ratio before imaging unless agents with a very high binding affinity are used.

Bioluminescence occurs when the enzyme luciferase (from Firefly) catalyses the reduction of luciferin. The luciferase gene comes from several organisms, including the firefly. Luciferase-mediated catalysis uses ATP hydrolysis to convert luciferin (the substrate) to oxyluciferin that emits a detectable photon.[131]



Scheme 1. Bioluminescence reaction catalysed by firefly luciferase.

Reporter genes with bioluminescence signatures have been used in cell culture, in small organisms and in *ex vivo* analyses after expression in larger animals. In these kinds of assays reporter genes are linked to genetic regulatory elements and can reveal spatial and temporal information about biological processes at the level of transcription. The use of BLI however is clinically limited as it involves genetic manipulation and the introduction of foreign genetic material.

1.4.6 Ultrasound Imaging

Molecular imaging agents detectable by ultrasound are now being investigated in animal studies. Microbubbles are used in ultrasound imaging; these agents have shells that are composed of lipids, proteins or polymers. Microbubbles can contain different gases based on the nature of the membrane. Microbubbles vibrate strongly in reaction to the high frequency sound waves used in diagnostic ultrasound imaging which amplifies their reflection several thousand times over than normal tissues allowing for picogram detection ranges. However, this imaging technique lacks a high spatial resolution.[132]

1.5 Magnetic Resonance Imaging (MRI) – Background and Principles

The first MR experiment to produce proton images of two glass capillaries containing water, immersed in a bath of D_2O was accomplished by Paul C. Lauterbur in 1971 using an in-house built MR machine.[133] Today MR scanners have become much more developed and are capable of producing high resolution 3D images of tissues containing water. The behaviour of paramagnetic nuclei under a magnetic field is the fundamental principle of this technique. In clinical imaging, hydrogen is the most frequently used nucleus, other possible nuclei used in MRI are ^{13}C, ^{23}Na, ^{19}F and ^{31}P. Hydrogen is an ideal atom for MR imaging as it has a large magnetic moment indicating that once placed in a magnetic environment it has a relatively high tendency to line up to the direction of the magnetic field.

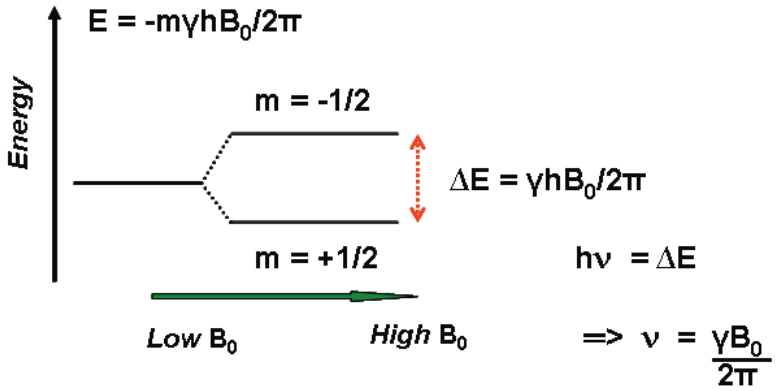


Figure 6. Spin states of a hydrogen's nucleus in a magnetic field where E is the energy, B_0 is the magnetic field, γ is the gyromagnetic ratio, m is the spin quantum number, h is Planck's constant and ν is the Larmour frequency at which resonant transitions occur.

The magnetic moment of protons is proportional to their angular momentum, where the constant of proportionality is the gyromagnetic ratio, γ. Once placed in a magnetic field (B_0), the proton spins can be separated in energy (**Figure 6**), and adopt one of two possible orientations; parallel or antiparallel to the external magnetic field. To align their spins parallel to the applied magnetic field requires less energy and therefore this remains the preferred alignment state. Antiparallel alignment requires more energy and is hence the higher energy state.

However, the number of spins that remain after parallel and anti-parallel states cancel each other out is actually very small indeed (+1/2 spin versus – 1/2 spin), and is the direct cause for the lack of sensitivity in MRI. The very few spins that are not cancelled out are then able to establish a net magnetisation vector in an MR scanner. The individual protons do not completely align with this established magnetic vector and in fact wobble or precess around the direction of this external magnetic field (**Figure 7**). The frequency (ν) of this precession is dictated by the Larmour equation as shown in **Figure 7**, and is proportional to the applied magnetic field (B_0), and the gyromagnetic ratio of the hydrogen nucleus (γ). The phase of precession, in other words the direction of the spin in the X-Y plane is different for each individual nucleus (see **Figure 8**).

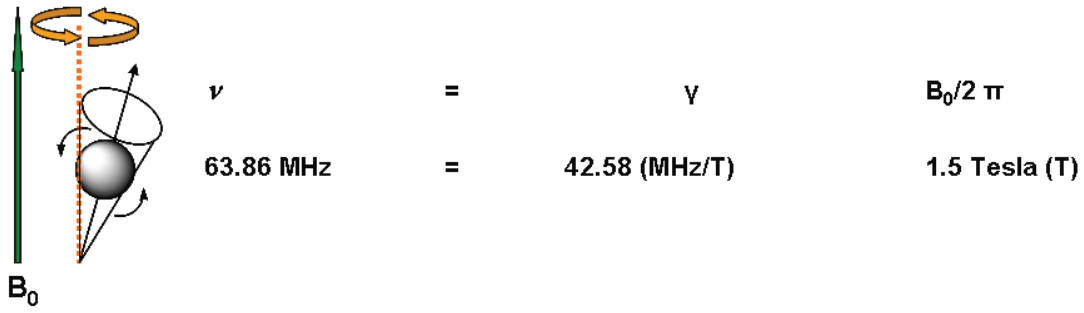


Figure 7. Hydrogen atoms precess or "wobble" around a magnetic field, the speed of which is governed by the Larmour equation shown, $\nu = \gamma B_0$. At 1.5 Tesla, the precessional frequency for hydrogen is equal to 63.86 MHz.

The established magnetisation vector in the Z direction described (**Figure 8**) is static and in order to measure signal, energy must be applied.

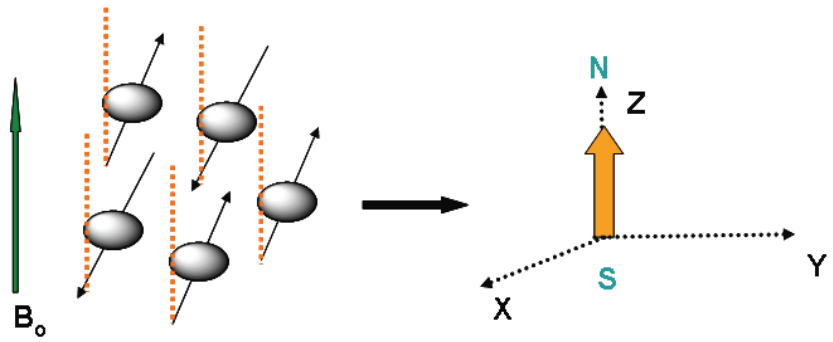


Figure 8. Magnetisation vector (orange arrow) established in the Z direction, from precessing hydrogen nuclei around the applied external magnetic field (B_0).

Energy is applied to the magnetisation vector through the induction of a radiofrequency pulse (RF) with the Larmour resonance frequency, for a defined time corresponding to either 90º or 180º degrees rotation. The purpose of the RF pulse is to change the direction of the magnetisation vector. When the short pulse is administered, the thermal equilibrium of the spinning nuclei is disturbed and energy is absorbed (**Figure 9**). The net magnetisation flips 90º or 180º from the positive Z axis to the transverse plane, where they precess at the Larmour frequency. This newly established rotating magnetisation induces an electrical signal which is picked up by the receiver coil placed around the subject or sample being imaged.

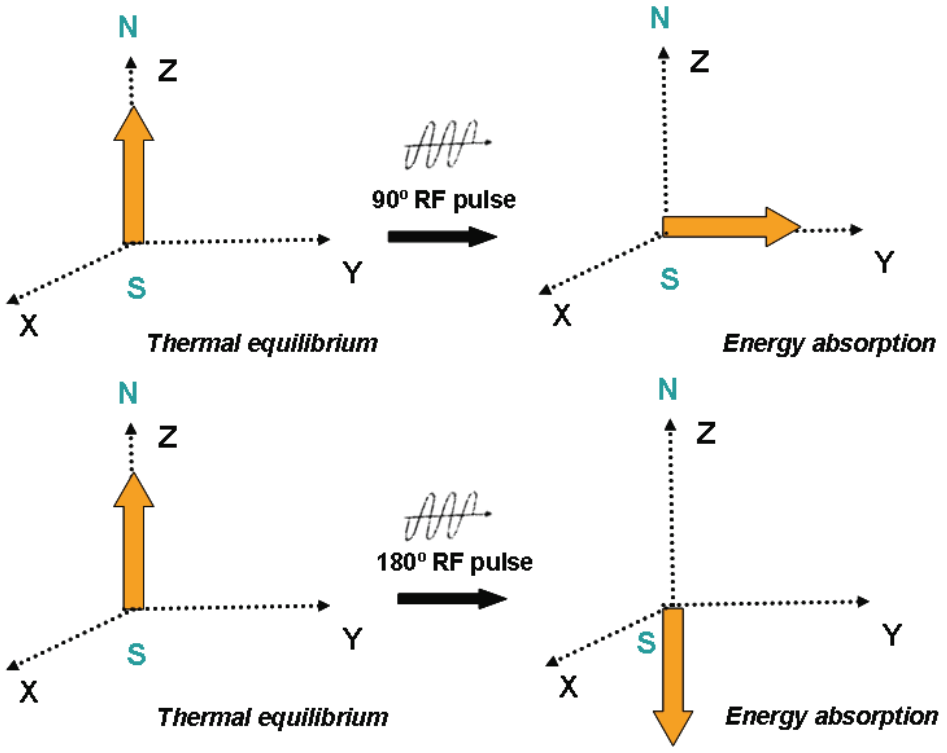


Figure 9. RF pulses "whip" the spinning nuclei into the transverse plane and cause them to precess at the Larmour frequency (same frequency as the RF pulse).

When the RF pulse is switched off, two independent events occur (see **Figure 10**). The magnetisation vector relaxes back to its original Z direction and as such, realigns to the external magnetic field B_0. This event is denoted as *spin-lattice relaxation* and has a time constant T_1. This is also sometimes referred to as "longitudinal relaxation". The second event that can occur is the *spin-spin relaxation* of the proton nuclei in the direction of the X-Y plane, which is given the time constant T_2. These spins precess

in phase together in the X-Y plane shortly after the RF pulse, however, with time, their coherence and therefore their signal decays. This is caused by the spins losing their phase (dephasing) due to spin-spin interactions with other nuclei, and local and external magnetic field inhomogeneities. Spin-spin relaxation is also sometimes referred to as “transverse relaxation”. The return of the magnetisation vector to the equilibrium state is favourable as it is the lower energy state. The magnetisation and therefore the induced signal decays over time and is called free induction decay (FID). The time required for the signal to return to thermal equilibrium is determined by T_1 relaxation time.

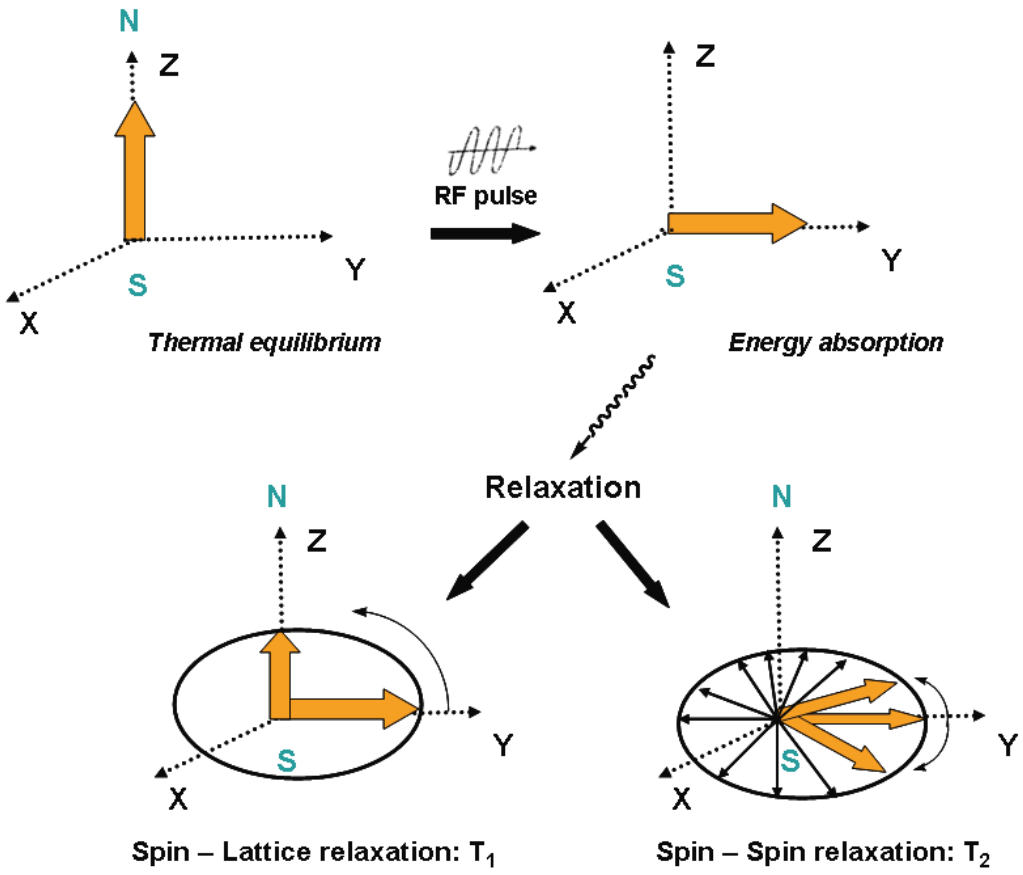


Figure 10. Two relaxation processes occur once the RF pulse is switched off: T_1 and T_2, which are termed spin-lattice and spin-spin relaxation respectively.

Spin-lattice relaxation, T_1 is in fact the time taken for the magnetisation vector to return to 63% of its equilibrium state post RF pulse (typically a 90º pulse). This relaxation is exploited in body MR imaging, since different tissues and organs have differing T_1 relaxation times. Spin-spin relaxation, T_2, is the time period in which the

spins decay through dephasing, to 37% of their original value. The T_2 relaxation period is also tissue dependent and is usually shorter than T_1 (**Figure 11**).

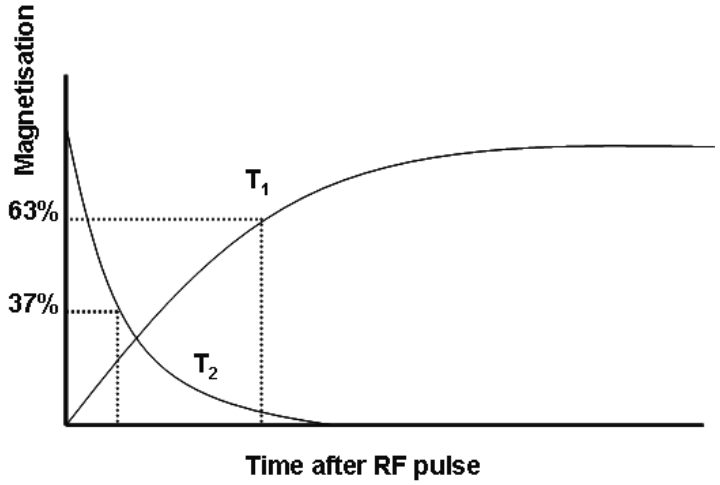


Figure 11. Graph showing T_1 and T_2 relaxation parameters. T_1 is time taken for excited spins to return to 63% of the original net magnetisation vector, and T_2 is the time taken for the spins to decay through dephasing to 37% of the original net magnetisation vector.

In order to obtain a black and white or contrasted image, information from the position of all hydrogen atoms in the subject is necessary. The processes by which this can be achieved are; slice selection, frequency encoding, and phase encoding (see **Figure 12**). Since the precessional frequency of hydrogen nuclei is proportional to the magnetic field and only resonating nuclei produce a signal, by applying a magnetic gradient from the direction of the foot to the head, the location of hydrogen nuclei can be pinpointed. By using combinations of magnetic gradients in three directions of X, Y and Z, information for a single slice of a few millimetres can be obtained. The frequency and phase encoding processes yield information on the local hydrogen environments of individual points or pixels in a slice. In phase encoding, a change in magnetic field is applied between the RF pulse and signal readout. This causes the precessional frequency of the hydrogen atoms to change, in turn, changing their phase also. This process can be repeated by using temporary gradients until spins with differing phases are generated and the alternating current is recorded. Frequency encoding is another parameter that can be manipulated in order to distinguish points with the same phase encoding. A further magnetic gradient is applied during the readout of the signal which changes the precessional frequency.

Apart from slice selection, which is the excitation of a single slice in space, phase and frequency encoding involve the application of a progressive gradient throughout the subject.

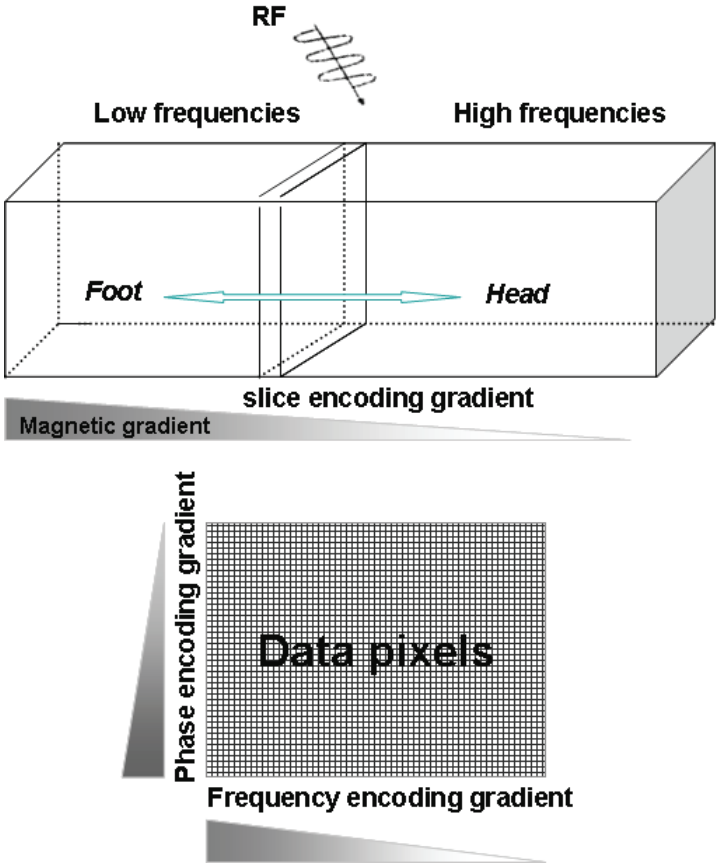


Figure 12. Top box: a single slice through the subject can be selected by superimposing a small magnetic gradient on to the main applied magnetic field. Bottom: Phase encoding further manipulates the spins and frequency encoding is used to distinguish pixels with the same phase encoding. Diagram adapted from Van Guns *et al*.[134]

Once phase and frequency data has been combined, a spatially encoded grid can be generated consisting of pixels with unique phase and frequency information (**Figure 12**). A Fast Fourier Transform (FT) is then produced in both the frequency and phase encoding directions and this process is repeated until all the data from the pixels is generated into an image using computer software (**Figure 13**).

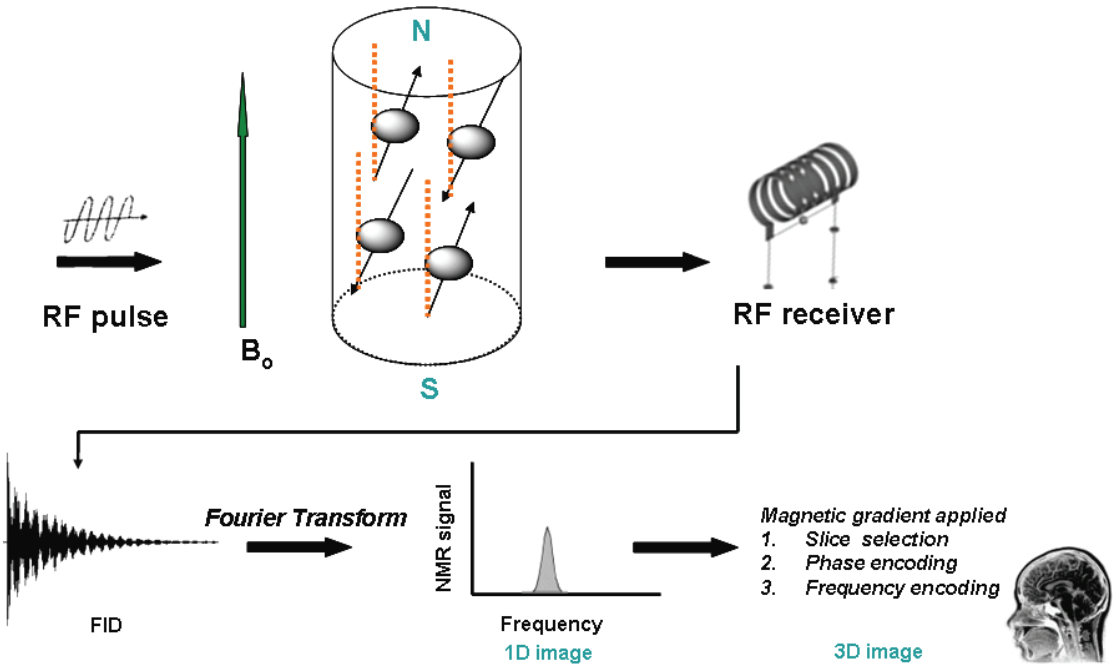


Figure 13. The overall process of image acquisition is presented: after the RF pulse is administered, the electrical signal generated by the magnetisation vector changing plane is picked up by an RF receiver and a Fourier Transform of the FID produces the NMR signal, which through the application of a magnetic gradient can be converted into a 3D image using slice selection, phase and frequency encoding.

The FID signal is short lived and the spatial encoding described thus far cannot be carried out fast enough, not least within the duration of the FID signal. As a result, a second electrical signal can be produced and sustained in order to gain further contrasted and better quality MR images. By applying a second RF pulse at 180º, a second electrical current is generated which reverses the spins (**Figure 14**). This rephasing of the spins causes an increase in the electrical current generated and is referred to as time of echo (TE). This echo signal is generated as a result of 90º and 180 º pulses and is referred to as a spin-echo sequence in MR imaging.

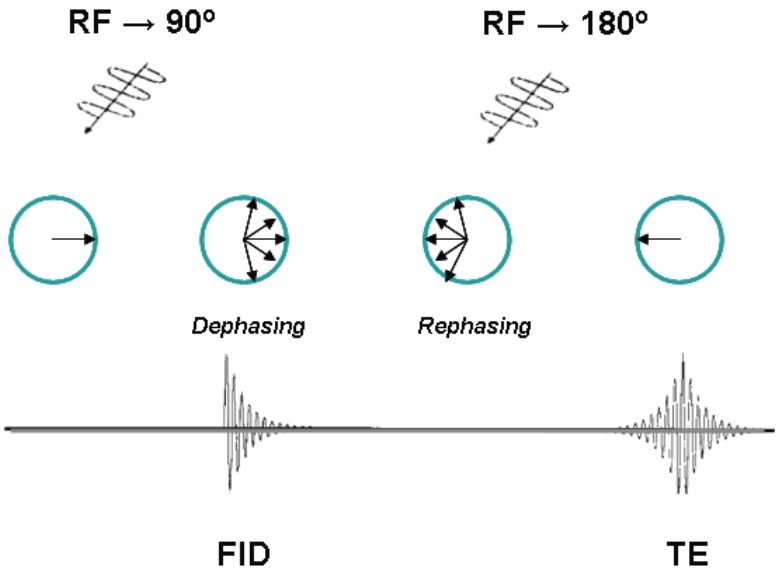


Figure 14. A second 180º RF pulse causes the dephasing spins to rephase and the height of the echo generated by this is called the time of echo (TE).

The time delay between the applications of RF pulses is known as time of repetition (TR) and is a parameter that can be controlled in order to obtain T_1 and T_2-weighted images of different tissues. For example, if the TR is short and a short TE is used, then the contrast in the image will be dependent on spin-lattice T_1 differences, and is said to be T_1-weighted. If a long TR and a long TE is used, then the image is dependent on spin-spin relaxation differences and the image is said to be T_2-weighted.

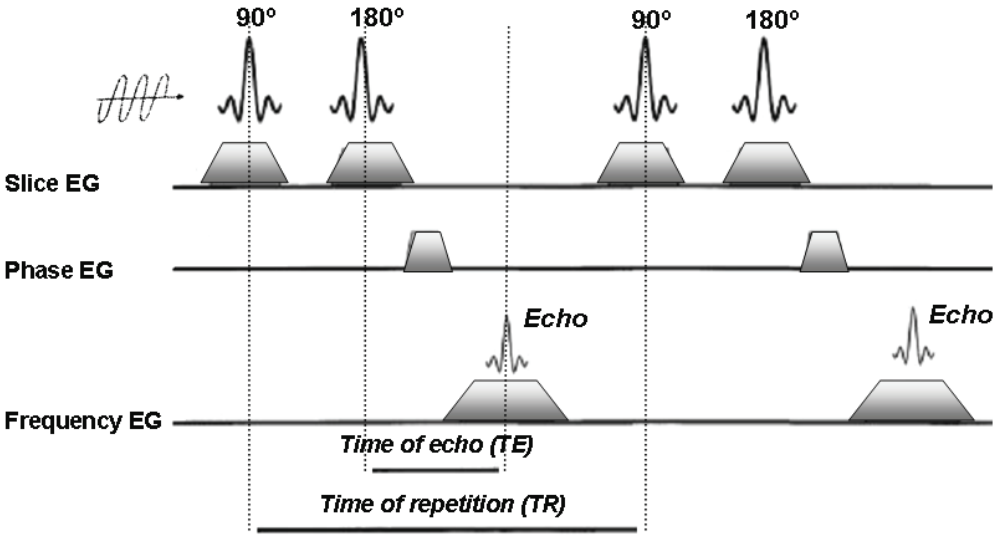


Figure 15. This figure presents a spin-echo sequence, EG = encoding gradient. Spatial encoding of the echo signal is carried out using gradient switches. Firstly, the slice selection

gradient is switched on during the first RF pulse, and one single thin slice through the subject is excited with the protons precessing at the Lamour frequency (RF pulse). The phase encoding gradient is applied during the second RF pulse and readout of the echo signal. Lastly, frequency encoding gradient is applied during the readout of the echo signal. This sequence can be repeated according to the number of pixels in the image matrix. For example, 256 x 256, this means 256 frequency encoding and 256 phase-encoding steps are required.

A great advantage of MR imaging is also the ability to image subjects in any plane (**Figure 16**), three planes are used in MR imaging, axial (perpendicular to the head-foot axis), sagittal (parallel to the left-right symmetry plane), and coronal (perpendicular to the dorsal-ventral axis).

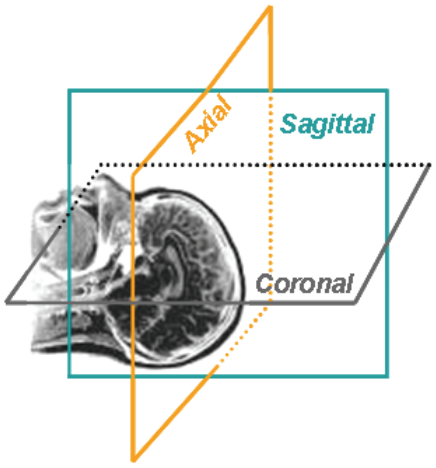


Figure 16. Three different orientations in which slices are obtained in MRI.

In addition to manipulating pulse sequences, using optimal RF coils and appropriate computer software parameters, MR imaging also utilises contrast agents in order to enhance the T_1 or T_2 relaxation of relevant localities. A discussion of contrast agents used in MR imaging is presented in section **1.7**.

1.6 Fluorescence Imaging – Background and Principles

Fluorescence imaging involves the use of in general, microscopy to visualise fluorescent molecules that absorb light. These molecules are usually polyaromatic or heterocyclic molecules referred to as fluorophores, fluorochromes or fluorescent dyes. These molecules are able to absorb light and in doing so become excited, transitioning to a measurable excited state. Their return to the ground state is a decay process which emits fluorescent photons. This process is summarised in **Figure 17**.

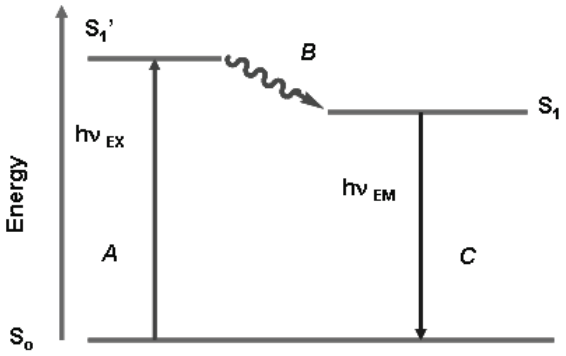


Figure 17. Jablonski diagram showing the electronic states involved in fluorescence emission. ***A*** represents the excitation state after optical absorption, ***B*** the excited-state life-time and ***C*** the emission state.

The production of fluorescence from fluorophores involves the three stages of excitation, excited-state life-time and the emission state. In the excitation stage (**Figure 17**, ***A***), photons coming from a light source, for example either a lamp or laser, are absorbed by the fluorophore and this can lead to the electronic singlet state S_1' (**Figure 17**). During this excited time (of the order of few nanoseconds) the fluorophores may go through conformational changes and become affected by environmental interactions. Some of the energy of this state is dissipated until the lower energy relaxed singlet state S_1 is reached (**Figure 17**). At this state energy photons are emitted ($h\nu_{EM}$), and the fluorophores return to their ground states, S_0. Some fluorescence techniques may not result in all the excited fluorophores returning to their ground states, these processes may involve for example, fluorescence resonance energy transfer (FRET) and collisional quenching. For fluorophores, the term fluorescence quantum yield is used to describe their fluorescence efficiency and refers to the ratio of the number of fluorescence photons emitted (**Figure 17**, ***C***) to the number of photons absorbed in the excitation stage (**Figure 17**, ***A***). Often a

charged-coupled device (CCD) camera is used to measure the intensity of the fluorescence emitted and this information is used to produce digital images of various samples. The fluorescence detection instrumentation generally consists of an excitation source, a fluorescent sample, appropriate wavelength filters and a detector component to measure the emitted photons (**Figure 18**). Fluorescence emission can be localised, measured and quantitated in this manner.

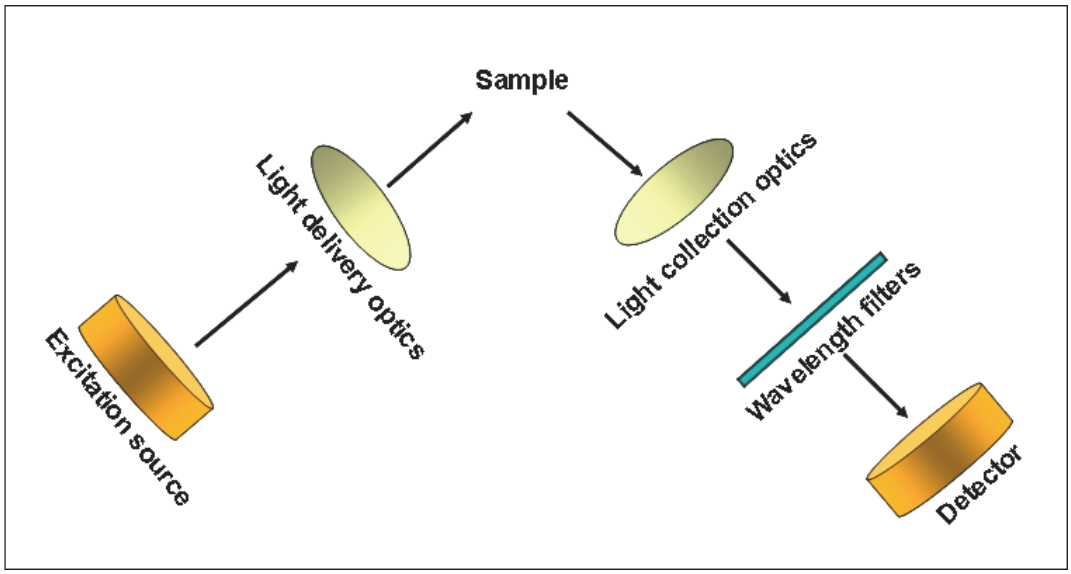


Figure 18. General example of a fluorescence detection system.

Fluorescence detection techniques are highly sensitive due to the fact that the same fluorophore can in fact be repeatedly excited and detected in a cyclical process, however photo-bleaching is an inherent property of fluorescent molecules. Fluorescent probes are used in many biological assays and techniques, and can provide highly sensitive detection of biologically tagged molecules. These probes have characteristic excitation and emission wavelengths and often can be used in multicolour experiments, where more than one fluorescence colour can be observed.

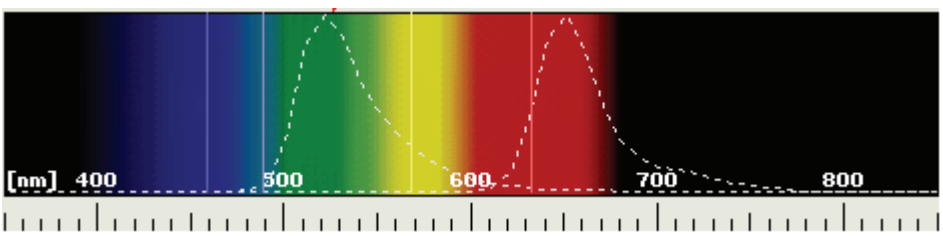


Figure 19. Fluorescence emission spectrum of two fluorophores, Alexa 488 and Alexa 633 (Invitrogen®).

The sensitivity of fluorescence techniques and reasonably low cost makes them an invaluable tool in molecular imaging. Cells can be labelled using a variety of techniques and followed both *in vitro* and *in vivo*. Perhaps one of the most frequently used fluorescence techniques in molecular imaging is the inducible expression of GFP which is an excellent marker used in gene expression studies.[124]

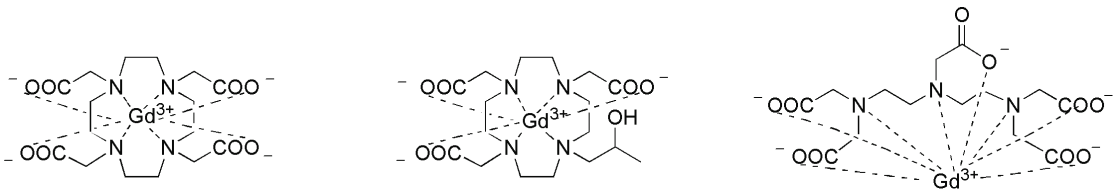
Fluorescence imaging has had prominent use in cell studies *in vitro* and histological analysis, however, *in vivo* imaging has recently benefited from the development of unique black box imaging systems which are capable of both fluorescence and bioluminescence imaging in real-time. These applications mainly make use of the near-infrared (NIR) spectrum wavelengths (700-1000 nm) in order to obtain the best tissue penetration depths and also to minimise autofluorescence from biological tissue. Bioluminescence measuring systems also exist for small animal imaging, which allow for multiple small animals to be imaged simultaneously.

1.7 MRI Contrast Agents

MRI contrast agents are routinely used in clinical diagnosis as they provide reliable means to interpret MRI images and play a key role in clinical imaging, with more than 35% of examinations routinely using contrast agents in the clinic.[52] The most commonly used contrast agents are thermodynamic and kinetically stable low molecular weight gadolinium compounds which, in general, enhance the relaxation rate of water protons within the blood pool. Commonly, these agents consist of a paramagnetic metal core, which is complexed to a strongly chelating ligand. In general, MR contrast agents consist of Gd^{3+} complexes, monocrystalline iron oxide nanoparticles, or Mn^{2+} chloride complexes. As well as characterising MR contrast agents according to the metal centre, another approach to categorise these agents is to distinguish them based on their biodistribution characteristics. Traditionally MR contrast agents have been classified as extracellular or intracellular agents, and some may even show organ specificity, in particular for the liver and can be termed tissue specific contrast agents.

1.7.1 Gadolinium Contrast Agents (T_1 Agents).

Gd.DTPA (**Figure 20**) was the first water soluble, renally excreteable contrast agent approved for clinical use by the FDA since mid 1988, and is currently routinely used under the commercial name Magnevist®.[135] This complex contains one inner sphere water molecule that exchanges rapidly with outer sphere water molecules and in turn relaxes the surrounding water protons simultaneously. **Figure 20** presents a few examples of the most commonly utilised contrast agents in the clinic.



Dotarem® $(Gd.DOTA)^-$ **Pro-hance®** (HP-DO3A) **Magnevist®** $(Gd.DTPA)^{2-}$

Figure 20. Gadolinium based clinical contrast agents approved by the FDA.

These compounds are generally inert stable complexes where the metal ion is strongly chelated to the poly(aminocarboxylate) ligands. These types of agents are non-specific, mainly reside within the blood stream and also accumulate in the kidneys due to their glomerular filtration and are generally excreted unmetabolised.[136] Nevertheless, their use in clinical MR imaging has great value as anatomical abnormalities such as gliomas and lesions within the brain can be visualised, since under normal physiological conditions these agents do not cross an intact blood brain barrier. Pathologies within the liver and other organs can also be visualised since these contrast agents rapidly accumulate into interstitial spaces and can therefore increase the signal to noise ratio, in such regions of increased fluid volume.[137]

Gadolinium is used in MRI because of its high magnetic moment (7 unpaired electrons in its outer shell, 7.9 Bohr magneton) and its relatively slow electron spin relaxation time which is also comparable to that of hydrogen nuclei. Once chelated to Gd^{3+}, the linear poly(aminocarboxylate) DTPA ligand forms a stable chelate in the form of a distorted tricapped trigonal prism and the DOTA macrocycle forms an even more stable chelate in the form of a monocapped square antiprism cage (see **Figure 21**).[138]

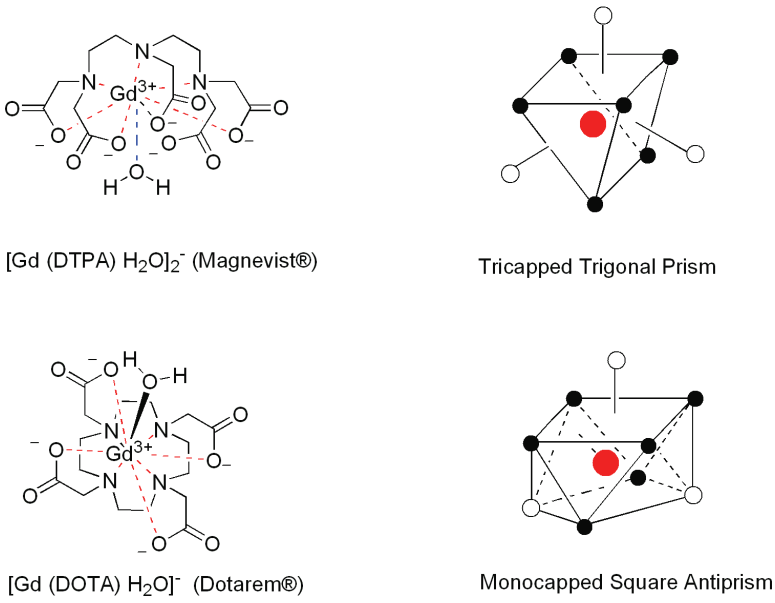


Figure 21. The crystal structures of the two common contrast agents Gd.DOTA and Gd.DTPA can generally be best described as a monocapped square antiprism and a tricapped trigonal prism respectively.

The principle mechanism of relaxation is due to the interaction of the inner sphere water molecule with the fluctuating local magnetic field on the Gd^{3+} ion (**Figure 22**). The inner sphere water molecule coordinates to the 9^{th} coordination site of the Gd metal, which leads to the subsequent relaxation of this water molecule. This relaxation has a catalytic effect which leads to the relaxation of the surrounding bulk water molecules in the vicinity of this co-ordinated water molecule via a chemical exchange process. A process that could be envisaged by the role of the Gd^{3+} ion polarising the O-H bond of the coordinated water molecule which in effect enhances the magnetic moment of this molecule, and therefore dynamically affects all other surrounding water molecules through hydrogen bonding (the outer water molecules are termed outer sphere water molecules).

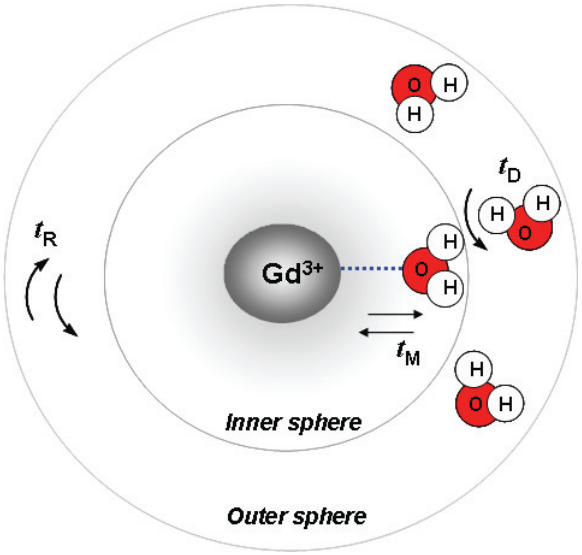


Figure 22. Gd relaxation mechanism and parameters.

As shown in **Figure 22**, various parameters exist that can influence the relaxation rate of water molecules within the contrast agent's vicinity. These parameters can be thought of as; the average time (nanoseconds) a water molecule remains co-ordinated to the metal ion in the first inner sphere (t_M), how fast the contrast agent tumbles in water, which is measured by the rotational correlation time (t_R) and the translational diffusion time of the outer sphere water molecules (t_D). This latter parameter is related to the hydrogen bonding of the carboxylate oxygens with surrounding water molecules that hydrate the complex (oxygen atoms are relaxed via dipolar mechanisms).

In summary, it can be concluded that three main points influence relaxivity; 1. The number of water molecules coordinated onto the paramagnetic metal ion and their exchange rate (t_M), 2. The rotational correlation time of the Gd complex (t_R), and 3. The electronic relaxation rate of the paramagnetic metal ion.[139] In addition to these contrast agent dependent qualities, the local concentration of the Gd metal also affects T_1, as above a given concentration (~mM), T_1 effects may lead to T_2 enhancement.

Gadolinium contrast agents most commonly administered are used with the postulation that they will remain intact in the blood before secretion. However, trans-metallation by other metallic ions in the body and protonation of the ligand are factors that may hinder their efficiency as they can cause their dissociation *in vivo*. Ions that could compete for the binding site of the ligands may be Ca^{2+}, Zn^{2+}, and Cu^{2+} ions, another factor that can cause dissociation is the precipitation of Gd^{3+} salts and may be a contributing factor to recent toxicity reports for Gd based clinical contrast agents.[140] It is a general belief that slow clearance from the body is likely to significantly increase the toxicity of any Gd^{3+} complexes. Charge density, size of the metal ion and the rigidity of the ligand are aspects that can influence the stabilities and dissociation speeds of contrast agents in the presence of protons.[141] An awareness of the abovementioned competitive reactions of Gd contrast agents under *in vivo* circumstances is necessary, although the incidence rate of adverse affects reported from their clinical use has remained low.[141] Other contrast agents based on Fe and Mn are also used clinically, however Gd based agents are most frequently used, with in excess of 10 million clinical MRI scans using Gd based contrast agents on an annual basis.[142]

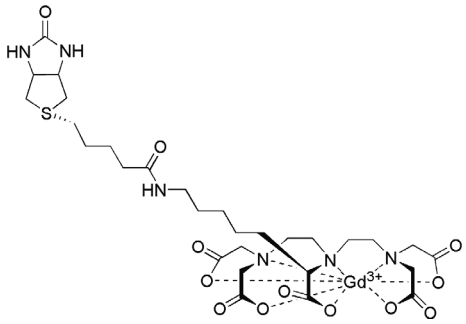
Gadolinium containing contrast agents have the advantage of being very effective contrast agents as gadolinium is the most paramagnetic element and is very versatile in its nature in order to be incorporated into a variety of complexing ligands. There are no susceptibility issues with gadolinium based contrast agents, and it is far easier to visualise T_1 enhanced brightness *in vivo* against, for example, organs that appear dark. A valuable addition to the potential of chelating agents such as DOTA and DTPA is their ability to also complex metallic radioisotopes such as indium, yttrium, gallium and lutetium. This bifunctional chelation enhances the capabilities of imaging using these agents as multiple types of imaging are made possible. Here, the complexation of Gd can allow for MR imaging and the complexation of radiotracers to the ligands can allow for PET and SPECT imaging.[143] This is very useful as there are many examples of radiometal labelled DOTA macrocycle derived tumour targeted

agents used in cancer and radioimmunotherapy medicines.[144] This inter-exchangeable metal ion centre approach offered by DOTA and DTPA ligands makes the use of Gd contrast agents indispensable since the biodistribution of these targeted therapeutic agents can be imaged *in vivo* dynamically when Gd is complexed, and therapy can be achieved by complexation of the radioisotope.[145]

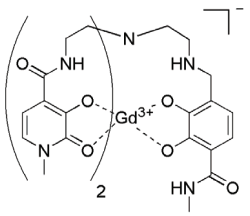
1.7.2 Small Molecular Weight Gadolinium Contrast Agents

Traditional MR contrast agents distribute mainly into the intravascular and interstitial spaces. These non-specific agents allow for the evaluation of physiological parameters, such as renal function. Agents such as Magnevist® show an organ specific distribution due to their glomerular filtration; these agents accumulate in the kidneys at much higher concentrations than in the blood or any other tissue.[136]
Extracellular gadolinium chelates are known to also improve the diagnosis of focal liver lesions, and contrast agents such as Teslascan® (mangafodipir, MnDPDP, Amersham Health-US), MultiHance® (gadobenate, Gd-BOPTA, Bracco) and Eovist® (gadoxetate, Gd-EOB-DTPA, Schering AG) have been shown to have specific uptake in hepatocytes.[137] There is clearly a high demand for pathology and receptor-specific contrast media and the field of MR contrast agents has subsequently geared towards the design of such specific contrast agents targeted to molecular disease markers of interest. Second generation contrast agents are now being continuously designed for molecular MRI. The successful coupling of Gd.DOTA or Gd.DTPA to various targeting molecules of interest has been described in the literature, with MR imaging providing a rapid visualisation and validation for the end point of targeting. Many newly investigated agents are evaluated against the efficiency of these poly(aminocarboxylate) ligands as they are approved compounds for human use.[146]

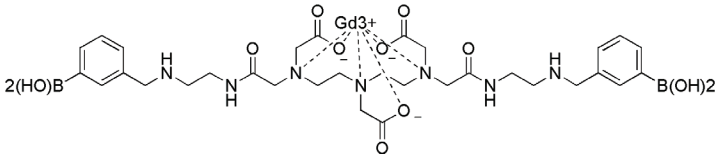
The general criterions for new potential contrast agents can be summarised as; an increased thermodynamic stability, favourable rate of excretion, lowered toxicity, lipophilicity, target specific biodistribution and an increase in MR relaxation. These points have been addressed in the design and synthesis of a range of Gd.DOTA and Gd.DTPA contrast agents which exhibit specificity and, pre-clinically, much effort is currently focused on molecular imaging using contrast agents as discussed in previous sections, for example, by targeting contrast agents to the $\alpha_v ß_3$ integrins in angiogenesis, to fibrin present in blood clots or to cells in order to track their biodistribution. “Smart” contrast agents have also been developed that are sensitive to pH[147-149], or enzymatic activity.[150] **Figure 23** depicts some examples of small molecular weight Gd contrast agents developed recently.



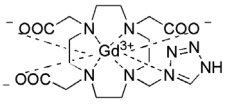
Biotinylated Gd.DTPA.[151]



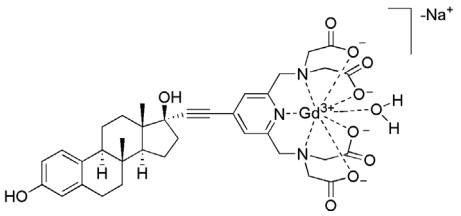
Gd-TREN-bis(Me-3,2-HOPO)-TAM-Me contrast agent for high relaxivity.[152]



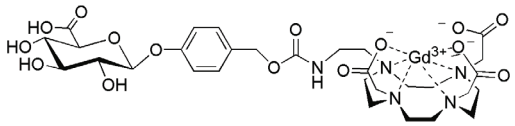
Gd.DTPA(bisamide)-boronic acid derivative.[153]



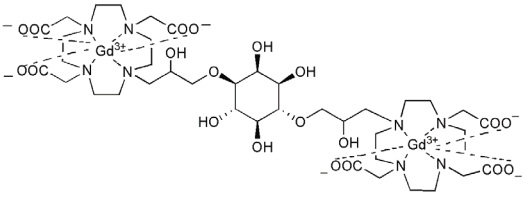
Tetrazole Gd.DOTA.[154]



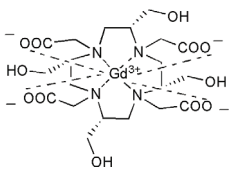
EPTA-Gd, water soluble contrast agent for the estrogen receptor localisation by MRI.[155]



An enzymatically labile β–glucuronic acid contrast agent.[150]



Dimeric Gd.DOTA contrast agent.[156]



Poly(hydroxymethyl) Gd.DOTA, a new low toxicity contrast agent.[157]

Figure 23. Examples of some targeted contrast agents from the literature.

1.7.3 Large Molecular Weight Contrast Agents

An effective means of increasing the signal-to-noise ratio of MR contrast agents involves the incorporation of more than one Gd moiety on molecules. This has been an approach undertaken in the design and synthesis of many large macromolecular Gd contrast agents, whereby the conjugation of many Gd.DOTA or Gd.DTPA moieties together in the form of polymers, dendrimers and other macromolecular structures greatly enhances the T_1 relaxation properties of these types of agents. The main area where these macromolecular agents have been used is for the imaging of the blood pool, as due to their increased size and sheer bulk they benefit from prolonged blood circulation times. However, their routine use in the clinic may be hampered due to their slow clearance and inherent toxicity if they are not broken down *in vivo,* although efforts to make these agents biodegradable have been undertaken. Nevertheless, macromolecular blood pool agents can be useful in applications such as MR angiography.[158] An advantage that a range of these dendrimers and polymers have, is the fact that most can be binfunctional, capable of condensing nucleic acids, hence acting as transfection agents, or they may also carry drug pay loads, making them useful drug delivery agents in addition to their paramagnetic properties.[159]

1.7.4 Polymeric and Dendrimeric Contrast Agents

Macromolecular contrast agents have the advantage of achieving high relaxivities and their large size allows for a longer blood pool circulation time, but perhaps the main advantage of multiple paramagnetic residues is the significant relaxation rates that these types of contrast agents provide. The conjugation of Gd moieties on to pre-existing polymeric or dendrimer structures is an attractive option which has been utilised frequently in the design of macromolecular contrast agents. Conjugation of paramagnetic Gd.DOTA or Gd.DTPA to the polyethylenglycol (PEG) polymer,[160-165] various sugar polymers,[166-168] oligomers,[169] and polyamino dendrimers has been achieved.[170-173] In addition to paramagnetic MR signal enhancers, these agents may also incorporate targeting moieties specific to targets of biological interest. For example, macromolecular contrast agents have been synthesised by conjugating various cell penetrating peptides for effective cell uptake.[11,174-177]

Dendrimers are highly branched synthetic polymers and many posses exposed end groups at their spherical peripheries for further functionalisation (usually primary amines). These dendrimers are grown using a “divergent” or “convergent” approach

whereby they are grown from a central core unit, with branching units added in a controlled manner. The potential of these dendrimers has been harnessed in MR imaging, whereby the empty spaces within them have been used to encapsulate Gd contrast agents, or contrast agents have been covalently attached. Kobayashi and co-workers have demonstrated the use of polyamidoamine dendrimers as contrast agents in MRI.[178] These dendrimers were reacted with ^{153}Gd for studying their biodistribution and blood clearance or they were reacted with ^{157}Gd for MRI studies in mice. The compounds showed high MR signal intensities in the kidneys of mice where they accumulated. The polyamidoamine (PAMAM) dendrimers are a relatively new class of highly branched spherical polymers that are highly soluble in aqueous solution and have a coated surface of primary amines available for further conjugation (**Figure 24**). Although good contrast agents for vasculature imaging, these agents are far too large for more specific imaging such as cellular imaging.

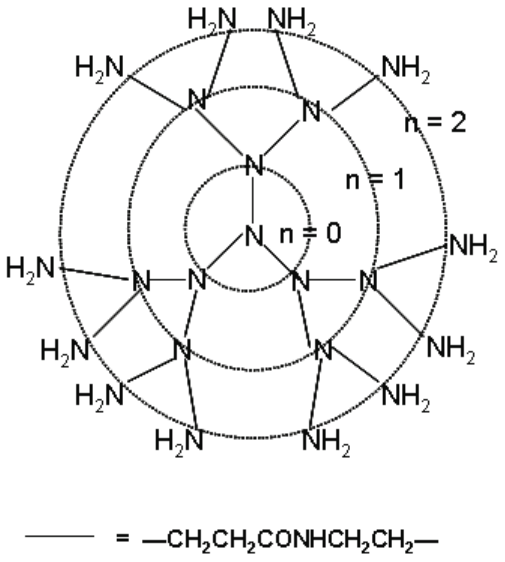


Figure 24. A core type PAMAM dendrimer, n = generation, [178]

1.7.5 CEST and LIPOCEST Contrast Agents

Amongst novel contrast agents; chemical-exchange saturation transfer (CEST) agents are an emerging class of MRI contrast agents which facilitate an activatable signal. As a substitute to T_1 shortening agents for MR contrast enhancement, contrast can also be introduced by altering the proton density or total water signal detected by the MRI scanner. This can be accomplished using an old NMR technique called

magnetisation transfer (MT), first introduced by Forsén and Hoffman.[179] Many protons in the body exchange with bulk water and so these exchanging protons can be selectively RF excited. After irradiating a mmol pool of metabolites (such as amino acids, sugars, nucleotides or other heterocyclics having exchangeable OH or NH groups that exchange protons with bulk water), the energy is transferred to a nearby pool of water, producing a strong increase in enhancement by chemical exchange.

Using CEST agents, contrast can be switched "on" or "off" as required, as each response is uniquely related to the specific absorption frequency of the CEST mobile protons and this makes the detection of several agents in the same place possible. The sensitivity of CEST can be improved further by incorporating larger numbers of exchangeable protons into a polymeric CEST agent. This has been done by LIPOCEST agents, whereby liposomes containing a paramagnetic shift reagent for water protons in their aqueous inner cavity have been made.[180]

1.7.6 Superparamagnetic Contrast Agents (T_2 agents)

T_2 contrast agents as mentioned previously consist mainly of iron oxide nanoparticles; superparamagnetic iron oxide (SPIO, size: 80-150 nm), very small paramagnetic iron oxide (VSPIO, size: 4-8 nm) or ultrasmall superparamagnetic iron oxide (USPIO size: 20-40 nm). These particles usually consist of a crystalline iron oxide core surrounded usually, by an outer layer that will facilitate uptake into the biological target. The advantage of these nanoparticles is that each particle can contain thousands of iron atoms, resulting in very high T_2 relaxivities of up to 200 $(mM)^{-1}$.[181]

Superparamagnetic iron oxide crystalline structures consist of the general formula $Fe_2^{3+}O_3M^{2+}O$, where M^{2+} can be either Fe, Mn, Ni, Co or Mg. Within this type of crystal material, the occurrence of regions of groups of unpaired spins can occur, which can exist as thermodynamically independent areas termed single domains. Once placed in a magnetic field these domains can therefore all line up to the external magnetic field in a similar fashion to other paramagnetic agents. This arrangement leads to much greater magnetic moments in comparison to other paramagnetic agents and is the cause of the high magnetic susceptibility attributed to superparamagnetic agents.

Although superparamagnetic contrast agents are very efficient signal enhancers and have been studied extensively, the problem with using iron contrast agents is the

issue of their hypersensitivity. Iron particles exert a magnetic susceptibility far beyond the local margin (**Figure 25**). For example iron particles provide targeted labelled cells with a large magnetic moment that creates substantial disturbances in the local magnetic field, leading to a rapid dephasing of protons, including those not directly in the vicinity of the targeted cell.

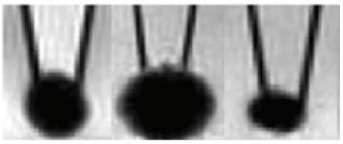


Figure 25. T_2 weighted MR image of cell pellets labelled with iron nanoparticles.[93]

Many examples of superparamagnetic agents exist to date, with successful agents entering clinical trials more readily. However, improved methods are still under investigation for the control of important characteristics of these compounds, including particle size, charge, and outer layer coating.[182] These particles are also under investigation for rendering them target specificity.

1.7.7 Nanoparticle Contrast Agents

Nanomedicine is set to make considerable contributions in the important areas of drug delivery, disease detection, therapy and stem cell based therapeutics. It is envisaged that the detection of disease by means of molecular imaging and subsequent therapy aimed only to the diseased sites can become standard practice in medical clinics. As such, the design and development of nanoparticle based contrast agents can be of significant value in medical practice.

Moffat *et al.* have been able to produce magnetic nanoparticle contrast agents with extremely high T_2 relaxation properties.[183] They were able to encapsulate multiple crystals of iron oxide within a polyacrylamide matrix and image gliomas in the rat brain. The addition of PEG polymers to the surface of these nanoparticles prolonged their blood circulation and accumulation in tumour tissue as validated by MRI.

In summary, the relaxivity of a contrast agent can be increased by restricting the free rotation by means of increasing the molecular weight. This has been achieved by using polymeric backbones or *in vivo* binding of small-sized contrast agents to serum

proteins.[184] The tissue concentration necessary to image with T_1 contrast agents is considerably higher than that of T_2 contrast agents and as discussed various labelling solutions have been developed. A number of approaches have been made to attain this result by the synthesis of covalently or non-covalently bound macromolecular gadolinium chelates such as dendrimers, linear polymers or proteins and also the use of gadolinium liposomes.

1.8 Paramagnetic Liposomes and MR Imaging

Liposomes are composed of lipid constituents, with hydrophobic head groups and hydrophilic tail groups (**Figure 26**). When hydrated, these lipids aggregate together to form self-assembled bilayer vesicles that enclose an aqueous compartment. Due to this aqueous cavity, they have traditionally been used as drug delivery vehicles, encapsulating water soluble drugs in order to improve drug pharmacokinetics.[185-187] In addition, nucleic acids have also been condensed into liposome formulations for effective transfection and gene delivery.[188-191] Despite these additional functionalities, liposomes were originally studied as models of biological membranes, and this is a key concept in the realisation of their biocompatibility.[192]

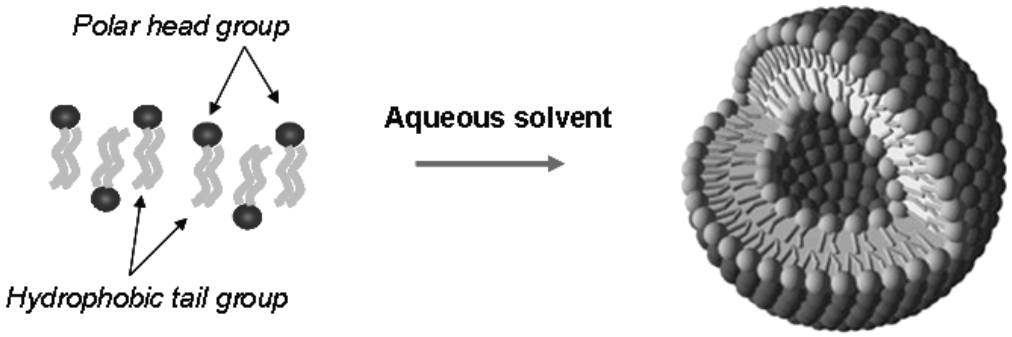


Figure 26. Liposome formation from amphipathic lipids.

The versatile nature of liposomes can be altered to change their interaction with various molecules or even larger structures such as cells. This can be done by altering the overall charge of the liposome surface by incorporating lipids with highly charged polar head groups in the liposome formulation. For example, the incorporation of cationic lipids in the formulation produces cationic liposomes. Cationic lipids have been used to formulate liposome/DNA complexes (lipoplexes) used as gene delivery systems *in vitro* and *in vivo.*[193-195]

Liposomes are typically characterised by their size, shape and lamellarity. They may be composed of a single bilayer (unilamellar), a few bilayers (oligolamellar), or multiple bilayers (multilamellar). The rigidity of the membrane can be modified with the use of suitable lipids; and the fluidity of the membrane may be varied by using phospholipids with high or low phase transition temperatures. In general lipid

derivatives of steric acids (fully saturated C18 lipidic chains) bestow rigidity and impermeability to the membrane, whilst lipid derivatives of oleic acid (unsaturated C18 lipidic chains) result in a more permeable and less stable lipid bilayer.

For *in vivo* applications and prolonged circulation of liposomes the liposome bilayer is frequently coated with the neutral polymer polyethylene glycol; PEG, which is routinely, used in the modification of the physiochemical properties of liposomes and the minimisation of bioadhesion and immunological response. In addition to this, PEG incorporation has been shown to increase relaxivity of agents used in MR imaging as the polymer adds bulk to a macromolecular structure, leading to reduced tumbling rates and hence increased Gd-metal water contact. The incorporation of PEG in liposomes as drug delivery systems significantly reduces their liver uptake and prolongs their circulation half-life. Steric stabilisation offered by the inclusion of PEG in the liposome formulations has proved extremely valuable in MR imaging of tumours *in vivo*.[196] Without a PEG layer, liposomes are extremely prone to uptake by the reticuloendothelial system (RES).[197] The biodistribution efficacy of liposomes can be improved by taking into account factors such as: liposome formulation composition, liposome size, surface charge, concentration of constituent lipids, the route of injection and the total volume injected *in vivo*.

Due to the variability of their composition liposomes have been used in a large range of biological developments. Their use has been applied to most imaging modalities discussed thus far, and they have also been targeted to a whole host of disease signatures of interest. An analysis of their use in all these various applications is beyond the scope of this thesis and therefore their utility only in MRI will be discussed.

By incorporating Gd lipids into the membranes of liposomes or by encapsulating paramagnetic contrast agents in their aqueous core, they can be rendered MRI visible and supramolecular systems with a better control of size can be obtained.[198,199] Liposomes are well suited as carriers of a high payload of Gd into cells. The incorporation of amphipathic gadolinium complexes into liposomal membranes has yielded paramagnetically labelled liposomes which significantly enhance proton relaxivity. These paramagnetic liposomes have been used in a number of investigations including that of cellular labelling and tracking.[76] The incorporation of Gd lipids into the liposome formulations was demonstrated by Kabalka *et al.* over 20 years ago and the Gd lipid (Gd.DTPA.BSA) used in their studies is frequently used to prepare paramagnetic liposomes today.[200]

Recently Vuu *et al.* presented an elegant study, demonstrating the effectiveness of bimodal paramagnetic liposomes in the labelling of breast cancer cells and the imaging of tumours in mice.[201] These bimodal liposomes were prepared using a novel Gd lipid that is designed to cross-link to other Gd lipids within the liposome formulation, producing stable covalently linked paramagnetic nanoparticles. A fluorescent rhodamine lipid was also included in the liposome formulation for *in vivo* fluorescence imaging and co-validation of MR results.

1.8.1 Paramagnetic Liposomes by Contrast Agent Encapsulation

The initial use of liposomes in MRI has mainly involved the encapsulation of the Gd or Fe label, where water-soluble agents were entrapped in the aqueous core of the liposomes or where the lipid soluble agents were held in the bilayer structure by van der Waals and hydrophobic interactions.

The encapsulation of the FDA approved clinical contrast agent Magnevist (Gd.DTPA) is the most common method of preparing paramagnetic liposomes, since this compound has excellent solubility and MR signal enhancement properties. Many paramagnetic contrast agents have been prepared using this agent with a range of applications.[202] Recently Port *et al.* demonstrated the simultaneous sustained release of a chemotherapeutic drug, fludarabine monophosphate and Gd.DTPA in rats.[203] This experiment was carried out to show the effectiveness of MR imaging using contrast agents for the assessment of the sustained-release of cytostatic agents. It was postulated that, upon drug release from the aqueous interior of liposomes, the contrast agent would also simultaneously release as evident by tumour signal enhancement at the injection site. The fluorinated drug and contrast agent were studied by ^{19}F MRS and MRI at 1.5 T over a period of six weeks. They were able to conclude that upon an initial lag time, the drug and contrast agent half-lives were 9 and 6 days respectively. This excellent study demonstrates the feasibility of monitoring drug release using contrast agent release from liposomes.

The incorporation of PEG into liposome formulations that encapsulate Gd.DTPA have also been reported, where due to this added masking layer their *in vivo* circulation times have been prolonged. Ayyagari *et al.* reported the use of PEGylated Gd.DTPA encapsulated liposomes in MR angiography, where their findings showed these liposomes to have a significant sustained (> 4 h) contrast enhancement of rat vasculature.[204] The utility of PEG coated liposomes for prolonged systemic circulation

was also demonstrated by Erdogan and co-workers who prepared anti-body immunoliposomes targeted to cancer cells.[205] The Gd encapsulation efficiency of these particles was increased through the usage of membrane-incorporated polychelating amphiphilic polymers. These polymers have attached multiple Gd metal chelating groups per single unit and also posses a lipidic moiety for anchoring into the liposome membrane. This method increases the Gd payload per particle, in addition to exposing most of the Gd chelating groups on the surface of the liposome, allowing for increased water contact.

Various other targeted Gd loaded liposomes have also been prepared and applied to glioma imaging,[206] and investigated for target-site delivery of their entrapped contrast agents.[207] In addition to Gd loaded liposomes; superparamagnetic liposomes have also been prepared with very high relaxivities. Superparamagnetic liposomes consist of magnetic fluid loaded liposomes that are capable of significantly reducing T_2 relaxation.[192,208] These highly efficient MR contrast agents have been further functionalised with the incorporation of PEG polymers for steric stabilisation and prolonged *in vivo* circulation times.[209] The properties and preparation methods of these Fe containing superparamagnetic liposomes is subject to continuous improvement, and their utility in MR angiography has also been established.[210-213]

In terms of an encapsulation method, liposomes can be useful for entrapping drugs within their internal aqueous compartments, however when encapsulated with MR contrast agents there are drawbacks. There are limitations such as contrast enhancement being limited to water flux across the membrane. This can be partially overcome by making the liposomes very small, such that a high surface to volume ratio facilitates water exchange. Alternatively, the membranes can be designed so that they can be permeable to water, but this raises issues of instability in media and serum.[214] Unger and co-workers however, attempted to develop the encapsulation method further. They carried out liposome encapsulation of non-lipidic Gd.DTPA in the aqueous compartment by implementing a freeze-thaw extrusion process where the encapsulation efficiency of the vesicles was greater than 35% (400 nm vesicles), although the relaxivity of encapsulated liposomes can only be improved marginally.[215]

1.8.2 Paramagnetic Liposomes by Gd Lipid Incorporation

The relaxivity of Gd encapsulated liposomes is a lot less than that of the free compound and therefore the incorporation of the Gd into the liposome membrane, where the Gd.DTPA or Gd.DOTA moiety will protrude on the surface of the liposome

will greatly enhance the relaxivity (more water contact is offered in this way, hence a more rapid relaxation event). Kabalka *et al.* demonstrated that the attachment of two hydrophobic chains to the DTPA chelate had little effect on the ability of DTPA to complex Gd.[216] They also showed that liposomes containing paramagnetic amphipathic agents significantly enhanced the MR signal intensity in T_1-weighted MRI. They observed that these agents were suitable for the imaging of liver, spleen, bone marrow, and other organs that are rich in macrophage activity. As such, a range of paramagnetic liposomes have been prepared using mainly, the lipidic contrast agent Gd.DTPA.BSA shown in **Figure 27**.

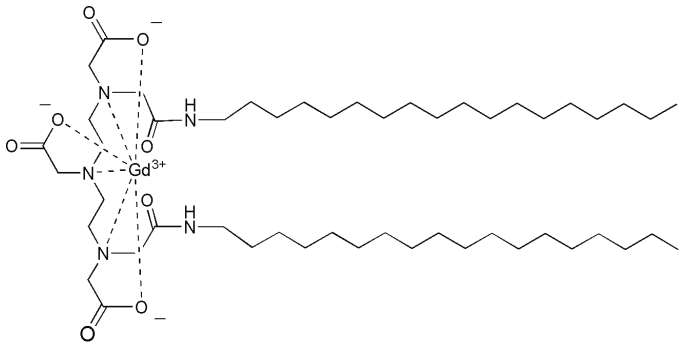


Figure 27. *N*,*N*-Bis-stearylamidomethyl-*N*`-amidomethyl]-diethylenetriamine tetraacetic acid (Gd.DTPA.BSA).

The effectiveness of paramagnetic liposomes as contrast agents has prompted a diversely investigated field for over 20 years and as well as exploring their passive targeting nature, they have also been altered by the incorporation of tissue targeting antigens and antibodies on the liposomal surface. The *in vivo* stability of these paramagnetic systems has been made favourable by the adjustment of their lipid composition; here, the huge variety of natural and synthetic lipids available provides many opportunities for the customisation of liposomes.

1.8.3 Targeted Gd Liposomes for MRI

The versatile nature of liposomes allows for their targeting to various disease markers. Targeting moieties in the forms of ligands, peptides, proteins or specific antibodies can be conjugated onto the surface of liposomes via the use of standard bioconjugation techniques. Gd based paramagnetic liposomes were formulated using the Gd.DTPA.BSA lipid by Brandwijk *et al*.[217] The incorporation of a maleimide PEG

lipid into the liposome formulation allowed for the surface attachment of anginex, a 33-mer angiostatic peptide which has been shown to home to activated endothelium undergoing angiogenesis. MRI and fluorescence microscopy of these targeted liposomes which also incorporated a fluorescent lipidic probe showed specific binding of these agents to activated endothelial HUVECs. A similar approach and liposome model was also used by Mulder *et al.* for the conjugation of an anti-E-selectin monoclonal antibody as a targeting ligand towards activated endothelial cells.[218]

The conjugation of proteins to the surface of liposomes was demonstrated by Reulen and co-worker's use of a cysteine-functionalised phospholipid, incorporated into liposome formulations, and shown to readily react with the mercaptoethanesulfonate-thioester of a model protein.[219] This conjugation method was also extended to the conjugation of a collagen-binding protein. This work demonstrated the feasibility of directly conjugating recombinant proteins to liposome surfaces specifically through native chemical ligation.

The surface functionalisation of liposomes by conjugation of a NIR-tagged annexin A5 protein was recently demonstrated by van Tilborg *et al*.[220] Here, bimodal Gd lipid based liposomes were prepared and a maleimide PEG-tethered lipid was also included in the liposome formulation. This targeted paramagnetic liposome was capable of specific binding to apoptotic cells and can be useful in the detection of cell death *in vivo* by MRI. The same researchers have developed similar systems for bimodal quantum dot and MR imaging of annexin A5-conjugated liposomes for the detection of apoptotic cells.[221]

1.8.4 Further Applications of Paramagnetic Liposomes

Due to the ease of liposome formulation and the flexibility offered with regards to the range of lipidic and lipophilic agents available for incorporation into their bilayers, liposomes have been used in a variety of MRI applications. As such, Gd liposomes have been used in various applications other than their intended original use in liver and spleen imaging. There are a number of areas in which paramagnetic liposomes have been utilised, allowing for optimal MR imaging systems to be designed. For example their use in CEST imaging and the development of thermosensitive and pH sensitive paramagnetic liposomes adds to their excellent utility profile.

LIPOCEST Agents

In chemical exchange saturation transfer (CEST), the total water signal observed can be altered by using selective irradiation at the resonance frequency of the contrast agent's protons. Once the contrast agent's hydrogens are excited at a selected RF, then the bulk water signal will decrease due to chemical exchange. In this manner, the MRI contrast can be switched on or off by using selected irradiative RF pulses at an exchangeable site close to the bulk water. This effect is greatest if the shift resonance of the probe and that of the bulk water is large. Liposomes (Liposome-CEST) have been used in this area since a large number of moving water molecules are enclosed in their aqueous core and if paramagnetic agents are also encapsulated or form part of the liposome membrane, then the difference in their chemical shift resonance is even more pronounced. This difference in intra-liposomal water chemical shift and external water resonance has been exploited by Terreno *et al.* extensively.[218] In a recent study, they demonstrated the use of encapsulated shift reagents (paramagnetic agents capable of effecting water chemical shifts) in liposomes and were able to show large irradiation frequency differences for these systems. This is important since, the larger the difference of the chemical shift of the protons inside the liposome in comparison to the outside, the more improved the *in vivo* signal can become.

LIPOCEST agents are capable of achieving excellent sensitivities and these saturation transfer techniques used can even be applied to specific compounds in a mixture within the liposomal core.[180]

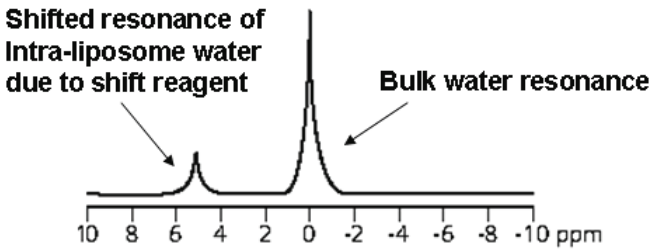


Figure 28. A cartoon of a prototype NMR spectrum of a LIPOCEST system.

Thermosensitive and pH Sensitive Paramagnetic Liposomes

Paramagnetic thermosensitive liposomes have been used to provide tumour temperature measurements. These types of liposomes can encapsulate temperature-dependent chemical shift paramagnetic chelates or they can have on or off switches as defined by the gel-to-liquid crystalline phase transition temperature (T_m) of the lipids that constitute the liposome membrane. These types of liposomes can be very beneficial in the real-time spatial non-invasive temperature measurements of areas where catheter probes are hard to reach. The mechanism of operation for paramagnetic thermosensitive liposomes relies on the phase transition that the phospholipid constituents undertake once hyperthermic temperatures (generally ~ 40-57 ºC) are reached. Here, the transition state of the lipids changes from a gel-phase to a liquid-crystalline phase, and in doing so increases the transmembrane permeability towards water. This in turn leads to an enhancement of the MR signal, since more water contact is allowed for the encapsulated contrast agents. Paramagnetic liposomes with a transition temperature of ~ 57 ºC have been used for MR-thermometry of thermal ablation at temperatures above 55 ºC *in vivo* for the imaging of rabbit liver and kidney.[222] Heating was carried out by using ultrasound. The enhanced areas which were due to the subsequent release of entrapped contrast agents within the liposomes were super-imposable with isotherms estimated from MR temperature images. This data also correlated with histological findings of damaged areas where the T_1 signal was also significant.

The acidic nature of tumour tissue has led to the development of novel pH-sensitive paramagnetic liposomes with improved MR properties. This method relies on the degradation of the liposome structure once in a tumour region in order to allow for the liposomal contents, such as drugs, to be released to the target site. This theory has also been investigated in the field of gene therapy, where the endosomal pH inside the cell could also be a trigger for liposome degradation and therefore the release of the therapeutic nucleic acids into the cytoplasm for eventual transport to the nucleus. Similarly, these systems must be stable in the blood stream, and subsequently able to release encapsulated materials upon exposure to the acidic pH in target tissue such as cancers.[223,224]

Other areas where paramagnetic liposomes have been used are in convection-enhanced delivery of liposomes in the brain (contrast agents are directly injected into the brain). This approach can be used to deliver greater volumes of drug loaded liposomes to solid tumours in the brain and MR imaging has been applied to the monitoring of liposomal distribution in gliomas in murine models.[225,226]

1.9 Thesis Synopsis

The aim of this project has been to design, synthesise and evaluate novel Gd lipids for liposomal cell labelling *in vitro* and solid tumour imaging *in vivo*.

Effective cell labelling agents should be capable of delivering a high payload of the labelling agent into cells. Liposomes which are composed of thousands of lipid molecules make ideal cell labelling systems, as they are able to deliver many molecules of contrast agent. By incorporating paramagnetic lipids into the liposome formulation, paramagnetic liposomes are created. This is an excellent method of improving contrast agent delivery *in vitro* or *in vivo*, since the versatile nature of liposomes allows for a good degree of control of parameters that can improve uptake and specificity of liposomes such as size, surface charge and targeting. As such, a unimodal paramagnetic lipid was synthesised, bearing a Gd.DOTA head group and a fully saturated hydrocarbon tail. This lipid was then used to optimise paramagnetic liposome formulations for effective cell labelling and uptake, utilising visualisation by both MRI and fluorescence microscopy which was made possible through the inclusion of a fluorescent lipid in the liposome formulation (DOPE-Rhodamine). These bimodal liposomes are useful for the labelling of cells *in vitro* and due to the presence of an excess cationic charge can also effectively encapsulate DNA within their aqueous cores. This results in bimodal fluorescent and paramagnetic liposomes that are also bifunctional, capable of simultaneous cellular imaging and nucleic acid delivery into cells.

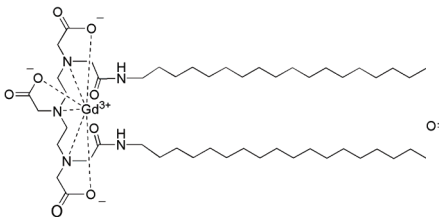
An improvement on these bimodal liposomes would be to develop a lipid that bore both the fluorescence and paramagnetic moieties on the same structure and as such this was a further aim of this project. The co-validation of contrast agent labelling either *in vitro* or *in vivo* by two techniques is valuable as in this manner, MR imaging can provide anatomical information with excellent spatial resolution and fluorescence analysis can provide sensitive and further proof of liposome biodistribution. In addition, progression from a unimodal, to bimodal fluorescent and paramagnetic lipids led to the design of trimodal agents, work towards which is presented.

The utility of the Gd lipids synthesised was assessed both *in vitro* and *in vivo* and their MRI signal enhancement efficacy measured and compared to clinical contrast agents. The results presented in this thesis show the effective use of novel contrast agent lipids for MR imaging of tumours and the labelling of cells; these results provide insight into the behaviour of nanoparticles as concomitant tumour imaging and therapy delivery agents for both *in vitro* and *in vivo* use.

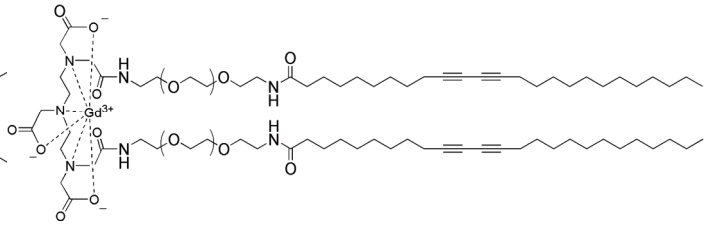
2. *Synthesis and MRI Analysis of First Generation Gadolinium Lipid - Gd.DOTA.DSA*

2.1 Paramagnetic Gd Lipids

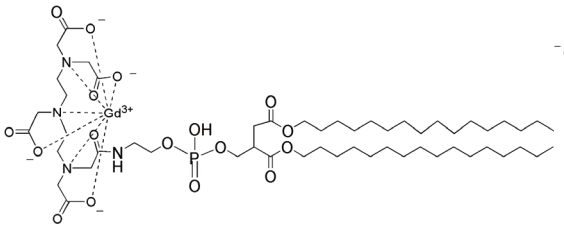
Gd based lipids have been incorporated into liposome formulations to achieve paramagnetic liposomes for over two decades now. The design of these lipids has mainly involved the conjugation of the FDA approved Gd.DTPA MRI contrast agent moiety onto a suitable lipidic tail for anchoring into the liposome bilayer. Some examples of paramagnetic lipids synthesised by various research groups are presented in **Figure 29**.



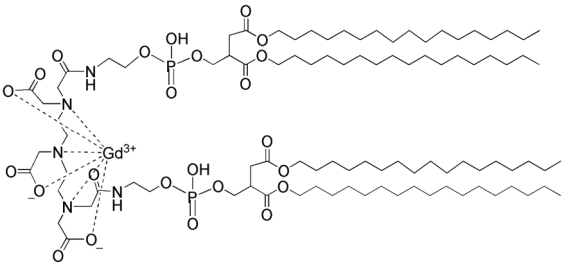
Gd.DTPA.BSA.[227,228]



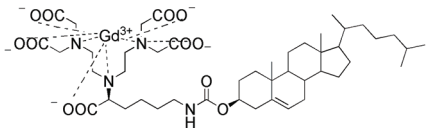
PPL: polymerisable paramagnetic lipids.[229]



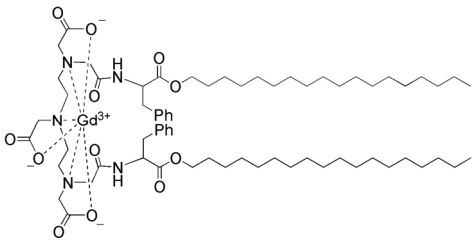
A paramagnetic dipalmitoylphospho lipid.[230]



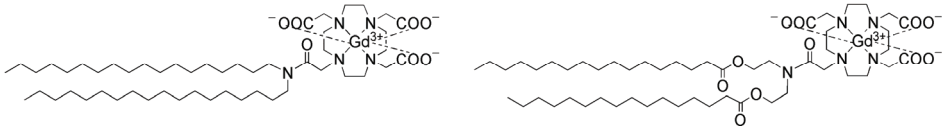
Gd.DTPA(DSPE)$_2$ derivative.[231]



Gd.DTPA.Cholesterol.[232]



Gd.DTPA with aromatic side chain groups.[233]



Gd.DOTA lipid derivatives.[234]

Figure 29. Examples of paramagnetic lipids with various hydrophobic tails.

Leclercq *et al.* have designed and synthesised a gadolinium paramagnetic lipid with an additional functionality.[235] They synthesised the novel gadolinium lipid MCO-I-68 (see **Figure 30**), which also incorporates a cationic head group for DNA condensation and liposomal gene delivery. This lipid showed successful transfection of NIH 3T3 cells *in vitro* and was injected into mouse tumours, where the transfection efficiency of the paramagnetic liposomal DNA system was analysed by MRI.

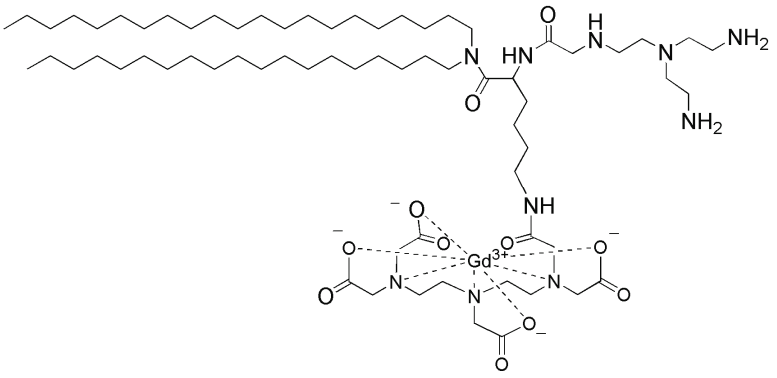
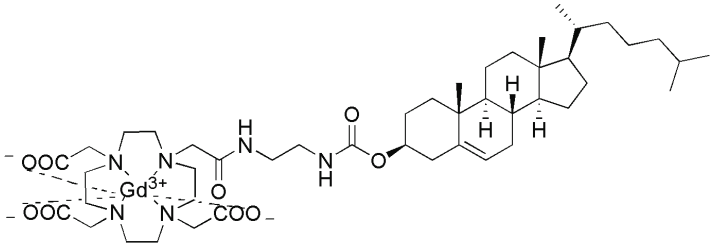


Figure 30. MCO-I-68/Gd complex. [235]

Lipidic Gd contrast agents allow for liposomal based MRI whereby thousands of contrast agent molecules can be incorporated per liposome leading to increased concentration of the paramagnetic metal agent and an increase in T_1 signal.

2.2 Synthesis of Gd.DOTA.DSA

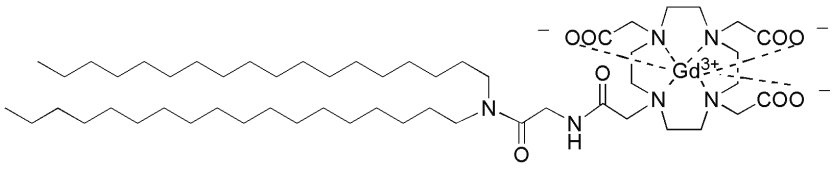
Previous work in the group has shown the novel gadolinium lipid Gd.DOTA.Chol **1** to be an effective MR signal enhancer, and MAGfect a liposome formulation containing this gadolinium lipid an efficient cellular dual labeling and transfection vehicle.[76]



1

Figure 31. Gd.DOTA.Chol, a T_1 lipidic contrast agent component of MAGfect.[76]

Although an effective cellular labelling lipid, formulation of high liposome concentrations using this lipid was observed to be problematic, perhaps due to the poor anchoring of the cholesterol tail in the liposome bilayers at high concentrations. Therefore, due to this limitation, the need to provide a more robust membrane anchor designed for *in vivo* applications where higher concentrations of liposome are required; lead us to the investigation of an alternative saturated alkyl chain moiety in place of the cholesterol anchor. For this purpose a novel paramagnetic lipid Gd.DOTA.DSA **2** (**Figure 32**) was synthesised using a combination of solution and solid phase chemistries.



2

Figure 32. Paramagnetic gadolinium lipid target, Gd.DOTA.DSA.

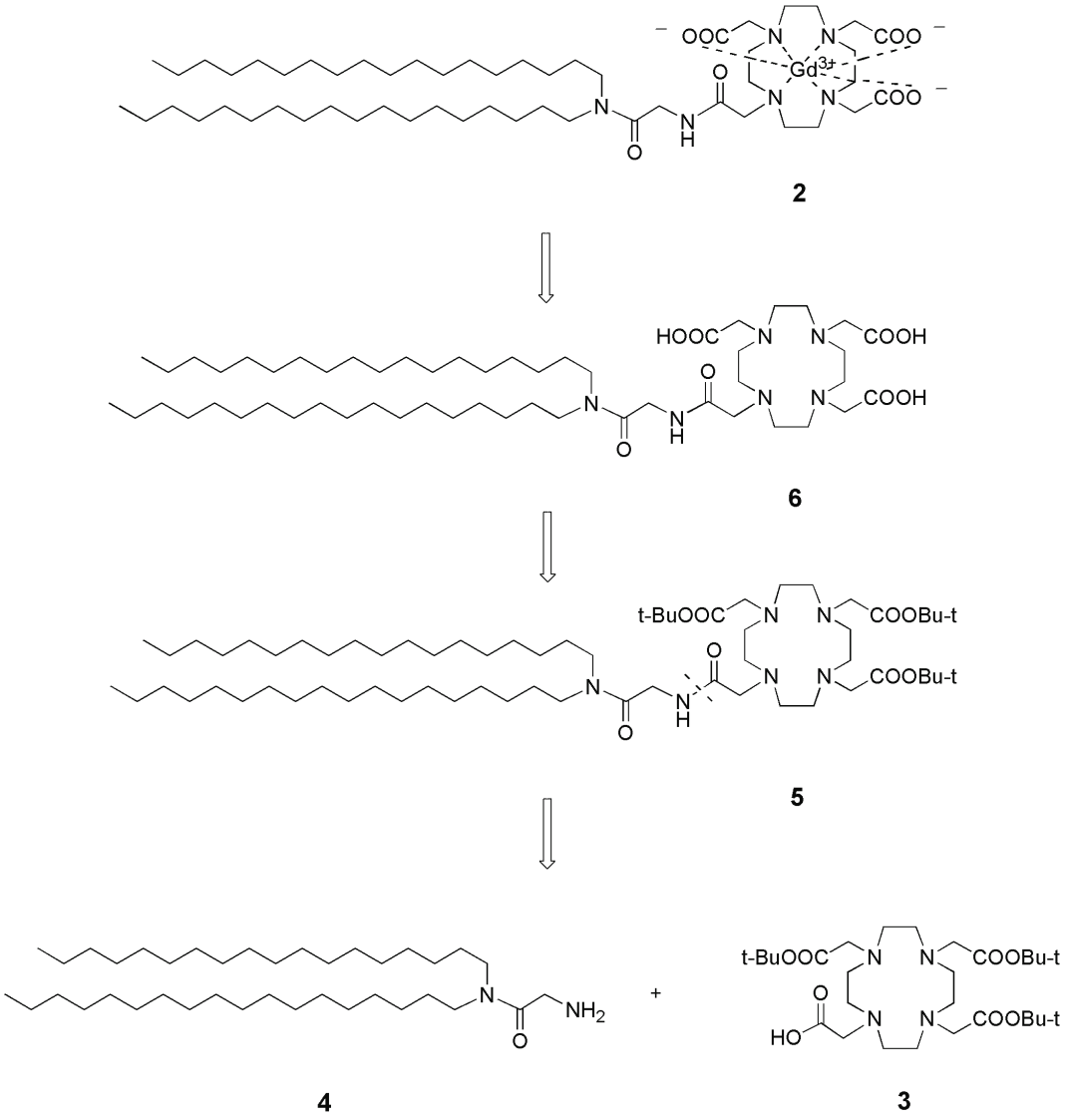
The DOTA chelate was conjugated to the lipid via a stable yet biodegradable amide functional group. Gadolinium lipid **2** was also designed with a five-atom spacer between the gadolinium chelator and lipidic alkyl chain moieties. This spacing between the head group and the lipidic alkyl tail was considered to be optimal in order to ensure maximum exposure of the gadolinium chelate to water on the hydrophilic surface of the liposome particles.

Furthermore, gadolinium lipid **2** was also designed with the DOTA ligand rather than the more frequently used DTPA, since the former macrocyclic ligand is considered to be a more effective chelator of gadolinium, able to retain the metal ion even in the acidic environment of the endosome.[236] The FDA approved Gd.DOTA chelate was chosen, since due to their higher stability constants, DOTA based conjugates are known to be more stable *in vivo* in comparison to DTPA ligands.[237]

A retrosynthetic analysis of the target lipid Gd.DOTA.DSA (Gadolinium (III) 2-{4,7-bis-carboxymethyl-10-[(*N*,*N*-distearylamidomethyl-*N*`-amido-methyl]-1,4,7,10-tetra azacyclododec-1-yl}-acetic acid) **2**, is presented in **Scheme 2**. Firstly, the gadolinium

lipid is made from the metal free ligand **6** (DOTA.DSA) by the addition of a gadolinium source such as gadolinium chloride. Ligand **6** is formed by the removal of the *tert*-butyl groups on the carboxylic acids of macrocyclic **5** in acidic conditions. Disconnection of the amide bond on **5** results in the protected macrocyclic DOTA **3** and the lipid amine **4**.

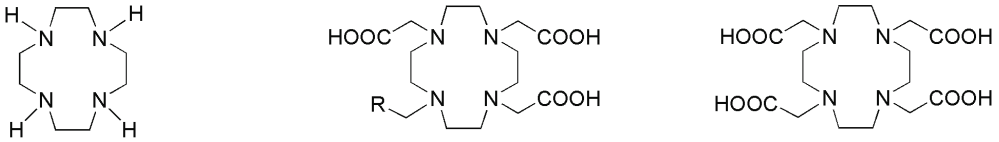
Most applications that involve conjugation to the DOTA macrocyclic ring are carried out through covalent linkage of a suitable synthon (usually an amine functional group) to one of the four carboxylate groups of the DOTA macrocycle. However, mono-functionalisation of the DOTA ring is necessary in order to prevent cross-linked products.



Scheme 2. Retrosynthetic analysis of Gd.DOTA.DSA.

2.2.1 Synthesis of Protected DOTA Ligand

Polyacetate derivatives of cyclen (**Figure 33**) such as DOTA (**9**) are part of a family of azacrowns that display excellent metal chelating properties, in particular towards heavy metal lanthanide cations. The synthesis of selectively *N*-functionalised cyclen derivatives has been met with many challenges.[238]



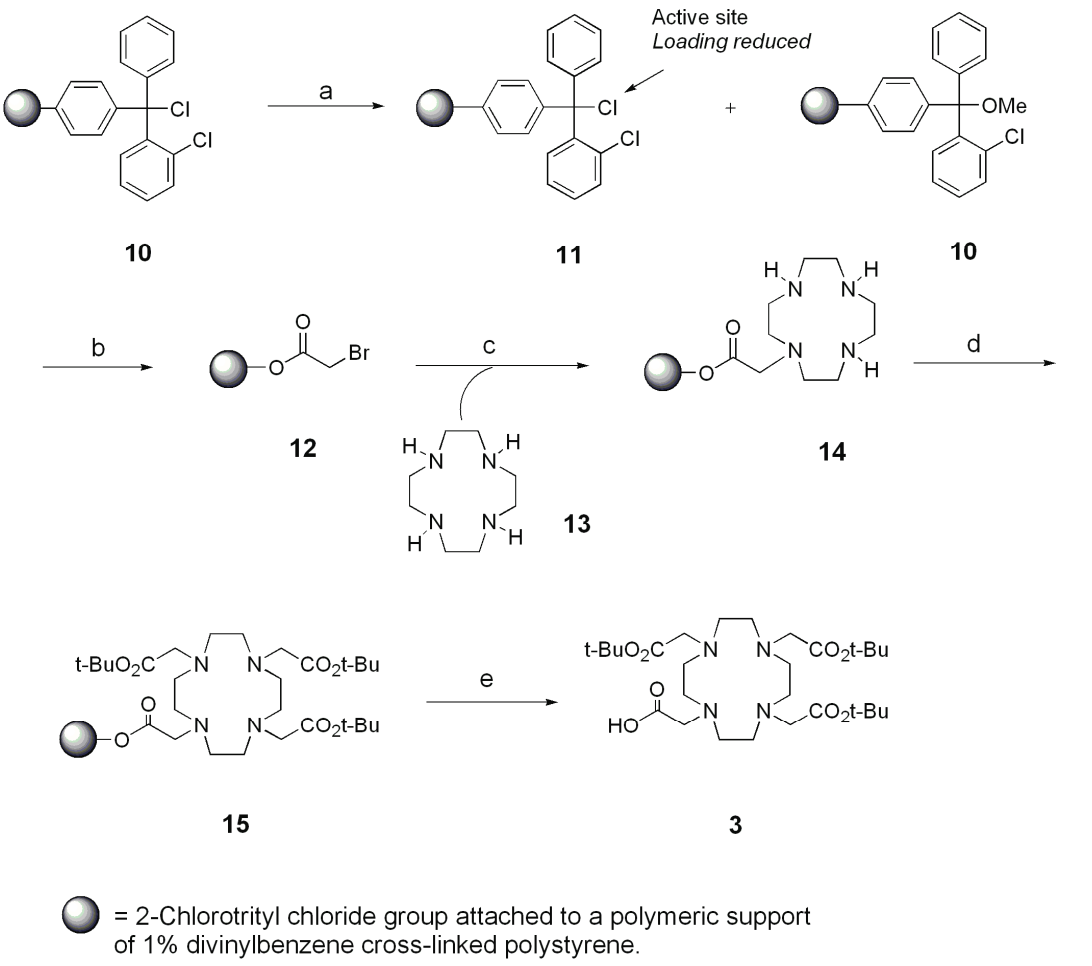
7 **8** **9**

Figure 33: Cyclen macrocycles.

Several selective functionalisations of cyclen to prepare compounds such as **8** have been reported. Prior to alkylation, three of the amines are usually temporarily protected by using stoichiometric amounts of protecting groups such as *tert*-butyloxycarbonyl, tosyl, formyl, trifuoroacetyl, or by the use of sterically hindered species like glyoxal aminal, and metal compounds $M(CO)_6$ (M= Cr, Mo, W).[239] All these procedures involve a protection, alkylation, and deprotection step, which in turn do not guarantee pure end-products, as competing reactions can yield di- and tri-functionalised side products.

Solid phase synthesis offers a cleaner and more selective option for the synthesis of compounds such as **8**; a range of nucleophilic groups such as carboxylic acids, alcohols and amines can be functionalised on to solid phase supports. The use of solid phase resins such as chlorotrityl resins, which can be generated by treating hydroxytrityl resins with thionyl chloride or acetyl chloride,[240] allow for the functionalisation of three sites on the azamacrocycle, in addition to the further temporary protection of the site attached to the resin itself. 2-Cholorotrityl resin is an acid labile resin, and its steric bulk allows for the mono attachment of cyclen. Also, the mild acidic conditions required for cleavage make this resin suitable for the synthesis of compounds such as **3** (**Scheme 3**)**.** Any unreacted material could easily be washed away with appropriate solvents.

For the synthesis of compound **3**, initially, MeOH partial capping was used to prevent molecular over-crowding of the chlorotrityl resin (**Scheme 3**). The resin was then functionalised with bromoacetic acid to yield acyl bromide **13**. An excess of cyclen was then added leading to resin-bound cyclen **14** wherein each cyclen was combined with the resin via a single acyl bromide leaving three uncombined secondary amine sites per bound cyclen. These remaining free amine sites were then further modified with the introduction of three *tert*-butyloxycarbonyl (Boc) protecting groups, and the reaction was then judged to have reached completion using the chloroanil test. A facile resin cleavage in mildly acidic conditions yielded macrocycle **3**, in reasonable purity and yield (60-70% yield, depending on the freshness of resin used).

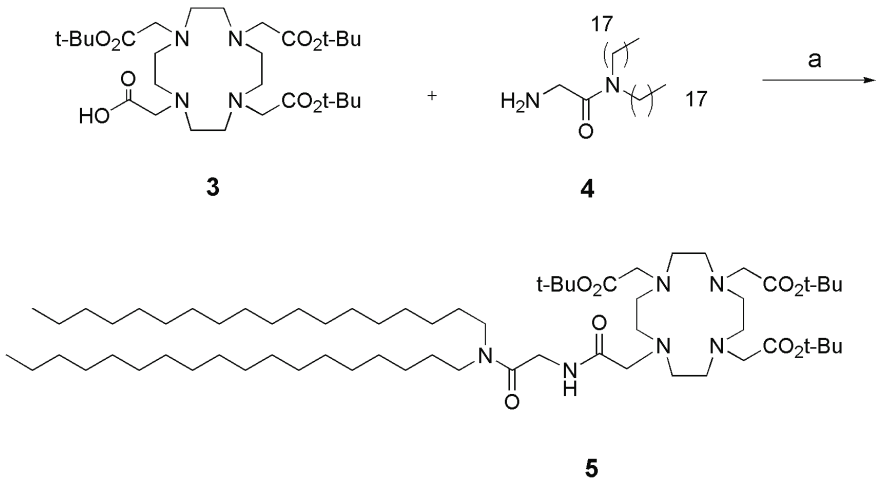


Scheme 3. a) MeOH, DIEA, CH_2Cl_2, rt, 4 h; b) $BrCH_2COOH$, DIEA, CH_2Cl_2, rt, 12 h; c) Cyclen, rt, 4 h; d) $BrCH_2CO_2C(CH_3)_3$, Et_3N, DMF, rt, 12 h; e) TFEtOH:CH_2Cl_2, rt, 2 h, 69%;

In each step the resin was washed by alternating between mainly protic solvents to filter any excess unreacted bromoacetic acid, cyclen or bromo-*tert*-butyloxycarbonyl. The final cleaved product was purified by an optimised flash coloumn chromatography method employing basic conditions and characterised by ^{1}H NMR, ^{13}C NMR, HPLC and MS.

2.2.2 Coupling of Protected DOTA and Lipidic Amine

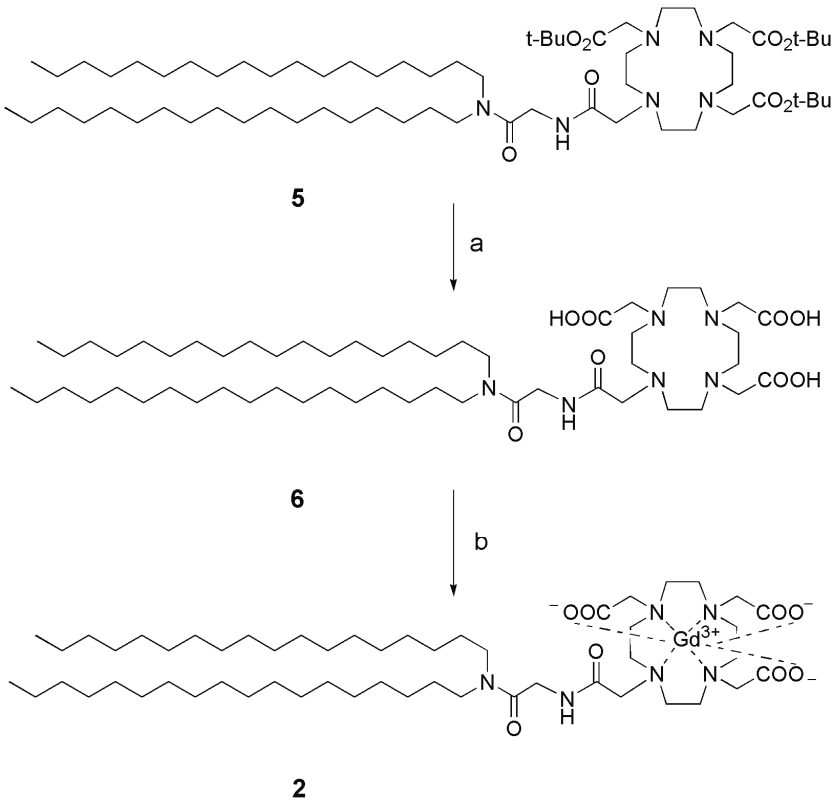
Macrocycle **3** was then reacted with lipidic amine **4** under typical peptide bond synthesis conditions to yield **5**, employing 2-(1H-benzotriazol-1-yl)-1,1,3,3-tetramethyluronium hexafluorophosphate (HBTU) and dimethylamino pyridine (DMAP) as carboxylic acid activators (**Scheme 4**). Initially, amide bond formation appeared to be significantly hindered by steric crowding imposed by the bulky Boc groups on DOTA, leading to poor yields of coupled product **5**. However, this problem was overcome by making use of highly pure reagents, dry chloroform and elevated reaction temperatures, leading to improved yields (ranging from 60-88%) and product quality. The DOTA cyclic ring is a highly conformationally strained system and can therefore adopt a more flexible conformation upon heating, rendering better access to the pre-activated carboxylate site for conjugation with lipid amine **4**.



Scheme 4. a) HBTU, DMAP, dry $CHCl_3$, 40 ºC, 12 h, 88%

A simple deprotection of **5** using HCl: dioxane at a 1:1 *v*/*v* ratio, gave DOTA.DSA **6** in good yield and purity. With **6** in hand, Gd complexation was carried out by simple stoichiometric addition of $GdCl_3.6H_2O$ to **6** in water at 90 ºC for optimum solubility of

the starting materials, thereby generating Gd-DOTA.DSA **2**. No significant free Gd^{3+} ions were detectable post complexation according to the xylenol orange assay (see below), and the pH was observed to have dropped to 3.5 (**Scheme 5**). Potentiometric studies of Moreau *et al.* have shown that the complexation of lanthanide cations to DOTA involves the instantaneous formation of metal ion complexes as soon as metal ions are combined with the ligand, leading to proton release and a sharp reduction in reaction pH.[141]



Scheme 5. a) c.HCl: dioxane, rt, 2 h, 68%; b) $6H_2O.GdCl_3$, H_2O, 90 ºC, 12 h, 99%.

Due to the paramagnetic nature of lipid **2**, NMR spectroscopy was not suitable as a characterisation tool due to the extreme peak broadening caused by the paramagnetic gadolinium metal. All gadolinium lipids were analysed by electrospray mass spectrometry (ESI-MS), HPLC and the xylenol orange assay was used to test for the presence of any free Gd^{3+} in the product samples. The xylenol orange assay is a colourimetric test whereby a colour change from orange to purple is indicative of Gd^{3+} complexation to the xylenol orange dye. This causes a bathochromic shift from 440 nm to 573 nm. Here, by using a standard calibration curve of known gadolinium concentrations versus absorbance, the amount of free Gd^{3+} in the sample could

therefore be assessed. As presented in **Figure 34** HPLC and MS analysis of Gd.DOTA.DSA **2** was carried out and no free Gd^{3+} was shown to be present, and the compound was prepared with 98% purity and excellent yields. The isotopic peaks of gadolinium were also visible in the MS trace and as a result the observation of the abundant isotopes of gadolinium confirmed complexation of the metal with the DOTA lipid. The HPLC, MS and the isotopic gadolinium peaks for compound **2** are shown in **Figure 34**. Subsequent gadolinium lipids were also analysed in a similar manner.

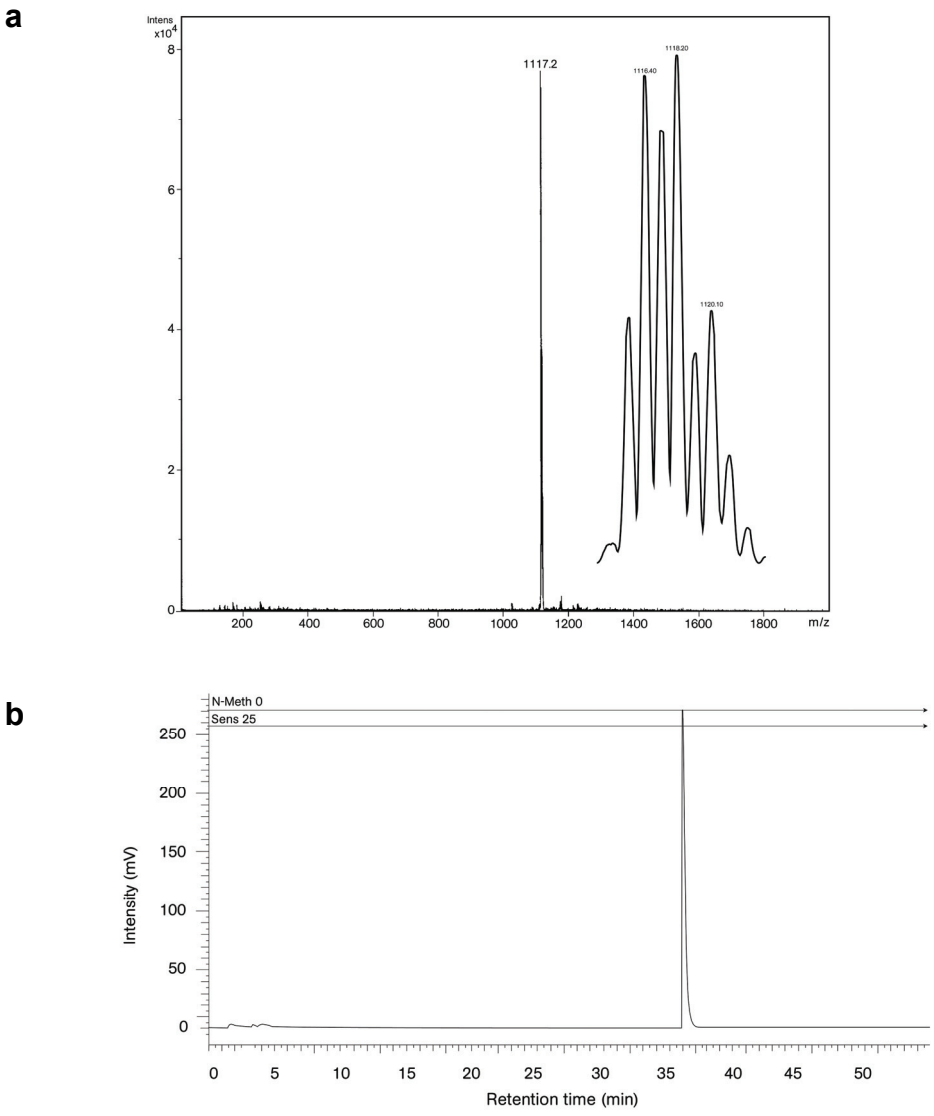
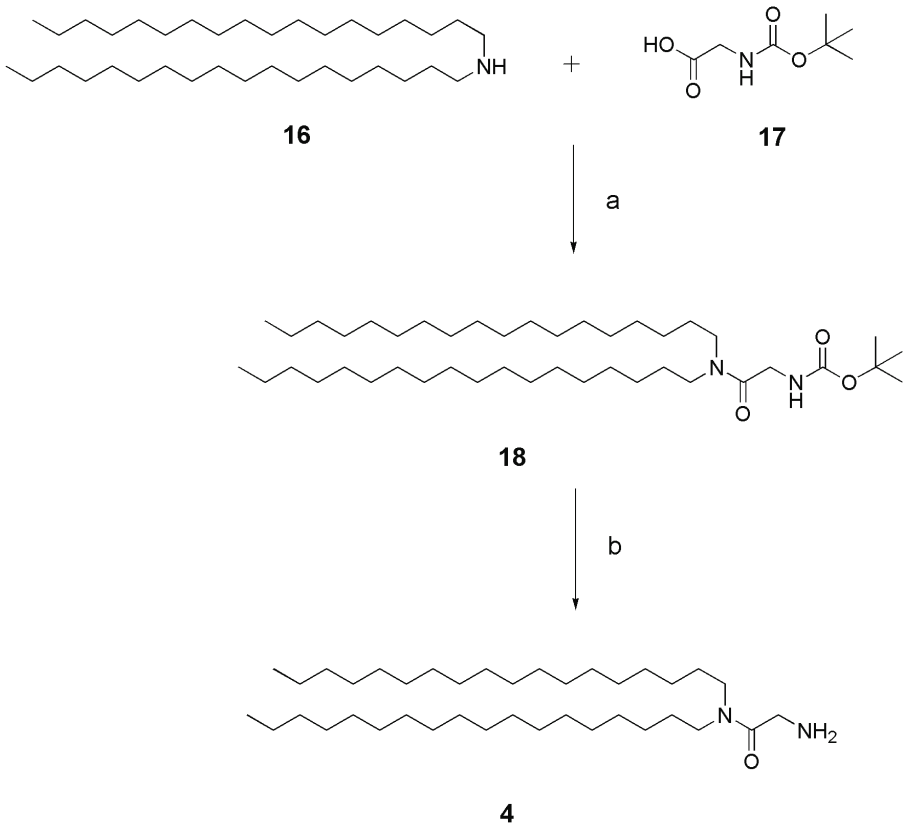


Figure 34. Characterisation of Gd.DOTA.DSA **2**: **a**; electrospray mass spectrum of Gd.DOTA.DSA, *m*/*z*: 1117.2 (M-H), the isotopic peaks of Gd are visible in the top right corner and **b**; HPLC trace of Gd.DOTA.DSA **2**: t_R = 36.22 min, column C-4 peptide; gradient mix A = MeCN/0.1%TFA; mix B = H_2O/TFA; mix C = MeOH/$CHCl_3$ mix D = MeOH, 0.0 min [100% B], 15-25.0 min [100% A], 25.1-45.0 min [100% D]; flow 1 mL/min.

2.2.3 Synthesis of Lipidic Amine Tail

Synthesis of precursor lipid amine **4** was accomplished in two steps as shown (**Scheme 6**). Amide coupling of Boc-glycine **17** with distearylamine **16** resulted in protected lipid amine **18**. A facile deprotection afforded lipid amine **3** [*N*,*N*-distearylamidomethylamine (DSA)] in good yield and purity (**Scheme 6**).

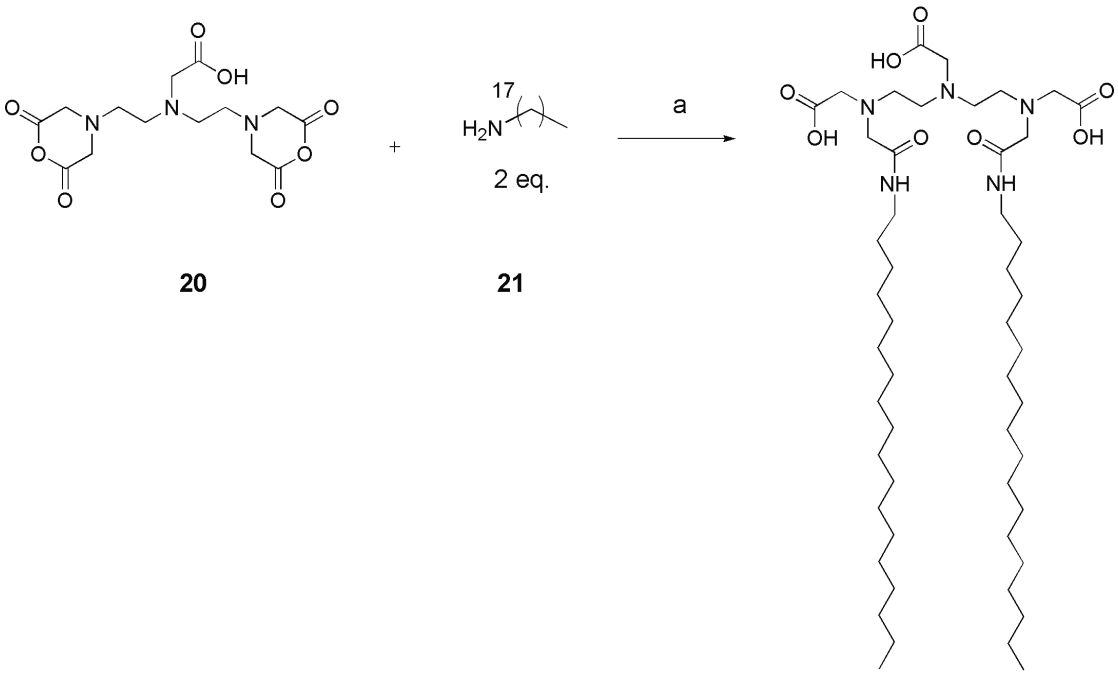


Scheme 6. a) HBTU, DMAP, rt, 12 h, 38%; b) TFA:CH_2Cl_2, rt, 3 h, 94%

2.2.4 Synthesis of Control Paramagnetic Lipid Gd.DTPA.BSA

Gd(III) [*N*,*N*-bis-stearylamidomethyl-*N*`-amidomethyl]-diethylenetriamine tetraacetic acid (Gd.DTPA.BSA) **19** was also synthesised for control MRI relaxivity studies since the use of this compound to formulate paramagnetic liposomes has had precedence in recent literature. The method of Jasanada *et al.* was adapted for the synthesis of this paramagnetic lipid.[241]

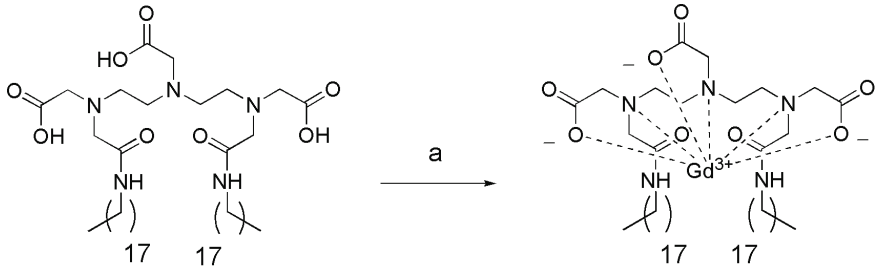
The synthesis for compound **19** involved two steps, the first step consisted of a nucleophilic attack of the octadecylamine **21** on the DTPA bisanhydride **20** to give DTPA-bis(octadecylamido) **22** (**Scheme 7**). DTPA.BSA **22** was solubilised in neat TFA for characterisation with NMR, MS and HPLC. The final step involved an analogous gadolinium complexation (**Scheme 8**) similar to that undertaken to obtain Gd.DOTA.DSA, **2**.



20 **21** **22**

Scheme 7. a) DMF: CH_2Cl_2, 40 ºC, 2h, 40%.

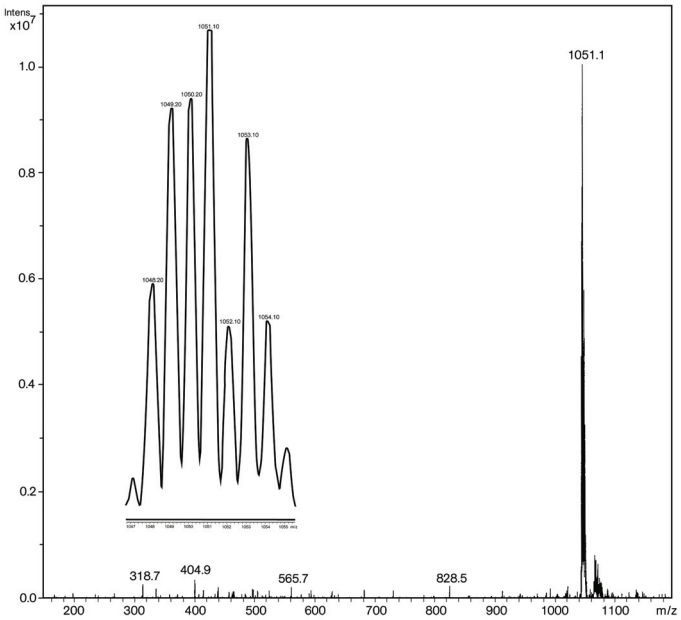
DTPA.BSA lipid **22** was easily complexed with Gd^{3+} by using gadolinium chloride in water at 90 ºC to yield compound **19** in good yields and purity (**Scheme 8**). This paramagnetic lipid was also characterised by HPLC, ESI-MS and the absence of free Gd^{3+} was confirmed with the xylenol orange assay (**Figure 35**).



22 **19**

Scheme 8. a) $6H_2O.GdCl_3$, 90 ºC, 12h, 98%,

a



b

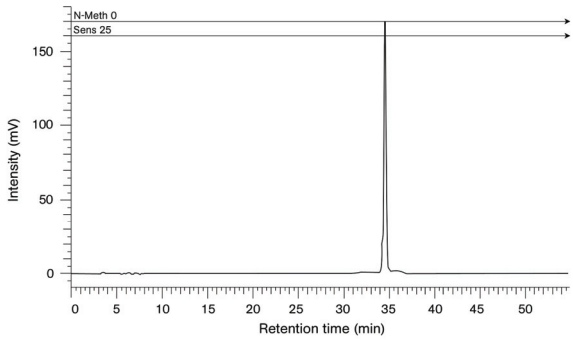


Figure 35. Characterisation of Gd.DTPA.BSA **19**: **a**; electrospray mass spectrum of Gd.DTPA.BSA, *m*/*z*: 1051.10 $(M+H)^+$, the isotopic peaks of Gd are visible in the top right corner and **b**; HPLC: t_R = 34.59 min, column C-4 peptide; gradient mix A = MeCN/0.1%TFA; mix B = H_2O/TFA; mix C = MeOH/$CHCl_3$ mix D = MeOH, 0.0 min [100% B], 15-25.0 min [100% A], 25.1-45.0 min [100% D]; flow 1 mL/min.

2.3 MRI Analysis of Paramagnetic Lipids Gd.DOTA.DSA and Gd.DTPA.BSA

In order to establish the relaxation properties of Gd.DOTA.DSA **2**, MRI studies of the lipid in aqueous solution were performed and T_1 values and relaxivity parameters generated in milliseconds. The efficacy of gadolinium lipid **2** was compared to the clinical contrast agent Magnevist® (Schering AG) and Gd.DTPA.BSA **19** (see **Table 2**), and was found to compare favourably at the clinically relevant dose. These data also showed **2** to have a comparable, if slightly better, T_1 relaxation than the widely used Gd.DTPA.BSA lipid. A standard T_1 saturation recovery method (spin echo sequence) was used to determine T_1 values (according to **Eq. 1**), where x is TR (time to repeat), and S_i is the measured signal for a given TR.

$$S_i = S_0(1 - e^{(-x/T1)})$$

Equation 1. T_1 saturation recovery equation used to determine T_1 values.

Table 2 presents T_1 relaxation values for the synthesised Gd lipids in addition to relevant controls.

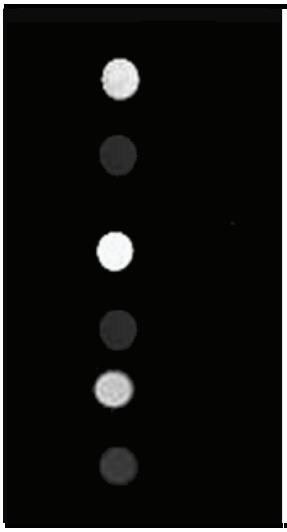
Sample		T_1 (ms)
	0.5 mM Gd.DOTA.DSA **2**	400.1 ± 15.92
	0.5 mM DOTA.DSA **6**	2356 ± 112.588
	Magnevist®	371.0 ± 4.321
	H_2O	2750 ± 121.8
	0.5 mM Gd.DTPA.BSA **19**	687.5 ± 26.03
	0.5 mM DTPA.BSA **22**	2760 ± 211.7

Table 2. T_1 values and images of Gd.DOTA.DSA **2** and Gd.DTPA.BSA **19** with relative controls.

The relaxivity of Gd.DOTA.DSA **2** was measured both in free lipid form in solution, and as part of liposome formulations. Relaxivity can be defined as the capability of a contrast agent to increase the relaxation rate of surrounding water proton spins within a range of Gd concentrations. For relaxivity measurements gadolinium liposomes were prepared using the series of formulations shown in **Table 3**. Five liposome formulations were prepared with gadolinium concentrations between 0.2 to 0.66 μM in 200 μL of distilled water. The relaxivity for Gd.DOTA.DSA **2** in these liposome formations was found to be 4.90 ± 0.60 $mM^{-1}s^{-1}$ (see **Figure 36**) according to calculations made using **Eq. 2**, where r_1 is the relaxivity, and $1/T_1[C]$ is the measured solvent relaxation rate in the presence of Gd.DOTA.DSA liposomes, with α_1 and [C] being the T_1 relaxation and gadolinium concentration values respectively. The relaxivity for Gd.DOTA.DSA **2** in liposome form is comparable to the relaxivity of other paramagnetic liposomes at 4.7 T.[242]

$$r_1\,[C] = 1/T_1[C] + \alpha_1 * C$$

Equation 2. Relaxivity equation to obtain r_1.

Liposome Formulation					
DOTAP (mol %)	**Cholesterol (mol %)**	**Gd.DOTA.DSA (mol %)**	**[Gd] μM**	**Liposome size (nm)**	**T_1 (msec)**
50	0	50	0.662	120.9 ± 33.2	117.4 ± 6.806
50	10	40	0.573	90.1 ± 45.8	157.2 ± 9.872
50	20	30	0.445	125.2 ± 36.7	196.5 ± 11.85
50	30	20	0.348	102.6 ± 31.9	247.2 ± 14.42
50	40	10	0.197	141.1 ± 45.9	285.6 ± 21.90

Table 3. Gadolinium liposomes used to calculate r_1 relaxivity of non-PEGylated liposomes.

Our choice of lipids (**Table 3**) for the liposome relaxivity measurements were based on the intended use of these lipids in preliminary *in vivo* experiments for intramuscular injections. However, it is important to note that relaxivity of Gd.DOTA.DSA may differ with respect to differing liposome formulations with varying sizes, and the inclusion or exclusion of PEG.

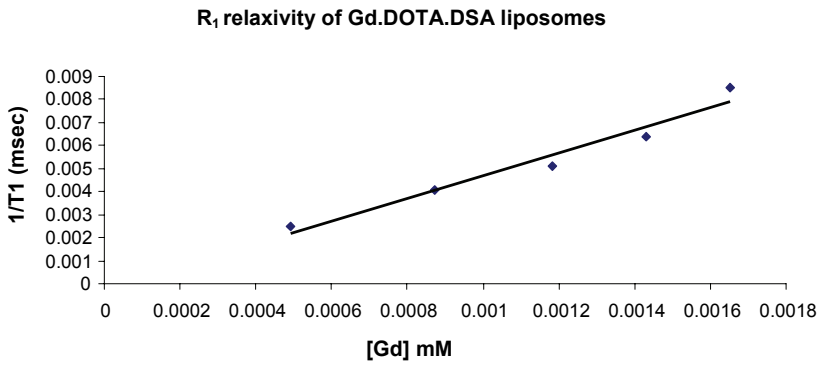


Figure 36. R_1 relaxivity measurement for Gd.DOTA.DSA liposomes (see **Table 3** for formulations). R_1 relaxivity is given by the slope of the linear fit, and is expressed in $mM^{-1}S^{-1}$. R_1 was found to be 4.90 ± 0.60 $mM^{-1}S^{-1}$ for these liposomes.

The r_1 relaxivity of the paramagnetic lipids Gd.DOTA.DSA **2** and Gd.DTPA.BSA **19** in aqueous solutions were obtained at 4.7 T. These values were found to be 0.62 ± 0.01 $mM^{-1}s^{-1}$ and 0.83 ± 0.04 $mM^{-1}s^{-1}$ respectively (**Figure 37**).

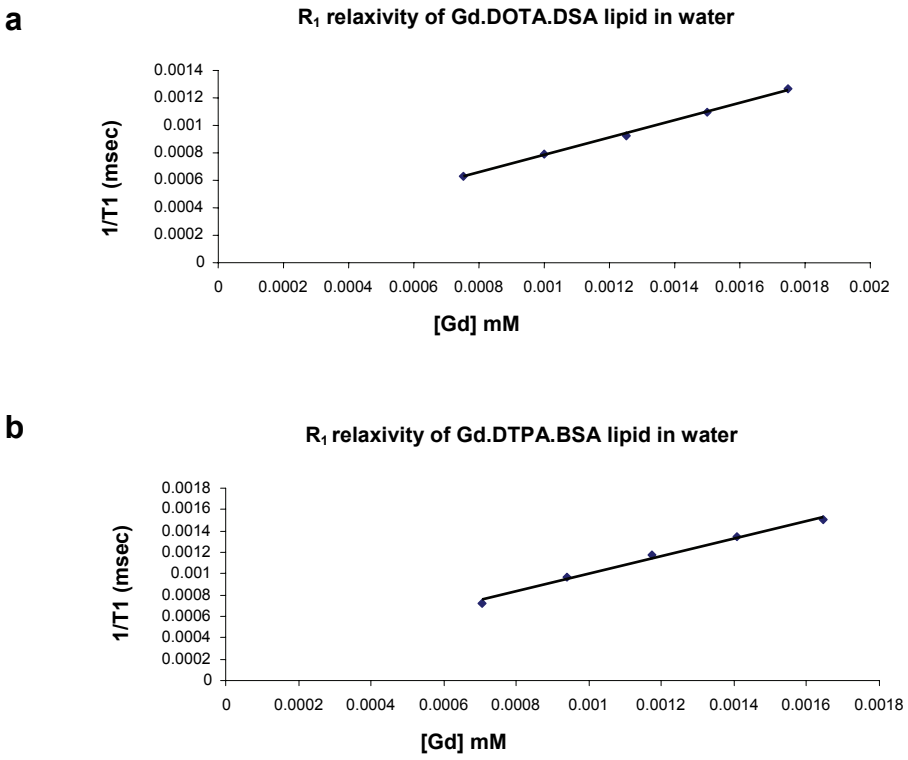


Figure 37. The r_1 relaxivities for aqueous solutions of the paramagnetic lipids alone; **a**: relaxivity graph for Gd.DOTA.DSA **2**, **b**: relaxivity graph for Gd.DTPA.BSA **19**.

The low values obtained for the r_1 relaxivity of the free Gd lipids in solution can be explained by the poor solubility of these lipids in water and their existence in a non-macromolecular liposome form (**Figure 37**). For the r_1 measurements in this instance, samples for both lipids were prepared with a gadolinium atom concentration within the same concentration range used for the liposomal relaxivity measurements (0.20 – 0.66 μM). These results show that paramagnetic lipids that are anchored into the liposome membrane once liposomes are formed, exhibit a much higher relaxivity than the free lipid in solution, based on these results, as high as eight fold.

Gadolinium lipid **2** was shown to have similar T_1 relaxation behaviour to the common clinical contrast agent Magnevist at the clinically relevant dose of 0.5 mM (see **Table 2**). This can be attributed to the mixed micellar structures of the Gd.DOTA.DSA lipid in water at the given concentration, whereby the rotational tumbling rate is reduced as a result of micelle aggregates. In addition, Gd.DOTA.DSA **2** was shown to be ~ 10% more effective than the commonly used Gd.DTPA.BSA lipid (**19**) at reducing bulk water T_1. The relaxivity of the paramagnetic liposomes has been shown to be mainly effected by the exchange rate (t_M) of the coordinated water molecule to the Gd metal centre of the membrane anchored paramagnetic lipid.[243] In addition to the exchange rate, the coordination number and the rotational correlation time (t_r) are also factors that affect the relaxivity of macromolecular contrast agents.[244] The possible motions through which the Gd metal water vector of the anchored lipid can lead to relaxation of surrounding water protons is shown in **Figure 38**.

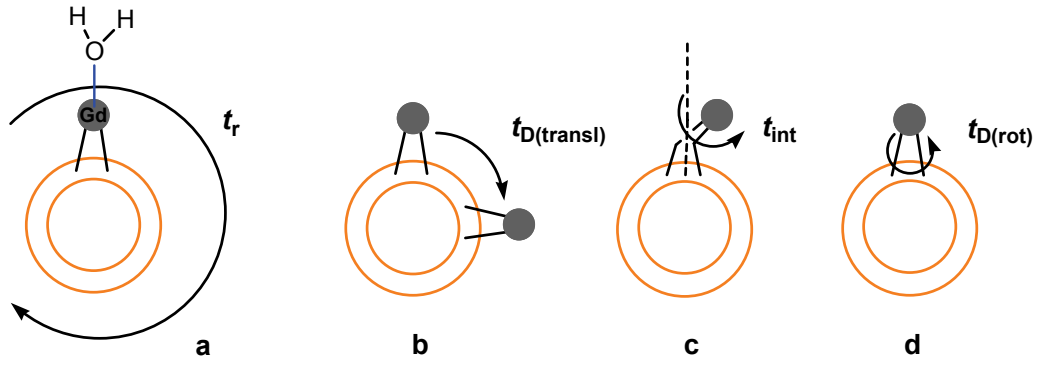


Figure 38. Cartoon of the possible motions that may occur involving the water molecule bound to the gadolinium atom of the lipid head group. Here, **a** shows the rotational motion of the whole liposome in water (t_r), **b** shows the translational diffusion of individual gadolinium molecules protruding the liposome surface ($t_{D(transl)}$), **c** presents the rotation of the gadolinium head group attached to the lipid tail (t_{int}) and **d** depicts the rotational diffusion of the entire gadolinium lipid in the liposome membrane ($t_{D(rot)}$).[243]

2.3.1 Chapter Summary

In conclusion, the synthesis of a novel gadolinium lipid was achieved and the MR relaxation efficacy of this lipid was evaluated. It was shown that T_1 measurements of aqueous solutions of this lipid at the clinically relevant dose compared favourably to Magnevist (FDA approved clinical contrast agent) and the relaxivity of this novel lipid was found to be comparable to similar paramagnetic liposomes studied at similar magnetic field strengths.[242] The difference in r_1 relaxivity between the lipid solutions and the liposome solutions is explained in terms of rotational tumbling rates, whereby as single lipids in solution, the gadolinium lipids are rotating at very high rates in comparison to their rotational behaviour once incorporated into liposome formulations. Liposomes are macromolecular structures, a property that reduces their molecular tumbling rates in water, leading to an increase in gadolinium metal water contact and an enhanced relaxation rate.

In order to gain more insight into the relaxation properties of the paramagnetic liposomes formulated with lipid **2**, future work could involve determining relaxivity as a function of magnetic field strength. This can be achieved by obtaining nuclear magnetic resonance dispersion (NMRD) profiles of the liposome series shown in **Table 3**. Information on the rotational tumbling rates (t_r) of these liposomes can also be deduced from such spectra. The effect of temperature on relaxivity of these paramagnetic systems can also be studied, since it has been shown that in general, r_1 increases with temperature which may suggest that at higher temperatures the liposome membranes are less rigid, resulting in an increased permeability, in turn, allowing for increased water contact with the inner-liposome gadolinium head groups.[242] In general, it is expected that Gd.DOTA based chelates used in the design of gadolinium lipid **2** will have faster water exchange rates (t_m) than their Gd.DTPA counterparts when studied at higher temperatures.[245]

3 . *In Vitro and In Vivo Biological Evaluations of Gd.DOTA.DSA*

3.1 In Vitro Evaluation of Gadolinium Liposomes

Cellular labelling to date has mainly involved the use of iron oxide nanoparticles, as strong signal enhancement arises due to the superparamagnetic nature of these labelling particles. However, recently gadolinium based probes have also been applied to the labelling of various cell lines and their subsequent *in vivo* tracking achieved using MRI. Cellular imaging is a growing field, for which novel probes and labels are under continuous development. For example, in addition to the labelling and tracking of cells of interest, novel contrast agents are being developed that are capable of monitoring functional cell status. Himmelreich *et al.* have recently studied a responsive gadolinium MRI contrast agent that is insoluble once outside the cell, however, once the probe enters cells through pinocytosis it is activated through enzymatic hydrolysis, and hence rendered soluble by intracellular lipases.[246] This type of cellular labelling can be applied to the monitoring of cell behaviour, for example, activation or differentiation of stem cells, and can be modified to respond to a range of enzymes that are expressed at various times within a particular cell cycle.

Given that cell membranes are themselves composed of lipids, the use of liposomes for the labelling of cells can be considered optimal, since liposomes also constitute lipids. It can be expected that a facile membrane fusion between these biocompatible agents and the extracellular cell membrane leads to their cell internalisation and entrapment. As such, we undertook to test the cell labelling efficiency of gadolinium liposomes formulated with the novel lipid Gd.DOTA.DSA **2**. The liposome formulation was optimised to allow for maximum cell uptake and the toxicity effects of the added liposomes were also assessed, cell labelling, and visualisation by both MRI and fluorescence microscopy was performed.

3.1.1 Gadolinium Liposome Formulation optimisation

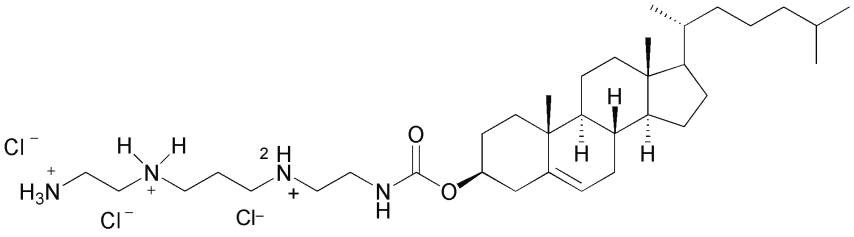
A simple method to quantify the uptake of gadolinium liposomes into cells is to include a fluorophore-tagged lipid in the liposome formulation. A very small molar percent of fluorescent lipids such as DOPE-Rhodamine is sufficient for this. Once liposomes are fused with the cell membrane and subsequently internalised into the cell via endocytosis, the liposome and therefore its constituents are trapped in the cytoplasm, and hence the emission of fluorescence from the cell lysate is indicative of the amount of intracellular liposome uptake. Any non-internalised liposomes will be washed away after the uptake period is complete, resulting in a fluorescence reading

obtained purely from cell internalised liposomes. The measured intensity at the appropriate excitation and emission wavelength of the fluorescent lipid probe is an indication of the amount of liposome, and more importantly the amount of gadolinium lipid that is internalised by the cells. Additionally, the incorporation of the fluorescent lipid also allows for fluorescence microscopy studies. A range of fluorescent gadolinium liposomes were prepared with various mol % ratios of Gd.DOTA.DSA **2** and the cationic lipid N^1-cholesteryloxycarbonyl-3,7-diazanonane-1,9-diamine (CDAN) **23**, the neutral lipid dioleoyl-L-α-phosphatidylethanolamine (DOPE) **24**, in addition to the red fluorescent lipid DOPE-Rhodamine **25**. These formulations were designed in order to assess the effect of increased cationic charge (CDAN lipid) of the liposome, increased neutral charge (DOPE lipid), and a high gadolinium lipid (Gd.DOTA.DSA) content on the efficiency of cellular uptake. The structures of CDAN, DOPE and DOPE-Rhodamine are shown in **Figure 39**.

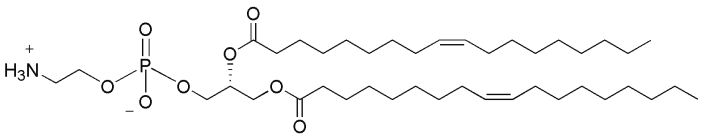
Other parameters investigated in addition to percent fluorescence uptake of the gadolinium liposomes into cells were incubation time and liposome concentration. The objective here was to determine a formulation, dose and incubation period that resulted in the most ample liposome uptake into cells without the appearance of cellular toxicity.

The incorporation of CDAN into the formulations renders a positive surface charge to the liposome membrane as CDAN has a cationic polyamino head group. Cellular uptake of liposomes is mediated by adsorption of these nanoparticles onto the cell surface followed by endocytosis. Charged liposomes are taken up more readily by cells in culture, due to the electrostatic interaction of the cationic liposome with the anionic cell surface. Thus, the fraction of positively charged lipid in a liposome is critical to cellular uptake, although a high percentage of cationic lipid results in toxicity and cell death.[247] It is therefore necessary to maintain the cationic nature of the liposome formulation whilst also balancing the molar ratio of the other constituents.

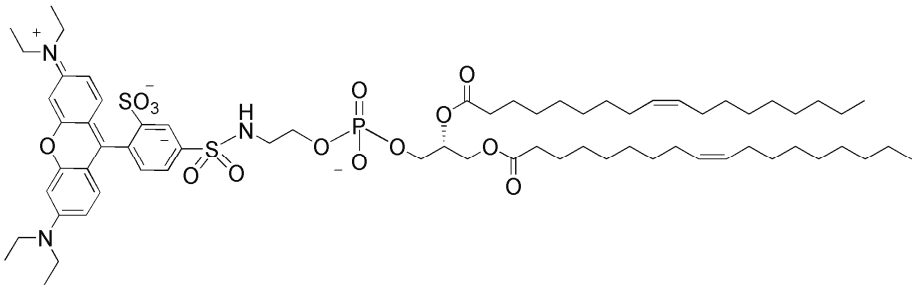
The inclusion of DOPE in the formulations is believed to aid in endosomal disruption. This is due to the fusogenic nature of DOPE. As the DOPE lipids fuse with the cellular or endosomal membrane, the endosome and its components are destabilised and readily released, therefore aiding in the cytoplasmic delivery of the liposomes *in vitro*.[248]



CDAN **23**



DOPE **24**



DOPE_Rhodamine (Lissamine Rhodamine B) **25**

Figure 39. Lipids used in Gd Liposome formulations.

In order to establish the cellular labelling efficiency of liposomes prepared with Gd.DOTA.DSA **2**, a series of eight liposome formulations were tested on HeLa cells so that an ideal non-toxic cell labelling liposome formulation could be determined able to deliver a maximal amount of Gd to the cells (**Table 4**). HeLa (human ovarian carcinoma) cells were chosen since they require minimum handling, are a robust cell line and therefore adequate for our proof of concept study of cellular labelling prior to progressing to more challenging and specialised cells. The gadolinium liposomes were prepared using the thin-film technique, hydrated in water, sonicated, and sized using photon correlation spectroscopy (sizes were between 200 – 300 nm on average, see **Table 4**).

Liposome	Gd.DOTA.DSA mol %	CDAN mol %	DOPE mol %	DOPE-Rhoda mol %	Liposome size (nm)
1	30	40	29.5	0.5	263.6 ± 45.67
2	30	30	39.5	0.5	275.1 ± 53.4
3	40	30	29.5	0.5	206.5 ± 20.5
4	40	40	19.5	0.5	209.6 ± 38.9
5	50	49.5	-	0.5	242.5 ± 46.5
6	50	-	50	0.5	261.6 ± 35.66
7	60	29.5	10	0.5	228.2 ± 34.56
8	60	19.5	20	0.5	297.0 ± 55.89

Table 4. Liposome formulations prepared for the labelling of HeLa cells, with their respective sizes as measured with photon correlation spectroscopy.

The fluorescence uptake assay used to quantitate the amount of internalisation of the gadolinium liposomes into HeLa cells is depicted in **Figure 40**. Here, liposomes **1**-**8** (**Table 4**), were added to ~ 80,000 HeLa cells in three doses (6, 12 and 18 µg of total lipid/well) and the liposomes were allowed to incubate with the cells for four incubation periods (4, 6, 8, and 10 hours). After completion of the incubation period, the cells were washed with PBS, and lysis buffer was added, upon a freeze-thaw cycle, the cell lysates were subjected to an organic extraction, where a MeOH: $CHCl_3$ (6: 1 v/v) organic solution was used to extract the DOPE-Rhodamine lipid out of the lysate mixture. The fluorescence emission of this layer was then measured on a spectrofluorophotometer at 585 nm. The % fluorescence uptake was calculated using a positive control, which consisted of 100 % of the added liposome dose, and a negative control, consisting of the organic extract from cell lysate with no added gadolinium liposomes.

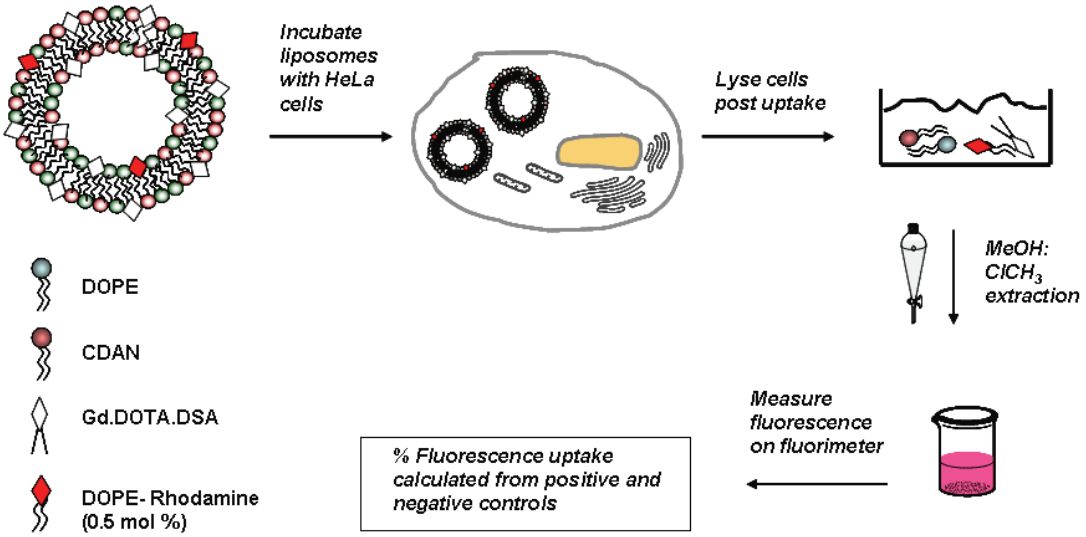


Figure 40. Fluorescence uptake assay used to assess uptake of gadolinium liposomes into HeLa cells. Liposomes were prepared with various mol % ratios of DOPE, CDAN, Gd.DOTA.DSA and DOPE-Rhodamine (maintained at 0.5 mol % for all formulations, see **Table 4.** for liposomes). The liposomes were incubated with HeLa cells for defined periods and post uptake, the cells were washed, the lysate obtained and the DOPE-Rhodamine fluorophore extracted using organic solvents. Fluorescence intensity measurements of lysates were used to calculate the amount of gadolinium uptake into cells.

Gadolinium liposomes **1**-**4** (**Table 4**) displayed a high percentage fluorescence uptake consistent with the presence of both CDAN and DOPE at high mol % (**Figure 41**). Gadolinium liposomes **5** and **6** were less effective, consistent with the absence of either DOPE or CDAN, supporting the hypothesis that both the cationic charge and fusogenic properties of CDAN and DOPE lipids respectively, are necessary for effective cellular entry and cytosolic delivery. Gadolinium liposome **8** was similarly less effective due to lack of effective cationic charge for cell surface adhesion.

The fluorescence uptake data was normalised to the total protein content per well using the BCA assay. As a result, the % fluorescence uptake into cells was also used to calculate the amount of gadolinium lipid taken up in cells and this was normalised to the protein content per well. Since the level of fluorescence emission from the cell lysate correlates to the total amount of liposome added to each well, the amount of Gd in each well was also calculated and expressed per mass of total protein content (see **Figure 42**).

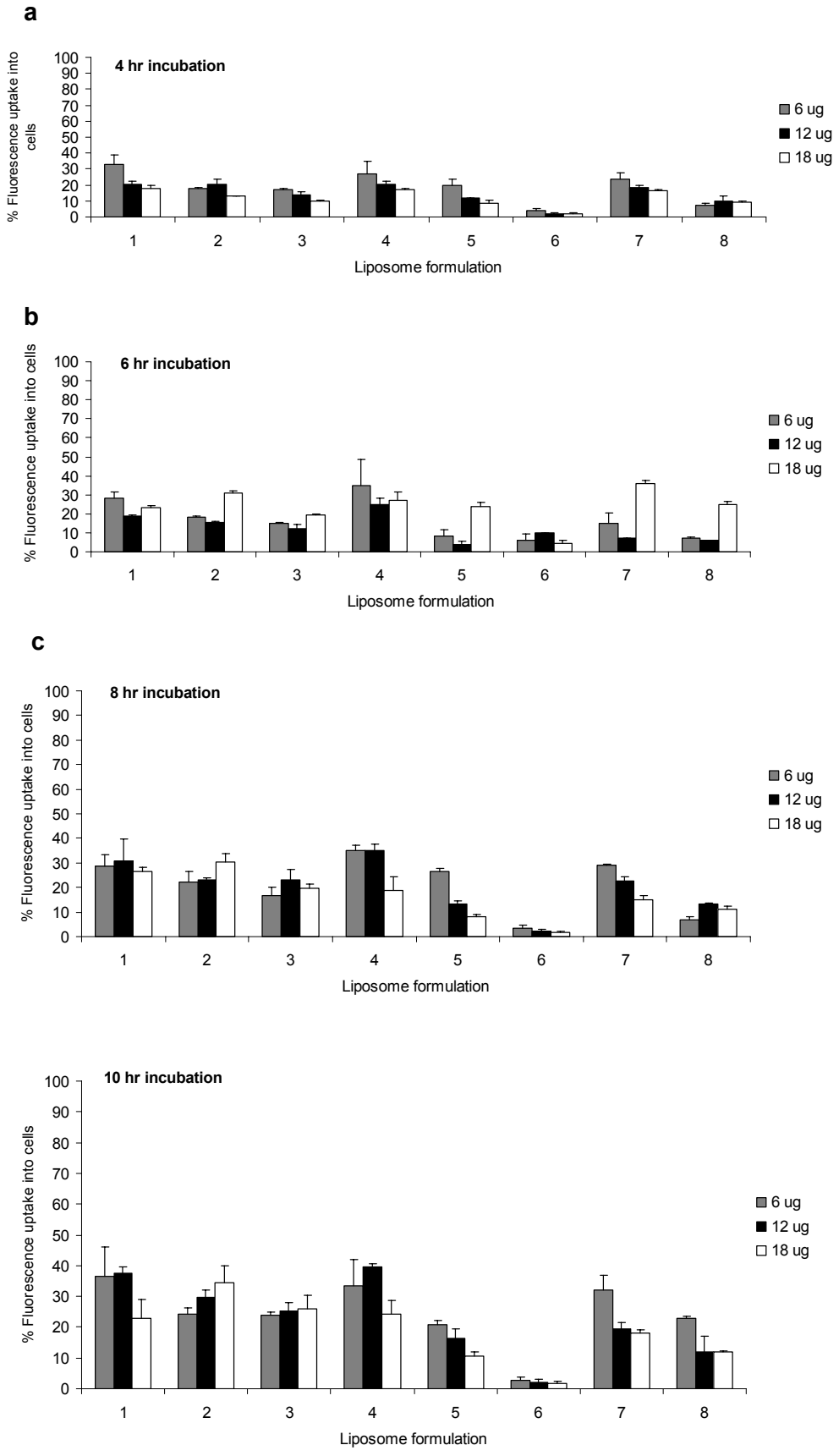


Figure 41. Fluorescence emission of HeLa cell lysate post incubation with gadolinium liposomes. Liposomes were added at three doses, 6, 12 and 18 µg's and incubated for **a**: 4, **b**:

6, **c**: 8 and **d**: 10 hours. The mol % of DOPE-Rhodamine was kept at 0.5 mol % in all liposome formulations. DOPE-Rhodamine fluorescence was measured at λ_{ex} 545 nm and λ_{em} 585 nm.

The trend for Gd uptake into cells (**Figure 42**), as evident, is similar to the fluorescence uptake results measured, in general liposomes **1**-**4** show increased uptake in comparison to formulations **5**-**8** due to the presence of an optimum balance of cationic CDAN and neutral DOPE lipids.

Upon normalisation of the results to protein content per well, a large uptake of Gd is apparent for liposomes **1**-**4** at the 18 µg dose (**Figure 42**, **d**). Liposome **6** has the poorest uptake into cells due to the total lack of cationic charge (**Figure 41** and **42**).

Liposomes **1**, **4** and **7** both have an excess of cationic charge, and liposome **2** has an excess of DOPE. From the normalised data (see **Figure 42**, **d**), it can be concluded that gadolinium liposome **2** delivers the highest amount of Gd into the HeLa cells upon a 10 h incubation period. However, prior to determining an optimal liposome formulation, the toxicity of each formulation should also be assessed. Cell toxicity studies were subsequently performed with gadolinium liposomes **1**, **2** and **7**. Gadolinium liposome **4** showed the highest fluorescence uptake (see **Figure 41**, **d**), however it was not carried forward for toxicity studies due to the presence of an excess of cationic charge (i.e. twice the amount of neutral DOPE lipid present in the formulation).

The fluorescence assay utilised in this cell uptake study (**Figure 40**) was designed in order to screen large numbers of liposome formulations for effective cell uptake, in triplicate, for the three administered concentrations and four incubation periods. This method is a quick and cost-effective means of assessing liposome cell internalisation, however a caveat to its use is the estimation of Gd uptake into cells in comparison to the actual measurement of Gd content, carried out by sensitive techniques such as inductively coupled plasma mass spectrometry (ICP-MS). The inclusion of a fluorescent lipid in liposome formulations is still a commonly used method for assessing liposome uptake into cells and can be used to refine large batches of liposome formulations to a smaller number of formulations that can be further characterised for their Gd delivery efficacy into cells using ICP-MS.

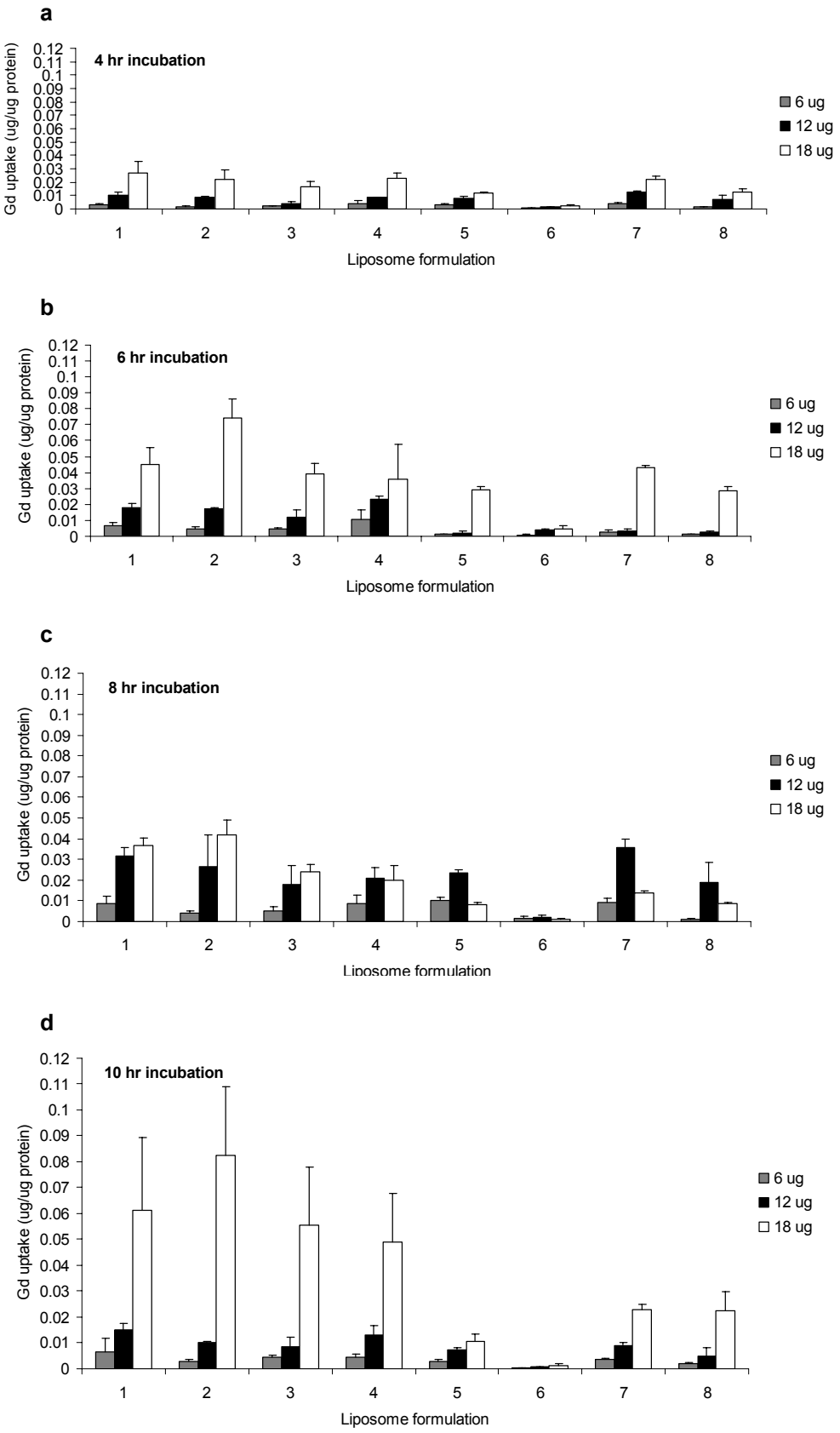


Figure 42. Calculated mass of Gd.DOTA.DSA lipid taken up into cells with 8 liposome formulations (**Table 4**). Liposomes **1**-**8** were added at three concentrations of 6, 12, 18 µg's of total lipid content and incubated with HeLa cells for **a**: 4, **b**: 6, **c**: 8 and **d**: 10 hours.

3.1.2 MTT Cell Viability Assay with Gadolinium Liposomes

The determination of cellular proliferation and viability are key areas assessed for *in vitro* assays of a cell population's response to external factors, therefore an MTT assay was carried out to measure the effect of the gadolinium liposomes on cell viability. The MTT assay measures the cell proliferation rate and conversely, when metabolic events lead to apoptosis or necrosis, the reduction in cell viability (balance between proliferation and cell death). This assay involves the reduction of tetrazolium salts by mitochondrial dehydrogenase enzymes. The yellow tetrazolium MTT (3-(4,5-dimethylthiazolyl-2)-2, 5-diphenyltetrazolium bromide) is converted to the purple product Formazan, by metabolically active cells, through the action of dehydrogenase enzymes (**Figure 43**). The resulting intracellular purple formazan can be solubilised and quantified spectrophotometrically.[249] In this manner, the viability of cells in the presence of the added gadolinium liposomes can be measured and quantitated.

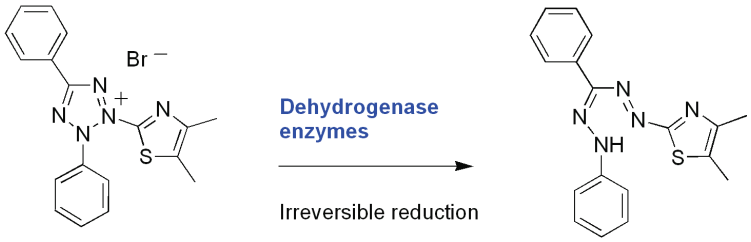


Figure 43: Reduction of MTT to Formazan in metabolically active cells in part, by the action of dehydrogenase enzymes.

Gadolinium liposomes **1**, **2** and **7** (**Table 4**) were tested for their effect on cell viability at the three previously used doses of 6, 12, and 18 µg/well, and were also incubated with HeLa cells for the same four hour incubation periods (4, 6, 8, and 10 h). Cells with no added liposomes were used as the positive control, and cell viability was measured and expressed as a percentage (**Figure 44**, **a**, **c**, **e**, and **g**).

In addition to the initial uptake periods (4-10 h), a further 24 h analysis of cell viability was also assessed, this involved removing the media and washing the cells after each incubation period, replacing the media and allowing the cells to grow for a further 24 h. The amount of Formazan in the media was then measured so that the effect of the added gadolinium liposomes could be determined for a full 24 cell growth-cycle (**Figure 44**, **b**, **d**, **f**, and **h**).

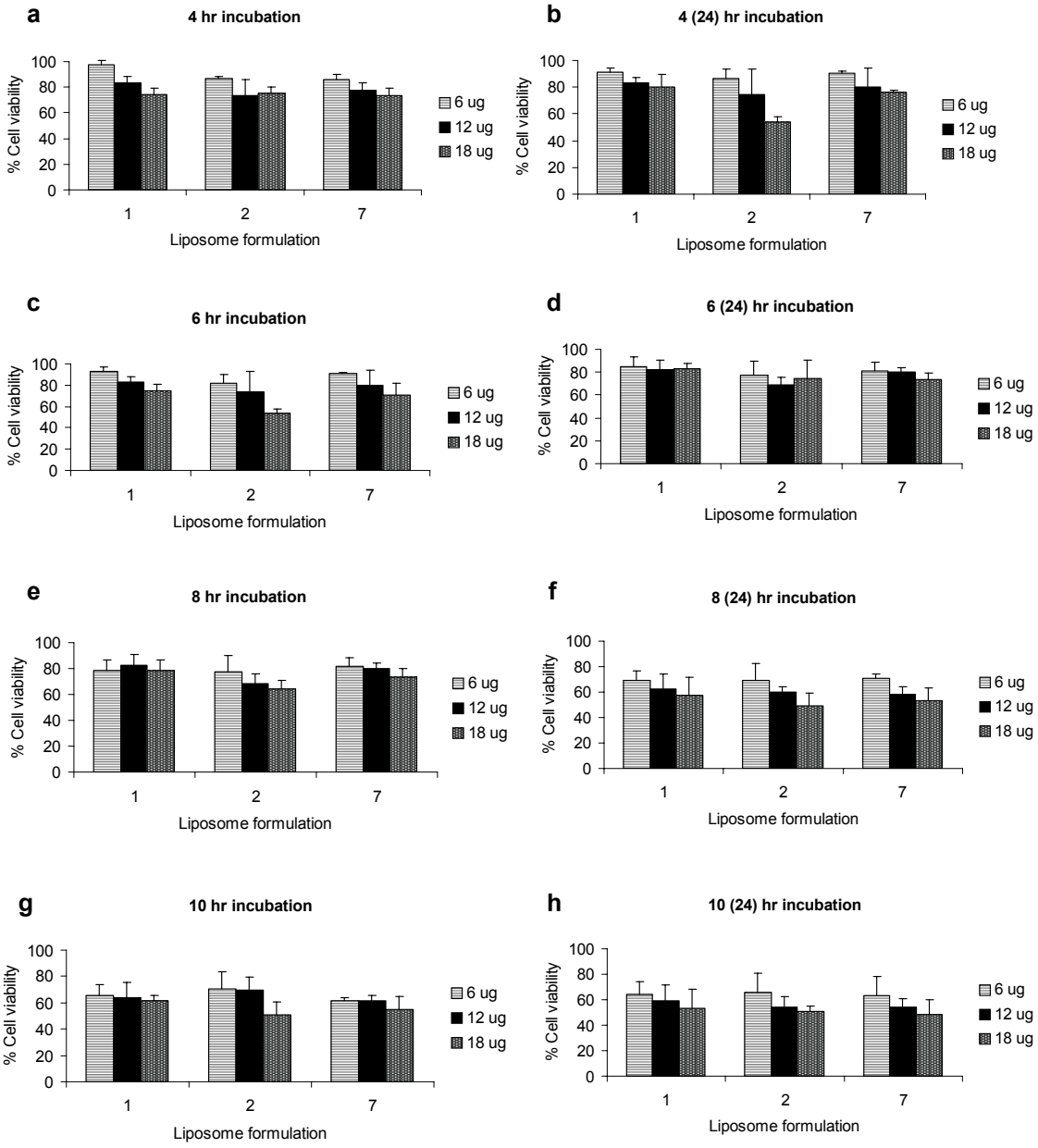


Figure 44. MTT cell viability assay for liposomes **1**, **2**, and **7** (**Table 4**) incubated with HeLa cells. Graphs on the left are for incubation periods of 4, 6, 8 and 10 h. Graphs on the right show cell viability of the added gadolinium liposomes with a further 24 h growth period. Here, the cells were washed post uptake period, the media replenished, and the cells were allowed to grow for a further day.

The MTT assay results showed acceptable levels of cell viability post incubation with gadolinium liposomes (**Figure 44**). As expected, cell viability decreases with increasing dose and incubation period. However, cell viability was not effected by more than, on average 40 % as a result of the added liposomes as observed for the highest dose and incubation period. Furthermore, when the cells were allowed to

grow for a further 24 h post uptake, their cell viability and therefore metabolism was not affected to any perceptible degree. From these results it could be concluded that gadolinium liposome **1** appears to effect cell viability the least. In general, cell viability data seem consistent for the 6 and 12 µg doses and the 8 h incubation period for all added gadolinium liposomes (**Figure 44**, **e**). However, since the MTT assay does not provide an assessment of cell death due to toxicity, as it only conveys information on the viability of cells, a further lactate dehydrogenase (LDH) cytotoxicity assay was carried out to quantify the level of cell death due to the added gadolinium liposomes.

3.1.3 Lactate Dehydrogenase Cytotoxicity Assay with Gadolinium Liposomes

In order to assess the toxic effects of the three liposome formulations chosen from the fluorescence uptake studies on HeLa cells, a toxicity assay was carried out using the CytoTox 96® Non-Radioactive Cytotoxicity Assay (Promega). The LDH assay is a non-radioactive colourimetric cytotoxicity assay that quantitatively measures LDH, which is a stable cytosolic enzyme that is released upon cell lysis during cell death. The amount of LDH released in the cell media is measured with a 30-minute coupled enzymatic assay, which results in the conversion of a tetrazolium salt (INT) into a red formazan product (**Figure 45**). The amount of colour formed is proportional to the number of lysed and therefore dead cells. The results are then normalised against controls such as the LDH released from cells with no compounds added to them.

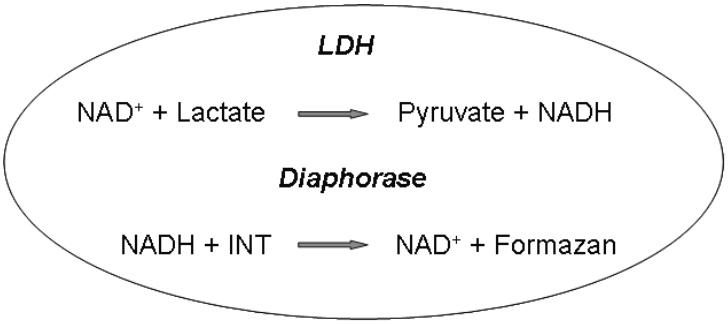


Figure 45. General chemical reactions for the LDH cytotoxicity assay.

The three selected gadolinium liposome formulations (see **Table 4**, liposomes **1**, **2** and **7**) chosen from the fluorescence uptake studies on cells were added to HeLa cells in a similar manner to the MTT assay, at three concentrations (6, 12, and 18 µg/well) and incubated for 4, 6, 8 and 10 h (**Figure 46**, **a**-**d**). In addition, the cells were washed post uptake period, the media replaced and the effect of toxicity measured during a full 24 cell growth-cycle (**Figure 46**, **e**-**h**).

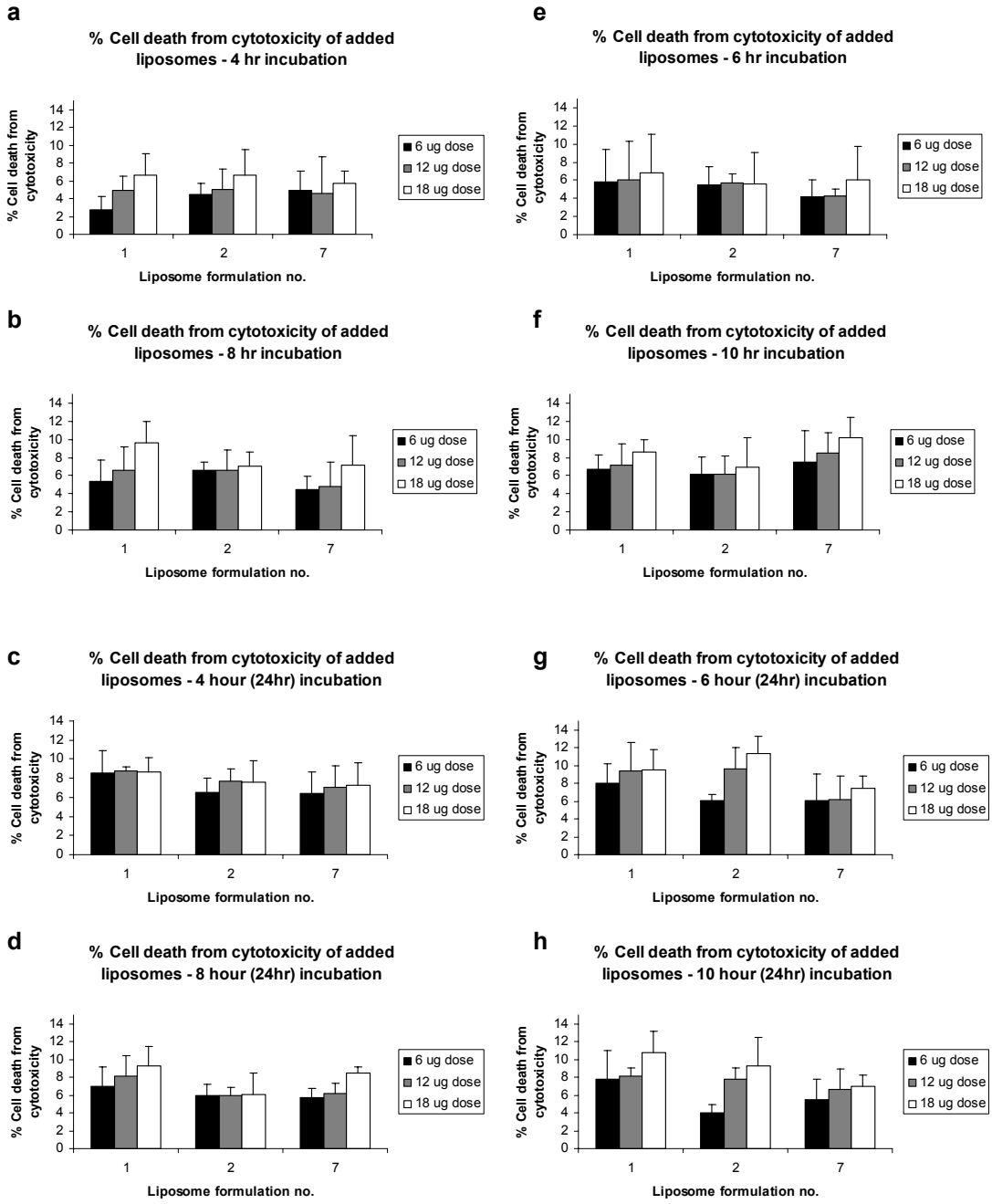


Figure 46. a-d: LDH assay results calculated to show % cytotoxicity as a result of added gadolinium liposome formulations **1**, **2** and **7** at three liposome doses (6, 12 and 18 μg/well) and four incubation periods (4, 6, 8, and 10 h). **e-h**: LDH assay calculated to show % cytotoxicity as a result of added gadolinium liposomes, in addition to cells being washed after the initial incubation periods and then allowed to grow for up to 24 h. These results show cytotoxicity induced by the added gadolinium liposomes to be in general < 10% of total cell death.

There was little difference in toxicity between all gadolinium liposome formulations studied irrespective of incubation times (4, 6, 8, 10 and an additional 24 h) and total lipid doses (6, 12 and 18 µg/well). After initial incubation periods (4, 6, 8, and 10 h), the cells were allowed to grow for 24 h, LDH release from these cells was minimal in all cases suggesting that normal cell growth and proliferation was taking place in spite of the presence of gadolinium liposomes (**Figure 46**). From the liposome fluorescence uptake assay, MTT and LDH toxicity assay data, it was concluded that the optimal formulation for cellular uptake and Gd cell labelling could be gadolinium liposome formulation **1** (Gd.DOTA.DSA/CDAN/DOPE/DOPE-Rhodamine: 30/40/29.5/0.5 mol %), administered at a total lipid dose of 12 µg/well (48-well plate, containing 0.716 µg/well of Gd) and an incubation period of 8 h. The zeta potential of gadolinium liposome formulation **1** was found to be 51.8 ± 3.58 mV, which corroborates the positive charge of this liposome formulation.

Although the MTT cell viability and LDH toxicity assays do not reveal major differences between liposome formulations **1**, **2** and **7**, formulation **1** has shown consistent uptake and an acceptable low level of toxicity. This formulation contains an optimal mol % of cationic and neutral lipid for effective cell entry and the use of 30 mol % gadolinium lipid in the formulation, resembles molar ratios of gadolinium lipids used by others formulating gadolinium liposomes.[218,244]

3.1.4 Inductively Coupled Plasma – Atomic Emission Spectroscopy (ICP-MS) of Gadolinium Liposomes

Once favourable *in vitro* conditions for gadolinium liposome cellular uptake were determined, ICP-AES studies were carried out using cell lysate post incubation with gadolinium liposome formulation **1** to further assess the amount of Gd internalised into the cells more precisely. The cell lysates were subjected to nitric acid destruction, and the samples analysed for their ^{157}Gd content. From this, it was determined that 21% of the administered Gd was retained within the cells, this is equal to 0.150 µg of Gd per well (~ 80, 000 cells), amounting to 1.880 picograms of Gd per HeLa cell. This result is within a 10% error in comparison to the fluorescence uptake assay results obtained for liposome **1**, which showed uptake for this liposome to be ~ 31 % (see **Figure 41**, **c**: liposome **1**, 12 µg/well, containing 0.716 µg of Gd per well), and validates this fluorescence uptake method as a quick and simple method for screening large numbers of differing formulations prior to more accurate ICP-MS analysis of Gd content.

3.1.5 MRI Visualisation of Gadolinium Liposome Labelled Cells

The ability of gadolinium liposome formulation **1** to produce *in vitro* MRI contrast enhancement post administration to cells was assessed with the labelling of HeLa cells. The optimised liposome dose of 12 µg per well, was scaled up 12.5 fold in order to label approximately 1 x 10^6 HeLa cells. After 8 h incubation with gadolinium liposome formulation **1**, cells were spun into pellets in PBS and imaged by MRI at 4.7 T using a spin echo T_1 weighted sequence. The MRI analysis of HeLa cell pellets labelled with gadolinium liposome **1** produced a brightly visible mass of cells, and the T_1 value for these cells was measured (**Table 5**). The T_1 values measured for the labelled cells were ~ 65% lower than the level measured in control cells labelled with control liposomes containing no Gd (**Table 5**). This promising result demonstrated the cell labelling efficiency of the novel gadolinium liposome formulation **1** *in vitro*.

Sample no.	Sample	T_1 (msec)
1	Gadolinium liposome **1** in water	311.4 ± 40.10
2	Gd liposome **1** incubated with HeLa cells	688.6 ± 53.60
3	Control liposome incubated with HeLa cells	1940 ± 65.95
4	HeLa cells alone	2149 ± 92.70
5	PBS	1750 ± 47.80

Table 5. T_1 values for gadolinium liposome formulation **1** incubated with HeLa cells and controls (sample 3; control liposome: CDAN/DOPE/DOTA.DSA: 40/30/30 mol %). Gadolinium liposome labelled cells were ~ 68% brighter than HeLa cells with no labelling.

T_1 weighted images of the samples are shown below (**Figure 47**), here vial 2 contains a clearly visible bright cell pellet, demonstrating the cell labelling efficiency of gadolinium liposome **1**, and hence successful MRI visualisation of the labelled HeLa cells.



Figure 47. T_1 weighted images obtained of samples 1-5 (**Table 5**). Vial no. 2 contains a cell pellet of ~ 1 x 10^6 HeLa cells (in PBS), labelled with the optimised gadolinium liposome 1. Here, a 65% signal T_1 enhancement is measured from these cells, compared to the control liposomes (eppendorf 3, where the formulation contained no Gd).

3.1.6 Fluorescence Microscopy of Gadolinium Labelled Cells

In order to examine the intracellular uptake of gadolinium liposome formulation **1** into HeLa cells, we chose to take advantage of the imaging-bimodality of this liposome, in that a fluorescent lipid was included with the paramagnetic liposome (DOPE-Rhodamine). In this instance, the cell labelling dose was scaled up for the labelling of 1.25 x 10^5 HeLa cells, and any non-internalised gadolinium liposomes not taken up were washed away after the conclusion of the uptake period of 8 h. Fluorescence microscopy revealed that the cellular uptake of these bimodal gadolinium liposomes led to intracellular, cytosolic accumulation of the fluorescent label which is in accordance with an endocytosis-mediated uptake (**Figure 48**). This result is consistent with successful Gd labelling implied by reduction of T_1 values, relative to controls (see **Table 5**).

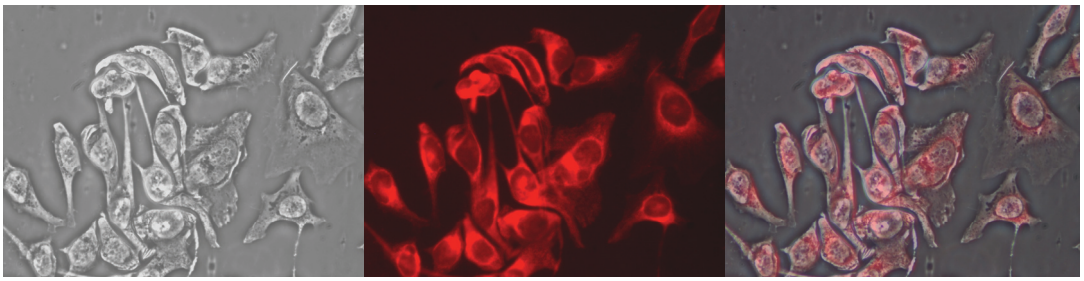


Figure 48. Left: bright field image of HeLa cells labelled with gadolinium liposome formulation **1**, middle: red fluorescence image of HeLa cells labelled with this formulation, and right image: merged bright field and fluorescence image (40 × magnifications).

The labelled HeLa cells were further examined by confocal microscopy and images were obtained in a serial manner through the cells (**Figure 49**). These results show an ample level of fluorescence visible within the cell cytoplasm due to the DOPE-Rhodamine lipid included in the formulation, and hence, in addition to the MRI results, also provide proof of gadolinium liposome uptake into the HeLa cells. It is clearly apparent that uptake is ubiquitous throughout the cytoplasm, the cell nucleus is clearly visible, and contains no fluorophore, suggesting that the lipids may not interfere with cellular DNA processes (**Figure 49**). The appearance of localised hyperintense fluorescence dots in these confocal images may indicate the endosomal enclosure of the DOPE-Rhodamine probe. Further analysis of the Z plane through the cells did not reveal these regions to be outside of the cell or liposomal aggregates on the surface (see **Figure 49**, part **b**). For these initial fluorescence microscopy studies the cells were not counterstained further (for example with the nuclear

labelling dye DAPI) in order to observe purely, the fluorescence signal from the DOPE-Rhodamine lipid within the cells.

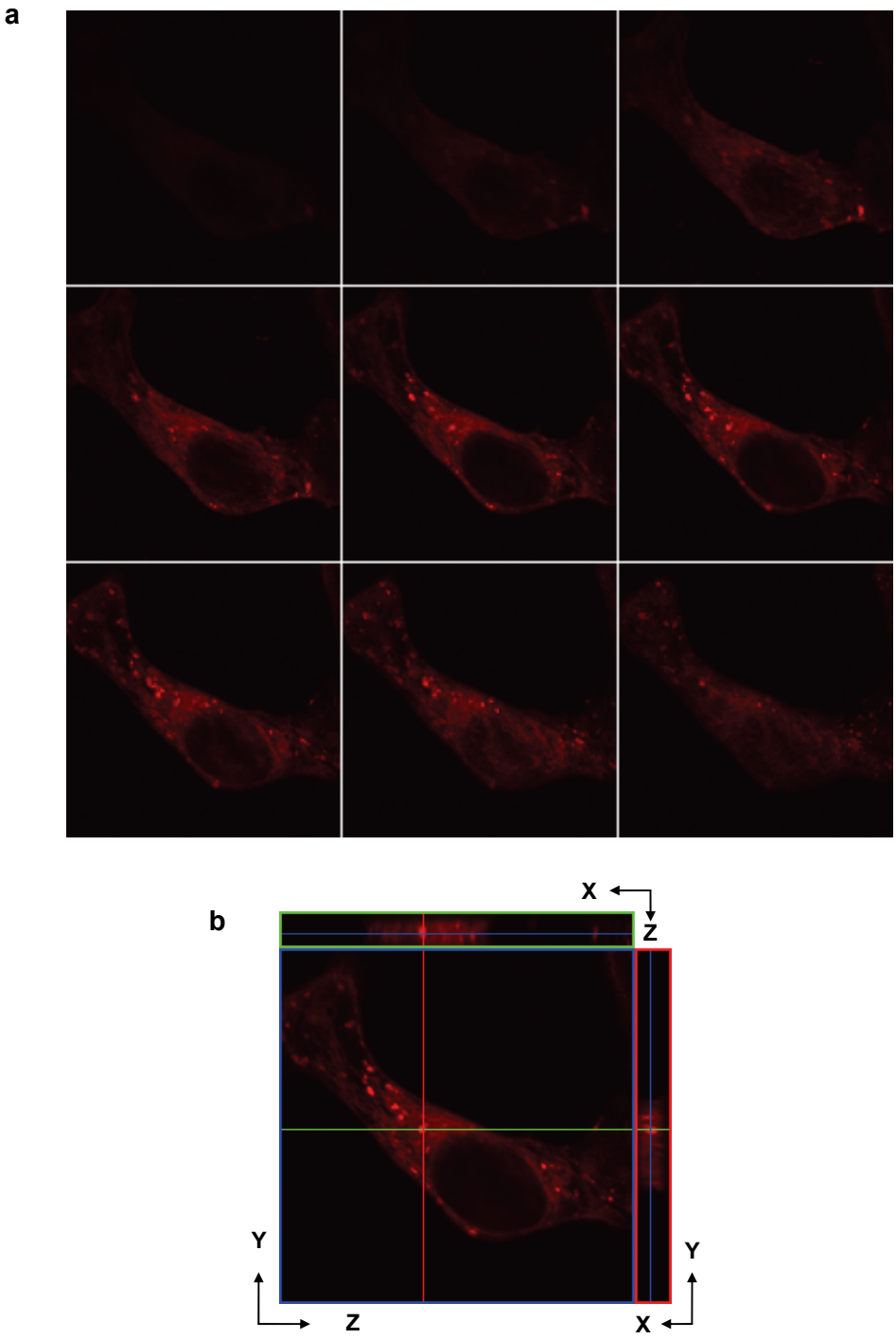


Figure 49. **a:** X-Y confocal microscopy images obtained from HeLa cells labelled with gadolinium formulation **1**. Stacks start at bottom of the cell (top left) and show sections through the cell, ending at the cell surface (bottom right), stack thickness: 0.05 µm, at 40 x magnification. **b**: Confocal Z plane projection through the cell (thickness: 0.50 µm, beam wavelength; 543 nm) at 40 x magnification.

3.1.7 Plasmid DNA Transfection with Gadolinium Liposomes

The cationic nature of the optimised gadolinium liposome formulation **1** allows for the encapsulation of DNA within its aqueous core. This produces bifunctional gadolinium liposomes, capable of both labelling cells and delivering nucleic acid payloads into cells. This is a valuable characteristic which can be further exploited to achieve a fully theranostics approach, whereby the delivery of therapeutic genetic material into cells can be monitored by both MRI and fluorescence imaging. Synthetic cationic lipids (also referred to as cytofectins) as DNA condensers are considered promising nonviral gene carriers in gene therapy.[248] These lipids once mixed with polyanionic DNA form lipoplexes (liposome plus DNA) which can be used to transfect cells.

The transfection ability of the novel gadolinium liposome **1** for delivering DNA into cells was assessed by introducing plasmid DNA encoding for the luciferase reporter gene. The expression of the luciferase gene allows for a quantitative measure of transfection efficiency in cells. The luciferase assay system (Promega) was used to assess the transfection ability of gadolinium liposome formulation **1**. Here, once the gene is transcribed and the enzyme luciferase is produced, the substrate luciferin is then added, the product of which gives oxyluciferin. This process produces bioluminescence once the enzyme and substrate have reacted. This emission is then measured on a luminometer and the amount of light is proportional to the transfection efficiency of the gadolinium lipoplex system.

HeLa cells were transfected with lipoplexes containing either; the gadolinium liposomes, control Gd free liposomes, and Trojene® (Trojene is a commercial transfection agent composed of a 1:1 DOPE and CDAN formulation) complexed with plasmid DNA (all liposomes were ~ 250 nm in size). The Trojene® transfection protocol was used to prepare the lipoplexes.[250] The lipoplexes were prepared by the addition of plasmid DNA to the gadolinium liposomes. This led to the formation of lipoplexes as evident from the increase in size of the gadolinium liposomes once DNA was encapsulated. The lipoplexes were then incubated with HeLa cells for 4 h. After this incubation period the cells were washed, the media replaced and transfection was allowed to take place over a 24 h period. The cell lysates were analysed for their bioluminescence content once luciferin was added, and this emission was normalised to the total cell protein content using the BCA (bicinchoninic acid) assay and expressed as relative light units per mg of protein (RLU/mg protein). The transfection data obtained showed the transfection efficiency of the gadolinium

lipoplexes to be at an acceptable level when compared to the commercial transfection agent Trojene® (**Figure 50**). The transfection efficiency of Gd liposomes is a log lower than Trojene® which can be explained by the lower molar ratio of cytofectins (CDAN).

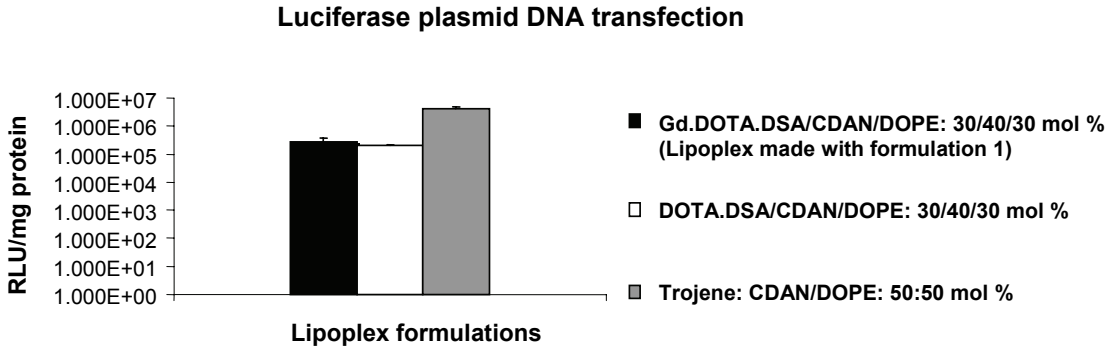


Figure 50. Gadolinium lipoplex (gadolinium liposome **1** plus DNA, black bar) transfection of HeLa cells compared with control Gd-free lipoplex (white bar) transfection, and Trojene® (CDAN/DOPE: 50/50 mol %, grey bar).

Interestingly, transfection and therefore effective DNA encapsulation in liposomes does not appear to be affected by presence of Gd^{3+} metal, as the transfection levels are very similar for both lipoplexes prepared with the Gd.DOTA.DSA and Gd free DOTA.DSA lipids (**Figure 50**, black and white bars). This result confirms the suitability and transfection "inertness" of the Gd.DOTA.DSA lipid in terms of its lack of interference with the functional DNA, and validates its use in the preparation of bifunctional paramagnetic liposomes. The cytotoxicity of the gadolinium lipoplex was also investigated using the LDH assay and was found to be no greater than 10 % (**Figure 51**).

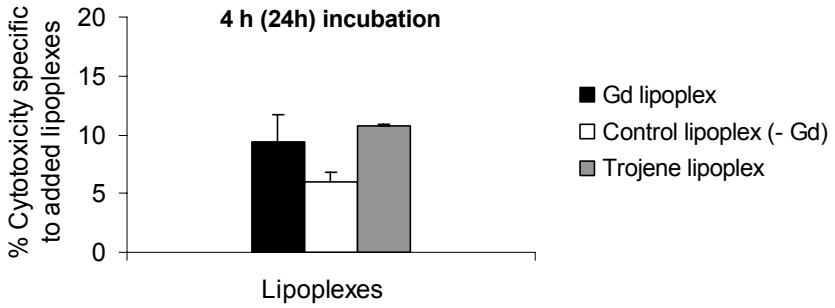


Figure 51. LDH assay of lipoplexes used in luciferase transfection assay. Lipoplexes were added to HeLa cells at the same dose used in transfection studies and incubated for the same 4 h period. After which the cells were washed, the media replaced and the level of cell death due to the added lipoplexes was measured 24 h later.

3.1.8 In Vitro Evaluation of Gd.DOTA.DSA: Conclusions

Gadolinium liposome formulation **1** mediated transfection of HeLa cells was investigated with plasmid DNA (pDNA) expressing the luciferase gene. Here, the level of luciferase enzyme activity in cells post pDNA delivery represents a quantitative measure of transfection efficiency. Gadolinium liposome formulation **1** was combined with pDNA to form Gd lipoplexes (**Figure 50**). Gadolinium liposome formulation **1** mediated transfection appears to be comparable to Trojene® mediated transfection, demonstrating that the Gd incorporation does not interfere with liposome-mediated transfection of HeLa cells to any perceptible degree. Furthermore, successful Gd lipoplex mediated transfection of HeLa cells provides functional proof for gadolinium liposome cellular entry by endocytosis followed by endosomolysis and cytosolic accumulation, as observed by fluorescence microscopy, since transfection is contingent on successful endocytosis and endosomolysis. Gd lipoplex particles prepared with gadolinium liposome formulation **1** were also shown not to be toxic to the cells and normal cell proliferation was not affected to any major degree (**Figure 51**).

The mechanism of cationic liposome entry into cells is believed to occur through endocytosis (pinocytosis).[251] However, in addition to this, it is thought that other events occurring within the plasma membrane can also be causative of cellular uptake, including membrane destabilisation reactions. Lipoplexes that contain DOPE in particular, have been shown to be capable of fusion to both the cellular and endosomal membranes. Xu *et al.* have postulated that the DNA is released from the cationic lipid/DNA complexes in cells by the action of anionic lipids initially located in the cytoplasmic face of the endosome.[252] Here, it is thought that cationic lipoplexes are initially internalised into the cytoplasm through electrostatic interactions with the cell membrane. This complex is then taken up into the early endosomes, and causes the destabilisation of these endosomes, inducing a flip-flop exchange of the anionic lipids from the cytoplasmic facing endosomal monolayer, which laterally diffuse and mix into the complex. This leads to the formation of charge neutral ion pairs with the cationic lipids and the displacement of the DNA into the cytoplasmic milieu.

3.2 In Vivo Evaluation of Gadolinium Liposomes

The effective cellular signal enhancement properties of Gd.DOTA.DSA *in vitro* led us to investigate the potential of paramagnetic liposomes prepared with this lipid for *in vivo* imaging of tumours. The ability to tune liposome size, surface charge and specificity allows for potential pathological imaging such as the imaging of solid tumours *in vivo*. This tuning of liposomes is made possible by adjusting the composition of the liposome formulation. Surface charges tending to neutrality are best suited for *in vivo* purposes in order to reduce the recognition of liposome particles by plasma proteins and the reticuloendothelial system (RES). This can be achieved through the inclusion of charge neutral lipids in the liposome formulation. The blood circulation time of the liposomes can be prolonged by incorporating a PEG polymer tethered onto a lipid and incorporated into the liposome formulation. Finally, the liposomal accumulation in sites of pathology such as tumours can be achieved by tuning their size, or by adding targeting moieties to the liposome, either directly attached to the surface or inserted into the liposome bilayer. These aforementioned points are further discussed in forthcoming paragraphs.

3.2.1 In Vivo Considerations of Liposome Size

Liposome based therapeutics have found their way to the clinic over the last few decades. The use of liposomes as drug delivery systems in cancer therapy has been achieved by formulations such as Doxil® which consists of a liposome formulation encapsulating the anti-cancer drug doxorubicin. This liposome formulation has been approved for clinical use in AIDS-related Kaposi's sarcoma, and recurrent and metastatic breast cancer.[253] Doxil® has a size distribution of between 85 – 100 nm. This size range is considered optimal for the accumulation of liposomes in solid tumours due to the characteristics of tumour tissue. Tumour tissue has been described to possess a universal affinity for lipidic and macromolecular agents, termed the enhanced permeation and retention effect (EPR), whereby macromolecular agents accumulate in tumour tissue. EPR was first introduced by Maeda *et al.*,[254] here, it is believed that tumour properties such as increased angiogenesis, a heterogeneous and destructive vascular infrastructure, impaired lymphatic drainage and a "leaky" endothelial layer are all factors that contribute to the accumulation of macromolecular structures within tumour tissue (**Figure 52**).

The EPR effect has become a standard model for the targeting of macromolecular drugs and polymeric or liposomal macromolecules to tumours. These agents are easily adapted for the imaging of tumours through their modification to include an imaging probe or moiety for signal localisation. The key mechanism here, being the retention of macromolecules in solid tumours, in contrast to low-molecular weight agents, such as Gd.DTPA (Magnevist™) which are re-circulated into blood through diffusion and cleared through the kidneys in relatively short periods post injection. This retention effect or particle accumulation within tumour tissue is also referred to as passive-targeting, and it has been shown that due to this effective phenomena very high levels (10-50 fold) of polymeric drugs can accumulate at tumour sites within a few days.[255] The mechanism of tumour accumulation of nanoparticles in tumour tissue has been established as the extravasation of large molecules through the disrupted endothelium lining tumour blood vessels. Yuan *et al.* have shown that the maximum particle size threshold above which the particles can no longer extravasate through the endothelial layer is approximately 400 nm.[256]

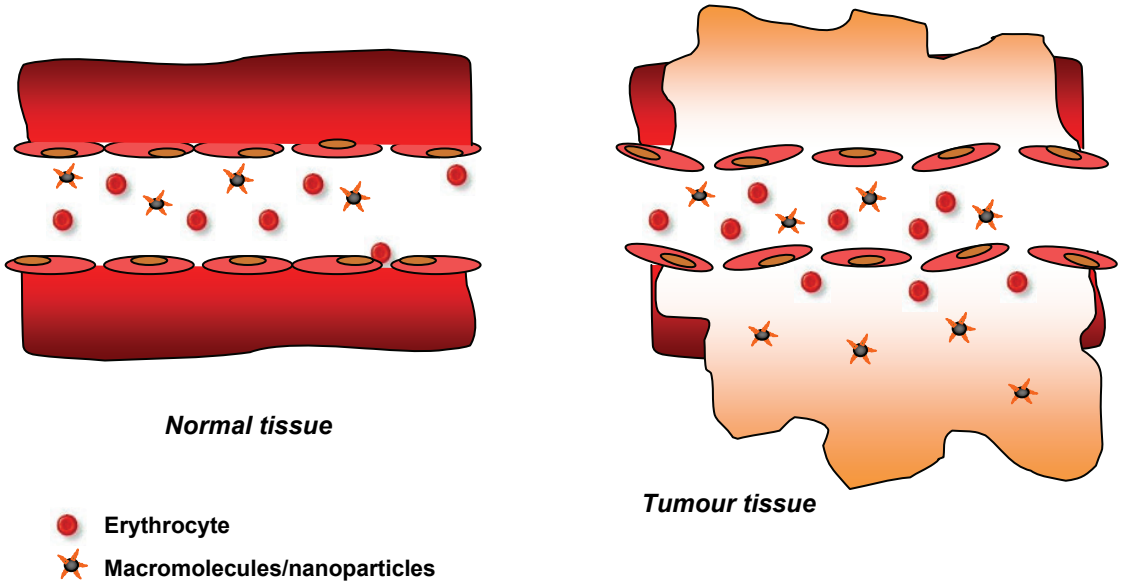


Figure 52. The EPR effect, normal tissue does not have endothelial gaps wide enough to allow for macromolecular or nanoparticulate agents to leak into the extracellular tissue lining blood vessels. Tumour tissue has a disrupted endothelial layer, allowing for larger particles to "seep" into the tumour extracellular domain.

It has been reported that the pore sizes in solid tumour vasculature vary from 100 – 780 nm, which is considerably larger than junctions in normal tissue where the gaps are usually < 6 nm. [257]

We chose to take advantage of this effective accumulation of macromolecular particles in tumour tissue by designing gadolinium liposome formulations to observe signal enhancement of tumour tissue *in vivo* by MRI, and *ex vivo* by fluorescence microscopy of excised and sectioned tumour slices.

In addition to complying with the tumour extravasation size threshold, a further reason for liposome size to remain within the 100 nm range for *in vivo* injections is due to clearance of large liposomes through the liver. Large liposomes are taken up by liver cells which include hepatocytes and Kupffer cells, liposomal particles may accumulate in liver or spleen tissue due to the larger endothelial lining in these organs.

3.2.2 Liposome Surface Charge

It has been shown that liposomes bearing a surface decorated with the neutral hydrophilic PEG polymer benefit from prolonged circulation times with half lives reported from 2 to 24 h in rodents, and as high as 45 h in humans.[258] The theory here is that surface-grafted PEG liposomes have reduced uptake by liver cells as the liposomes are not effectively bound by plasma proteins.[259] These liposomes are also referred to as sterically stabilised liposomes. Here, the PEG layer sterically inhibits both electrostatic and hydrophobic interactions of plasma components with the liposome bilayer. For *in vivo* purposes, phospholipids with neutral head groups have been incorporated in the liposome formulation, these include but are not limited to; 1,2-dioleoyl-*sn*-glycero-3-phosphocholine (DOPC), 1,2-distearoyl-*sn*-glycero-3-phosphoethanolamine (DSPC) or 1,2-dimyristoyl-sn-glycero-3-phosphocholine (DMPC) lipids. The utilisation of neutral lipids in addition to the incorporation of between 5-10 molar ratios of a PEGylated lipid in the liposome formulation, provides steric stabilisation and protection from blood plasma proteins such as opsonins, and leads to the reduction of Kupffer cell uptake. It is thought that stabilisation occurs by the formation of highly hydrated shields of polymer molecules around the liposome surface. Due to this “shielding” characteristic, these types of liposomes are often referred to as “Stealth” liposomes.

3.2.3 Liposome Tumour Specificity

In addition to the accumulation of liposomal particles within tumour tissue, their specificity to tumour sites can be improved through the use of receptor targeting approaches. This strategy involves the use of targeting moieties such as anti-bodies, peptide ligands, glycoproteins or small molecular ligands either conjugated to the surface of the liposome, or incorporated into the liposome bilayer by previous tethering to a lipid anchor. This effective approach leads ultimately to the internalisation of liposomes into tumour cells through endocytosis.

A targeting approach can increase the specificity of the interaction of liposomes with cancer cells and can be exploited to selectively deliver drugs into these cells. The targeting components can be directed to receptors that are over-expressed or selectively expressed on cancer cells. [260] This type of targeting to tumour tissue has been referred to as “active-targeting”. Allen *et al.* have shown the specificity of immunoliposomes designed with anti-body fragments on their surface, towards cancer cells.[261]

Taking into consideration the aforementioned tenets, the novel gadolinium lipid Gd.DOTA.DSA was incorporated into liposome formulations in order to test the efficacy of such gadolinium liposomes for the imaging of xenograft tumours in mice.

3.2.4 Preliminary In Vivo Evaluation of Gd.DOTA.DSA

Prior to establishing a tumour model for MRI using gadolinium liposomes *in vivo*, preliminary experiments were carried out using Gd.DOTA.DSA **2**, involving the direct intramuscular (IM) injection of gadolinium liposomes made with this lipid. The aim here was to assess MRI signal enhancement post injection of a high concentration of gadolinium liposomes containing Gd.DOTA.DSA. Liposome formulations consisting of Gd.DOTA.DSA, and DOTAP lipids (50: 50 mol %, gadolinium formulation **9**) were injected into the hind leg muscle of C57BL/6 mice and the mice were imaged at 5 min, 24 h and 7 days post injection at 4.7 T (**Figure 53**). Control liposomes made with Gd not complexed into the lipid (DOTA.DSA) were also injected in the opposite leg muscle of the mice.

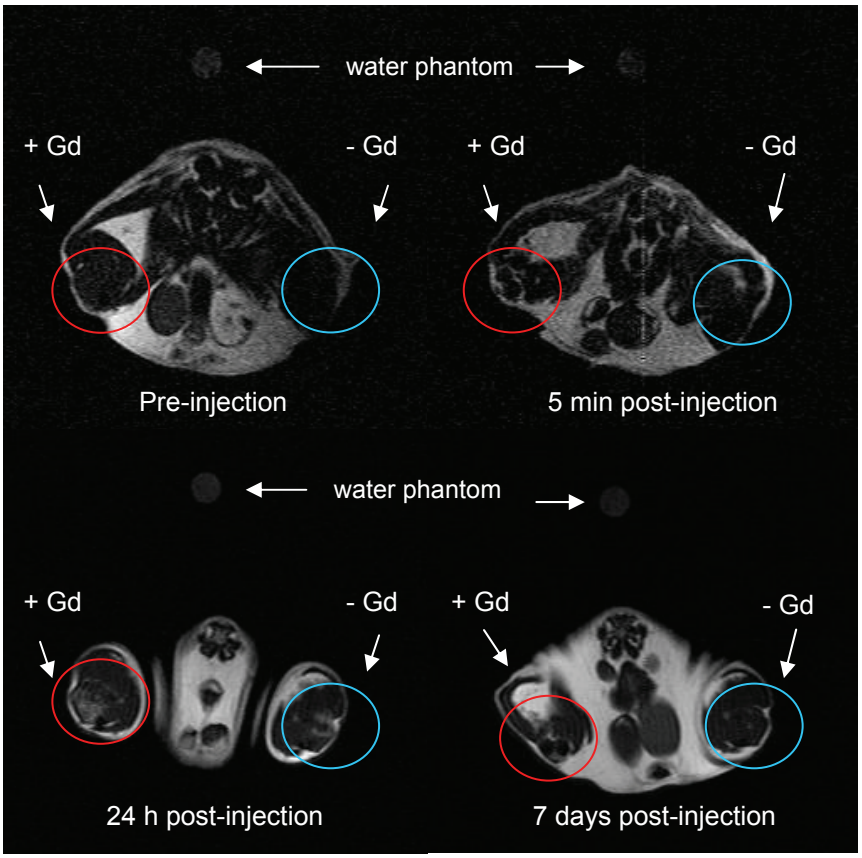


Figure 53. T_1-weighted MR images of intramuscular injection of gadolinium liposome formulation **9** into mice hind leg muscle, **a**: pre-injection slice, **b**: 5 min post-injection, **c**: 24 h post-injection and **d**: 7 days post injection. The T_1 images show a clear enhancement observed at 5 min and 24 h post-injection (area within white circles, **b** and **c**) of the gadolinium liposomes. The clearance of the liposomes is also apparent 7 days post-injection as a loss of signal (**d**).

Figure 53 shows the results of IM injections of the cationic Gd liposomes, we can see that within just 5 min and at 24 hours the injected region appears bright and a positive enhancement is visible (**Figure 53**, **c** and **d**). Signal enhancement appears to become more diffuse from 5 min to 24 h post-injection in the muscle tissue, this maybe due to the diffusion of the liposomes throughout the muscular region (white circles, **Figure 53**). In addition, the spreading of the liposomes as observed (**c** to **d**, **Figure 53**) may be due to the accumulation of interstitial fluid within the injected site and the mixing of the gadolinium liposomes with the accumulated lymphatic fluid. The gadolinium liposomes also appear to be cleared from the injection site within 7 days post injection which suggests clearance of the gadolinium liposomes from the site of injection. This promising data led us to develop further gadolinium liposome formulations for systemic circulation *in vivo*, with the aim of tumour imaging by MRI, utilising the widely reported EPR effect.

3.2.5 Serum Aggregation Study with Gadolinium Liposomes

Successful circulation of liposomes post intravenous injection *in vivo* may be hampered by events that can lead to their rapid clearance, such as their binding to serum proteins, in particular if the liposome surface is charged. The binding of serum proteins (opsonins) to liposome complexes may lead to structural re-organisations which can lead to the aggregation or dissociation of the liposomes. Aggregation can result in rapid clearance and increased toxicity of the injected liposomes. Subsequently, for the purpose of our *in vivo* tumour imaging efforts using the novel gadolinium lipid Gd.DOTA.DSA **2**, we constructed neutral liposome formulations. However, the assessment of liposome aggregation in a serum model is necessary prior to injection. In this instance, we replaced the *in vitro* suited optimised cationic formulation **1** with a charge neutral gadolinium liposome formulation consisting of Gd.DOTA.DSA/DOPC/Cholesterol/DSPE_PEG_{2000} (30/32/30/7 mol %, gadolinium liposome formulation **10**). This formulation also contained DOPE-Rhodamine (at 1 mol %), for fluorescence microscopy following histology. This formulation was rendered stable to biological fluids by the incorporation of a stealth biocompatibility layer comprised of PEG, tethered to a distearoylphosphatidylethanolamine (DSPE) lipid anchor.

Cholesterol was incorporated into the formulation since this lipid induces diverse effects on the liposomal bilayer. Cholesterol has been shown to increase the head group spacing in liposome formulations and stabilise the resulting bilayer membranes.[262] Here, cholesterol presence in the liposome formulation controls membrane permeability of both fluid and rigid bilayers by inducing conformational ordering of the lipid chains (**Figure 54**). In addition, cholesterol can reduce serum induced aggregation as a direct result of its neutral charge.[186]

In addition to cholesterol, the inclusion of DOPC in these liposome formulations is thought to add to the stability of the gadolinium liposomes, since this unsaturated phospholipid, in combination with cholesterol has been shown to yield monodisperse and stable liposomes with high relaxivities. Strijkers *et al.* have obtained cryo-TEM (transmission electron microscopy) images of liposomes containing cholesterol and DOPC, where spherical particles of good size (~ 100 nm) were obtained. In contrast, for gadolinium liposomes without cholesterol or with the saturated phospholipid DSPC, triangular shaped vesicles were observed. [242]

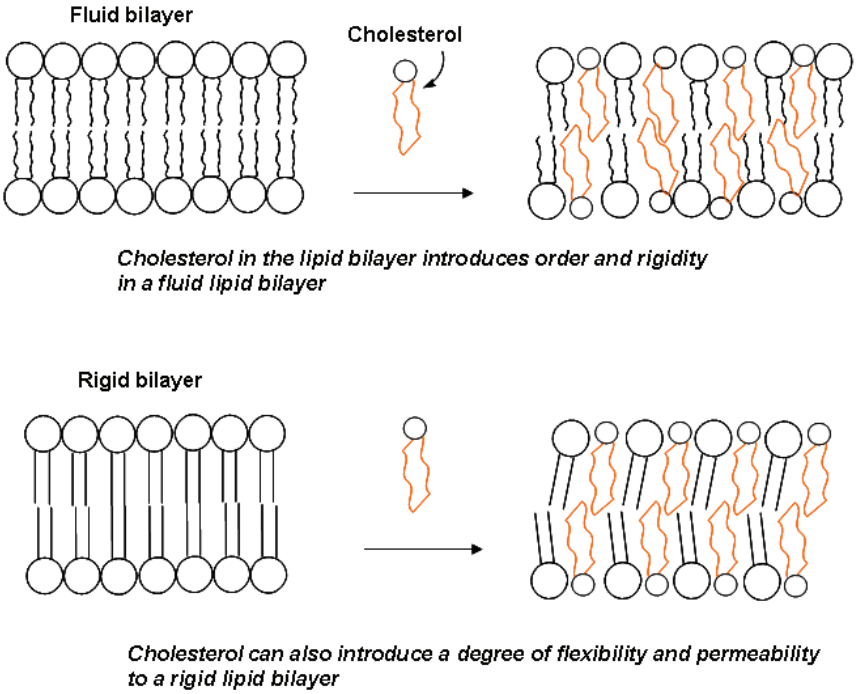


Figure 54. Influence of cholesterol lipid on liposome bilayer permeability and rigidity.

The serum aggregation effects of six liposome formulations were tested for their size aggregation in serum over a 10 h incubation period at 37 ºC. The molar ratio of the PEG lipid was adjusted for each formulation in order to test the effect of small increments of this stabilising lipid on liposome aggregation in serum. Initially, three gadolinium liposome formulations were tested for their aggregation in serum (see **Table 6**). Gadolinium liposome formulations were formulated and their size and polydispersity (PI) measured using photon correlation spectroscopy. The liposomes were sonicated for an appropriate length of time (30 min) in order to ensure an overall size uniformity of approximately ~ 100 nm.

Liposome Formulation (mol %)						
Gd.DOTA.DSA	**DOPC**	**Cholesterol**	**DOPE-Rhodamine**	**DSPE-PEG_{2000}**	**Initial size (nm)**	**PI**
30	34	30	1	5	104.9 ± 34.6	0.420
30	33	30	1	6	114.5 ± 45.3	0.201
30	32	30	1	7	104.3 ± 36.8	0.309

Table 6. Sterically stabilised gadolinium liposomes investigated for *in vivo* i.v injection.

Once formed, the gadolinium liposomes were added to a 1:1 solution of fetal calf serum and HEPES buffer (20 mM, NaCl, 135 mM, pH 6.5) and incubated at 37 °C with their size and polydispersity index measured every hour for up to ten hours. These results indicated that there is indeed very little aggregation of the PEGylated liposomes as measured as a function of their size increase (**Figure 55**).

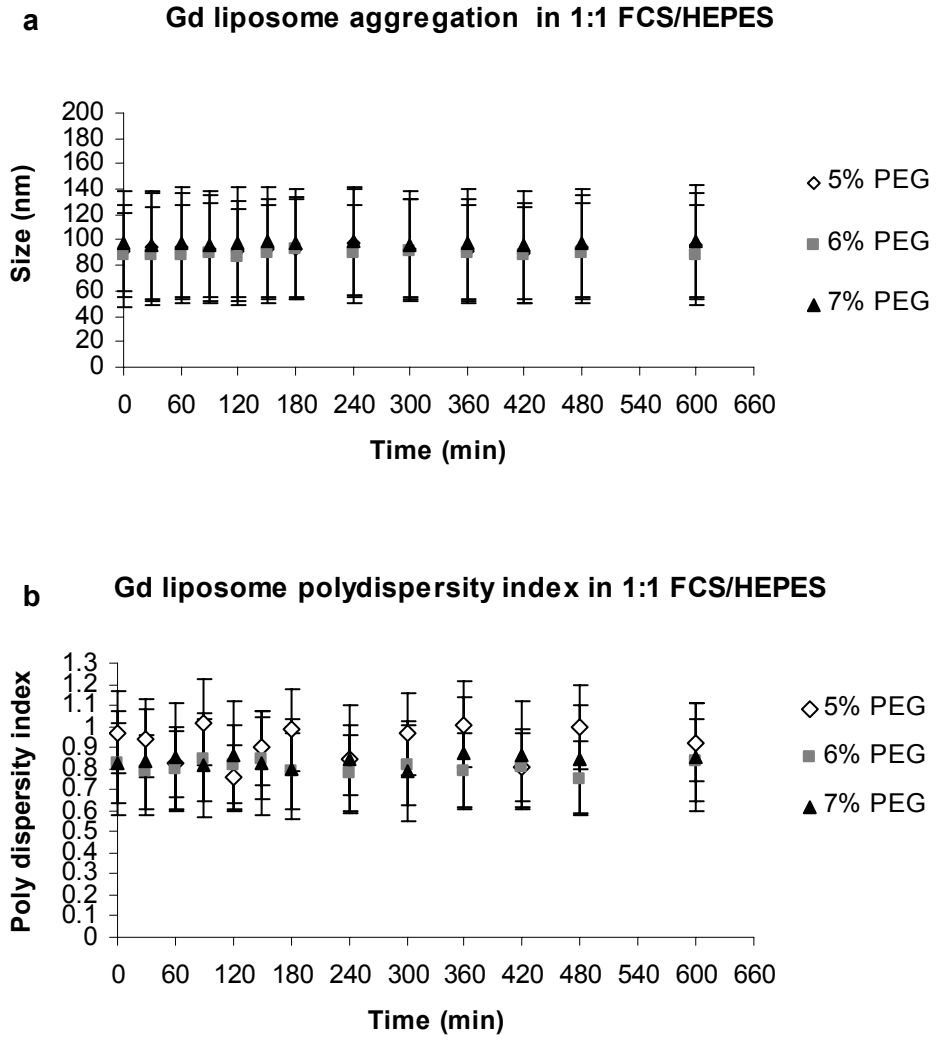


Figure 55. The size (**a**) and polydispersity (**b**) distribution of PEGylated liposomes (**Table 6**) over a 10 h incubation period at 37 °C was measured by photon correlation spectroscopy. No major increase in size was observed.

In order to test the effect of the chelated gadolinium of the Gd.DOTA.DSA lipid on liposome aggregation in serum, the above described incubation experiment was also carried out on three analogous liposome formulations containing the Gd free DOTA.DSA lipid in place of the gadolinium lipid (see **Table 7**).

Liposome Formulation (mol %)						
DOTA.DSA	**DOPC**	**Cholesterol**	**DOPE-Rhodamine**	**DSPE-PEG_{2000}**	**Initial size (nm)**	**PI**
30	34	30	1	5	123.9 ± 43.5	0.455
30	33	30	1	6	111.6 ± 50.7	0.366
30	32	30	1	7	114.8 ± 42.9	0.339

Table 7. Sterically stabilised Gd free liposomes investigated for *in vivo* i.v injection.

It was expected that the presence of the three carboxylic acid groups of the DOTA.DSA lipid (**6**) would lead to an increase in liposome size due to aggregation resulting from ionic effects. However, to the contrary, it was found that the size of the Gd free liposomes did not vary to any significant degree over the 10 h incubation period (**Figure 56**). It can be postulated that the presence of the PEG polymer (non-ionic) on the surface of the liposome particles shields lipid charge, and reduces inter-particulate attractive Van der Waals forces while increasing the repulsive barrier between two approaching liposome particles. Here, lack of aggregation is favourable as once liposomes aggregate, their size increases and the particles de-stabilise, which leads to their increased recognition by plasma proteins and also accumulation within the liver.

PEGylation of liposomes is an excellent means of stabilising liposomes for the purpose of prolonging *in vivo* circulation. Trubetskoy *et al.* have shown the effect of T_1 signal enhancement of PEGylated gadolinium liposomes in the imaging of lymph nodes. This signal intensity was 3.5 fold greater in just 4 min post i.v injection of PEGylated paramagnetic liposomes compared to non-PEGylated liposomes.[263]

The polydispersity index is a measure of the distribution of particles of different size and in general, values < 1 and nearing zero are considered optimal for liposome vesicles of uniform size and shape. The polydispersities measured for both sets of liposome formulations, incorporating Gd.DOTA.DSA or DOTA.DSA, were found to be less than 1.

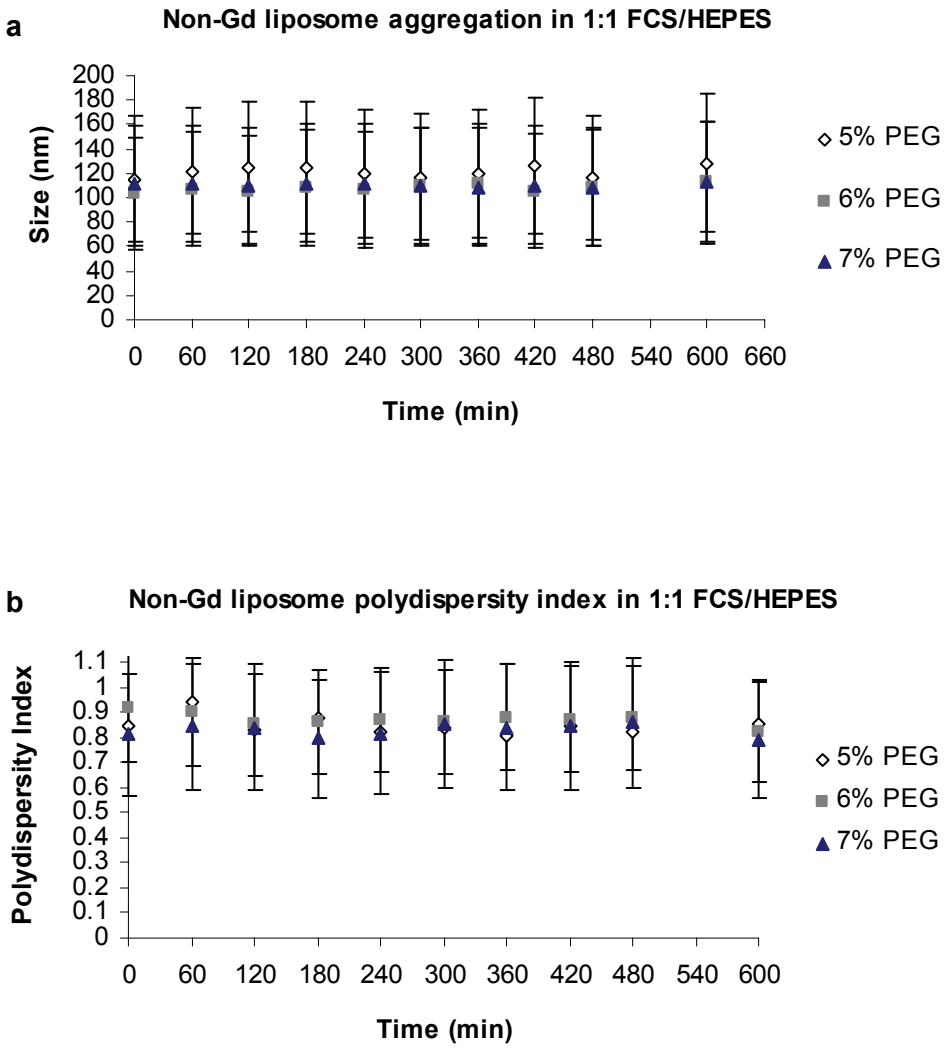


Figure 56. The size (**a**) and polydispersity (**b**) distribution of PEGylated Gd free liposomes (**Table 7**), was measured over a 10 h incubation period at 37 °C by dynamic light scattering.

From the data obtained for the serum aggregation studies, it was concluded that no significant size increase due to liposome aggregation is envisaged for these PEGylated liposome systems. Therefore, it was established to utilise the gadolinium liposome formulation with the highest molar ratio of PEG lipid for *in vivo* use, in this case, the gadolinium formulation with 7 mol % DSPE-PEG_{2000} (**Table 6**). This liposome is hereafter referred to as gadolinium liposome formulation **10** (Gd.DOTA.DSA/DOPC/Cholesterol/DSPE_PEG_{2000}/DOPE-Rhodamine: 30/32/30/7/1 mol %).

The zeta potential of gadolinium liposome formulation **10** was also measured. The zeta potential of a particle is a measure of the overall charge that the particles have in a particular solution. The zeta potential of this liposome formulation should average to near zero, as any excess cationic or negative charge can affect the fate of the liposomes *in vivo* and lead to their clearance from the blood pool. A zetasizer nanoseries instrument was used to measure the eletrophoretic mobility of gadolinium liposome **10** in water and this value was found to be 5.76 ± 0.0673 mV, which is close to 0 and the overall surface charge of the liposomes is considered to be neutral.

3.2.6 Cryo-Transmission Electron Microscopy (Cryo-TEM)

In order to assess the uniformity and size distribution of gadolinium liposome **10**, cryo-TEM images were obtained of the frozen liposomes (**Figure 57**). These images revealed the PEGylated liposome formulation **10** to be perfectly spherical and uniform in solution with an average size distribution of ~ 100 nm.

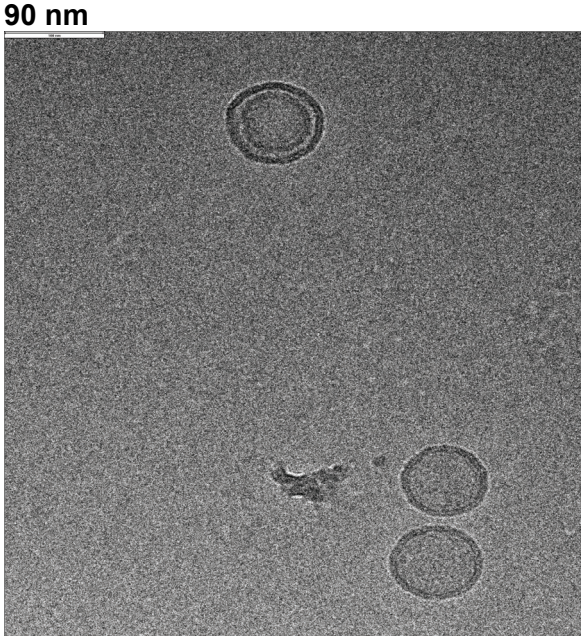


Figure 57. Cryo-transmission image of gadolinium liposome formulation **10** (Gd.DOTA.DSA/DOPC/Cholesterol/DSPE_PEG_{2000}/DOPE-Rhodamine: 30/32/30/7/1 mol %), white bar represents 100 nm.

Here, the inclusion of DOPC and cholesterol leads to the formation of uniform spherical paramagnetic liposomes as also demonstrated by others.[242]

3.2.7 Relaxivity of PEGylated Gadolinium Liposomes

In order to evaluate the relaxivity efficacy of gadolinium liposome formulation **10**, a series of liposomes were formulated using the same lipid components studied in the serum aggregation experiments. Here, the molar ratio of the gadolinium lipid Gd.DOTA.DSA was varied so that r_1 relaxivity measurements could be obtained from the PEGylated liposomes (**Table 8**). It was expected that the relaxivity of PEGylated liposomes would be higher for these of liposomes, as the PEG polymer layer adds further bulk to the liposome macromolecular structure, leading to a decrease in rotational tumbling (t_r) and an increase in T_1 relaxation rates.

Liposome Formulation (mol %)						
Gd.DOTA.DSA	**DOPC**	**Cholesterol**	**DOPE-Rhodamine**	**DSPE-PEG_{2000}**	**Initial size (nm)**	**PI**
50	13	30	1	7	176.37 ± 42.5	0.498
40	23	30	1	7	135.93 ± 33.5	0.737
30	33	30	1	7	238.73 ± 38.5	0.539
20	43	30	1	7	222.78 ± 47.5	0.669
10	53	30	1	7	192.40 ± 36.2	0.590

Table 8. Gadolinium liposomes used to calculate r_1 relaxivity of PEGylated liposomes for *in vivo* mouse tumour MRI.

From the PEGylated gadolinium liposomes formulated to measure r_1 relaxivity T_1 values were generated for 5 PEGylated gadolinium liposomes (**Table 8**) with Gd concentrations within the range 0.089 to 0.384 μmol. The r_1 relaxivity of these liposomes was found to be very high, 16.879 ± 1.55 $mM^{-1}S^{-1}$ at 4.7 T (**Figure 58**), which is considerably higher than the non-PEGylated liposomes measured previously (4.90 ± 0.60 $mM^{-1}s^{-1}$ for cationic liposome formulation **1**). Here, it can be envisaged that the PEG-polymer layer adds bulk to the overall liposome structure, in addition to providing further water solubility to the liposomes, leading to a greater degree of hydration around the liposomes. This property directly influences relaxation, whereby the co-ordinated Gd atom influences the relaxation of many water molecules within the second hydration sphere. In addition, the liposome size was smaller for these liposomes too, another factor that may contribute to an increased relaxivity.

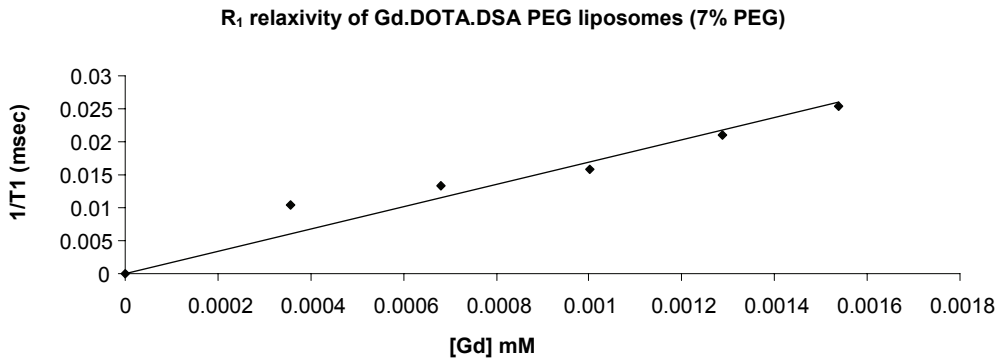


Figure 58. Relaxivity of PEGylated gadolinium liposome formulation **10**, at 4.7 T and ambient temperature. R_1 relaxivity is given by the slope of the fitted linear regression of the graph (16.879 ± 1.55 $mM^{-1}s^{-1}$).

Having demonstrated successful bimodal cellular MRI and fluorescence imaging of HeLa cells by means of gadolinium liposome formulation **1**, in addition to bifunctional labelling and transfection, the efficacy of the novel gadolinium lipid Gd.DOTA.DSA **2**, towards imaging of mouse xenograft tumours *in vivo* was investigated.

3.3 In Vivo Tumour Imaging with Gadolinium Liposomes

Mouse tumours of human cancer are a good model for preliminary investigations of imaging agents and their effectiveness as tumour signal enhancers. The human ovarian cancer cell line IGROV-1 was used to induce tumours in Balb/c nude mice. Here, cells were injected under the right flanks of 6-8 week old female mice, and after two weeks the mice had grown large enough tumours suitable for imaging. Stealth gadolinium liposomes (Gd.DOTA.DSA/DOPC/Cholesterol/DSPE-PEG_{2000}: 30/32/30/7 mol%, also containing 1 mol% DOPE-Rhodamine, total concentration; 30 mg mL^{-1}, formulation **10**) were prepared in HEPES buffer and injected through the tail vein of tumour bearing mice, a method that ensures rapid entry of the liposomes into the blood circulation. Prior to injection, baseline MRI scans were obtained on a 4.7 T magnet in order to identify the tumour and measure T_1 baseline values. Post liposome injection, the mice were then imaged at 3 h, 16 h and 24 h post injection. T_1-weighted images for each time point were obtained and the percent signal enhancement as a result of the accumulation of the PEGylated gadolinium liposomes within the tumour tissue was calculated from T_1 values generated from the tumour tissue (**Figure 59**).

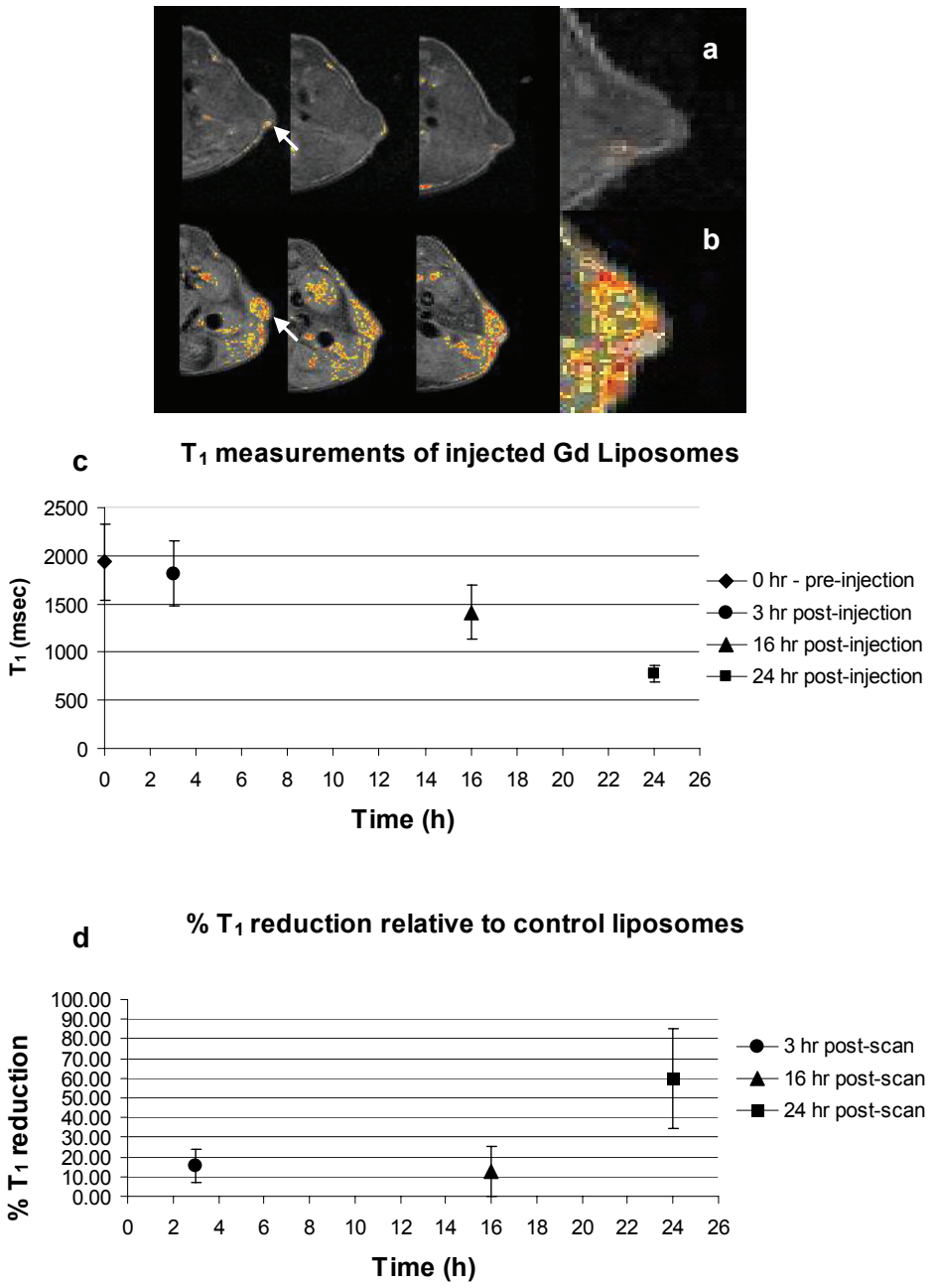


Figure 59. **a**: Pre-injection MR image of induced IGROV-1 tumours under the right flanks of nude Balb/c mice, the image on the right represents enlarged image of tumour area marked with white arrow. **b**: MR images 24 h post i.v. injection of stealth gadolinium liposomes **10**; the pseudo colour-map shows enhancement of tumour area, together with the enlarged image to the right of the white arrow. **c**: T_1 measurements from tumour slices 24 h post-injection. **d**: Image enhancement is supported by a 60 % measured reduction in tumour-T_1 values 24 h post i.v.-injection relative to control liposomes (Gd.DOTA.DSA replaced with Gd free DOTA.DSA).

As confirmed by T_1 measurements of tumours post injection of formulation **10**, a clear and excellent level of tumour MR signal enhancement is achieved in comparison to pre-injection baseline T_1 tumour images (**Figure 59**, **a** and **b**). The accumulation of the liposomes within the tumour area peaks at the 24 h end point measurement of T_1 signal, and conveys the gradual accumulation of the gadolinium particles within the tumour tissue. The presence of signal enhancement around the tumour vicinity is also visible and may suggest macrophage activity, or rather the uptake of the gadolinium liposomes by these cells. It has been shown that a prerequisite for the EPR effect is that the plasma concentration of the macromolecule or polymeric drug should remain high for > 6 h in rodents. [255] These results clearly demonstrate the prolonged residence time of the stealth gadolinium liposomes in the blood pool as signal enhancement peaks at 24 h post injection in our experimental model.

At 24 h post injection, the mice were sacrificed and their tumours excised. The tumours were frozen, fixed and subjected to cryo-sectioning, where 10 μm sections were cut and the slides analysed for their fluorescence using microscopy. The inclusion of the red fluorescent lipid DOPE-Rhodamine in the gadolinium liposome formulations allows for the bimodal assessment of liposome localisation within the tumour tissue. As expected, histological analysis of the tumour sections revealed a very high level of fluorescence signal in the tumour tissue (**Figure 60**). These encouraging results confirmed the presence of the liposomes in the tumour tissue and revealed an extremely heterogeneous pattern of fluorescence emission throughout the tumour (tumour sections were taken from the surface levels and mid to deep middle layers of the tumours). The appearance of hyper fluorescence signals within the tumour tissue was observable. These fluorescence intensity results provided qualitative visual congruence with the MR images and validated the accumulation of the stealth gadolinium liposomes (formulation **10**) within the xenograft tumours. Tumour tissue has microvessels with large fenestrations and as such the gadolinium liposomes are able to extravasate into the tumour. These extravasated liposomes are not cleared due to an impaired lymphatic drainage system and may accumulate within the tumour extracellular fluid (see **Figure 60**, **c**).

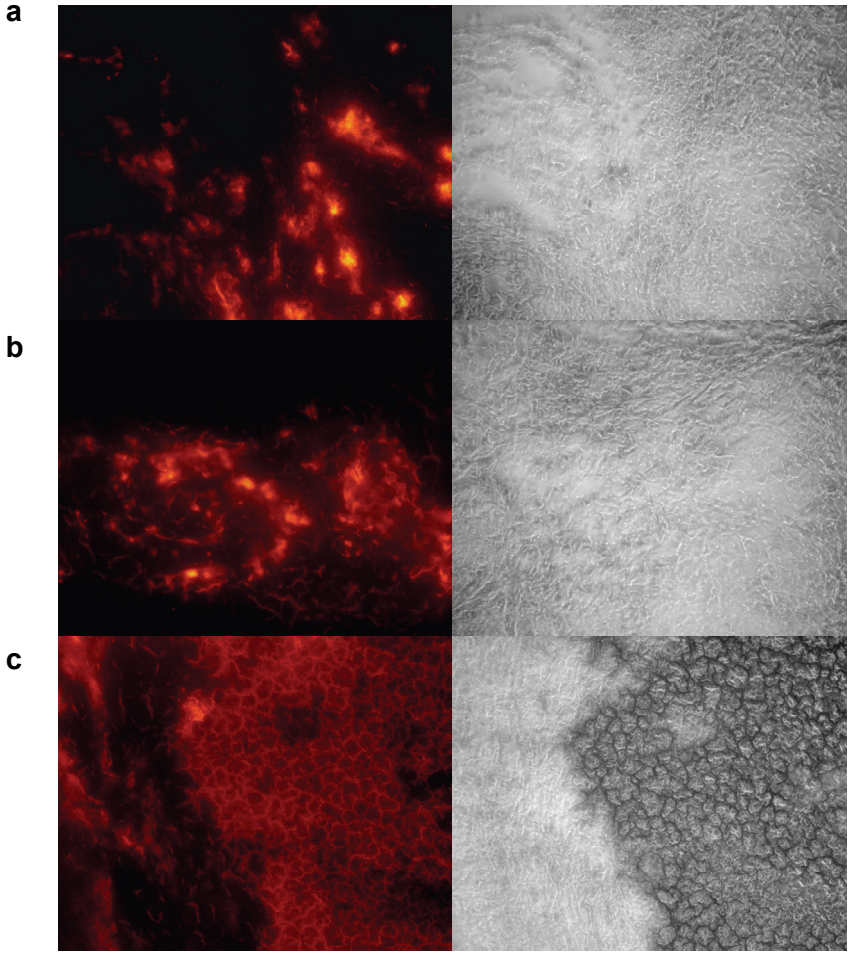


Figure 60. Fluorescence microscopy of tissue sections post gadolinium liposome injection. **a**: surface slices from the IGROV-1 tumours, images on the left are fluorescence images, images on the right are corresponding bright field. **b** and **d**: are mid-tumour slices. Other filters other than for Rhodamine were applied to tumour sections; no fluorescence was visible under these settings confirming the emission obtained to be due to the DOPE-Rhodamine included in the gadolinium liposome formulations alone (x 20). No fluorescence was observed from tumour sections of control liposomes injected containing no DOPE-Rhodamine (data not shown).

From the fluorescence images obtained (see **Figure 60**), it can be concluded that the IGROV-1 tumours do indeed posses great spatial heterogeneity. As a consequence extravasated liposomes are heterogeneously distributed throughout the tumour and are mainly located in perivascular regions. The fluorescence pattern obtained from the tumour tissue may be indicative of chaotic structures within tumours, including; collapsing vessels, and fragile vessels lacking a smooth muscle cell lining. The hyper-intense areas of more localised fluorescence may also be due to hypoxic or

necrotic tissue resulting from collapsing vasculatures, which are unable to meet the rapid growth of the surrounding cancer cells. It has been shown that only 20-80 % of the microvessels in tumours are perfused at any given time, which can explain the substantial heterogeneity of the microcirculation.[264]

The fluorescence images obtained from the tumour periphery areas presented some hyper-intense emissions visible in patches (**Figure 61**). These signal intensities may be due to the increased host macrophage activity around tumour marginal regions, where it has been shown that macrophages can "cluster".

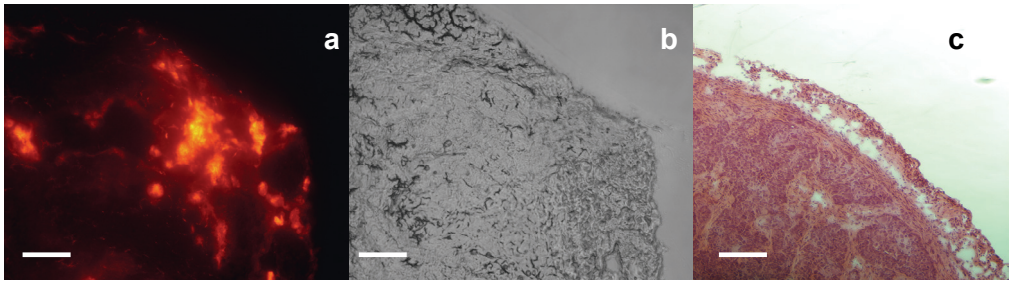


Figure 61. Peripheral tumour sections. **a**: red fluorescence image of peripheral tumour sections, **b**: corresponding bright field image and **c**: H & E stained section (x 20, white bar represents 50 µm).

3.3.1 Laser Ablation – Inductively Coupled Mass Spectrometry of Tumour Sections.

The presence of the gadolinium liposomes in the tumour tissue was further validated by the analysis of the sectioned tumour slices with laser-ablation inductively coupled plasma mass spectrometry (LA-ICP MS). This technique benefits from a coupled laser in addition to being capable of producing ICP-MS analysis of metal isotopes. LA-ICP MS is an incredibly versatile technique that can produce isotopic analysis of solid samples providing the laser can couple with the sample material. **Figure 62** shows the elemental profiles obtained from the mouse tumour sections post analysis with LA-ICP-MS. Signal enhancement for both iron and gadolinium at 90, 165, 200 and 230 seconds were observed, this corresponds to blood present in the section and confirms the presence of the gadolinium liposomes in the tumour tissue, and the blood circulation of these nanoparticles. The signal response for the remaining elements, calcium, manganese, copper and zinc are relatively stable across the section.

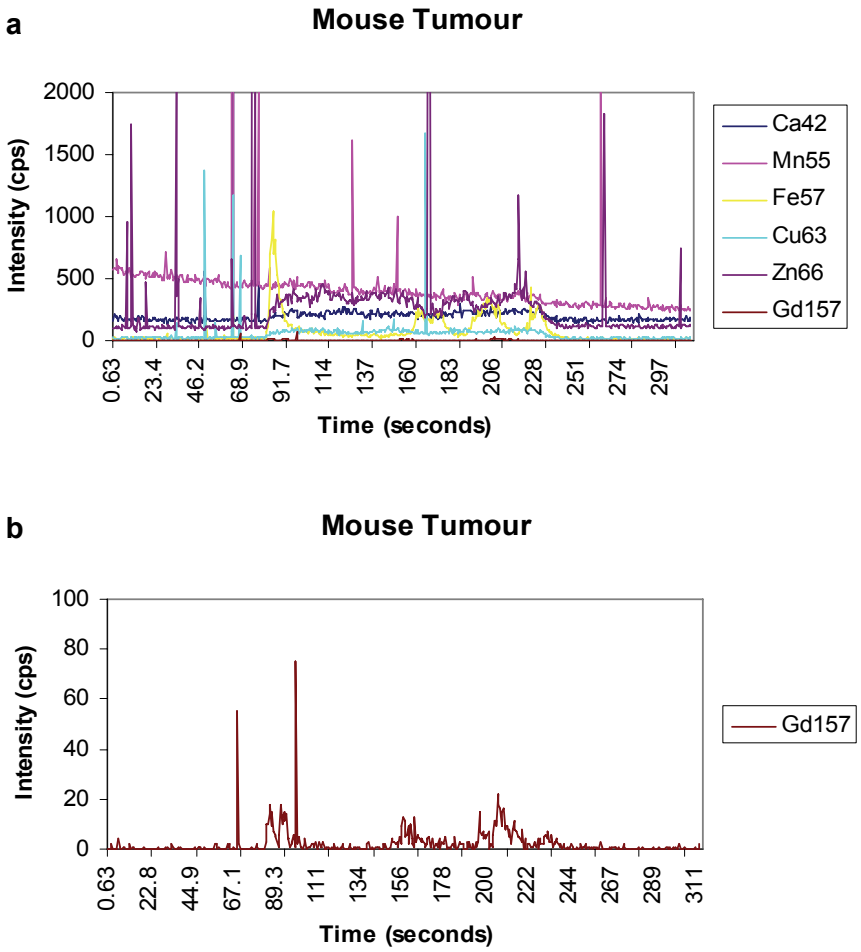


Figure 62. Single line raster via LA-ICP-MS through a section of mouse tumour showing elemental profiles for **a**: calcium, manganese, iron, copper, zinc, gadolinium and **b**: scaled to show the ion-time response for gadolinium.

In conclusion, the passive targeting of the stealth gadolinium liposomes to tumour tissue was achieved. Signal enhancement post i.v injection of gadolinium liposome **10** in xenograft tumours (n = 3) was monitored by MRI over a 24 h period. Over this period, a substantial 60% reduction in tumour-T_1 values compared to the situation with control liposomes (without Gd) was observed, in addition to visibly enhanced tumour-image brightness (**Figures 60** and **61**). This outcome suggested that the neutral gadolinium liposome **10** was in fact a liposome system with a substantial systemic half-life capable of long term circulation in the blood and passive targeting to the xenograft tumor by an enhanced permeation and retention (EPR) mechanism. This finding was supported by fluorescence imaging of tumor tissue slices (post-mortem) taking advantage of the bimodal imaging capacity of the gadolinium liposomes for both MRI and fluorescence microscopy. The fluorescence images obtained demonstrate liposome accumulation in subcutaneous tumour xenograft grown from implanted IGROV-1 cells.

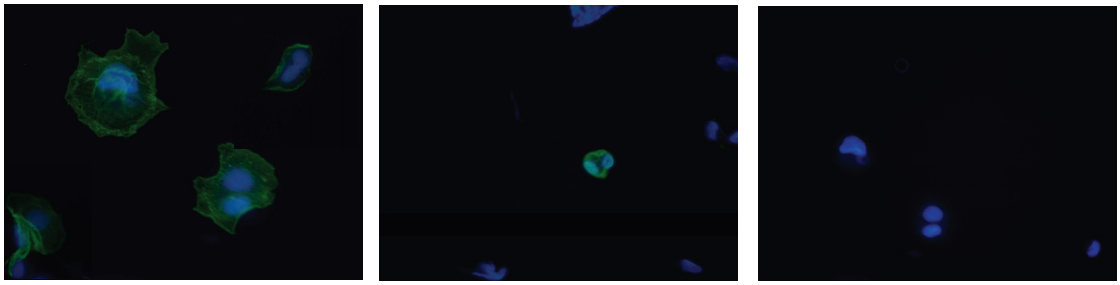
3.3.2 Targeted Tumour Imaging with PEGylated Folate Gadolinium Liposomes

As described previously, liposome accumulation in tumour tissue can be improved through the use of targeting moieties that are either conjugated to the surface of liposomes, or are attached to lipids that become incorporated within the liposomal bilayer. Since successful results were demonstrated with the IGROV-1 xenograft tumour model, the same cells were chosen for these series of targeted tumour MRI experiments. We chose to exploit the membrane-bound folate receptor (FR) in this study, as the natural ligand for this receptor (folic acid) tethered onto a PEG lipidic anchor (DSPE-PEG_{2000}(Folate), Avanti Lipids inc, USA). Folic acid is a vitamin that is utilised in the biosynthesis of nucleotides and is consumed in very high levels by proliferating cells such as cancer cells. In fact, the FR is over-expressed in several cancers, in particular epithelial carcinomas such as ovarian cancer, in addition to brain, kidney, lung and breast cancers. It has also been shown that aggressive or undifferentiated tumours at an advanced stage have an increased FR density and this could suggest that cancer therapy could benefit from the broad approach that FR mediated drug delivery offers.[265] The levels of FR on different cell lines can be assessed using immunohistochemistry techniques and fluorescence assisted cell sorting (FACS). In terms of FR expression levels, the human nasopharyngeal KB carcinoma cell line is considered to have the highest level of FR expression, however, the number of cases for this cancer are low in comparison to ovarian cancer which has the highest frequency (> 90 % of cases).[266] As such, we were interested in using this receptor and target model in order to test the efficacy of *in vivo* targeted gadolinium liposomes for the imaging of tumours by MRI. Effective signal enhancement is expected here since the FR is expressed in significantly lower amounts in normal tissue, limited mainly to kidney tubuli, lung epithelium, and placenta tissue.[253]

Folate targeted technology has been successfully applied to radio-imaging of therapeutic agents,[267] MRI contrast agents,[268] and gadolinium liposomes.[269] Choi *et al.* have demonstrated the use of folate-targeted iron oxide nanoparticles for the imaging of induced KB tumours and showed these particles to have a 38% signal intensity decrease compared to controls.[270] The FR binding affinity (K_D ~ 1^{-10} *M*) does not appear to be affected when its ligand, folic acid is conjugated to an imaging agent or therapeutic moiety via its γ-carboxyl.[271]

3.3.3 Immunohistochemistry Analysis of Ovarian Carcinoma Cell Lines

In order to establish whether the IGROV-1 cell line does indeed express a sufficient level of the folate receptor, FACS analysis of four different cell lines were carried out. For this purposes, the α-folate receptor (α-FR) which is a folate transporter with restricted expression levels in normal tissues was chosen. To measure the α-FR expression levels of the human ovarian cell lines IGROV-1, OVCAR-3 and HeLa cervical cancer cells, both fluorescence microscopy and flow cytometry experiments were carried out. In addition to these cell lines a breast cancer cell line (SKBR-3) was also analysed as a negative control cell line with no FR expression. Cells were grown in folic acid free media and incubated with serum to block any non-specific interactions. Immunostaining was carried out with a monoclonal antibody (MAb Mov18/ZEL, Axxora, UK) specific for the α-FR, and post incubation with this antibody, a secondary FITC labelled antibody (Goat anti-body IgG, FITC conjugated, Santa Cruz Biotechnology, inc. USA) was allowed to incubate with the cells. Post staining, the cells were fixed and analysed by fluorescence microscopy. Firstly, qualitative results were obtained whereby fluorescence microscopy of the cell lines revealed a high level of FITC fluorescence from the IGROV-1 cells, in comparison to the OVCAR-3 and the control SKBR-3 cell lines (**Figure 63**).



IGROV-1 **OVCAR-3** **SKBR-3**

Figure 63. Fluorescence microscopy images of three immunostained cell lines for α-FR. The presence of a higher level of α-FR is observed for the IGROV-1 cell line. There is some FITC fluorescence visible from the stained OVCAR-3 and non visible for the SKBR-3 α-FR negative cell line. The blue fluorescence observed is due to DAPI staining, which is a cell nucleus labelling agent. The images for the HeLa cell line are not shown as no FITC fluorescence was observable from these cells (x 40 for IGROV-1, x 20 for OVCAR-3 and SKBR-3 images).

From the FACS (**Figure 64**) α-FR expression analysis, where all cell lines were cultured under the same standardised conditions using folate free cell culture medium, it was shown that the IGROV-1 cell line exhibited a distinctly higher level of α-FR expression. The α-FR expression was shown to be in the order: IGROV-1>>OVAR-3>HeLa>SKBR-3 (**Figure 64**).

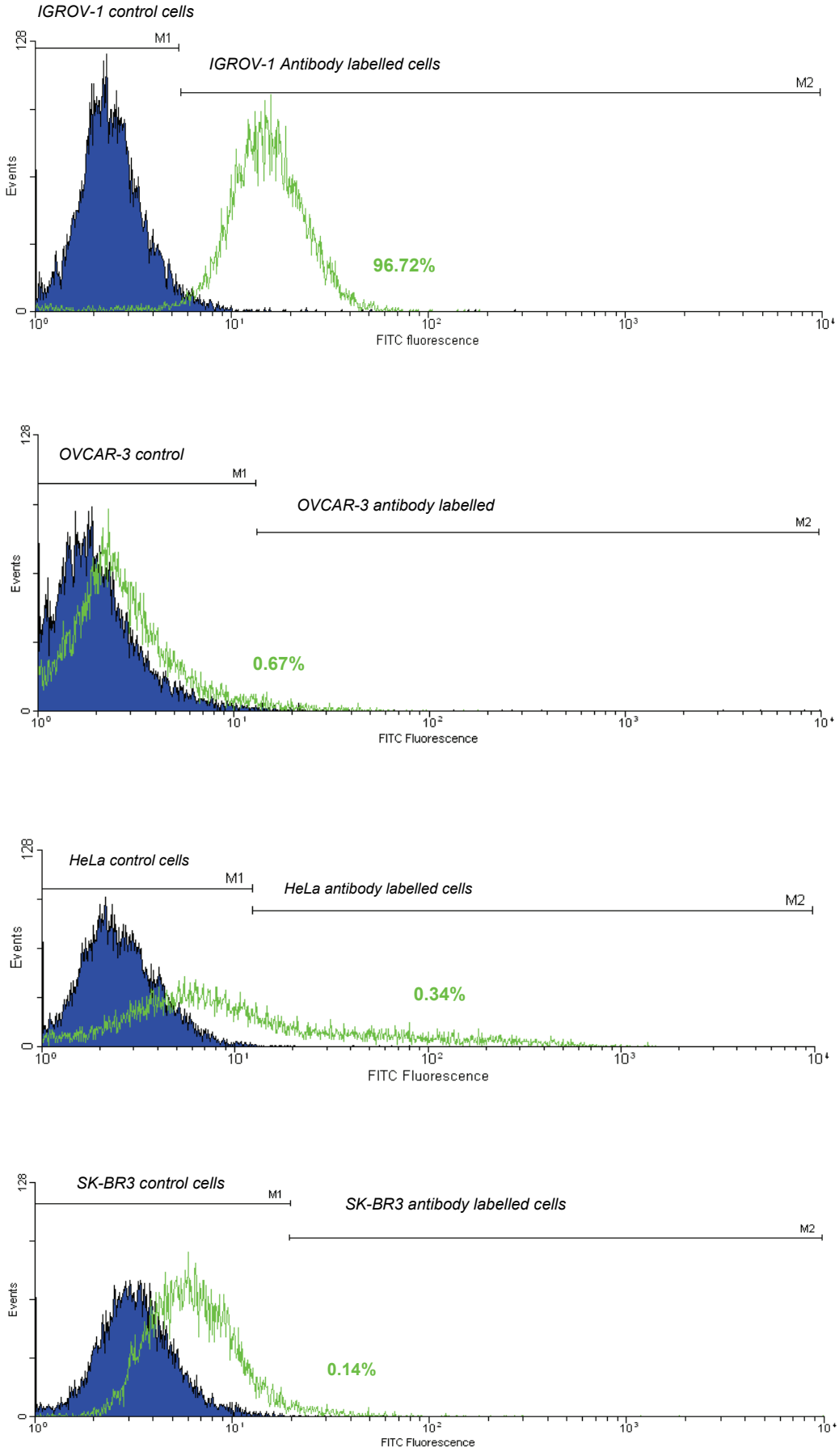


Figure 64. FACS analysis of four cell lines for α-FR expression levels.

3.3.4 Folate Targeted Gadolinium Liposomes for Tumour Imaging

Having established the over-expression of the α-FR on the IGROV-1 cell line, folate targeted gadolinium liposomes were prepared for specific cell receptor binding and uptake into the IGROV-1 tumour cancer cells. These liposomes consisted of a similar formulation than the non-targeted PEGylated gadolinium liposomes prepared for passive-targeting to tumours *in vivo* (gadolinium liposome **10**). For the folate targeted liposomes a 3 mol % of the targeting ligand; DSPE-PEG_{2000}Folate (Avanti Polar Lipids inc. USA) was also incorporated into the formulation, rendering Gd.DOTA.DSA/DOPC/Cholesterol/DSPE-PEG_{2000}/DSPE-PEG_{2000}Folate/DOPE-Rhodamine: 30/32/30/4/3/1 mol % (gadolinium liposome formulation **11**, see **Figure 65**).

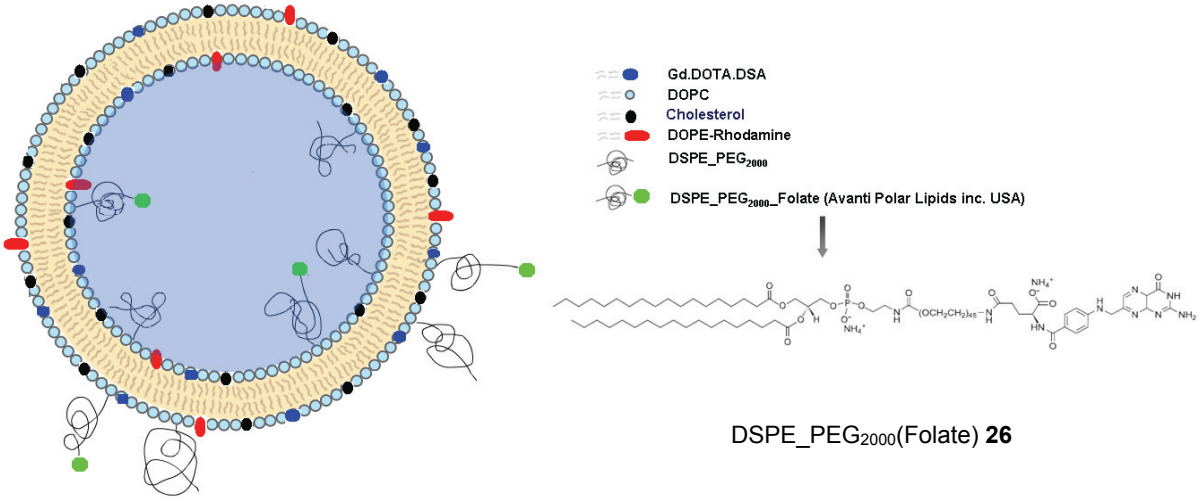


Figure 65. Folate-targeted gadolinium liposomes for IGROV-1 tumour imaging *in vivo*.

The serum aggregation of these targeted liposomes was also assessed as per section **3.2.5**, no significant change in liposome size was observed over a 24 h incubation of folate-targeted liposomes in a FCS: HEPES mixture (data not shown). The relaxivity of these liposomes was also measured by formulating a range of liposomes with varying Gd.DOTA.DSA lipid concentrations, and was found to be comparable to the non-targeted gadolinium formulation **10** (relaxivity for liposomes **11** is 14.520 ± 1.55 $mM^{-1}s^{-1}$). The zeta potential of folate-targeted PEGylated liposome **11** was also obtained, and this value was found to be close to zero, indicating an overall neutral charge for these liposomes (zeta potential: 3.21 ± 0.284). These liposomes were also formulated with a controlled size of approximately 105.23 ± 19.2 and a good polydispersity index (0.23).

The folate-targeted liposomes were injected into Balb/c nude mice in an identical manner to the non-targeted gadolinium liposomes, with the exception that the folate targeted liposomes were injected at half the dose of the non-targeted liposomes. It was postulated that due to the presence of the folate targeting moiety, an increase in tumour signal will be apparent post-injection by MRI, in comparison to the control liposomes (non-targeted). Indeed, this expectation was apparent at just 2 h post-injection of the folate targeted liposomes (see **Figure 67**).

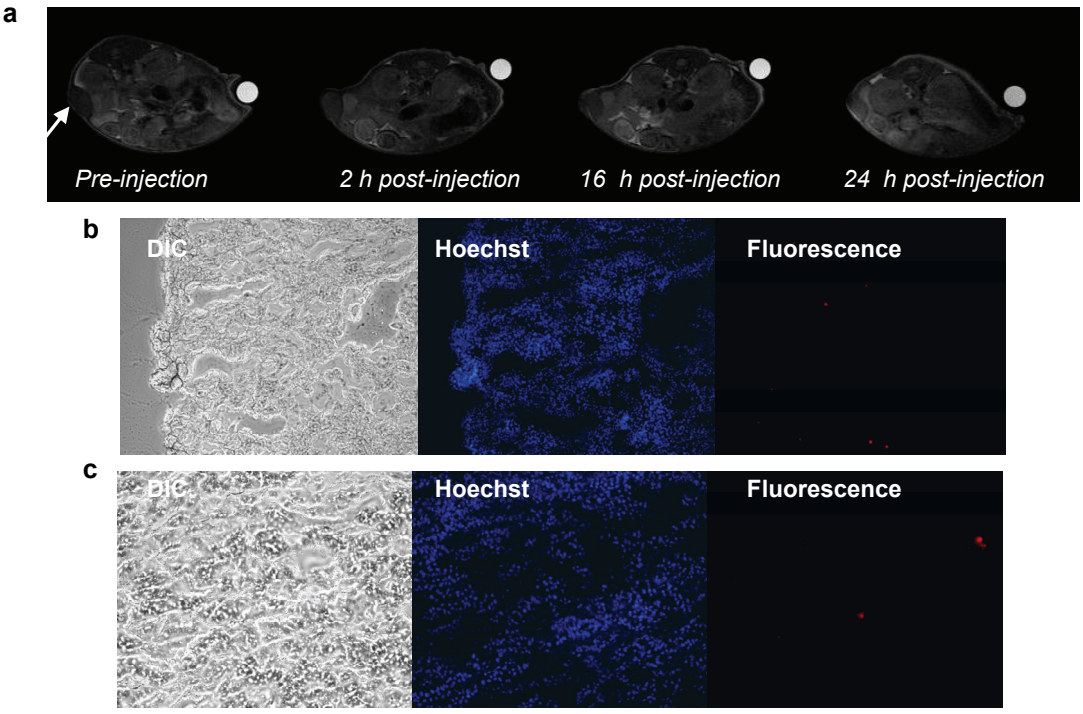


Figure 66. a: MRI of IGROV-1 tumour bearing Balb/C nude mice, from left to right; pre-injection, 2 h post-injection, 16 h and 24 h post injection of PEGylated gadolinium liposomes **11** (white arrow shows location of tumour). **b:** Microscopy images of sectioned liver from tumour bearing mice injected with gadolinium liposome **11**, these results do not show significant accumulation of the liposomes in the liver and **c**: microscopy images of sections from excised kidneys, where the presence of the fluorescent lipid DOPE-Rhodamine and therefore gadolinium liposomes is minimal 24 h post-administration (x 20 magnification).

Figure 66 presents MR images taken from mice bearing IGROV-1 xenografts that were injected with the FR-targeted liposome formulation **11**. From these results the positive enhancement of tumours 24 h post injection is visible **(Figure 66**, **a**) and the presence of the liposomes within other organs such as the liver and kidneys was found to be minimal (**Figure 66**, **b** and **c**). This suggests that these targeted

gadolinium liposomes do not accumulate in the kidney tissue and therefore subjects may not suffer from nephrotoxic adversities reported recently with the use of gadolinium based contrast agents.

The measured tumour T_1 values show that within just 2 h post i.v. injection the active and specific targeting effect of the folate liposomes is apparent and a substantial 65% T_1 reduction is achieved within 16 h post injection compared to ~ 13% for the non-targeted gadolinium liposomes. This significant enhancement is observed despite injection of targeted liposomes at half the concentration of the non-targeted liposomes (**Figure 67**).

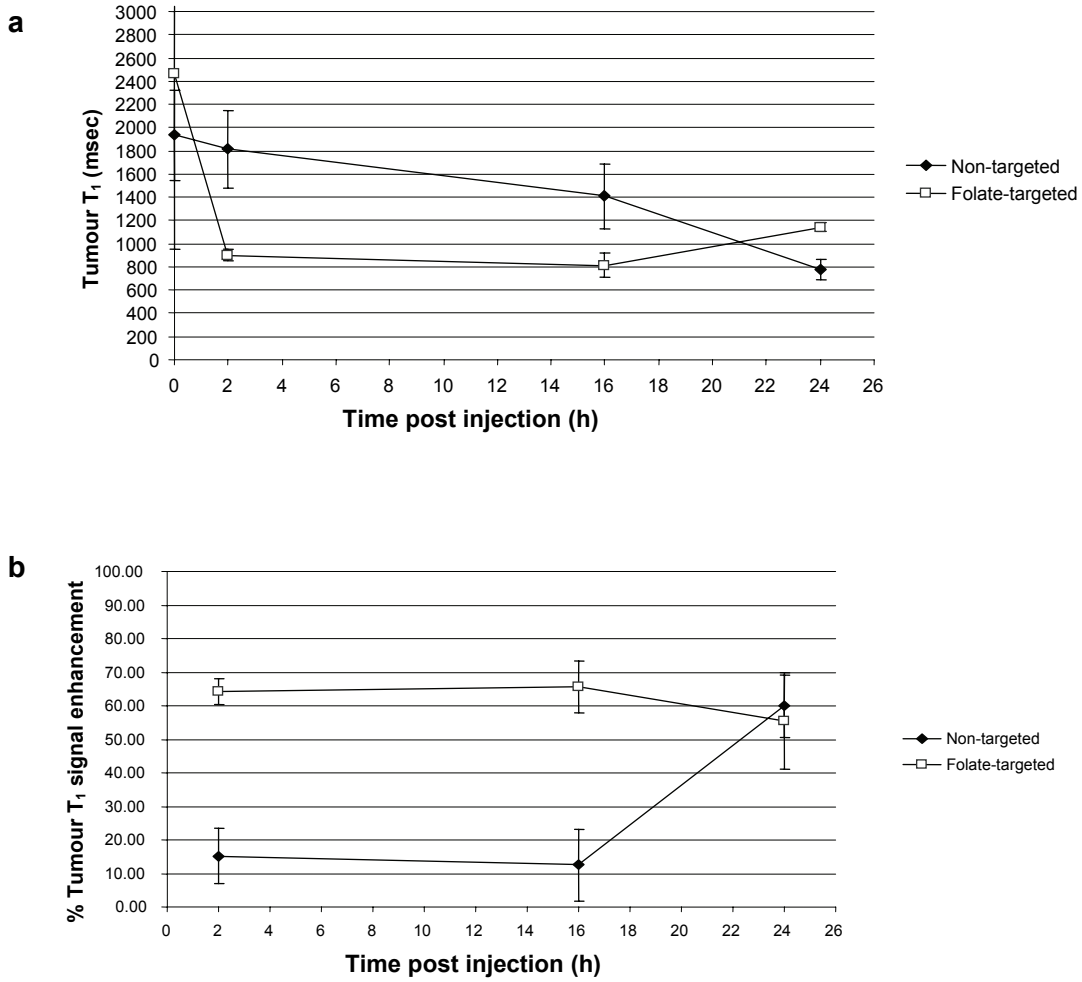


Figure 67. Mouse tumour signal enhancement with folate-targeted (liposome formulation **11**) and non-targeted gadolinium liposomes (formulation **10**), **a**: tumour T_1 measurements at 4.7 T, **b**: signal enhancement (%) calculated from mean tumour T_1 values pre and post- liposome injections).

Following MRI, the mice were then sacrificed and their tumours excised, frozen, fixed and sectioned for histological analysis. As with the previous non-targeted liposomes, the inclusion of the fluorescent DOPE-Rhodamine lipid in the liposome formulation allows for post-mortem analysis of the presence of liposomes within the tumour tissue. **Figure 68** presents fluorescence microscopy images of sectioned tumours 24 h post folate-liposome injections. The presence of intense red fluorescence from these sectioned tumour slices is indicative of the accumulation of the targeted liposomes in the tumour tissue. The T_1 tumour signals measured (**Figure 60**) indicate a rapid accumulation of the targeted liposomes, and histological results show that the folate-targeted gadolinium liposomes may be accumulating within areas of hyperpermeability in the tumour tissue.

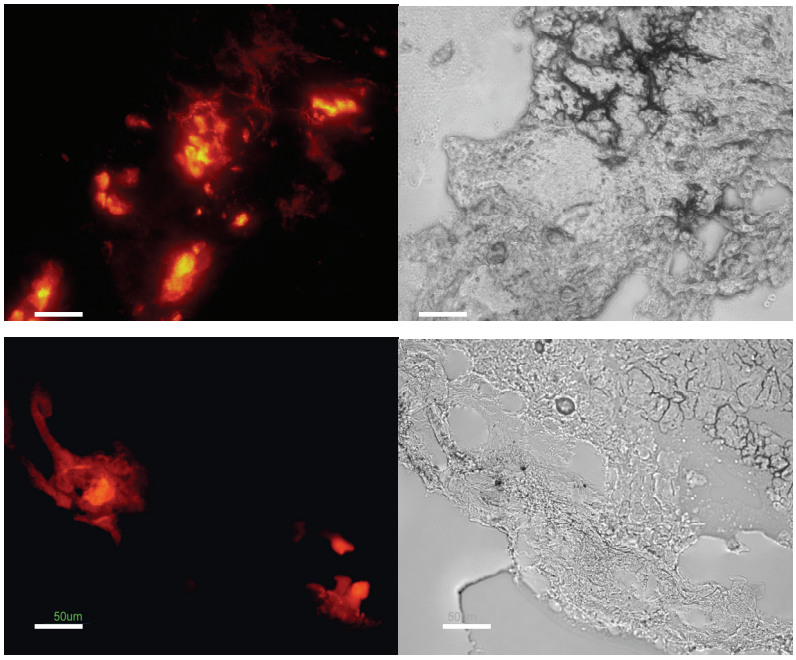


Figure 68. Fluorescence microscopy images of IGROV-1 sectioned tumours. Images on the left are red fluorescence and on the right are the corresponding bright field images showing heterogeneous tumour tissue. (x 20, white bar represent 50 μm).

The fluorescence pattern observed for the targeted liposomes appears to be more localised, and the type of diffused and dispersed fluorescence observed for the passively accumulated liposomes is not reflected from these images (**Figure 68**). It has been suggested that, in particular with immunoliposomes targeted to tumours, there may exist a "binding site barrier" hypothesis that affects targeted liposome binding in tumours. Weinstein *et al.* have suggested that immunoliposomes will not penetrate deeply into the tumour but will bind to the first target cells encountered. [272]

As such, it appears that the non-targeted gadolinium liposomes (see **Figure 60**) may show a better penetration into solid tumours, however, the folate-targeted liposomes show a more rapid accumulation within the IGROV-1 tumours. Here, it is important to note that the MR signal enhancement data for the folate-targeted liposomes were obtained by drawing regions of interest (ROI) around the entire surface area of the tumour slices and as such represent signal enhancement of the entire tumour section. As the molar ratio of the fluorescence lipid is far less than the amount of gadolinium lipid in the liposome formulation (1: 30), this explains the difference in the fluorescence and Gd enhancement signal levels within the tumours. In addition, the binding site theory may only be a limit of immunoliposomes with bulky antibodies/antibody fragments, further work to clarify the localisation of the folate-targeted liposomes within the tumour, could involve the direct antibody staining of the sectioned tumour slices for α-FR expression.

The enhanced and rapid onset of signal enhancement in the case of the folate-targeted liposomes may be due to the uptake of the targeted liposomes by the tumour cells as demonstrated by the persistence of the signal for up to the 24 h end-point (see **Figure 67**, **a**, **b**), which also suggests that the rate-limiting step for non-targeted liposomes is indeed extravasation. Since a near 60% signal enhancement is achieved for the non-targeted liposomes only after 24 h post injection, suggesting continuous circulation and gradual accumulation of these passively-targeted liposomes, which is in line with current EPR theories. The dose used in these experiments is also noteworthy, the folate-targeted liposomes were administered at a gadolinium lipid concentration of 0.719 μmol per 20g mouse, which in comparison to the lower end of the clinical dose at which contrast agents are used (0.01 mmol/Kg), makes the injection dose approximately 14 fold lower.

For the folate-targeted liposomes the ligand-liposome ratio was not optimised, at 3 mol % of the overall liposome formulation, this may have been an excess of targeting ligand. It has been shown that effective *in vivo* tumour folate targeting may only require < 0.3 mol% of the ligand.[273] It has been suggested that the folate receptor function is regulated by cellular folate requirements and therefore even a small amount of folic acid is sufficient to trigger the down-regulation of the folate receptor cycle.[274] However, the observed 65% signal enhancement in our case may suggest that perhaps only a slight decrease in ligand ratio may be necessary to achieve even higher tumour signal enhancement rates.

Another interesting point arising from the folate-targeted liposome data obtained may be that the folate ligand is indeed retained during circulation. Since if the ligand is lost

in vivo during circulation, then the liposome particles would have lost the ability to bind to the tumour cells. Gabizon *et al.* have tested the ligand-liposome association of folate targeted liposomes *in vivo* using an ascetic tumour that did not express folate receptors.[265] Here, the injected folate liposomes were collected from the ascetic fluid 48 h after i.v injection and were tested *ex vivo* for their FR binding on relevant FR expressing cell lines. They successfully showed that the folate-targeted liposomes retain their FR receptor binding post *in vivo* injection, and extravasation to the ascetic fluid. These findings suggest that folate targeting for the *in vivo* imaging of tumours presents a robust and broad platform for both tumour imaging and the delivery of therapeutic agents over a prolonged period of time to the tumour tissue.

A further interesting observation was made when the folate-targeted liposomes (formulation **11**), were formed at larger sizes > 100 nm and injected into the Balb/c IGOV-1 tumour bearing mice. These liposomes which were on the order of 150-200 nm in size did not reach the IGROV-1 tumours and were shown to accumulate extensively within the liver tissue (**Figure 69**). Non-targeted liposomes of a similar size were also injected for comparison and a significant difference within the liver accumulation of the PEGylated folate-targeted liposomes (gadolinium liposome formulation **11**) and the PEGylated non-targeted liposomes (gadolinium liposome formulation **10**) was observed 2 h post-injection of the liposomes.

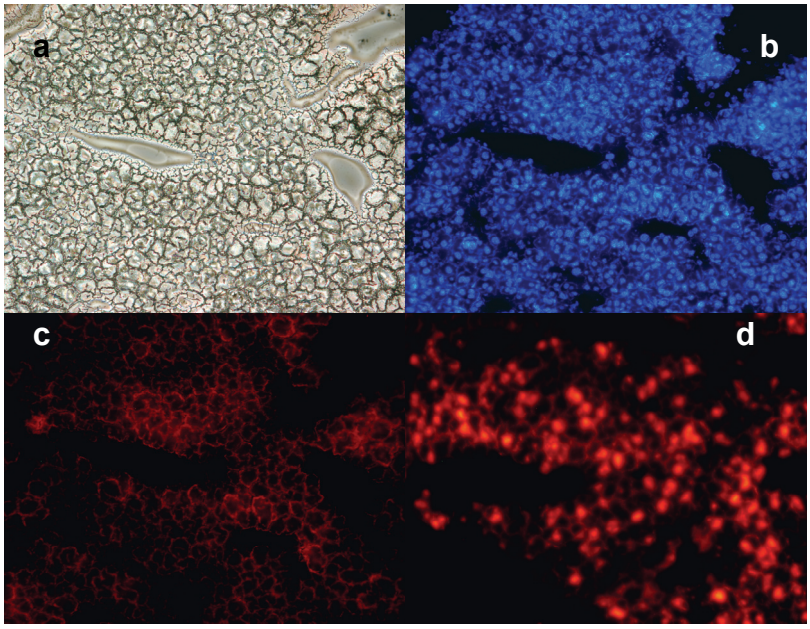


Figure 69. Fluorescence microscopy of liver sections 2 h post gadolinium liposome injections of > 100 nm. **a**: Bright field image of the liver, **b**: Hoechst stain of liver, **c**: fluorescence image of the liver post non-targeted gadolinium liposome injection (formulation **10**) and d:

fluorescence image of the liver post folate-targeted gadolinium liposome injection (formulation **11**).

From the images in **Figure 69** (part **c** and **d**), it is apparent that the folate-targeted liposomes have a more localised pattern of fluorescence and appear "internalised" into cells. This may most likely be as a result of Kupffer cell accumulation, however the liver fluorescence observed from the liver histology sections of the non-targeted liposomes shows a more distinct pattern of "extracellular" accumulation of the liposomes (**Figure 69**, **c**). From these results it can be concluded that due to the folate ligand on their surface, the folate-targeted liposomes are readily taken up by the Kupffer cells, in comparison to the non-targeted liposomes, suggesting that the Kupffer cells may have an affinity for the folate ligand. An alternative explanation may be that due to the surface folate ligand; the targeted liposomes are recognised by certain opsonins in the blood which mark these liposomes for Kupffer cell uptake, despite the presence of the PEGylation layer in these formulations.

The fluorescence pattern observed from the liver sections of the non-targeted liposomes can be explained by the "endothelial massage" theory put forward by Wisse and McCuskey.[275]. This theory describes the movement of fluid and small particles in and out of the Space of Disse, which is the area located between the endothelial lining of the hepatic sinusoid and the hepatocytes. This is similar to the notion of the squeezing of white blood cells between the endothelial cells within the narrow sinusoidal spaces.[259] Liposomes are also able to squeeze through fenestrations in the liver and due to their deformable nature can be squeezed into the Space of Disse and this may only require their transient electrostatic interaction with the endothelial lining. It has also been shown that Kupffer cells take up far more liposomes per cell than the hepatocytes and this may explain the strong fluorescence observed in **Figure 69**, part **c**. The uptake of the folate targeted liposomes may be due to opsonins binding, a whole host of opsonising proteins have been found that may absorb onto liposomal surfaces, amongst these are C-reactive protein, fibronectin, complement factor C3b, immunoglobulins, and alpha$_2$-macroglobulin.[259]
These results demonstrate the importance of nanoparticle size control and shed light on the behaviour of liposomes > 100 nm in size *in vivo*. Both targeted and non-targeted liposomes of > 100 nm were shown to accumulate within the liver, suggesting that the size of gadolinium liposomes is indeed an important factor in their liver clearance and prolonged blood circulation *in vivo*.

3.4 Chapter Summary

The *in vitro* cationic liposome **1** formulated with the novel Gd.DOTA.DSA lipid **2** was shown to be an effective bimodal cell labelling agent, which was made possible by mediating the delivery of chelated-Gd to HeLa cells and led to the subsequent shortening of cellular T_1 relaxation times. This formulation was found to be non-toxic to the HeLa cells as assessed by MTT cell viability and LDH toxicity assays. In addition, the bifunctional capability of this gadolinium liposome formulation was demonstrated by the successful transfection of HeLa cells using a plasmid DNA encapsulated version of gadolinium liposome **1**. This suggested that this formulation is capable of bifunctional labelling with transfection which is consistent with a cell labelling mechanism in which gadolinium liposomes enter by endocytosis followed by endosomolysis and subsequent cytoplasmic release of the gadolinium, fluorescent lipid and DNA.

Further neutral PEGylated liposomes were developed and their serum aggregation and magnetic relaxation properties were assessed. Cryo-TEM images of the optimised paramagnetic liposome **10**, showed this liposome formulation to be perfectly spherical and uniform in size (~ 100 nm). The *in vivo* PEGylated gadolinium liposome **10** was shown to enhance MR signal of xenograft tumours in mice substantially 24 h post injection, which led to the demonstration of the enhanced retention and permeation of these liposomes within the tumour tissue. The bimodal imaging approach of tumours using this formulation was successfully demonstrated.

Tumour signals were drastically enhanced when folate-targeted liposomes were injected i.v into the same IGROV-1 xenograft models used to assess the passive accumulation of the gadolinium liposomes. These active-targeting results showed a rapid and persistent tumour signal enhancement, and merit the investigation of signal enhancement ability of these liposomes beyond the experimental 24 h time point.

4 . Synthesis of Second Generation Bimodal Gadolinium Lipid - Gd.DOTA.Rhoda.DSA

4.1.1 Bimodal Fluorescent and MRI Probes

Discoveries in molecular imaging are certain to play a vital role in the early detection, diagnosis and treatment of disease, and help decipher the biological mechanisms responsible for disease states at a molecular and cellular level. The field of molecular imaging has made use of imaging agents that mostly provide single signature information. Multi-modal imaging agents have the potential to provide more than one signal from a biological sample and in this way can enhance the visualisation of biological material.

A number of multimodal probes with both MR and fluorescence signatures have been developed for cell labelling and use in the imaging of developmental biology. Thomas Meade and co-workers have been primary developers of such probes, where high-molecular weight polymers with both gadolinium and fluorescent moieties (tetramethylrhodamine) were synthesised (**Figure 70**).[276] These highly effective bimodal probes were used to study the initial stages of embryonic development, and were shown not to interfere with the normal development of the *Xenopus laevis* embryos post-injection. More recently, Brekke *et al.* demonstrated the use of one of these bimodal polymeric contrast agents (GRID, a gadolinium rhodamine dextran polymer) for the labelling of neuronal stem cells. The addition of this agent to the cells did not appear to affect the cellular viability, stem cell migration mobility or multipotency of these sensitive and delicate cells. This study also demonstrated the utility of a bimodal imaging approach, whereby the labelling of the neuronal stem cells was confirmed *in vitro* by both fluorescence and T_1-weighted MRI.[277] Neuronal stem cells were also labelled with GRID *ex vivo*, and their transhemispheric migration to stroke lesions was assessed by both longitudinal *in vivo* MRI and fluorescence analysis of histology samples from rat brain specimens.[96]

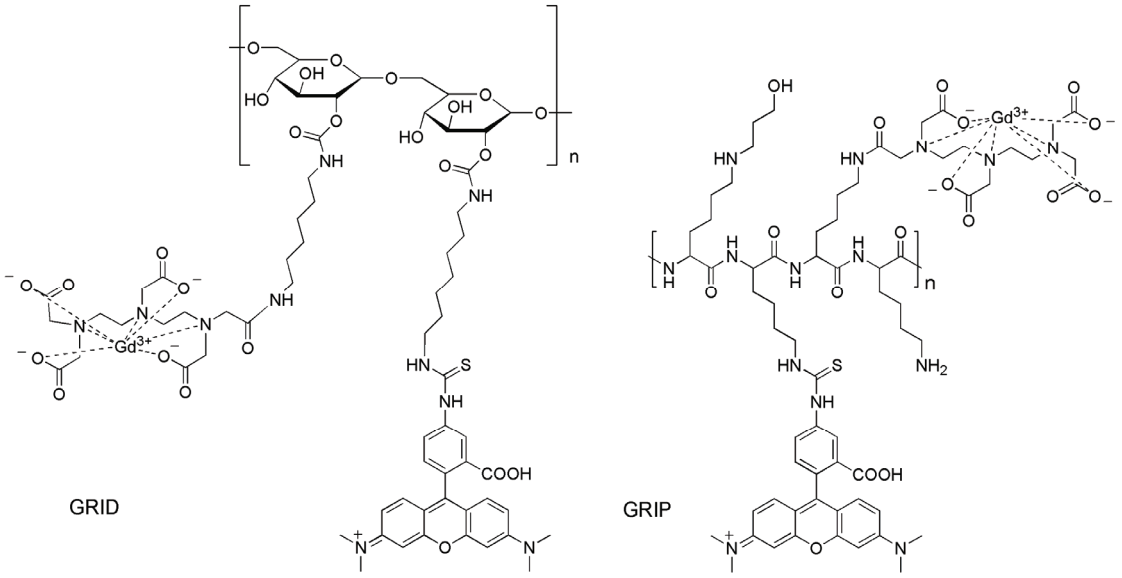


Figure 70. Two bimodal polymeric contrast agents.[276]

Bimodal agents with target specificity have also been developed, Dirksen and co-workers have recently designed and synthesised a bimodal contrast agent based on a cyclic peptide (target-specific sequence), Gd.DTPA, and conjugated to the dye Oregon green 488. This dual-labelled probe was shown to be suitable for both MRI and optical imaging of angiogenesis (**Figure 71**).[278]

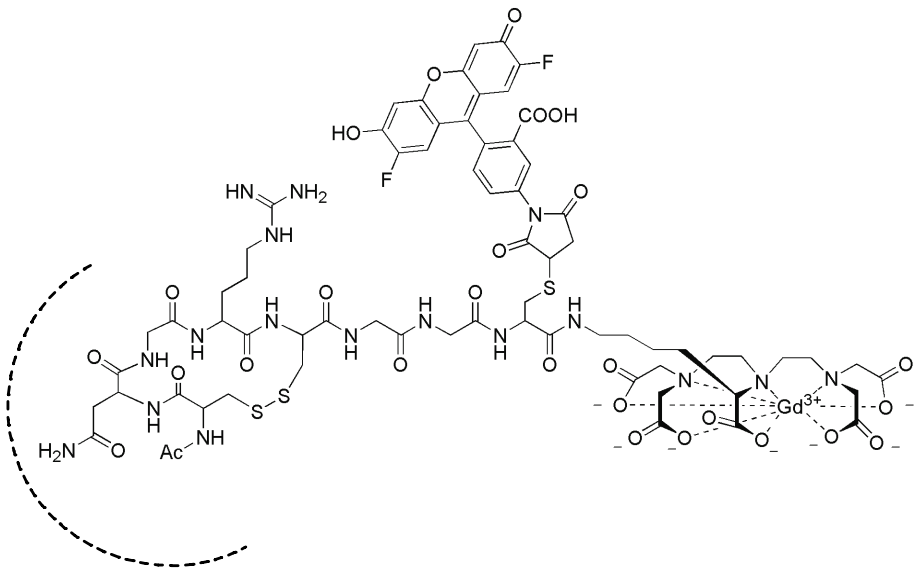
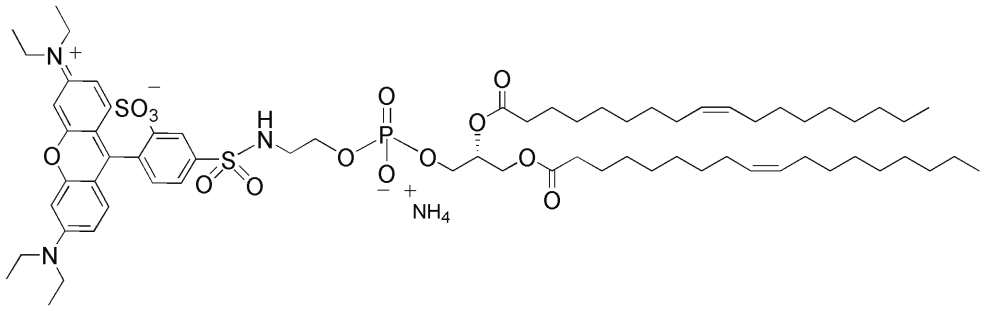


Figure 71. An angiogenesis specific bimodal fluorescent and paramagnetic contrasts agent (dotted line indicates targeting region).[278]

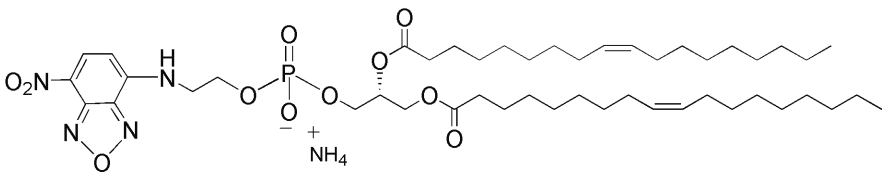
As demonstrated in **Chapter 3**, MRI and optical techniques are excellent complementary imaging methods, and as such a further aim of this project has been to synthesise a novel bimodal Gd lipid that also incorporates a fluorescent moiety. This contrast agent is thought to be valuable for the bimodal imaging of tumours or labelled cells, since in addition to MRI, fluorescence microscopy or *in vivo* fluorescence imaging could provide further proof of liposome localisation, and both a qualitative and quantitative analysis of liposome biodistribution may be achieved.

4.1.2 Synthesis of the Novel Bimodal Lipid: Gd.DOTA.Rhoda.DSA

Fluorescent lipids have been used extensively for the investigation of lipid trafficking and sorting in both model and real cellular membranes, in particular, fluorescent lipids have been used to highlight cellular processes such as membrane fusion.[279] In principle there are two regions on lipids where a fluorophore may be attached, this is achieved either through covalent attachment of the fluorescent moiety to the head group region or attachment to the lipid chain. The most frequently utilised fluorescent lipids are fluorescent analogues of DOPE; which are DOPE-Rhodamine and DOPE-NBD (**Figure 72**).



DOPE-Rhodamine (lissamine rhodamine B)



DOPE-NBD

Figure 72. Structures of two commonly utilised fluorescent lipids, DOPE-NBD and DOPE-Rhodamine.

To our knowledge only one type of bimodal *lipidic* molecule has been developed thus far that incorporates both a paramagnetic contrast agent and a fluorophore onto a single molecular framework. Li *et al.* have designed and synthesised this bimodal probe which has lipophilicity due to the attachment of a single alkyl chain, that can incorporate into lipidic membranes (**Figure 73**).[280] This bimodal agent was used to label low-density lipoprotein (LDL) particles for the *in vivo* detection of LDL receptors.

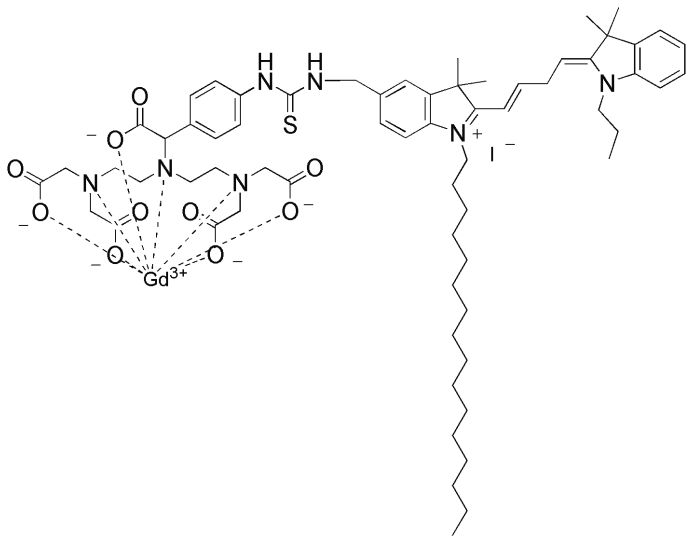
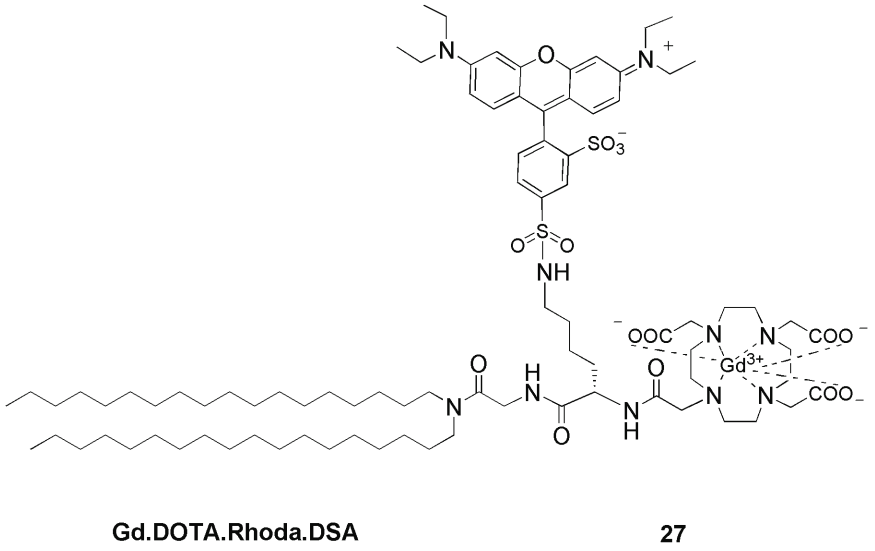
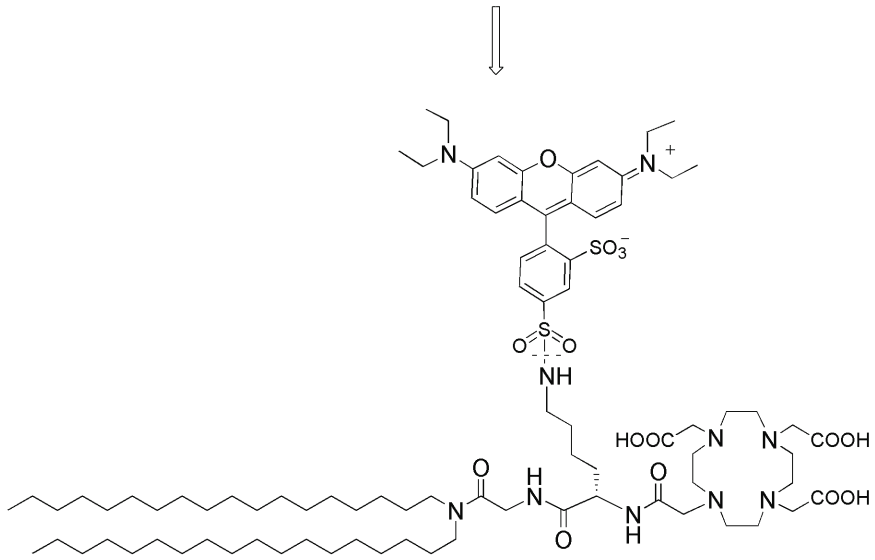


Figure 73. PTIR267: a bimodal agent for MR and fluorescent imaging of low density lipoprotein receptors.[280]

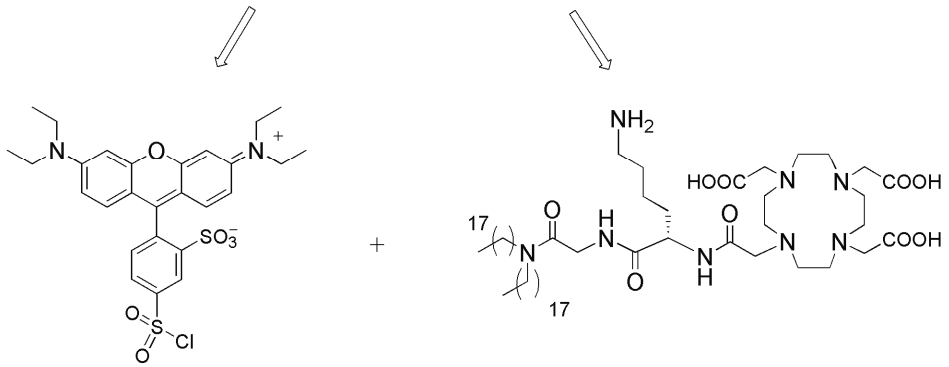
Most bimodal liposomal agents that have a fluorescent and paramagnetic signal are based on the use of two separate lipids in the liposome formulation, one lipid component bearing the Gd moiety and another a fluorescent moiety usually in place of the head group (most commonly DOPE-Rhodamine is used).[220] However, we designed a bimodal lipidic molecule bearing both fluorophore and contrast agent groups on the same structure, in order to create a more robust bimodal liposome for both MR and fluorescence microscopy. The retrosynthetic analysis for this novel lipid (Gd.DOTA.Rhoda.DSA, **27**) is presented in **Scheme 9**. The dual-modality concept considered in the synthesis of this new paramagnetic and fluorescent lipid is valuable in that anatomical information (MRI) as well as very sensitive localisation is achievable (*ex vivo* fluorescence microscopy).



Gd.DOTA.Rhoda.DSA **27**



28

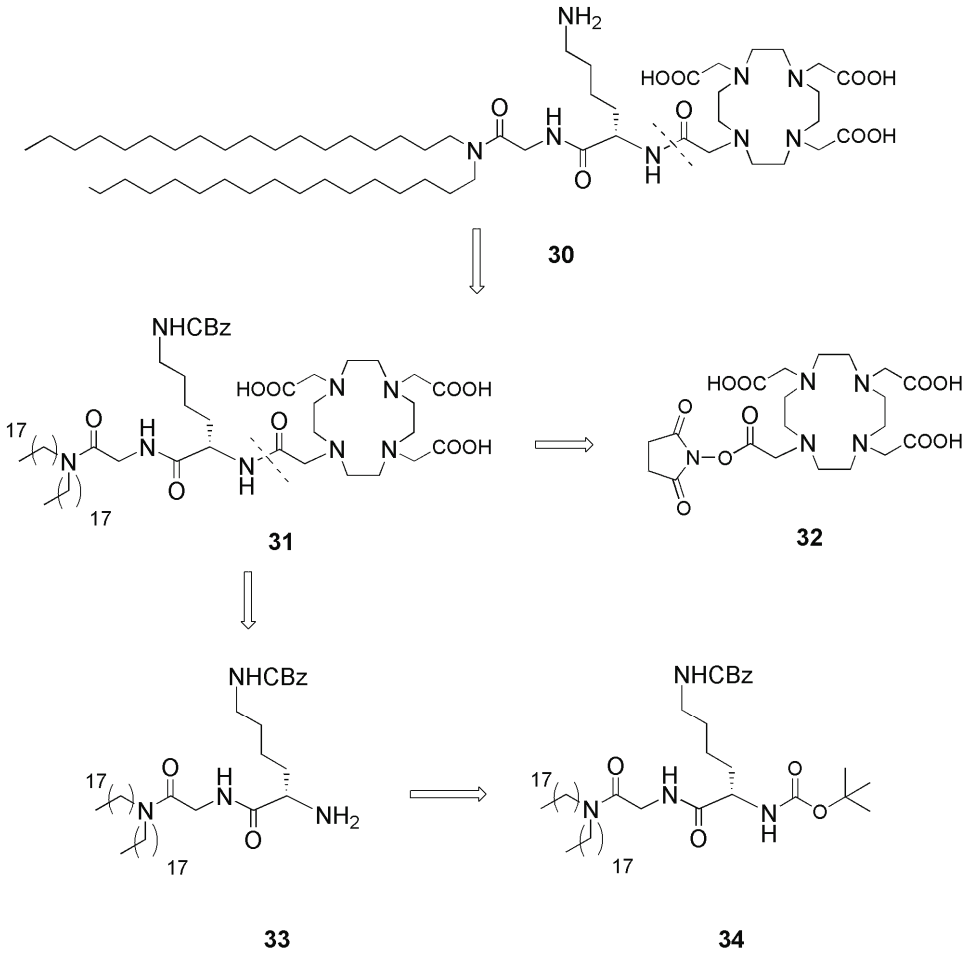


29 **30**

Scheme 9. Retrosynthetic analysis of novel bimodal lipid Gd.DOTA.Rhoda.DSA **27**.

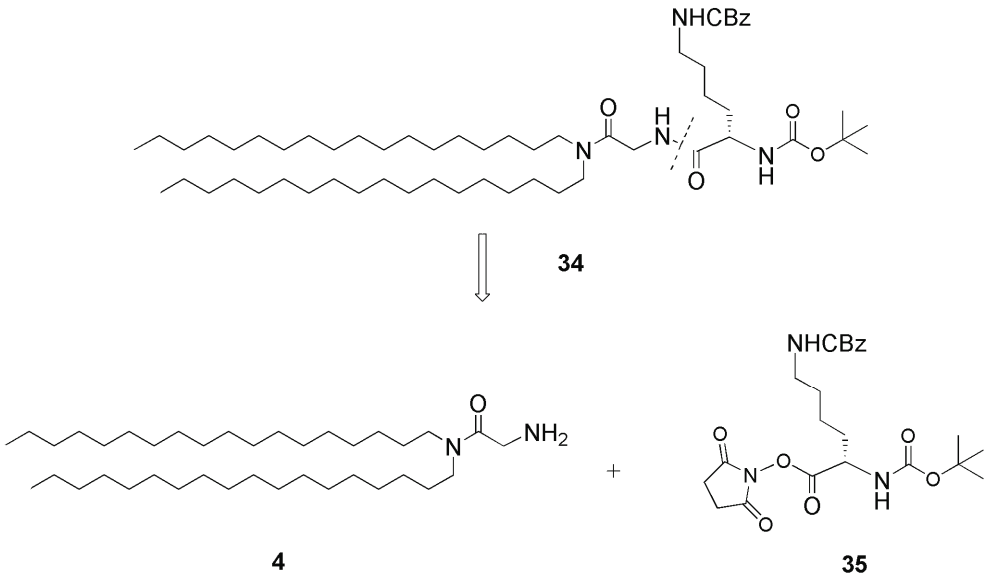
The retrosynthetic analysis of Gd.DOTA.Rhoda.DSA **27** leads initially to the Gd free fluorescent rhodamine lipid **28**. A disconnection of the sulfonamide bond of **28** yields the rhodamine sulfonyl chloride precursor **29** and the primary amine lipid **30** (**Scheme 9**). The same lipidic anchor used for the synthesis of Gd.DOTA.DSA **2** was also used for **27** as it is a robust, fully saturated alky chain that bestows a good level of rigidity and anchorage into the liposome bilayer. The rhodamine sulfonyl chloride starting material is commercially available. We chose to take advantage of this readily available and cheap fluorophore since we had also used the rhodamine fluorophore in previous cell labelling studies *in vitro* and tumour imaging *in vivo* and as such, the use of an identical fluorophore will allow for analogous assessment of the efficacy of the new bimodal lipid also. In addition, the majority of conjugating dyes available are amine-reactive reagents and the rhodamine sulfonyl chloride seemed a suitable fluorophore since the sulfonamide product formed is stable in aqueous conditions.

A retrosynthetic analysis of the amine lipid **30** arrives at the carboxybenzyl (CBz) protected lipid **31** (**Scheme 10**). Here, a disconnection of the amide bond results in the DOTA macrocycle **32** and structure **33**. DOTA.NHS.ester is a commercially available source of the mono-carboxylate activated DOTA (Macrocyclics, USA) and was utilised in this synthesis for ease of reactivity due to the pre-activated carboxylic acid. The CBz protected lipid **33** results from Boc group removal from the orthogonally protected lipid **34**.



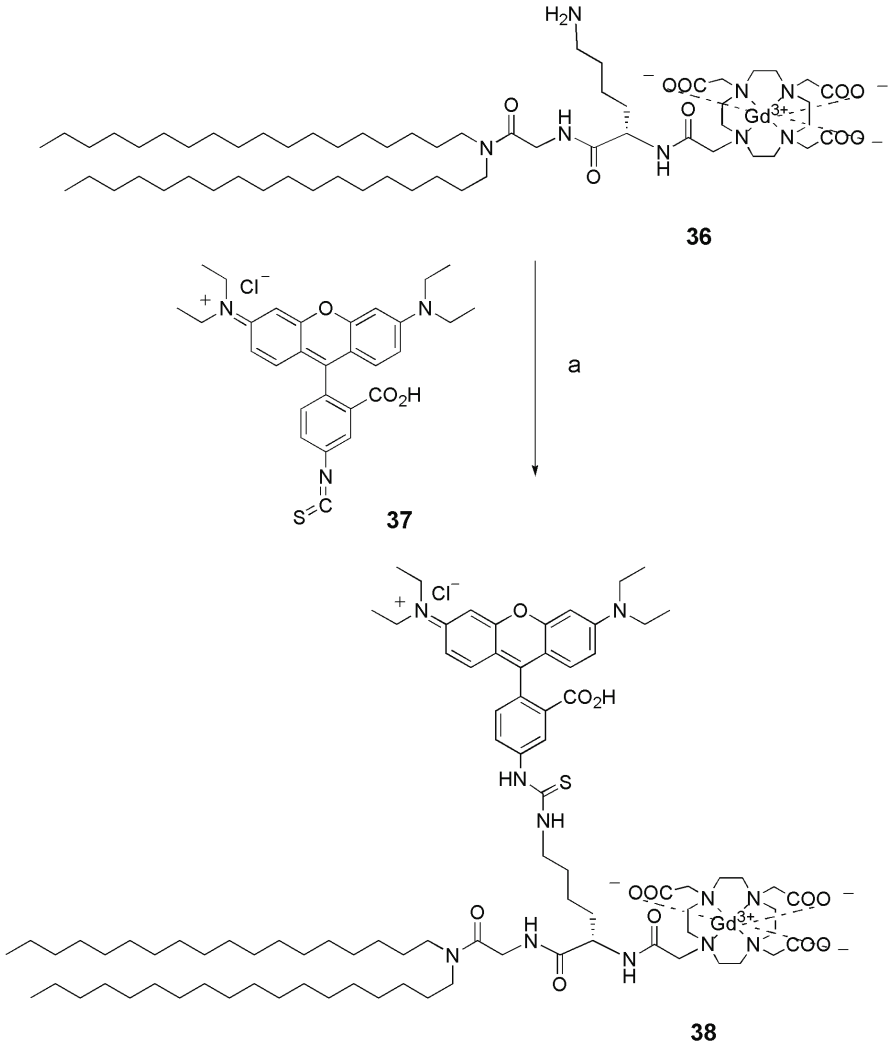
Scheme 10. A retrosynthetic analysis of precursor molecules utilised in the synthesis of Gd.DOTA.Rhoda.DSA **28**.

The Boc and CBz protected DSA lipid **34** is a direct product of reacting the orthogonally protected *N*α-Boc-*N*ε-CBz-L-lysine-*N*-hydroxysuccinimide ester **35** (**Scheme 11**) and the lipidic amine **4** synthesised previously as shown for the synthesis of Gd.DOTA.DSA **2** (**Chapter 2**).



Scheme 11. A restrosynthetic analysis of orthogonally protected lipid **34**.

Initially, prior to the coupling of the Rhodamine sulfonyl chloride fluorophore with lipid amine **30**, a Rhodamine isothiocyanate version of the fluorophore was used since it is one of the most commonly utilised fluorescent probes for conjugation to primary amines, and as such was deemed to be very selective for the modification of the ε-terminal amine of the lysine residue of the gadolinium amine lipid **36** (**Scheme 12**). The Rhodamine isothiocyanate coupling reaction involves attack of the amine nucleophile on the central, electrophilic carbon of the isothiocyanate group which leads to a thiourea bond with no leaving group involved (**Scheme 12**). Lipid **36** has the gadolinium metal complexed in the DOTA previous to the Rhodamine isothiocyanate coupling step. This order was initially adhered to since it has been shown that gadolinium complexation can be significantly hindered due to the presence of a bulky Rhodamine moiety within the vicinity of the polyamino ligand DTPA.[276]



Scheme 12. a) Et_3N, DMF, rt, 24, 30 %.

The synthesis of **38** however, led to poor yields and extremely difficult purification steps. Isothiocyanate compounds react most readily under basic conditions and it was thought that the aliphatic amine of the lysine's ε-amino group is moderately basic and reactive towards most acylating agents, including the Rhodamine isothiocyanate fluorophore. In order to improve the yield of the thiourea product **38**, the pH of the reaction was maintained around 8 and above, for the primary amine to remain mostly deprotonated. However, even the utilisation of various bases, and variations on reaction solvent, time and temperature did not lead to improved yields for this step (see **Table 9**).

Base	Solvent	Temperature (ºC)	Time (h)	Yield (%)
3 eq. Et_3N	MeOH: DCM: 1:1	0	3	20
3 eq. Et_3N	MeOH: DCM: 1:1	0 → rt	12	20
3 eq. Et_3N	DMF	4	12	25
3 eq. Et_3N	DMF	rt	24	30
3 eq. DMAP	DCM	45	12	30
0.5M $NaHCO_3$	DMSO: Pyridine: 50:1	85	24	31

Table 9. Reaction conditions employed for the synthesis of Gd.DOTA.Rhoda.DSA (isothiocyanate product).

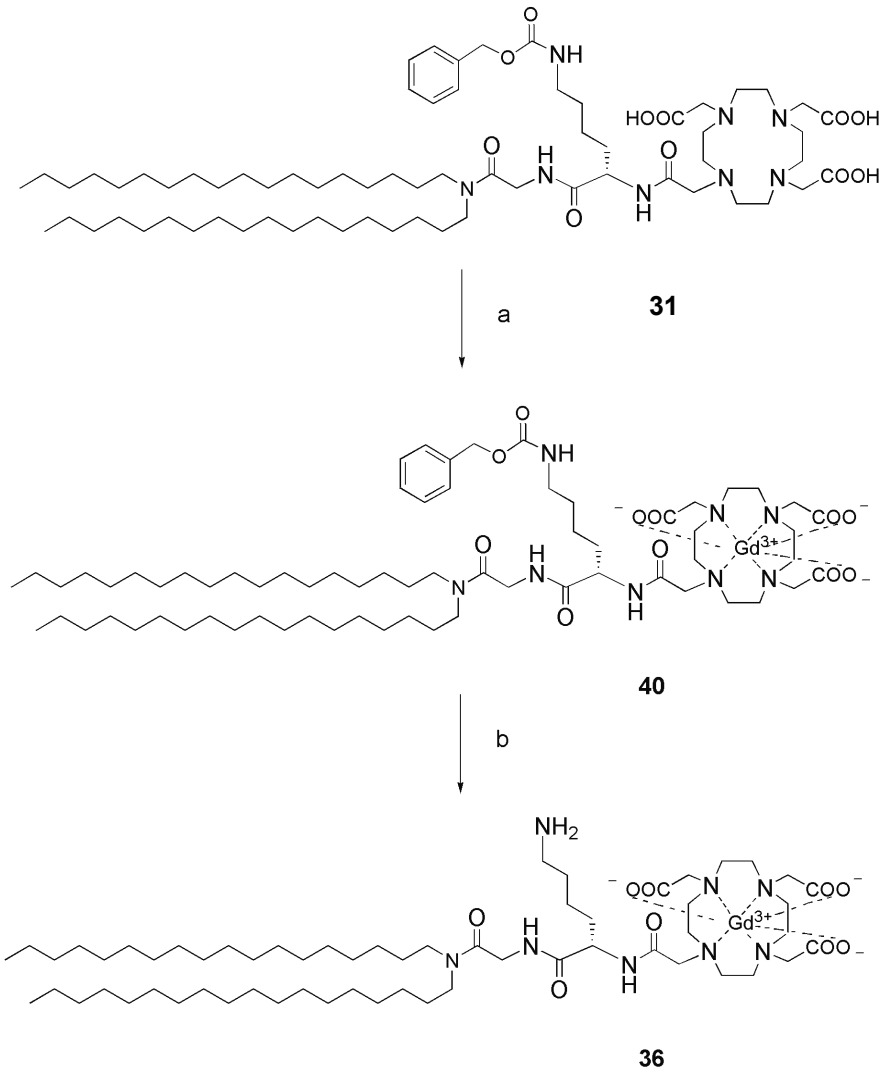
The poor yields for the coupling of the Rhodamine isothiocyanate fluorophore to lipid **36** may be due to the poor solubility of the Gd.DOTA head group (**Scheme 12**). This neutral head group may hinder an effective solvation of the amino group and in fact cause the formation of inverse micelles. Amphiphilic molecules may form micelles with the head groups on the inside and tail groups on the outside. Since the head group of lipid **36** is neutral in charge and non-ionic (no excess charge), there is a possibility that inverse micelle formation is favoured in solution.

Lipid **30** was complexed with Gd using a stoichiometric amount of the chelating agent $GdCl_3$ and heating the reaction in pure water, quantitative yields were obtained and the final compound (**36**) was characterised by ESI-MS and HPLC. The presence of free Gd^{3+} ions was investigated for by using the xylenol orange colourimetric assay and no free Gd ions were detected. In addition, the isotopic peaks of Gd were apparent in the mass spectrum of this compound. The next step was to couple the fluorescent Rhodamine isothiocyanate group, leading to the bimodal fluorescent and paramagnetic lipid **38** (**Scheme 12**). This lipid was also characterised by ESI-MS, HPLC and the xylenol orange assay was used to check for free Gd ions.

The complexation of **31** with gadolinium was achieved with the addition of a stoichiometric amount of $GdCl_3$ to this lipid in pure water and heating at 90 ºC (**Scheme 13**). The Gd complexed product was then characterised using HPLC and ESI-MS, the xylenol orange colourimetric assay revealed no free Gd^{3+} ions post

complexation and the Gd isotopic peaks were apparent in the mass spectrum of this product.

The CBz deprotection of **40** was carried out with H_2 gas and palladium on carbon (**Scheme 13**). This reaction led to very poor yields initially, and a range of conditions were assessed in order to improve the rate of hydrogenolysis (see **Table 10**).



31

40

36

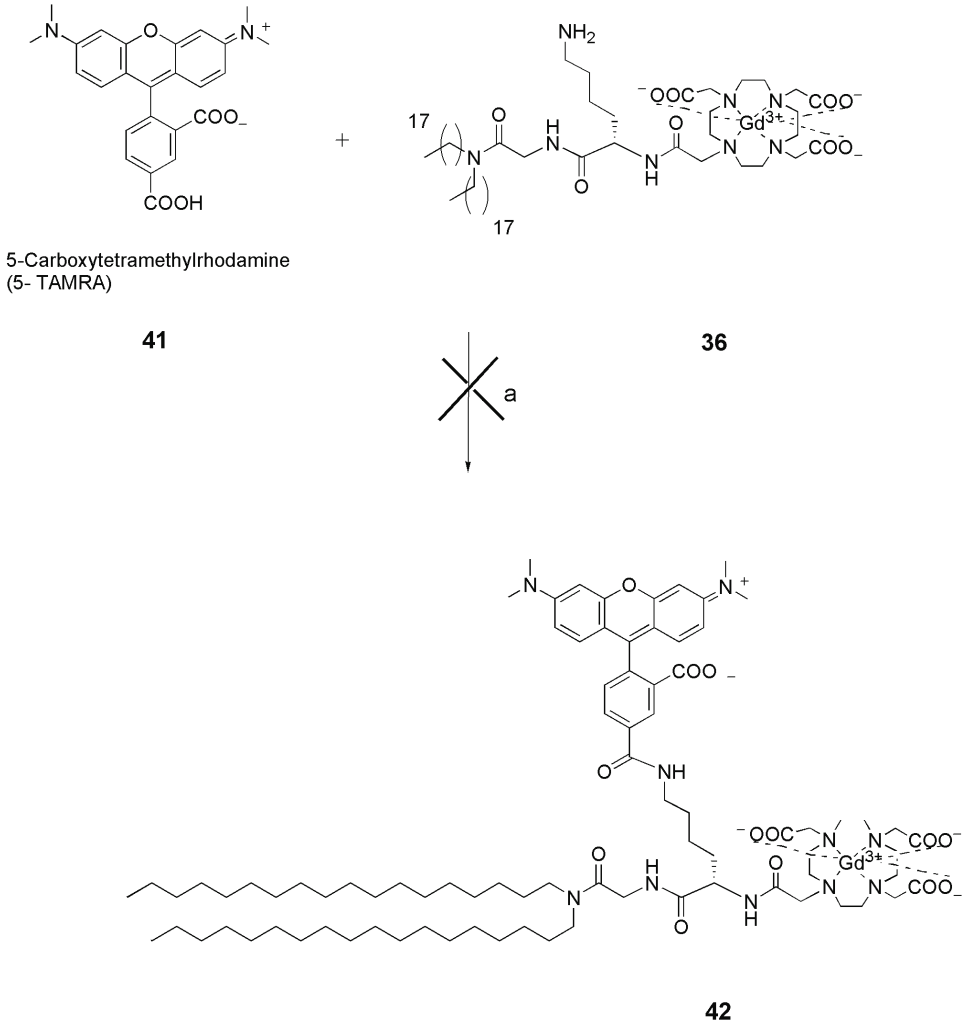
Scheme 13. a) $6H_2O.GdCl_3$, H_2O, 90 ºC, 12 h, quantitative; b) H_2, Pd-C 10%, 1,4 cyclohexadiene, MeOH: H_2O, 60 ºC, 3 h, 60%.

Catalyst	Solvent	Temperature (ºC)	Time (h)	Yield (%)
H_2, Pd-C 10%	EtOH	rt	2	10
H_2, Pd-C 10%	EtOH	50	2	10
H_2, Pd-C 10%	EtOH	rt	17	24
H_2, Pd-C 10%	EtOH: EtOAc: 1:1	rt	17	25
H_2, Pd-C 10%, 1,2 cyclohexene	EtOH	75	12	57
H_2, Pd-C 10% 1,4 cyclohexadiene	MeOH: H_2O: 2:1	60	3	60

Table 10. Hydrogenation conditions employed for CBz protecting group removal (**Scheme 13**).

A major improvement in hydrogenolysis of **40** was achieved by the addition of either 1,2 cyclohexene or 1,4 cyclohexadiene hydrogen donors to the reaction mixture. The chelation integrity of Gd to the DOTA macrocycle was assessed post CBz removal and the chelated Gd ion was found to be intact as confirmed by HPLC and ESI-MS. The isotopic peaks of Gd were also still present, confirming that the use of Pd-C did not lead to any undesirable palladium-gadolinium exchange for instance.

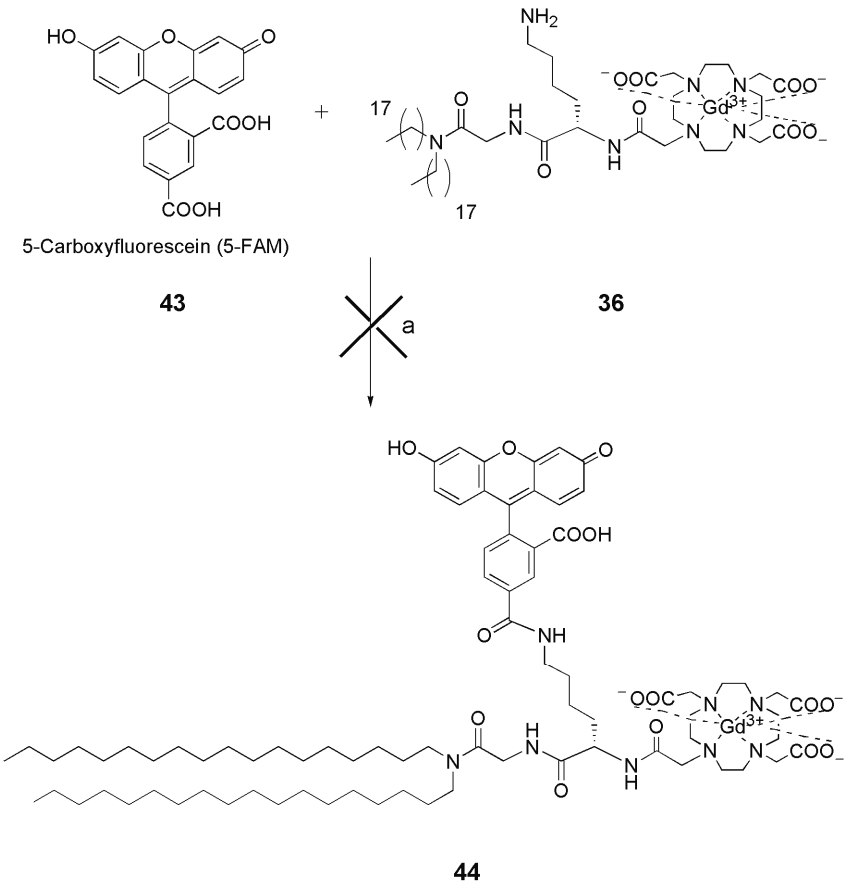
Lipid **36** was coupled further with a range of other fluorescent probes, including carboxytetramethylrhodamine (TAMRA) **41** (**Scheme 14**), carboxyfluorescein (FAM) **44** (**Scheme 15**) and fluorescein isothiocyanate (FITC) **46** (**Scheme 16**).



Scheme 14. a) DMAP, HBTU, CH_2Cl_2, rt, 6 h

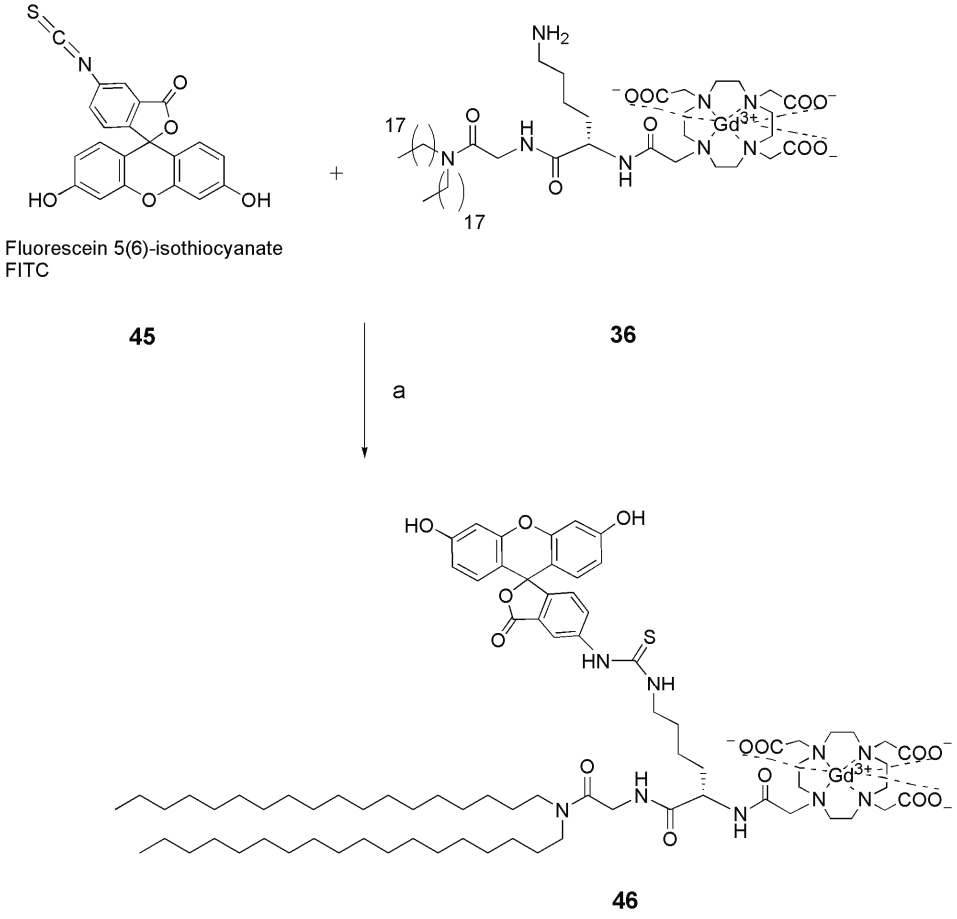
The amide coupling of **41** with **36** was undertaken using HBTU and DMAP as carboxylic acid activators. This reaction did not proceed to completion and was not developed further (**Scheme 14**). It is believed that the activation and subsequent amide coupling of aromatic carboxylic acids of fluorophores such as **41** is often problematic due to the strong delocalisation of the carbonyl electrons with the benzene ring.

A similar lack of amide bond formation was observed when using the carboxyfluorescein fluorophore **43**, no reaction to form **44** took place when HBTU and DMAP were used for the activation of the aromatic carboxylic acid (**Scheme 15**).



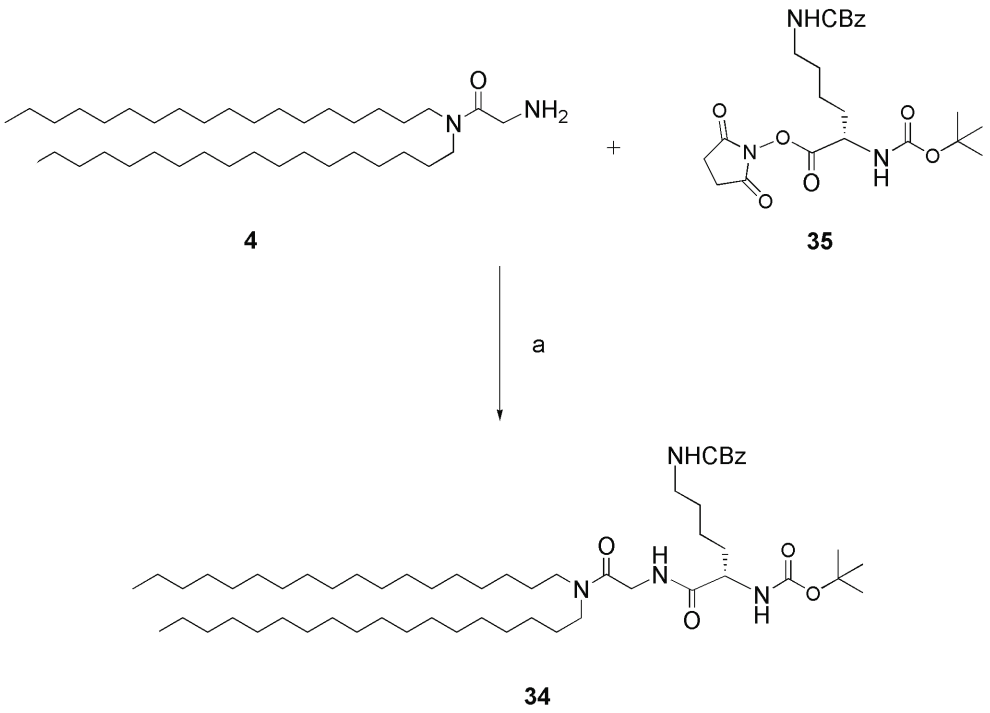
Scheme 15. a) DMAP, HBTU, DMF, 40 ºC, 12 h

In order to also utilise green fluorescence, a fluorescein isothiocyanate (FITC) fluorophore was coupled with the amino lipid **36**, however, the yields for this reaction were poor and quantities obtained were not sufficient for *in vitro* or *in vivo* experimentation using this dual labelled fluorescent lipid (**Scheme 16**).



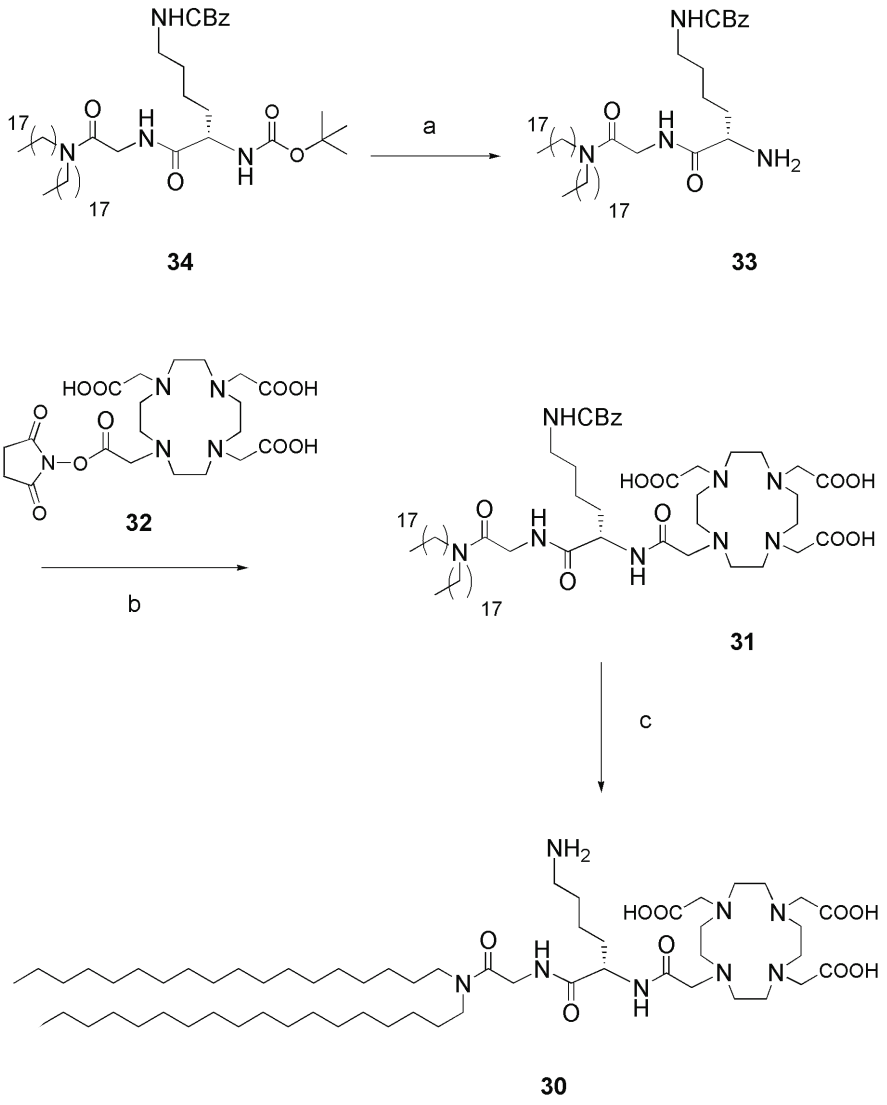
Scheme 16. a) Et_3N, DMF, 4 ºC, 3 days, 25 %

The excitation and emission wavelengths measured for **46** were found to be 497 nm and 535 nm respectively.



Scheme 17. a) Et_3N, CH_2Cl_2, 40 ºC, 5 h, 92%

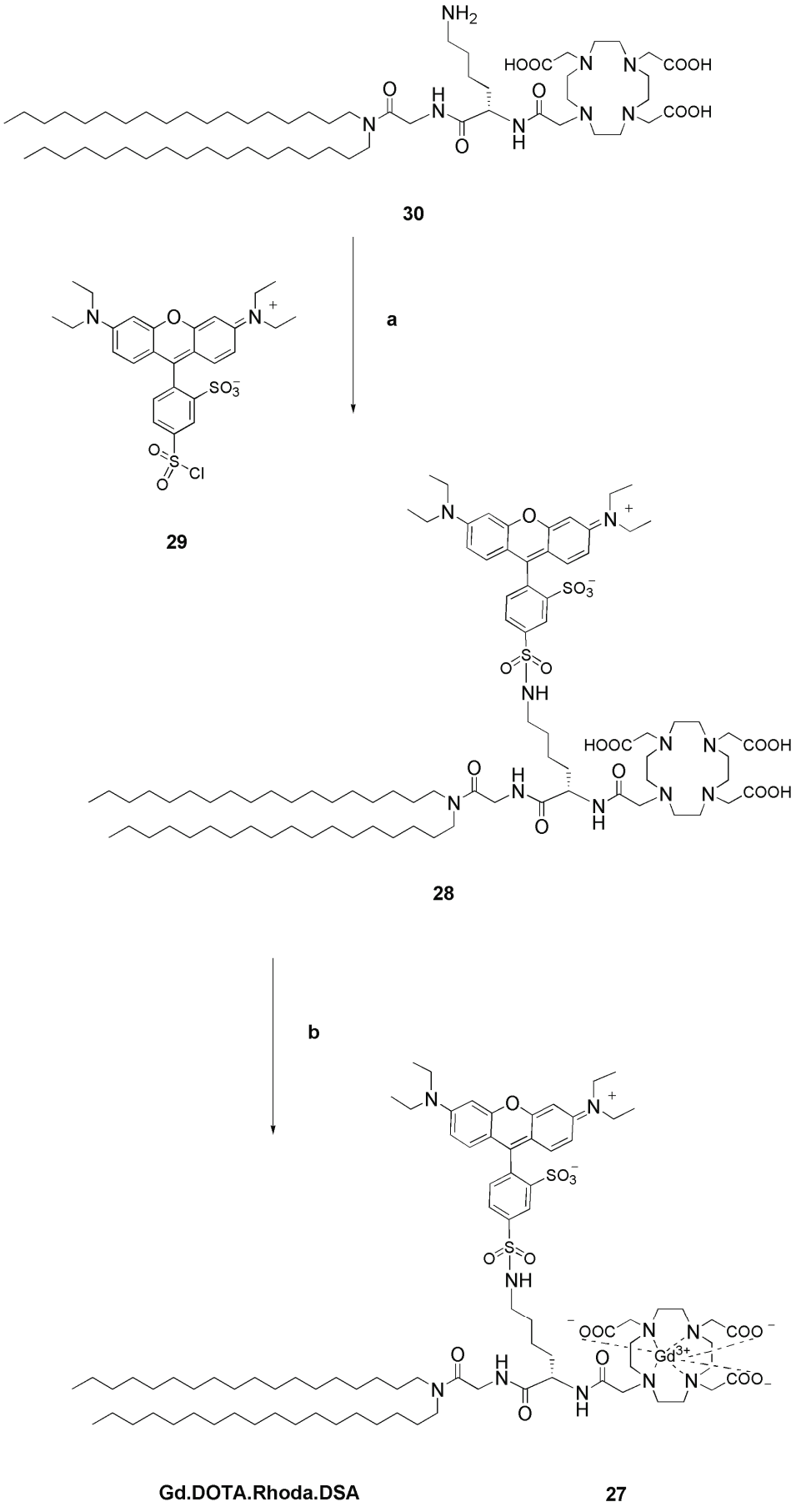
The synthesis of the lipid tail and the lysine linker utilised for the synthesis of the bimodal lipid **27** is shown in **Scheme 17**. The orthogonally protected CBz and Boc lysine linker (**35**) was purchased as the activated NHS ester and reacted with the previously synthesised lipid amine **4** in dry DCM and the protected lipid **34** obtained in good yield and purity (**Scheme 17**).



Scheme 18. a) TFA: CH_2Cl_2: 1:1 v/v, rt, 2.5 h, quantitative, b) Et_3N, CH_2Cl_2, 45 ºC, 12 h, 67%, c) H_2, Pd-C 10%, MeOH: H_2O: 2:1 v/v, 60 ºC, 3 h, 60%.

The Boc protection was then removed using TFA to give the primary amine **33** (**Scheme 18**). This was then reacted with the mono-activated DOTA macrocycle **32** to give **31**. The CBz group was removed using the optimised hydrogenolysis conditions and led to the amine DOTA lipid **30** (**Scheme 18**).

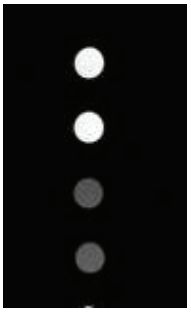
Since the Rhodamine isothiocyanate coupling led to poor yields of the conjugated product **38**, and the complexation of Gd appears to lead to very poor solubility of the head group region, an alternative Rhodamine fluorophore in the form of Rhodamine Lissamine B sulfonyl chloride was utilised in place of **37**. This sulfonyl chloride fluorophore has an extremely high extinction coefficient (up to 93 000 $M^{-1}cm^{-1}$) and forms a sulfonamide linkage with the primary amine of **30**. The synthesis of the novel fluorescent lipid **27** was achieved in excellent yield and purity by using the sulfonly chloride Rhodamine fluorophore **47** in basic conditions (**Scheme 19**). This was then complexed with gadolinium in aqueous conditions to give the bimodal fluorescent and paramagnetic lipid **27** in excellent yields. This bimodal lipid was characterised with ESI-MS, HPLC and its gadolinium isotopic peaks were visible in the MS trace. The presence of free Gd ions was tested for by using the xylenol orange assay and no free Gd^{3+} ions were detected. The excitation and emission wavelengths measured for Gd.DOTA.Rhoda.DSA **27** were found to be 545 nm and 568 nm respectively.



Scheme 19. a) 1% Et_3N, CH_2Cl_2, rt, 12 h, 95%, b) $6H_2O.GdCl_3$, H_2O, 90 ºC, 12 h, quantitative.

4.1.3 MRI Analysis of Bimodal Gd.DOTA.Rhoda.DSA

With the synthesis of the bimodal gadolinium lipid successfully achieved, the T_1 signal enhancement ability of this lipid in water was measured (**Table 11**). Additionally, the r_1 relaxivity of Gd.DOTA.Rhoda.DSA **27** in liposome form was also assessed at 4.7 T. Aqueous solutions of Gd.DOTA.Rhoda.DSA were prepared at the clinically relevant dose of 0.5 mM, and T_1 measurements were obtained using **Eq. 1**. T_1 measurements for controls including a 0.5 mM solution of Gd.DOTA were also obtained.



Sample		T_1 (msec)
1	0.5 mM Gd.DOTA	817.5 ± 93.5
2	0.5 mM Gd.DOTA.Rhoda.DSA	205.8 ± 30.8
3	0.5 mM DOTA.Rhoda.DSA	3735 ± 275.5
4	H_2O	3905 ± 311.3

Table 11. T_1 images and values for Gd.DOTA.Rhoda.DSA **27** in addition to controls.

The T_1 measurement results obtained show the novel bimodal lipid Gd.DOTA.Rhoda.DSA to be an effective T_1 signal enhancer, being 16% more effective than Gd.DOTA (Dotarem®) at reducing bulk water T_1 (see **Table 11**).

A series of neutral PEGylated liposomes were formulated in water incorporating Gd.DOTA.Rhoda.DSA **28**, in addition to the same DOPC and cholesterol lipid components used previously for tumour imaging *in vivo* (liposome formulation **10**). These PEGylated liposomes were prepared for subsequent tumour imaging *in vivo* and as such contained DSPE-PEG_{2000} (**Table 12**). The total Gd concentration in these liposomes ranged between 0.285 and 0.084 μM. The r_1 relaxivity was determined by plotting $1/T_1$ (s^{-1}) with the total Gd concentration (mM) and was measured to be 14 ± 4.605 $mM^{-1}S^{-1}$ (**Figure 74**). This relaxivity is quite high and may be attributed to the PEG polymer incorporated in these liposomes, which renders both steric bulk and additional hydrophilicity to the liposomes. It can be envisaged that due to the large and bulky head group of bimodal Gd.DOTA.Rhoda.DSA **27,** the head group end of the lipid is further exposed on the surface of the liposomes as the Rhodamine moiety will most likely be protruding outwards from the surface of the liposomes.

Liposome Formulation (mol %)					
Gd.DOTA.Rhoda.DSA	**DOPC**	**Cholesterol**	**DSPE-PEG$_{2000}$**	**Initial size (nm)**	**PI**
50	13	30	7	256. 78 ± 23.10	0.85 ± 0.12
40	23	30	7	284.93 ± 3.88	0.20 ± 0.05
30	33	30	7	239.20 ± 6.77	0.53 ± 0.12
20	43	30	7	257.60 ± 7.10	0.64 ± 0.33
10	53	30	7	257.50 ± 22.10	0.89 ± 0.11

Table 12. Liposome formulations used to determine r_1 relaxivity of Gd.DOTA.Rhoda.DSA.

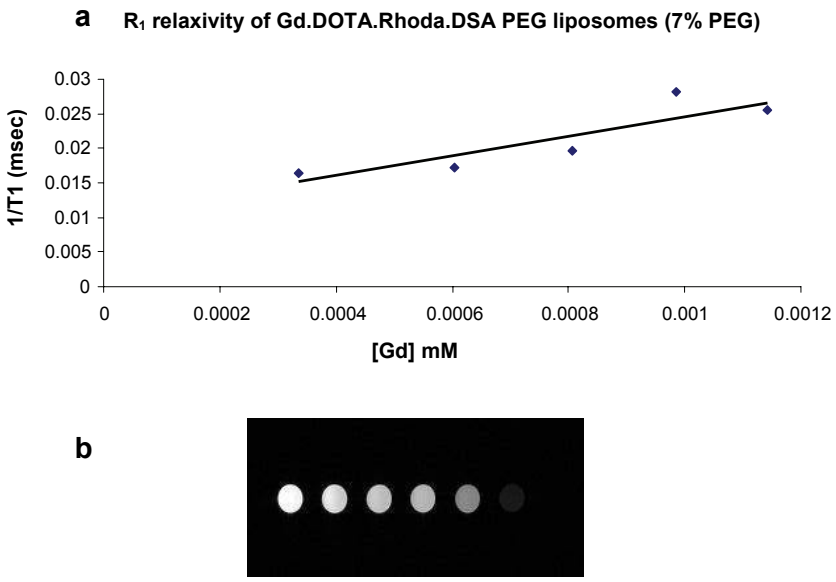


Figure 74. a: R_1 relaxivity for PEGylated neutral Gd.DOTA.Rhoda.DSA liposomes, **b**:T_1-weighted images of Gd.DOTA.Rhoda.DSA liposomes with 5 different Gd concentrations, decreasing left to right (last sample = water).

Gd.DOTA.Rhoda.DSA was shown to have an effective T_1 signal enhancement property and it appears to have a comparable r_1 liposomal relaxivity (PEGylated liposomes) with that of PEGylated Gd.DOTA.DSA liposomes, suggesting that relaxivity is dominated by the Gd.DOTA head group moiety, regardless of the presence of the Rhodamine fluorophore nearby on the same molecule.

A 3D model of Gd.DOTA.Rhoda.DSA is shown in **Figure 75**; here the C-18 saturated alkyl chain extends in to a cone shaped tail structure. The rhodamine moiety is further away from the Gd.DOTA moiety and due to the lysine spacer between the tail and the rhodamine fluorophore; it can most likely protrude out of the liposome surface.

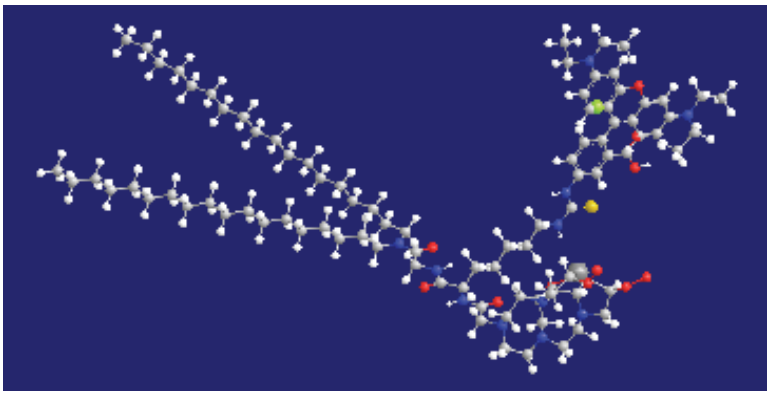


Figure 75. 3D model of Gd.DOTA.Rhoda.DSA

London *et al*. have demonstrated the location of fluorescent lipidic probes with charged groups in model membranes using parallax analysis; a fluorescence quenching method where the amount of quenching induced by nitroxide-labelled phospholipids located at different depths in the bilayer is used to measure fluorophore depth up to 1.4 Å of resolution. [281] It was shown that charged aromatic probes tend to locate at the polar surface of membranes; and due to the charged groups the deep burial of these lipids within the hydrocarbon region of the bilayer is prohibited. These findings also revealed that a charged group will rarely be closer than 16 – 18 Å from the centre of the bilayer, with lipid attached rhodamine occupying a shallow location; 31-55 Å from the bilayer centre.

4.2 Chapter Summary

The bimodal fluorescent and paramagnetic lipid Gd.DOTA.Rhoda.DSA was successfully synthesised. T_1 values and r_1 relaxivity measurements at 4.7 T were conducted using this lipid and data obtained showed this novel bimodal lipid to have excellent T_1 relaxation and relaxivity properties. The fluorescence excitation and emission values obtained for Gd.DOTA.Rhoda.DSA **27** were comparable to that of the free Rhodamine sulfonyl chloride precursor, suggesting that conjugation onto the lipid backbone does not interfere with Rhodamine's fluorescence properties.

5 . *In Vitro and In Vivo Biological Evaluations of Bimodal Gadolinium Lipid - Gd.DOTA.Rhoda.DSA*

5.1 In Vitro Cell Labelling with Gd.DOTA.Rhoda.DSA

The ability to label cells and to visualise these labelled cells using an appropriate imaging modality can be valuable in the tracking of therapeutic cells of interest, such as the imaging of stem cell migration in a stroke model, or the imaging of labelled metastatic cancer cells and their localisation post-injection *in vivo*. As such, novel cell labelling systems such as paramagnetic and fluorescent liposomes developed in this project can be useful in the labelling of and subsequent tracking of a range of cells including therapeutically relevant cells.

We were interested in assessing the cell labelling capabilities of liposomes formulated with the bimodal lipid Gd.DOTA.Rhoda.DSA **27**. For this purpose, based on the successful cell uptake results demonstrated through the use of the cationic lipid CDAN and the neutral helper lipid DOPE, cationic liposomes were formulated with Gd.DOTA.Rhoda.DSA for IGROV-1 cell labelling. Cationic liposomes consisting of CDAN/DOPE/Gd.DOTA.Rhoda.DSA: 50/45/5 mol % (Gd liposome formulation **12**), were formulated in water and their size and pH checked and adjusted. The initiative here was to use a liposome formulation that bore very close resemblance to the successful transfection agent Trojene®, and as such the choice for CDAN and DOPE, both constituents of Trojene®. These lipids were also used at similar molar ratios.

A 5 mol % composition of Gd.DOTA.Rhoda.DSA **27** was used in these liposomes for preliminary cell labelling experiments since this ratio would ensure an adequate and non-excessive amount of rhodamine fluorescence in the cells. IGROV-1 cells were used here too since xenograft tumours from this cell line was previously developed and as such their subsequent use will lead to comparable data. Approximately 5×10^5 IGROV-1 cells were grown and labelled with Gd liposome formulation **12**; the cells were incubated with the liposomes (150 µL, 1.2 mg mL^{-1}, 1.976 µM of Gd) for 8 hours. After the completion of the uptake period, the cells were washed, trypsinised and then spun into cell pellets and imaged at 4.7 T whilst covered in PBS. Interestingly, the labelled cells looked bright pink under normal light and this was corroborated with the MR images obtained of the same cell samples. **Figure 76** presents these findings, where the labelled cells look pink in comparison to unlabelled control cells and the T_1-weighted image of the same cell samples reveals a bright cell pellet.

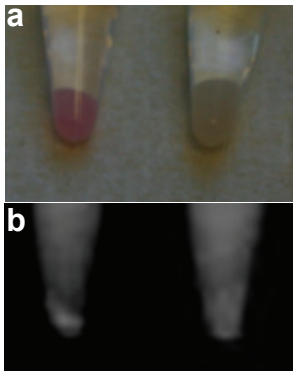


Figure 76. a: Photograph of cells labelled with cationic Gd.DOTA.Rhoda.DSA liposomes, **b**: T_1-weighted image of the cells, vials to the left contain labelled cells and the vials to the right are unlabelled cells alone.

The pink appearance of the IGROV-1 cells is due to either uptake or association of the bimodal liposomes with the cells, and these data are co-validated with MRI findings which revealed a bright cell pellet mass (**Figure 76**, **b**). In order to assess the intracellular uptake of the bimodal gadolinium liposome formulation **12**, microscopy experiments were carried out using this formulation. IGROV-1 cells (2.5×10^5) were grown on cover slips for fluorescence microscopy experiments and were incubated with Gd liposome formulation **12** for 8 h. Post-uptake period the cells were washed and fixed. Fluorescence microscopy of the fixed IGROV-1 cells revealed uptake of these liposomes to be intracellular, ubiquitous and dispersed through out the cytoplasm (**Figure 77**).

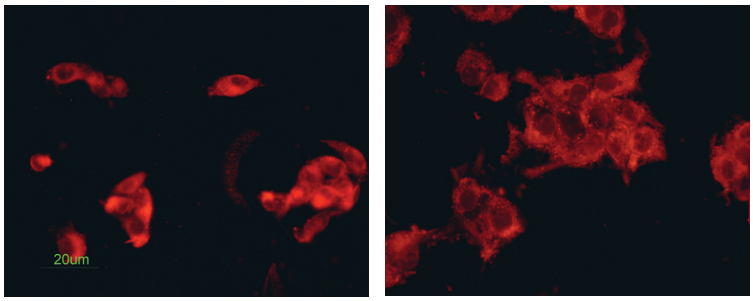


Figure 77. Fluorescence microscopy of IGROV-1 cells labelled with the bimodal cationic liposome formulation **12** (image on the left-side is x 20 and the image on the right is x 40 magnification).

The successful *in vitro* cell labelling of IGROV-1 cells and visualisation by both MRI and fluorescence microscopy revealed Gd.DOTA.Rhoda.DSA **27** to be an effective bimodal cell labelling vehicle and qualitative results were obtained that co-validated the presence of the liposomes within cells by both MRI and fluorescence microscopy.

5.2 In Vivo Solid Tumour Imaging with Gd.DOTA.Rhoda.DSA PEGylated Liposomes

Successful tumour imaging is valuable in the assessment of a range of characteristics of solid tumours, whereby, tumour type, level of aggressiveness, location and response to therapy can be both visualised and quantitated with the use of appropriate probes. A range of bimodal probes have been applied to the imaging of tumours.[282,283] Based on the successful tumour imaging results using the first generation Gd.DOTA.DSA lipid, we were interested in evaluating the use of the novel second generation bimodal Gd.DOTA.Rhoda.DSA for tumour imaging of IGROV-1 xenografts *in vivo*. Nude Balb/c mice were inoculated with IGROV-1 cells where two weeks post administration the tumours had reached an appropriate size for imaging experiments. In order to make a direct comparison with the previously formulated PEGylated gadolinium liposome **10**, the exact same formulation was also used, with Gd.DOTA.Rhoda.DSA in place of Gd.DOTA.DSA. This gave liposome formulation **13**; Gd.DOTA.Rhoda.DSA/DOPC/Chol/DSPE_PEG_{2000}: 30/33/30/7 mol % (formulated at 15 mg mL^{-1} of total lipid content). Baseline MR images were obtained pre-injection, of the tumour bearing mice, after which a 150 µL solution of PEGylated gadolinium liposome **13** (containing 0.613 µM of Gd) was injected via the tail vein and the mice imaged at 2, 14 and 24 h post-injection at 4.7 T. A further interesting observation was that, upon immediate injection of these liposomes, the mice turned bright pink, initially in their extremities and subsequently throughout their body. This effect persisted for approximately 30 min, and demonstrates the rapid blood circulation of the liposomes prior to clearance and/or extravasations.



Figure 78. Balb/c nude mice; mouse on the left has been injected with Gd.DOTA.Rhoda.DSA liposome **13**, mouse on the right had no injection.

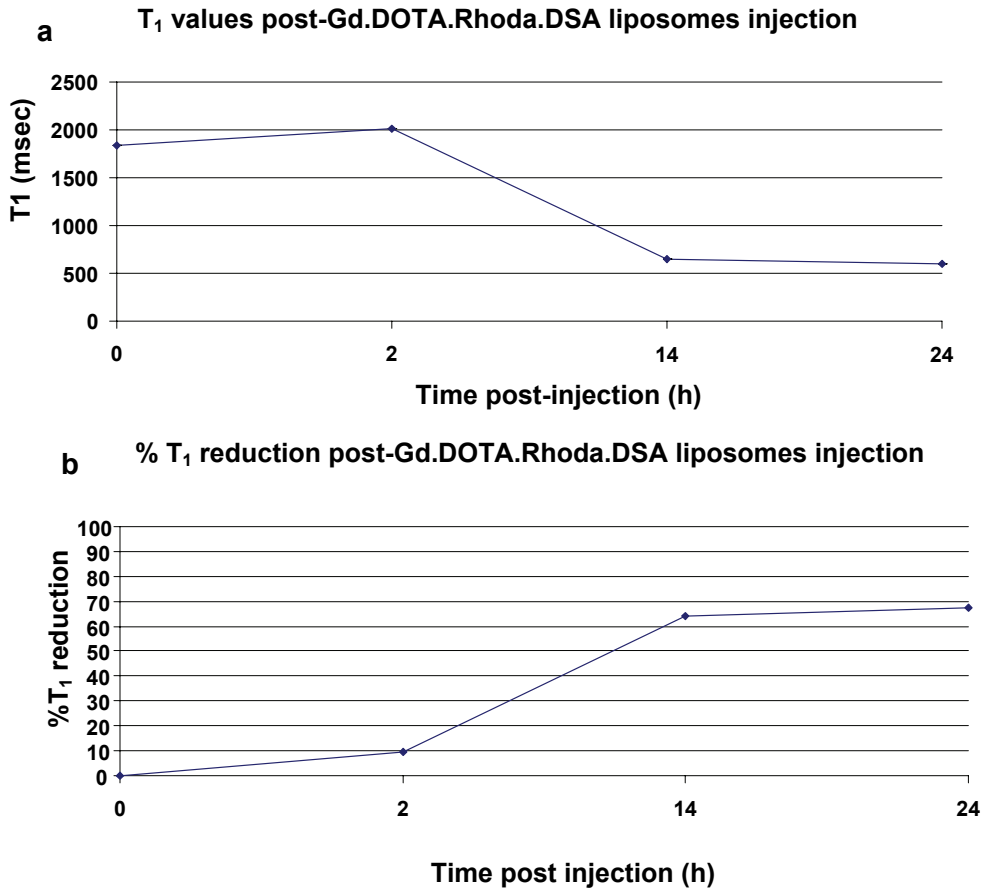


Figure 79. Tumour T_1 measurements post injection of Gd.DOTA.Rhoda.DSA liposome formulation **13**. **a**: Tumour T_1 values at 0, 2, 14 and 24 h post administration of liposomes. **b**: Tumour signal enhancement calculated as percentage of T_1 signal enhancement compared to baseline (at 4.7 T).

The measured T_1 relaxation values from the tumour areas revealed an excellent level of tumour signal enhancement of up to ~65 % at 14 h post injection of liposomes **13**, and this signal enhancement was maintained up to the 24 h end-point (**Figure 79**, **b**). These results show the effectiveness of PEGylated liposomes formulated with Gd.DOTA.Rhoda.DSA for tumour MRI and reveal their tumour signal enhancement ability to be superior (even at half the dose used) to PEGylated gadolinium liposomes formulated using Gd.DOTA.DSA (formulation **10**, see section **3.3**). This accelerated rate of accumulation in the tumour tissue may be attributed to the effectiveness of Gd.DOTA.Rhoda.DSA in becoming "trapped" in tumour tissue, or may be attributed to the incorporation of this lipid within tumour cell membranes, given the hydrophilicity of the Rhodamine fluorophore moiety. T_1-weighted images of axial tumour slices were also obtained and revealed the images taken at the 14 h and 24 h time points to be brighter than the baseline and 2 h post-injection images (see **Figure 80**).

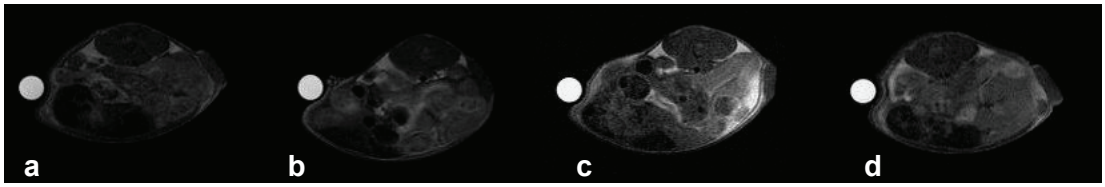


Figure 80. T_1-weighted tumour images of Balb/c mice injected with PEGylated Gd.DOTA.Rhoda.DSA liposome formulation **13**. **a**: Baseline scan prior to injection, **b**: 2 h post-injection, **c**: 14 h post-injection and **d**: 24 h post injection at 4.7 T.

After the 24 h post-administration, the mice were sacrificed and the tumours excised, frozen and sectioned for histology. Fluorescence microscopy of the sectioned tumour slices revealed a high level of fluorescence signal in the tumour tissue (**Figure 81**). These results validate the MRI results presented in **Figure 79** and show the ubiquitous presence of the PEGylated liposomes and therefore Gd.DOTA.Rhoda.DSA lipid in the tumour tissue.

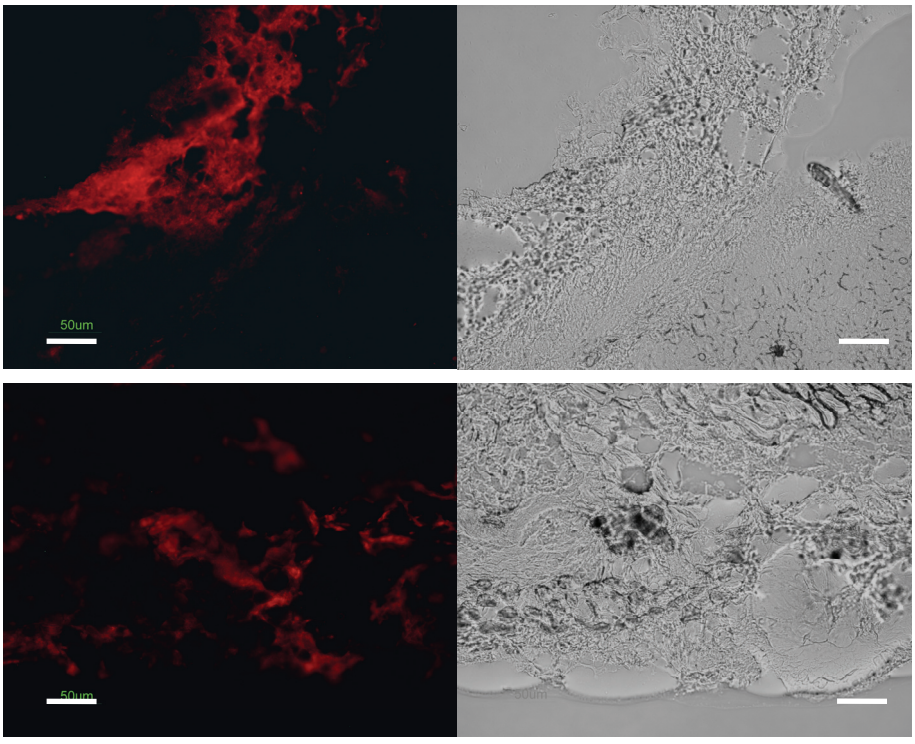


Figure 81. Fluorescence microscopy images of sectioned tumours (7 µm thick) post Gd.DOTA.Rhoda.DSA liposomes injection. The images on the left are red fluorescent images and the images on the right hand side are corresponding bright field images (x 40, bar represents 50 µm).

The fluorescence pattern observed from the sectioned tumour tissue post liposome **13** administration appears to be more uniform and spread-out throughout the tumour tissue (**Figure 81**). This pattern is also different to the fluorescence observed post injection of liposome formulations **10** and **11**, where more hyperintense and localised fluorescence signal was observed. Images obtained and presented in **Figure 81** may support the idea that the Gd.DOTA.Rhoda.DSA lipid is able to incorporate within the cancer cell membranes. However, further confocal microscopy studies are necessary to elucidate more information on the precise localisation of PEGylated bimodal liposomes formulated with the bimodal lipid Gd.DOTA.Rhoda.DSA **27**.

5.2.1 Chapter Summary

The novel bimodal fluorescent and paramagnetic lipid Gd.DOTA.Rhoda.DSA was utilised for the *in vitro* cell labelling of IGROV-1 human ovarian cells, and was shown to be an effective IGROV-1 tumour T_1 signal enhancer, producing a 65 % signal enhancement of tumour tissue 14 h post injection. This T_1 signal enhancement of tumour tissue was maintained up to the 24 h experiment end-point.

These findings were co-validated successfully in a bimodal manner using both fluorescence microscopy of histological tissue and real-time MRI of tumour bearing mice.

6 . *Work Towards Trimodal Gadolinium Lipids*

6.1 ^{19}F MRI Agents

Given that the Larmour frequencies for both ^{1}H and ^{19}F nuclei are close, the imaging of agents containing both these nuclei can be achieved on the same MRI scanner. Fluorine MRI has recently gained much interest within the field of molecular imaging, as so called “hot spot” imaging is made possible with the use of agents such as perfluorocarbon emulsions. Since background ^{19}F signal is absent in most body tissue apart from teeth, ^{19}F based spectroscopy and/or MRI can provide extremely unique signatures. Fluorine signals can be intrinsically quantitated based on ^{19}F spectroscopy and can be used to report the actual concentration of particles within a given region. This data can then be corroborated with ^{19}F MRI where spatial and anatomical information may be obtained.

Fluorine imaging agents are now under investigation for a range of molecular imaging applications.[284] Fluorine MRI has mostly been carried out with the use of perfluorocarbon emulsions where very high numbers of fluorine atoms are present. Perfluorocarbon emulsions are colourless and odourless liquids that are denser than water and capable of dissolving physiologically important gases such as oxygen and carbon dioxide.

Fluorine imaging may be hampered due to the requirement for very high ^{19}F concentrations in order to improve image resolution. Perfluorooctanoic acid ($C_7F_{15}COOH$) has been encapsulated into liposomes and it was shown that the lowest concentration necessary to visualise distribution of this agent *in vivo* is approximately 1 mmol/kg of tissue. [285]

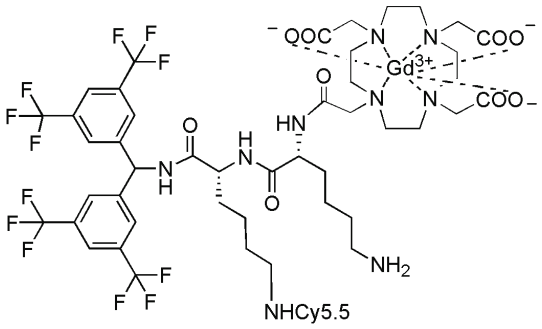
Liposomal based ^{19}F MRI has been achieved by Oishi *et al*. who have developed pH-sensitive PEGylated nanogels constructed with tethered PEG chains and a polyamine gel core containing ^{19}F compounds.[286] These agents which act as specific smart ^{19}F MRI probes showed remarkable on/off MR signal in response to the extracellular pH (6.5) of the tumour environment at very low concentrations of ~ 55 μM. This suggests that liposomal based ^{19}F MRI is a possibility, with the potential of incorporating thousands of fluorine molecules in a single macromolecular structure.

6.1.1 Towards Trimodal ^{19}F Paramagnetic and Fluorescent Lipids

The efficient visualisation of signals from imaging probes used in molecular imaging of disease states such as cancer is of great value for the assessment of disease gravity and response to treatment. A trimodal probe, capable of producing three signatures at the same time can be an attractive tool for the visualisation of difficult *in vivo* aberrant biological processes such as the imaging of metastatic cancer cells where a high signal to noise ratio is required and desirable.

To this end, work towards the synthesis of a trimodal imaging probe was undertaken, which included the attachment of fluorescent, paramagnetic and fluorine moieties onto a single framework.

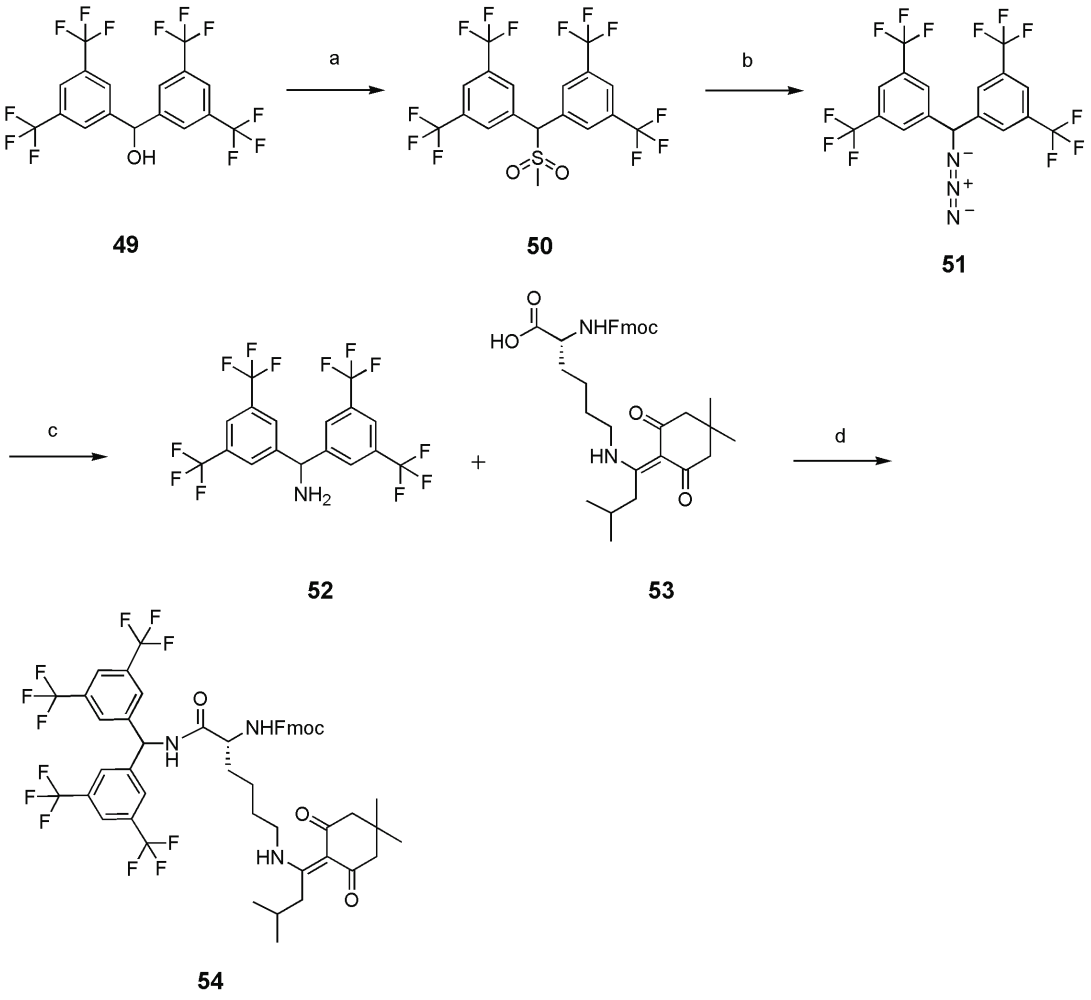
The trimodal head group shown in **Figure 82** was designed with the ultimate aim to couple the primary amine to the distal end of a PEG tethered lipid, yielding a trimodal PEG lipid for incorporation into liposome formulations. Alternatively this trimodal "war head" may be conjugated to a short PEG linker and post-coupled onto the surface of suitable liposomes bearing an appropriate functional group for conjugation.



48

Figure 82. A trimodal probe bearing a fluorine moiety for ^{19}F MRI and spectroscopy, a Gd.DOTA moiety for contrast agent MRI and a Cy5.5 NIR dye for fluorescence imaging.

The forward synthesis towards the trimodal probe **48**, involved the initial conversion of the *tetrakis*-trifluorobenzhydrol to the amine compound **52** (**Scheme 20**). First the alcohol was converted into a good leaving group by reaction with methanesulfonyl chloride in the presence of triethylamine to give the methanesulfonate ester **50**. This was then reacted with an excess of sodium azide in DMF to yield the azide product **51**.



Scheme 20. a) Et_3N, MsCl, CH_2Cl_2, rt, 12 h, 60%, b) NaN_3, DMF, 80 ºC, 12 h, 49%, c) PPh_3: H_2O, THF, 70 ºC, 12 h, 40%, d) DMAP, HPTU, DMF, 40 ºC, 12 h, 60%.

Azide **51** was then reduced to amine **52** utilising the Staudinger Reduction conditions. Using this mild reduction, azides may be converted to amines as an alternative to the use of hydrogenation. The mechanism for this reaction is given in **Figure 83**. Here,

triphenylphosphine initially reacts with the azide in order to generate a phosphazide which subsequently loses N_2 to give an iminophosphorane. Aqueous work up of this intermediate leads to the amine and the stable phosphine oxide.

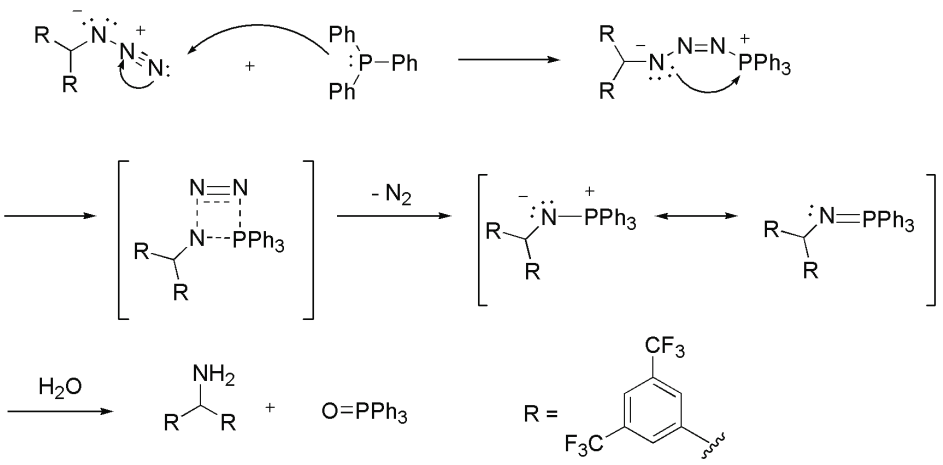
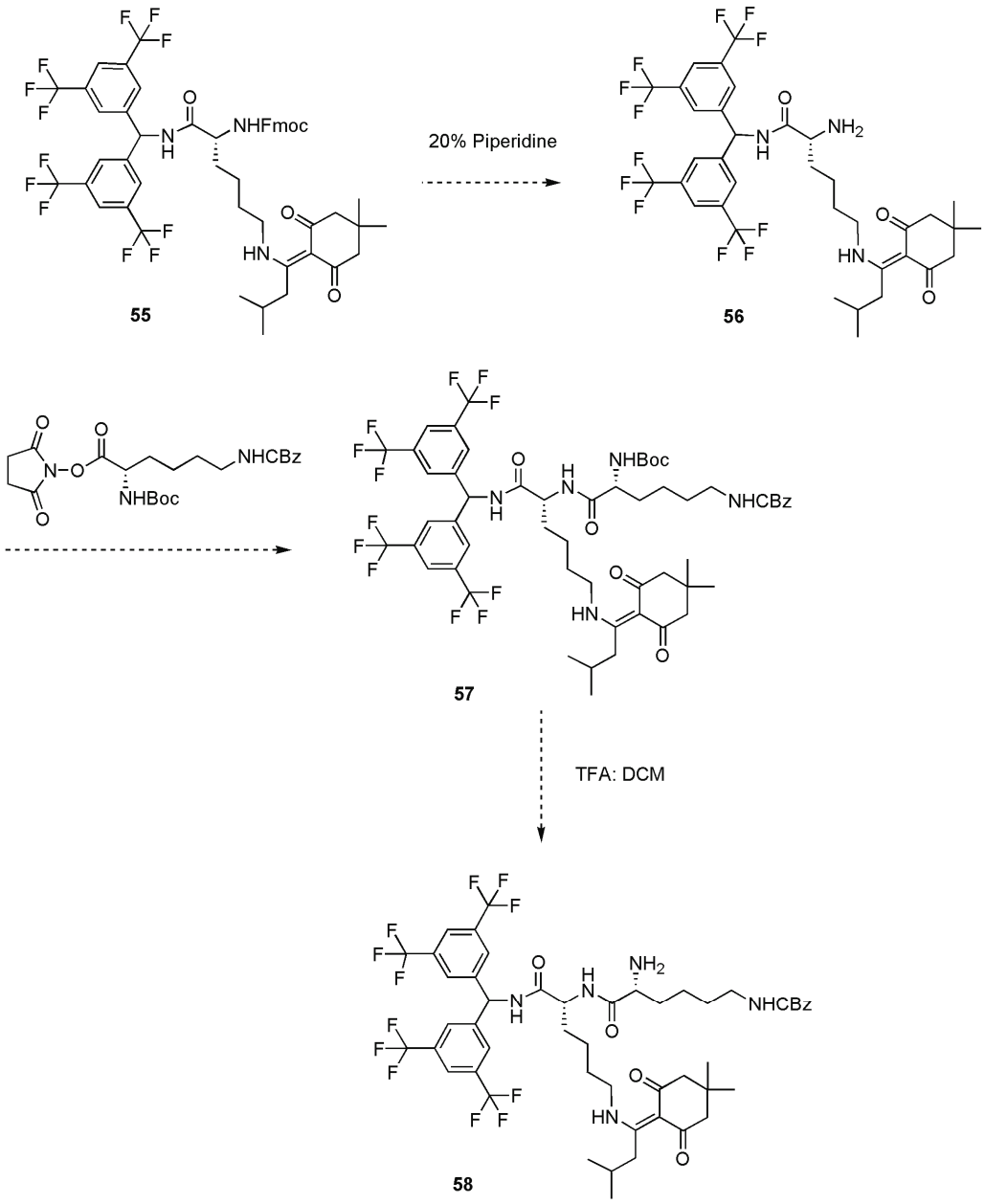


Figure 83. Mechanism for the Staudinger Reduction of an azide to an amine.

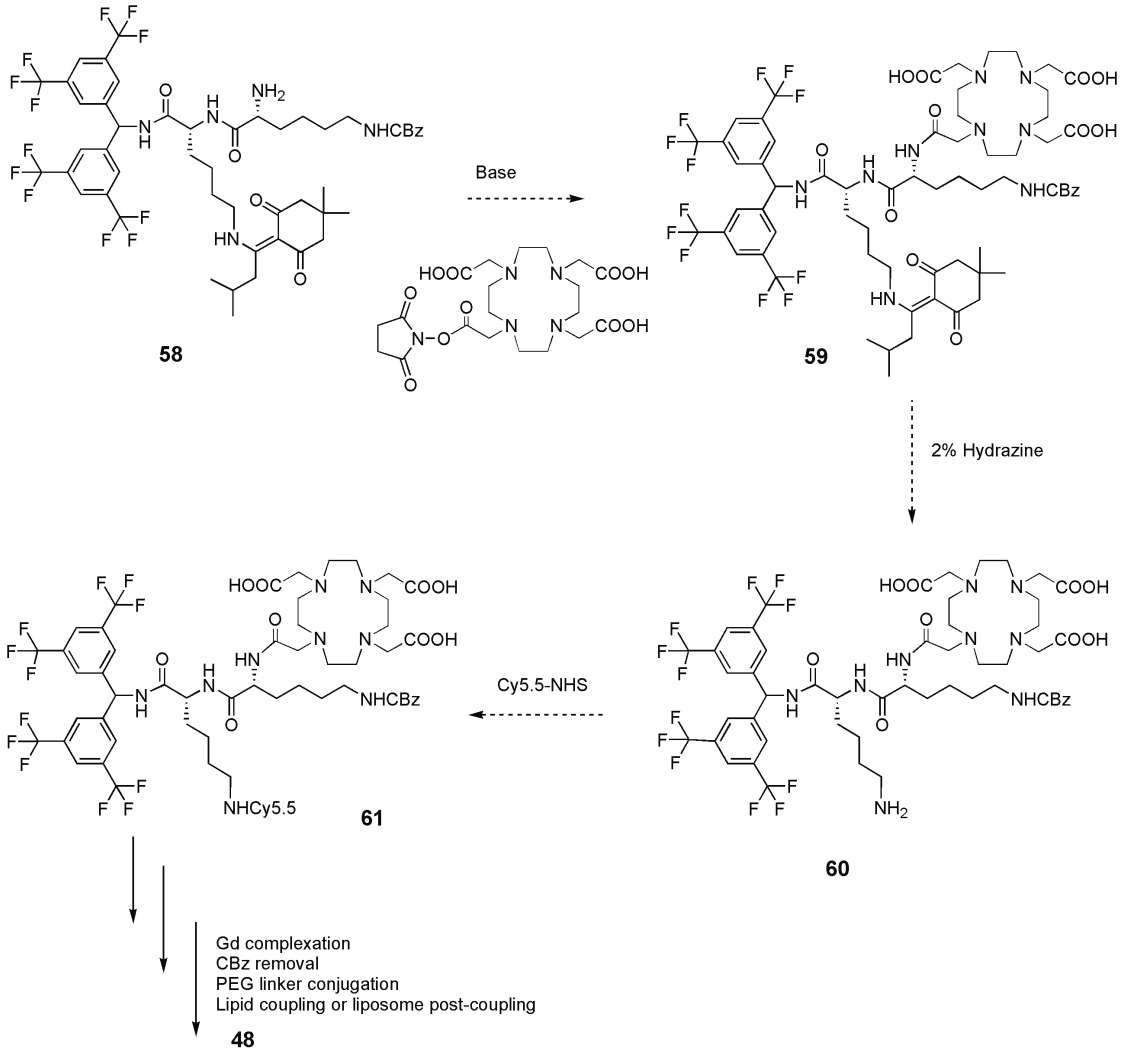
The orthogonally protected *tetrakis*-trifluorobenzamide **54** was obtained by reaction of the carboxylic acid linker **53** with the primary amine of **52** under typical amide bond synthesis conditions, using the carboxylic acid activators HBTU and DMAP. It was also noted that reaction yields for the series of transformations shown in **Scheme 20** could not be improved upon further. This may be due to the steric hindrance of the bulky trifluorobenzyl groups flanking the various methylene bonded functional groups.

Further reactions towards the synthesis of **48** are shown in **Schemes 21** and **22**. The Fmoc protection of **55** may be removed by reaction with 20 % piperidine, yielding compound **56**. The coupling of the CBz and Boc protected lysine linker in dry DCM should yield **57** in good yields. Here, a facile Boc deprotection in acidic conditions would give **58** (**Scheme 21**).



Scheme 21. Proposed scheme towards the synthesis of tri-protected precursor **58**.

Compound **58** can be reacted with the commercially available DOTA.NHS ester to give the DOTA precursor **59**. Treatment with 2% hydrazine results in the removal of the ivDde protecting group rendering the primary amine product **60** which can be reacted with a NIR Cy5.5 NHS ester to give **61** (**Scheme 22**). Ensuing Gd complexation, CBz deprotection, and PEG lipid conjugation provides **48** which can be used in a range of coupling reactions.



Scheme 22. Proposed scheme towards the synthesis of trimodal head group **48**.

Using trimodal head group **48**, Gd enhanced MRI, ^{19}F spectroscopy, ^{19}F MRI and *in vivo* fluorescence imaging may be achieved. It is expected that the relaxivity of liposomes coupled onto PEG linked **48** will be high, due to the hydrophilic nature of PEG and also due to the added macromolecular effect as a result of post-coupling of **48** to liposomes surfaces.

7 . *Conclusions and Future Directions*

7.1 Conclusion

Two novel gadolinium lipidic probes were designed and synthesised. Initially a unimodal paramagnetic lipid Gd.DOTA.DSA was synthesised and its MRI signal enhancement measured. At the clinically relevant concentration of 0.5 mM in aqueous solutions, this lipid was found to compare favourably with the most commonly used clinical contrast agent Magnevist®. The relaxivity of this lipid once incorporated into liposomes was also assessed and was found to be comparable to similar paramagnetic liposomal systems at 4.7 T, and 8 fold higher than the relaxivity of the free lipid in solution.

Bimodal cationic liposomes (both fluorescent and paramagnetic) were formulated with Gd.DOTA.DSA and the molar ratio of this lipid in these liposomes was optimised so that an ideal non-toxic formulation could be identified, capable of maximum Gd delivery into cells. Using HeLa cells, it was shown that between 21-35 % of the gadolinium liposomes were taken up into cells which translated to a 65% signal enhancement of labelled cells, compared to non-labelled cells. The toxicity of these optimised gadolinium liposomes was assessed to be < 10% of overall cell death. Confocal microscopy post cell labelling using HeLa cells, revealed uptake of these liposomes to be intracellular and dispersed throughout the cytoplasm. The bifunctionality of these liposomes was also shown with the successful encapsulation of plasmid DNA encoding for luciferase. This transfection result looked promising and was comparable to expression levels obtained with a commercial transfection agent. These gadolinium liposomes show promise as both cell labelling and transfection agents and may be developed further.

A limitation here has been the testing of gadolinium liposomes formulated with Gd.DOTA.DSA only on a single HeLa human ovarian cell line. Future work could involve the further optimisation of the cell labelling liposome formulations towards a more “universal” formulation, capable of uptake into a range of cell lines.

The novel Gd.DOTA.DSA lipid was also used to formulate PEGylated liposomes for *in vivo* tumour imaging. Physical characteristics of these liposomes were extensively studied, whereby their serum aggregation, zeta potential and size were assessed. The inclusion of a fluorescent lipid in the liposome formulation produced bimodal liposomes which were then used to image xenografts in mice. Due to the EPR effect of tumour tissue, the successful accumulation of these nanoparticles was shown and

effective tumour signal enhancement post-injection was observed. These liposomes were shown to have excellent *in vivo* circulation properties, whereby due to their ~100 nm size, they were able to clear the liver and circulate in the blood for over 12 h, gradually accumulating in the tumour tissue through leaky vasculature. The tumour signal measurements were taken 24 h post-injection of the liposomes and shortly before the mice were sacrificed; these promising tumour signal enhancement data suggest the need for longer imaging windows, where a longitudinal imaging of the tumours post-injection of up to 3-7 days would be appropriate. In addition, further experiments could include comparisons with control clinically used contrast agents such as Magnevist® or Dotarem®, as well as established tumour imaging agents.

In order to improve the specificity of PEGylated liposomes formulated with Gd.DOTA.DSA, use was made of a targeting ligand in the form of the folate molecule, which is the natural ligand for folate receptors. This ligand was incorporated into the liposome formulation at 3 mol %. Since these folate receptors are highly over-expressed on cancer cells, the effect of signal enhancement post-administration of these targeted liposomes in tumour bearing mice was investigated. It was shown that just within 2 h post injection of the folate-targeted gadolinium liposomes, a 65% enhancement in tumour T_1 was observed compared to signal achieved with non-targeted liposomes alone (only ~ 13%). This very promising result suggested that folate targeting accelerates the rate of tumour accumulation of these liposomes and the persistence of T_1 signal up to the 24 h end-time point suggests that there may be a tumour accumulation equilibrium effect present, whereby accumulated particles are retained and occupy available accumulation sites. Tumour signal enhancement of both targeted and non-targeted gadolinium liposome formulations plateaus between 60-70% at 24 h post injection. This may be due to the Gd saturation level for the IGROV-1 xenografts. Further studies using the folate PEG tethered ligand could involve the optimisation of ligand to liposome ratio, since it has been shown that liposomal targeting ligands may actually be most effective *in vivo* when used at < 1 mol% of overall liposome formulation.

A second bimodal fluorescent and paramagnetic lipid, Gd.DOTA.Rhoda.DSA was also synthesised and was used to successfully label IGROV-1 cells *in vitro* and image tumours *in vivo*. Tumour results post injection of PEGylated liposomes formed with this lipid revealed these liposomes to be extremely effective at reducing tumour T_1 signal, with a 65% signal enhancement observed at 14 h post injection. In addition, these liposomes were injected at half the concentration injected for the non-targeted

liposomes formulated using Gd.DOTA.DSA. This suggests that the Rhodamine moiety of Gd.DOTA.Rhoda.DSA may be aiding the accumulation of liposomes in the tumour tissue, and could be as result of tumour cell membrane incorporation of Gd.DOTA.Rhoda.DSA.

Future work using this lipid could involve the assessment of liposome biodistribution of liposomes made with this lipid by optical *in vivo* imaging methods. For this, the conjugation of a NIR dye (see **Figure 82**) in place of the rhodamine moiety would be appropriate.

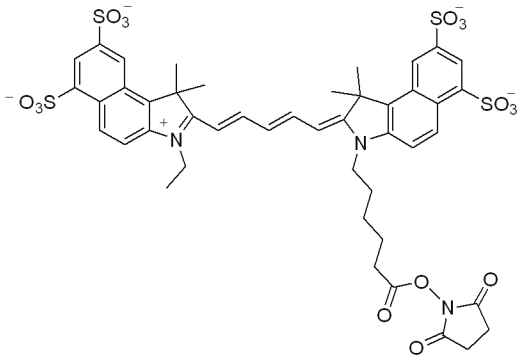


Figure 84. A NIR dye; Cy5.5 with superior fluorescence properties (λex: 673 and λem: 692)

A major limitation of optical methods is the low tissue penetration of light and as such, the current bimodal Gd.DOTA.Rhoda.DSA lipid could only be of value in histology. However, the use of the Cy5.5 NIR dye in place of the rhodamine fluorophore can increase the depth of fluorescence signal observed and would be an improvement on the design of these bimodal fluorescent and paramagnetic lipids.

Work towards the synthesis of a trimodal imaging probe was also initiated. This probe is expected to lead to an excellent multimodal imaging strategy whereby three types of signal may be observed as a result of probe localisation; ^{1}H MRI contrast enhancement and ^{19}F MRI/MRS can be achieved, as well as a fluorescent signature from the fluorophore. Future directions for this project could involve the completion of synthesis of this timodal probe, and its subsequent post-coupling to the surface of similar *in vivo* liposomes used for tumour imaging so far. These trimodal liposomes will posses a high degree of sensitivity due to the NIR probe and facilitate fluorescence imaging paving the path for fluorescence molecular tomography as well.

8. *Experimental*

8.1 General Information

8.1.1 Materials

N[1]-cholesteryloxycarbonyl-3,7-diaza-1,9-diaminonane (CDAN), 1,2-Dioleoyl-sn-glycero-3-phosphoethanolamine (DOPE), phosphatidylethaolamine-lissamine rhodamine B (DOPE-Rhodamine), Cholesterol, 1,2-Dioleoyl-sn-Glycero-3-Phosphocholine (DOPC) and 1,2-Distearoyl-sn-Glycero-3-Phosphoethanolamine-N-Methoxy(Polyethylene glycol)-2000 (DSPE-PEG_{2000}) were purchased from Avanti Polar Lipids Inc. (Alabaster, AL, USA). All other chemicals were of analytical grade or the best grade available and purchased from Sigma-Aldrich (UK) or Macrocyclics (USA).

8.1.2 General Procedures

^{1}H NMR spectra were recorded on a 400 MHz Bruker Advance 400 spectrometer. Chemical shifts are reported in parts per million (ppm) downfield from TMS, using residual chloroform (7.27 ppm) as an integral standard. Data are supported as follows: chemical shift, s = singlet, br = broad singlet, d = doublet, t = triplet, q = quartet, m = multiplet, coupling constants *J* are given in hertz (Hz). ^{13}C NMR spectra were recorded on a 400 MHz Bruker Advance 400 spectrometer. Chemical shifts are reported in parts per million (ppm) downfield from TMS, using the middle resonance of $CDCl_3$ (77.0 ppm) as an integral standard. Infrared (IR) spectra were recorded on a JASCO FT/IR-620 infra-red spectrophotometer; absorption's are recorded in wavenumbers (ν_{max} in cm^{-1}). Analytical HPLC was conducted on a Hitachi-LaChrom L-7150 pump system equipped with a Polymer Laboratories PL-ELS 1000 evaporative light scattering detector. HPLC gradient mixes assigned as follows: gradient mix A = H_2O/0.1%TFA; mix B = MeCN/0.1%TFA; mix C = MeOH. Mass spectra were performed using VG-070B, Joel SX-102 or Bruker Esquire 3000 ESI instruments. Melting points were determined on a Stuart Scientific SMP3 apparatus and are reported without correction. Reactions with air sensitive material were carried out by standard syringe techniques. CH_2Cl_2 was distilled over P_2O_5. Thin layer chromatographic (TLC) analyses were performed on Merck 0.2 mm aluminium-backed silica gel 60 F_{254} plates and components were visualised by illumination with UV light or by staining with potassium permanganate, acidic ammonium molybdate (IV), iodine, ninhydrin, Rhodamine B, dilute aqueous sulphuric acid or bromocresol green, where appropriate a Pharmacia LKB – Ultrospec III (deuterium lamp at 300

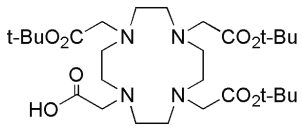
nm) was used to visualise the UV absorbance. Flash column chromatography was performed using Merck 0.040 to 0.063 mm, 230 to 400 mesh silica gel.
UV spectroscopy was conducted on a Pharmacia Biotech Ultrospec 4000 spectrometer at defined wavelengths. Fluorescence measurements were carried out on a Shimadzu RF-5301 PC spectrofluorophotometer. Zeta potentials were recorded on a Nanoseries Nano-ZS zetasizer (Malvern instruments). Microscopy experiments were conducted on an Olympus or Nickon Eclipse E600 microscope and confocal microscopy was carried out with an upright Leica instrument. FACS analysis was conducted on a Becton Dickinson FACSCalibur machine. All MRI experiments were conducted on a 4.7 T Magnex magnet (Oxford, UK) Varian Unity Inova console (Palo Alto, CA, USA).

All procedures on animals were conducted in accordance with UK Home Office regulations and the Guidance for the Operation of Animals (Scientific Procedures) Act (1986).

8.1.3 Chemical Synthesis

8.1.4 Synthesis of Gd.DOTA.DSA

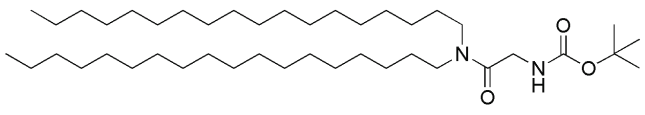
2-(4,7,10-Tris(2-*tert*-butyloxycarbonylmethyl)-1,4,7,10-tetra-azacyclododecan-1yl)acetic acid, **3**.



2-Chlorotrityl chloride resin (916.7 mg, 1.265 mmol) was added to a solid phase synthesis vessel and swelled by the addition of CH_2Cl_2 (40 mL) and the vessel agitated for 30 min (0.8 mmol.g^{-1} loading). Bromoacetic acid (1.758 g, 12.65 mmol, 10 eq.) and *i*Pr_2NEt (1.107 mL, 6.325 mmol, 5 eq.) were added to the resin and the vessel was agitated on a motor shaker overnight at room temperature. MeOH (1000 eq.) was added as a capping reagent and the reaction agitated for a further 10 min; the solution was filtered and the resin was washed by alternating between; CH_2Cl_2 and *i*PrOH (× 3) and MeOH (× 2) and finally dried. Cyclen (2.179 g, 12.65 mmol, 10 eq.) was dissolved in CH_2Cl_2 (40 mL) and added to the vessel containing the bromoacetyl resin, the reaction was agitated for 4 h. The solvent was filtered and the

resin washed alternating between; CH_2Cl_2 and *i*PrOH (× 3), CH_2Cl_2 and MeOH (× 3), distilled H_2O (× 2) and finally CH_2Cl_2 and *i*PrOH (× 3). The chloroanil test was positive. The resin was then washed with DMF (× 2) and dried. *tert*-Butyl bromoacetate (3.064 mL, 18.975 mmols, 5 eq. per free amine), NEt_3 (1.587 mL, 11.389 mmol, 3 eq. per free amine) were dissolved in DMF (40 mL) and added to the cyclen functionalised resin. The reaction was left shaking for a further 12 h. The solvent was removed by filtration and the resin was washed with *i*PrOH and distilled H_2O (× 3), CH_2Cl_2 and *i*PrOH (× 3), MeOH (× 2), toluene (× 2) and finally diethylether (× 2). The chloroanil test was negative. The resin was transferred to a round-bottomed flask and stirred in a solution of CH_2Cl_2: trifluroethanol 2: 1 (v/v) for a further 2 h at room temperature and subsequently filtered and washed with CH_2Cl_2 (× 3), the filtrate was collected and reduced *in vacuo* to give a yellow oil. The compound was purified by flash column chromatography (eluted with (CH_2Cl_2: MeOH: H_2O: 34.5: 9: 1): CH_2Cl_2 3:7, v/v) to yield a crystalline pale yellow solid (361.79 mg, 51%, mp = 88-93 ºC), R_f [CH_2Cl_2: MeOH: H_2O: 34.5: 9: 1 v/v] 0.48. ^{1}H NMR (400 MHz, d_6-DMSO, 400K) δ_H (ppm) 3.14 (8H, s, br, 4 × C*H*$_2$COOC(CH$_3$)$_3$), 2.58 (16H, s, br, 4 × NC*H*$_2$C*H*$_2$N), 1.46 (27H, s, C(C*H*$_3$)$_3$ × 3). ^{13}C NMR (400 MHz, d_6-DMSO, 400K) δ_C (ppm) 174.92 (*C*OOH), 172.30 (*C*OO*t*-Bu), 82.35 (*C*(CH$_3$)$_3$ × 2), 82.02 (*C*(CH$_3$)$_3$), 56.70 (*C*H$_2$COOH), 56.11 (*C*H$_2$COOt-Bu), 55.74 (*C*H$_2$COOt-Bu), 50.96 (*C*H$_2$ × 2), 50.22 (*C*H$_2$ × 2), 28.15 (C(*C*H$_3$)$_3$, FTIR: νmax (nujol)/cm^{-1} 3735.53, 2726.56, 2366.78, 1731.76, 1262.32. HPLC t_R = 16.0 min, column C-4 peptide, gradient mix: 0.0 min [100% A], 15-25.0 min [100% B], 25.1-45.0 min [100% C], 45.1-55.0 min [100% A]; flow: 1 mL/min. HRMS (FAB$^+$) calculated for $C_{28}H_{52}N_4O_8$ *m/z* 572.3785, found 573.386 (M + H)$^+$.

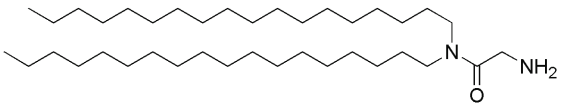
N, *N*-Distearylamidomethylcarbamic acid *tert*-butyl ester, **18**.



Boc-glycine (310 mg, 1.77 mmol) and dioctadecylamine (923.96 mg, 1.77 mmol) were dissolved in dry chloroform (30 ml). HBTU (804.12 mg, 2.12 mmol) and DMAP (648.72 mg, 5.31 mmol) were added to the solution and the reaction was stirred at

room temperature under N_2 for 12 h. The solvents were removed *in vacuo*. The mixture was dissolved in CH_2Cl_2 (50 mL) and extracted with H_2O (3 × 50 mL). The combined aqueous extracts were back extracted with 2: 1 CH_2Cl_2: MeOH (2 × 50 mL), the solvents reduced and re-dissolved in diethyl ether and a subsequent extraction with 7% citric acid and H_2O was performed; the organic layer was washed with brine, collected and filtered through celite and finally dried over $MgSO_4$. The diethyl ether was evaporated *in vacuo* to yield a pure white solid (1.164g, 97% yield, mp = 82-85 ºC). R_f [CH_2Cl_2: MeOH: H_2O: 34.5: 9: 1 v/v] 0.56. ^{1}H NMR (400 MHz, $CDCl_3$) δ_H (ppm) 5.50 (1H, s, br, amide N*H*), 3.99 (2H, s, br, NHCH_2), 3.35-3.25 (2H, d, br, OCNCH_2), 3.17-3.07 (2H, d, br, OCNCH_2), 1.44 (9H, s, C(CH_3)$_3$), 1.61-1.44 (13H, m, C(CH_3)$_3$ and OCN(CH_2CH_2)), 1.25 (60H, s, CH_2's alkyl chain), 0.872 (6H, s, br, CH_3 x 2). ^{13}C NMR (400 MHz, $CDCl_3$) δ_C (ppm) 167.6 (*C*ON(CH_2)$_{17}$), 156.0 ($C(CH_3)_3CO$*C*O), 79.0 (*C*(CH_3)$_3$), 46.9 (N(*C*H_2CH_2)$_9$), 46.1 (N(*C*H_2CH_2)$_9$), 42.2 (NH*C*H_2CO), 31.9-26.9 (*C*H_2 x 30), 22.7 (N(*C*H_2CH_2)$_9$), 14.1 (C(*C*H_3)$_3$). FTIR: νmax (nujol)/cm^{-1} 2360.56, 1723.85, 1650.78, 1580.63, 1377.25. HPLC: t_R = 36.08 min, column C-4 peptide, gradient mix: 0.0 min [100% A], 15-25.0 min [100% B], 25.1-45.0 min [100% C], 45.1-55.0 min [100% A]; flow: 1 mL/min. HRMS (FAB+) calculated for $C_{43}H_{86}N_2O_3$ *m/z* 678.6638, found 679.6953 (M + H)$^+$.

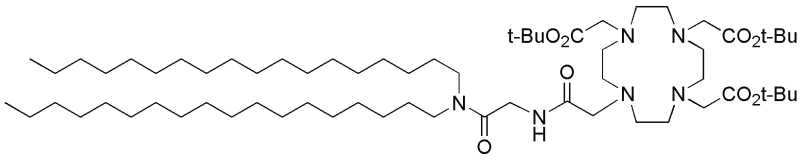
N,*N*-Distearylamidomethylamine (DSA), **4**.



The protected amine **18** was dissolved in anhydrous CH_2Cl_2 (5 mL), to which was added trifluoroacetic acid (3 mL). The reaction was stirred under an atmosphere of N_2 for 2 h. The solvents were removed *in vacuo* and the product dried under vacuum to obtain a white powder (158 mg, 94% yield, mp = 59-64 ºC). R_f [Hexane: Ethyl acetate: 9:1 v/v] 0.44. ^{1}H NMR (400 MHz, $CDCl_3$) δ_H (ppm) 3.85 (2H, s, OCC$H_2$$NH_2$), 3.32 (2H, t, *J* 7.2 Hz, OCNC$H_2$$CH_2$), 3.13 (2H, t, *J* 7.2 Hz, OCNC$H_2$$CH_2$), 2.39 (2H, s, very br, NH_2), 1.61-1.55 (4H, m, OCNCH_2CH_2), 1.26 (60H, s, chain CH_2's), 0.86 (6H, t, *J* 6.8, CH_3 × 2). ^{13}C NMR (400 MHz, $CDCl_3$) δ_C (ppm) 168.8 (*C*O), 43.7 (OCN*C*H_2), 41.9 (OCN*C*H_2), 35.6 (CH_3CH_2*C*H_2), 33.4 (alkyl chain *C*H_2's), 32.3, 31.1

($NCH_2CH_2CH_2$), 22.7-14.1 (alkyl chain CH_2's). FTIR: νmax (nujol)/cm^{-1} 1681, 1534, 1313, 1206, 1174. HPLC: t_R = 31.46 min, column C-4 peptide, gradient mix: 0.0 min [100% A], 15-25.0 min [100% B], 25.1-45.0 min [100% C], 45.1-55.0 min [100% A]; flow: 1 mL/min. HRMS (FAB+) calculated for $C_{38}H_{78}N_2O$ *m/z* 578.6114, found 579.6199 $(M+ H)^+$.

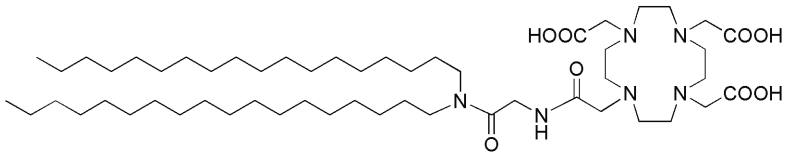
2-{4,7-Bis-*tert*-butyloxycarbonylmethyl-10-[(*N*,*N*-distearyl-amidomethyl-*N*`-amidomethyl]-1,4,7,10-tetraazacyclododec-1-yl}-acetic acid *tert*-butyl ester, **5**.



N,*N*-distearylamidomethylamine (DSA), **4** (4.837 mg 0.0084 mmol) *tert*-butyloxycarbonyl DOTA acid (**3**) (4.35 mg, 0.0076 mmol) and were added to a dry round-bottomed flask followed by the addition of dry $CHCl_3$ (8 mL). HBTU (3.46 mg, 0.0091 mmol) and DMAP (2.785 mg, 0.022 mmol) were also added, and the reaction was stirred at 40 ^oC for 6 h until TLC indicated completion. The solvents were removed *in vacuo*, and the crude mixture was purified by flash column chromatography (eluted with (CH_2Cl_2: MeOH: H_2O: 34.5: 9: 1): CH_2Cl_2 1:9 → 1:1, v/v) to yield a yellowish oil (7.58 mg, 88% yield). R_f [CH_2Cl_2: MeOH: NH_3 34.5: 9: 1 v/v] 0.84. ^1H NMR (400 MHz, $CDCl_3$, 318K) δ_H (ppm) 3.98 (2H, s, $OCCH_2NCH_2$), 3.31 (2H, t, *J* 7.6 Hz, $OCNCH_2CH_2$), 3.15 (8H, s, br, 4 × $CH_2COOC(CH_3)_3$), 3.13 (2H, t, *J* 7.6 Hz, $OCNCH_2CH_2$), 2.58 (16H, s, br, 4 × NCH_2CH_2N), 2.35 (2H, s, very br, CH_2NH), 1.67-1.59 (4H, m, $OCNCH_2CH_2$), 1.46 -1.44(27H, d of s, *J* 6.0, $C(CH_3)_3$ × 3),1.25 (60H, s, chain CH_2's), 0.90 (6H, t, *J* 6.8, CH_3 x 2). ^{13}C NMR (400 MHz, $CDCl_3$) δ_C (ppm) 172.9 ($C(CH_3)_3OCO$), 171.3 (NCH_2CONH), 166.8 ($CONCH_2(CH_2)_{16}$), 81.7 ($C(CH_3)_3$), 81.5 ($C(CH_3)_3$), 55.8 ($C(CH_3)_3OCOCH_2N$), 53.4 (NCH_2CH_2N), 47.1 (NCH_2), 41.1 ($NHCH_2CON$), 32.0 ($NCH_2CH_2CH_2CH_2$), 29.7-27.1 ($C(CH_3)_3$ and chain CH_2's), 22.7 (CH_2CH_3), 14.6 (CH_2CH_3). FTIR: νmax (nujol)/cm^{-1} 3054.52, 2306.23, 1265.85, 896.66. HPLC: t_R = 27.71 min, column C-4 peptide, gradient mix: 0.0 min [100% A], 15-25.0 min [100% B], 25.1-45.0 min [100% C], 45.1-55.0 min [100% A]; flow: 1

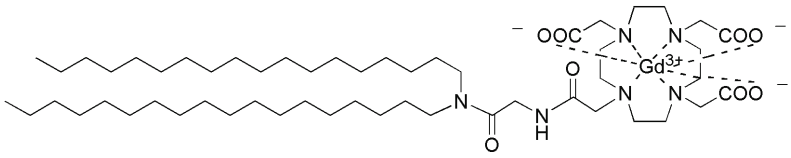
mL/min. HRMS (FAB+) calculated for $C_{66}H_{128}N_6O_8$ *m/z* 1132.9794, found 1155.9669 $(M + Na)^+$.

2-{4,7-Bis-carboxymethyl-10-[(*N*,*N*-distearylamidomethyl-*N*`-amidomethyl]-1,4,7,10-tetra-azacyclododec-1-yl}-acetic acid (DOTA.DSA), **6**.



tert-Butyl protected DOTA.DSA (**5**) was dissolved in a 1:1 mixture of c.HCl/1,4-dioxane and the reaction stirred for 2 h. The solvents were removed *in vacuo*, the mixture suspended in water and freeze-dried to yield a white powder of DOTA.DSA (50 mg, 68% yield, decomposition = 235-245 ºC). R_f [CH_2Cl_2: MeOH: H_2O: 34.5: 9: 1 v/v] 0.61. ^{1}H NMR (400 MHz, $CDCl_3$: MeOD: AcOD: 3: 1, 300K) δ_H (ppm) 10.55 (3H, s, br, 3 × COO*H*), 5.30 (1H, s, br, CH_2NHCOO), 3.65 (6H, m, 3 × NCH_2COOH), 3.22 (6H, m, 2 × NCH_2CH_2, 1 × NCH_2CONH), 2.58 (16H, s, br, 4 × NCH_2CH_2N), 2.29 (2H, s, br , CH_2NH), 1.67-1.59 (4H, m, $OCNCH_2CH_2$), 1.46 -1.44(27H, d of s, *J* 6.0, $C(CH_3)_3$ × 3),1.25 (60H, s, chain CH_2's), 0.90 (6H, t, *J* 6.8, CH_3 x 2). FTIR: νmax (nujol)/cm^{-1} 3750.56, 2726.56, 1889.87, 1793.63, 1681.21, 1534.22. HPLC: t_R = 34.16 min, column C-4 peptide, gradient mix: 0.0 min [100% A], 15-25.0 min [100% B], 25.1-45.0 min [100% C], 45.1-55.0 min [100% A]; flow: 1 mL/min. HRMS (FAB+) calculated for $C_{54}H_{104}N_6O_8$ *m/z* 964.7916, found 987.7833 $(M + Na)^+$.

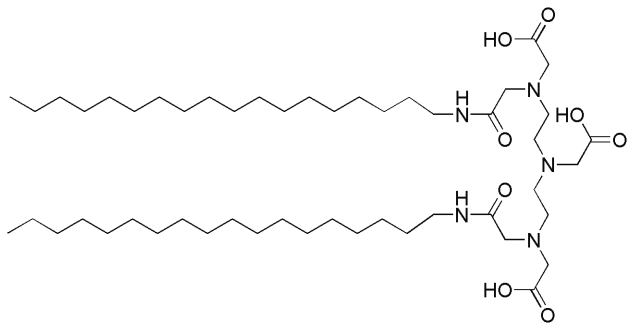
Gadolinium (III) 2-{4,7-bis-carboxymethyl-10-[(*N*, *N*-distearylamidomethyl-*N*`-amido-methyl]-1,4,7,10-tetra-azacyclododec-1-yl}-acetic acid (Gd.DOTA.DSA), **2**.



A stoichiometric amount of $GdCl_3.6H_2O$ (28.118 mg, 0.075 mmol) was added to DOTA.DSA (**6**) (73 mg, 0.0757 mmol), and the reaction was stirred in distilled H_2O (20 mL) at 90 ºC overnight (pH dropped to 3.5 upon Gd addition). The water was freeze-dried to yield a white powder (83.9 mg, 99% yield, decomp. = 345-348 ºC). R_f [CH_2Cl_2: MeOH: H_2O: 34.5: 9: 1 v/v] 0.55. The xylenol orange test indicated no detectable free Gd^{3+} ions. FTIR: νmax (nujol)/cm^{-1} 3750.23, 2234.78, 1991.59, 1889.89, 1793.44, 1681.90.77. HPLC: t_R = 36.22 min, column C-4 peptide, gradient mix: 0.0 min [100% A], 15-25.0 min [100% B], 25.1-45.0 min [100% C], 45.1-55.0 min [100% A]; flow: 1 mL/min. MS (ESI+) calculated for $C_{54}H_{101}GdN_6O_8$ *m/z* 1119.67, found 1120.10 $(M + H)^+$.

8.1.5 Synthesis of Gd.DTPA.BSA

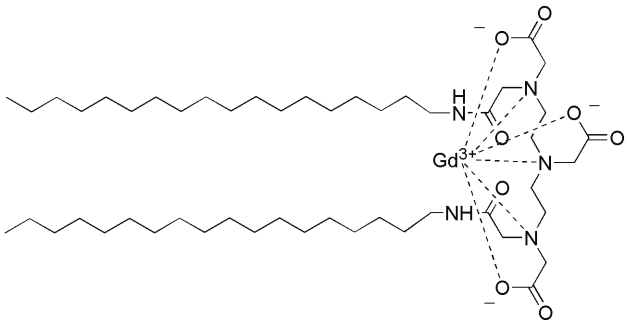
[*N*,*N*-Bis-stearylamidomethyl-*N*`-amidomethyl]-diethylenetriamine-tetra-acetic acid (DTPA.BSA), **22**.[287]



A solution of octadecylamine (301.86 mg, 1.2 mmol) dissolved in chloroform (30 mL) was added to a solution of DTPA bisanhydride (200 mg, 0.560 mmol) previously dissolved in DMF (40 mL). The reaction was stirred at 40 ºC for 2 h. The white precipitate formed was collected by filtration and washed with acetone and dried under vacuum overnight. The white solid was stirred in water at 80 ºC for 3 h to dissolve any excess DTPA. The insoluble residue was filtered and dried under vacuum overnight. The white solid was then washed with boiling chloroform and stirred in chloroform for 2 h, and then filtered and dried (198 mg, 40% yield, mp = 168-173 ºC, Lit. mp = 168 ºC).[287] R_f [CH_2Cl_2: MeOH: H_2O: 34.5: 9: 1 v/v] 0.50. ^1H

NMR (400 MHz, CF_3-COOD at δ = 11.30 ppm) δ_H (ppm) 4.55 (8H, d, *J* 5.2, HOOCC*H*$_2$N), 4.09 (6H, t, NC*H*$_2$CH$_2$N × 2 and HOOCC*H*$_2$N), 3.69 (4H, t, *J* 4.8 and *J* 19.6, NC*H*$_2$CH$_2$N × 2), 3.34 (4H, t, *J* 7.2, NHC*H*$_2$ × 2), 1.57 (4H, d, *J* 6.0, NHCH$_2$C*H*$_2$ x 2), 1.27 (60H, d, 30 × CH_2 alkyl chain), 0.83 (6H, t, *J* 7.2, CH_2C*H*$_3$ × 2). ^{13}C NMR (400 MHz, CF_3-COOD at δ = 116.6 and 164.2 ppm) δ_C (ppm) 170.2 (*C*H$_2$COOH), 166.1 (N*C*H$_2$CONHCH$_2$CH$_2$-), 58.5 (HOOC*C*H$_2$), 57.2-55.0 (N*C*H$_2$CONH), 51.8 (NCH$_2$*C*H$_2$N(CH$_2$COOH)CH$_2$CH$_2$N), 42.5 (NH*C*H$_2$CH$_2$), 32.8 (NH*C*H$_2$CH$_2$), 30.5-30.2 (chain *C*H$_2$'s), 27.4 (NHCH$_2$CH$_2$*C*H$_2$), 23.1, 14.1 (-*C*H$_3$). FTIR: νmax (nujol)/cm^{-1} 3675.06, 2272.91, 1991.37, 1869.23, 1771.48, 1684.66. HPLC; t_R = 34.23 min, column C-4 peptide: gradient mix: 0.0 min [100% A], 15-25.0 min [100% B], 25.1-45.0 min [100% C], 45.1-55.0 [100% A]; flow: 1 mL/min. HRMS (FAB$^+$) calculated for $C_{50}H_{97}N_5O_8$ *m/z* 895.7337, found 896.7423 (M + H)$^+$.

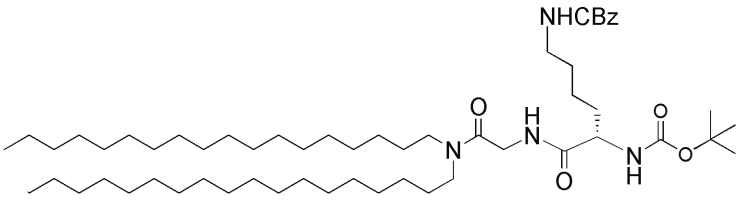
Gd (III) [*N*, *N*-bis-stearylamidomethyl-*N*`-amidomethyl]-diethylenetriamine tetra-acetic acid (Gd.DTPA.BSA), **19**.



A stoichiometric amount of Gd.Cl_3.6H_2O (45 mg, 0.0502 mmol) was added to BSA.DTPA **22** (18.67 mg, 0.0502 mmol) and the reaction was stirred in distilled H_2O (20 mL) at 90 ºC for 3 h (pH dropped to 3.5). The water was freeze-dried to yield a white powder (48 mg, 91% yield, decomp. = 350 ºC). R_f [CH_2Cl_2: MeOH: H_2O: 34.5: 9: 1 v/v] 0.43. The xylenol orange test indicated no detectable free Gd^{3+} ions. FTIR: νmax (nujol)/cm^{-1} 3779.8, 3674.69, 2271.73, 1868.68, 1771.3, 1683.55. HPLC; t_R = 34.60 min, column C-4 peptide, gradient mix: 0.0 min [100% A], 15-25.0 min [100% B], 25.1-45.0 min [100% C]; 45.1-55.0 min [100% A]; flow: 1 mL/min. MS (ESI+) calculated for $C_{50}H_{94}GdN_5O_8$ *m/z* 1050.56, found 1051.10 (M + H)$^+$.

8.1.6 Synthesis of Gd.DOTA.Rhoda.DSA

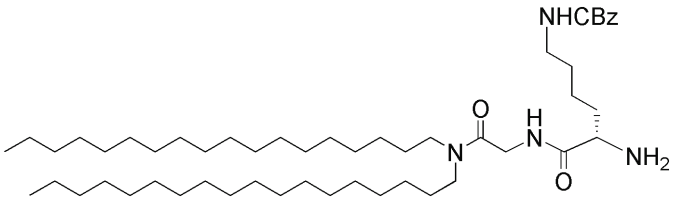
6-Benzyloxycarbonylamino-2-(*tert*-butoxycarbonylamido) hexa-amido-*N*,*N*-dioctadecylacetamide, **34**.



The boc-Lys-(CBz)-succinimide ester (5.0 g, 10.471 mmol) and *N*,*N*-distearylamidomethylamine (DSA), **4** (6.96 g, 12.041 mmol) were added to an air evacuated flask and dissolved in anhydrous CH_2Cl_2 (200 mL). The solution was briefly stirred, followed by the slow addition of Et_3N (4.38 mL, 31.413 mmol, 3 eq.). The reaction was stirred for a further 5 h at 40 ^oC until TLC indicated completion. The reaction was stopped and the organic layer washed with water (× 3, 50 mL) and the aqueous layer back extracted with 2:1 CH_2Cl_2: MeOH (× 3, 50 mL). The combined organic layers were subsequently washed with 7% citric acid (× 3, 50 mL) and the aqueous layer extracted further with CH_2Cl_2 (× 3, 50 mL). The final combined organic layers were collected and dried over $MgSO_4$, filtered and reduced *in vacuo* to yield a hygroscopic white solid (9.05 g, 92%). R_f [CH_2Cl_2: MeOH: H_2O: 34.5: 9: 1 v/v] 0.56. ^1H NMR (400 MHz, $CDCl_3$) δ_H (ppm) 7.35 (m, 6H, *J* 8.8 aromatic and Boc-N*H*), 6.99 (t, 1H, CBz-N*H*), 5.08 (s, 1H, PhCH_2-), 4.85 (s, 1H, Boc-NHC*H*-), 4.03 (d, 1H, CH_2NHCOCH(NH-Boc)CH_2-), 3.31 (m, 2H, CBz-NHCH_2-), 3.19 (m, 4H N(CH_2)$_2$), 1.81 (s, br, 2H, CHCH_2-), 1.52 (m, 6H, N(CH_2CH_2)$_2$ and -C$H_2$$CH_2$NHCBz), 1.43 (s, 9H, -OC(CH_3)$_3$), 1.26 (s, 60H, chain CH_2's), 0.88 (t, 6H, (C$H_3$$CH_2$$CH_2$)$_2$). ^{13}C NMR (400 MHz, $CDCl_3$) δ_C (ppm) 172.13 (-NH*C*OCH(NHBoc)), 167.28 (-N*C*OCH_2NH), 156.82 (PhCH_2O*C*O), 155.87 (-O*C*O*t*-Bu), 136.98 (-*C*$_1$ aromatic), 128.79 (-*C*$_3$, *C*$_5$ aromatic), 128.42 (-*C*$_2$, *C*$_6$ aromatic), 128.34 (-*C*$_4$ aromatic), 80.30 (*C*(CH_3)$_3$), 66.90 (Ph*C*H_2), 54.65 (Boc-NH*C*H-), 47.62 (-N(*C*H_2)$_2$), 41.46 (CBz-NH*C*H_2-), 40.87 (*C*H_2NHCOCH(NH-Boc)CH_2-), 32.23 ((C$H_3$$CH_2$*C*$H_2$-)$_2$), 29.88 (12 chain *C*$H_2$'s), 29.66 (-C(*C*$H_3$)$_3$), 29.03 (-*C*$H_2$$CH_2$NHCBz), 27.32 (N($CH_2$*C*$H_2$)$_2$), 22.99 ((C$H_3$*C*$H_2$-)$_2$), 22.80 (-*C*$H_2$$CH_2$$CH_2$NHCBz), 14.41 ((*C*$H_3$$CH_2$-)$_2$). FTIR (nujol) νmax: 3322.75, 1721.16, 1643.05, 1246.75, 1171.54 (cm^{-1}). HPLC; t_R = 36.28 min, column C-4 peptide,

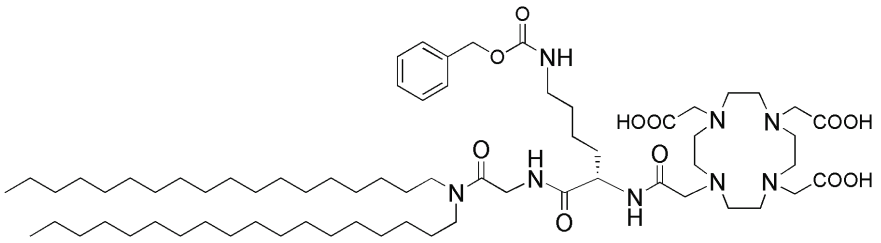
gradient mix: 0.0 min [100% A], 15-25.0 min [100% B], 25.1-45.0 min [100% C], 45.1-55.0 min [100% A]; flow: 1 mL/min. HRMS (FAB+) calculated for $C_{57}H_{104}N_4O_6$ *m/z* 940.7956, found 941.8031 $(M + H)^+$.

6-Benzyloxycarbonylamino-2-(amino) hexa-amido-*N*,*N*-dioctadecylacetamide, **33**.



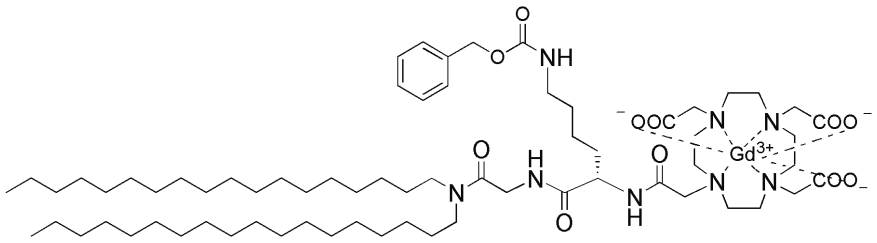
The Boc protected lipid **34** (288.0 mg, 0.306 mmol) was added to a round-bottom flask and to this was added a 1:1 TFA: CH_2Cl_2 (20 mL, v/v) solution. The reaction was stirred at room temperature for 2 h until TLC indicated reaction completion. The solvents were removed *in vacuo* and the product freeze-dried from water to yield a white hygroscopic solid (257.09 mg, quantitative, mp = 47-50 ºC). R_f [(CH_2Cl_2: MeOH: H_2O: 34.5: 9: 1): CH_2Cl_2: 1:1 v/v] 0.39. ^{1}H NMR (400 MHz, $CDCl_3$) δ_H (ppm) 8.2 (s, br, 2H, N*H*$_2$), 7.35 (m, 5H, *J* 15.2 aromatic) 5.07 (s, 1H, PhC*H*$_2$-), 4.18 (d, 1H, -NCOCH$_2$N*H*CO), 3.87 (d, 1H, -NCOC*H*$_2$NHCO), 3.26 (s, br, 1H, -C*H*NH$_2$), 3.15 (m, 4H N(C*H*$_2$)$_2$), 1.92 (s, br, 2H, NH$_2$CHC*H*$_2$-), 1.48 (m, 8H, (C*H*$_2$CH$_2$)$_2$N-, -C*H*$_2$CH$_2$NHCBz and -C*H*$_2$CH$_2$CH$_2$NHCBz), 1.27 (s, 60H, chain C*H*$_2$'s), 0.89 (t, 6H, *J* 13.6 (C*H*$_3$CH$_2$CH$_2$)$_2$). ^{13}C NMR (400 MHz, $CDCl_3$) δ_C (ppm) 169.26 (-NH*C*OCHNH$_2$), 167.51 (-N*C*OCH$_2$NH), 157.20 (PhCH$_2$O*C*O), 136.99 (-C_1 aromatic), 128.78 (-C_3, C_5 aromatic), 128.30 (-C_2, C_6 aromatic), 128.26 (-C_4 aromatic), 80.30 (*C*(CH$_3$)$_3$), 66.95 (Ph*C*H$_2$), 54.01 (NH$_2$*C*H-), 47.56 (-N(*C*H$_2$)$_2$), 41.45 (CBz-NH*C*H$_2$-), 40.30 (*C*H$_2$NHCOCHNH$_2$), 32.24 ((CH$_3$CH$_2$*C*H$_2$-)$_2$), 31.10 (12 chain *C*H$_2$'s), 29.89 (-C(*C*H$_3$)$_3$), 28.97 (-*C*H$_2$CH$_2$NHCBz), 27.37 (-N(CH$_2$*C*H$_2$)$_2$), 23.00 ((CH$_3$*C*H$_2$-)$_2$), 21.71 (-*C*H$_2$CH$_2$CH$_2$NHCBz), 14.42 ((*C*H$_3$CH$_2$-)$_2$). FTIR (nujol) νmax: 3848.26, 1676.8, 1203.36, 722.21 (cm^{-1}). HPLC; t_R = 27.98 min, column C-4 peptide, gradient mix: 0.0 min [100% A], 15-25.0 min [100% B], 25.1-45.0 min [100% C], 45.1-55.0 min [100% A]; flow: 1 mL/min. HRMS (FAB+) calculated for $C_{52}H_{96}N_4O_4$ *m/z* 840.7432, found 841.7529 $(M + H)^+$.

6-Benzyloxycarbonylamino-2-(amido-{1,4,7,10-tetra azacyclododec-1-yl}-acetic acid) hexa-amido-*N*,*N*-dioctadecylacetamide, **31**.



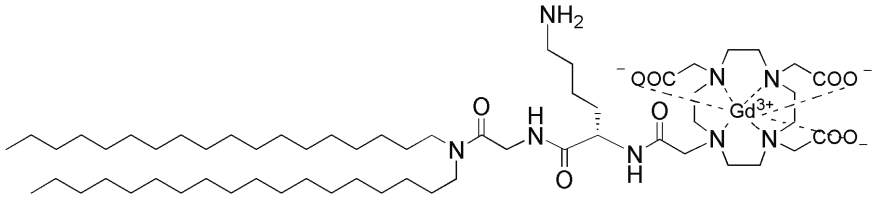
Amine **33** (84.44 mg, 0.100 mmol) and DOTA-NHS ester (100 mg, 0.120 mmol) were added to an air evaporated flask fitted with a reflux condenser. Anhydrous CH_2Cl_2 (20 mL) was added and the reaction stirred briefly at room temperature. To this was added Et_3N (41.81 µL, 0.300 mmol, 3 eq.) and the reaction stirred at 45 ºC under reflux for an overnight period. The solvent was evaporated *in vacuo* to yield a white hygroscopic solid (64.98 mg, 53%). R_f [CH_2Cl_2: MeOH: H_2O: 34.5: 9: 1 v/v] 0.26. ^{1}H NMR (400 MHz, $CDCl_3$) δ_H (ppm) 7.44 (m, 5H, benzene ring), 5.24 (s, 2H, HNCOOC*H*$_2$-), 4.42 (s, 1H, C*H*), 4.21 (m, 2H, NCOC*H*$_2$NH), 3.41 (m, 6H, 3 x HOOCCH$_2$N), 3.24 (m, 4H, 2 x NC*H*$_2$CH$_2$), 3.11 (m, 2H, HNCOC*H*$_2$N), 3.05 (m, 2H, OOCNHC*H*$_2$), 1.85 (s, 2H, CHC*H*$_2$), 1.65 (m, 6H, 2 x NCH$_2$C*H*$_2$- and OOCNHCH$_2$C*H*$_2$), 1.43 (s, 60H, chain C*H*$_2$'s), 1.01 (t, 6H, 2 x C*H*$_3$) (ppm) ^{13}C NMR (400 MHz, $CDCl_3$) δ_C (ppm) 175.42, (*C*OOH), 175.14 (-HN*C*OCH), 174.85 (-CHNH*C*OCH$_2$), 172.59 (-HN*C*OCH$_2$), 157.42 (HN*C*OO), 136.59 (COOCH$_2$*C*=C), 128.38 (aromatic), 127.93 (aromatic), 127.80 (aromatic), 66.49 (COO*C*H2), 51.03-50.58 (DOTA *C*H$_2$'s), 48.88 (N(*C*H$_2$CH$_2$-)$_2$), 47.81 (-NCO*C*H$_2$NH), 46.18 (-OOCNH*C*H$_2$), 31.79 (-CH*C*H$_2$CH$_2$), 29.56 (-N(CH$_2$*C*H$_2$)$_2$), 29.51-26.90 (chain *C*H$_2$'s), 22.50 (-CHCH$_2$*C*H$_2$), 21.00 ((CH$_3$*C*H$_2$)$_2$),14.9 (*C*H$_3$ x 2) (ppm). FTIR (nujol) νmax: 3741.23, 3681.44, 3621.66, 2360.44, 2333.45, 1953.54, 1835.9, 1743.33, 1691.27, 1646.91, 1513.85, 1481.06 (cm^{-1}). HPLC; t_R = 29.33 min, column C-4 peptide, gradient mix: 0.0 min [100% A], 15-25.0 min [100% B], 25.1-45.0 min [100% C], 45.1-55.00 min [100% A]; flow: 1 mL/min. MS (ESI) calculated for $C_{68}H_{122}N_8O_{11}$ *m/z* 1226.9233, found 1227.80 $(M + H)^+$.

6-Benzyloxycarbonylamino-2-(amido-Gd(III) {1,4,7,10-tetra azacyclododec-1-yl}-acetic acid) hexa-amido-*N*,*N*-dioctadecylacetamide, **40**.



DOTA lipid **31** (61.69mg, 0.0503 mmol) was added to a round-bottom flask and stirred in pure distilled water (80 mL). To this was added a stoichiometric amount of $Gd.Cl_3.6H_2O$ (18.7 mg, 0.0503 mmol) and the reaction stirred at 90 ºC for 12 h. The water was freeze-dried to yield a white solid (69.46 mg, quantitative, decomp. = > 300 ºC). R_f [CH_2Cl_2: MeOH: 1:1 v/v] 0.60. FTIR (nujol) νmax: 3748.94, 2952.48, 2854.13, 2360.44, 2017.18, 1992.11, 1967.04, 1918.82, 1843.61, 1793.47, 1747.19, 1650.77, 1558.2, 1508.06, 1396.21, 1261.22, 1043.3, 669.179 (cm^{-1}). HPLC; t_R = 34.38 min, column C-4 peptide, gradient mix: 0.0 min [100% A], 15-25.0 min [100% B], 25.1-45.0 min [100% C], 45.1-55.00 min [100% A]; flow 1: mL/min. MS (ESI) calculated for $C_{68}H_{119}GdN_8O_{11}$ *m/z* 1381.82, found 1381.00 $(M + H)^+$.

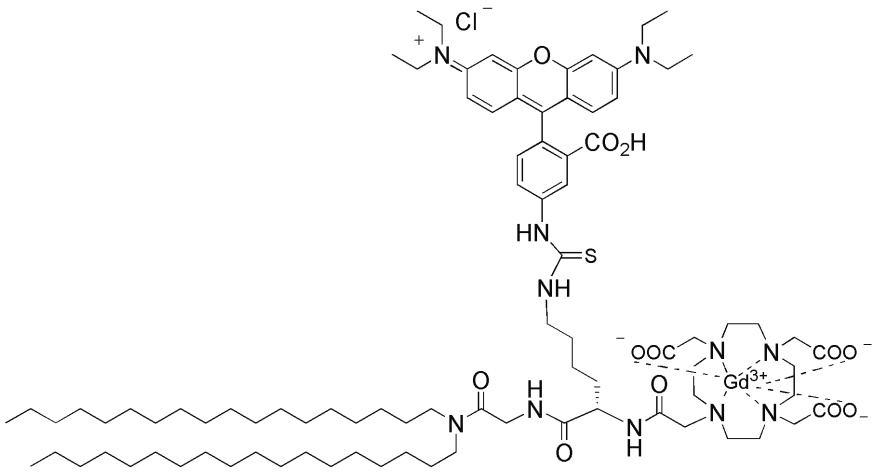
6-Amino-2-(amido-Gd(III) {1,4,7,10-tetra azacyclododec-1-yl}-acetic acid) hexa-amido-*N*,*N*-dioctadecylacetamide, **36**.



The CBz protected gadolinium lipid **40** (93.7 mg, 0.068 mmol) was added to a two necked round-bottom flask equipped with a reflux condenser and stirrer bar. To this was added a 2:1 MeOH: H_2O solution (30 mL, v/v) followed by the addition of 1,4-cyclohexadiene (200 µL, 2.13 mmol). The reaction was stirred and 10% Pd-C (10 mg) was added, whilst ensuring the catalyst was fully dispersed under the surface of the

solution. The air was displaced with H_2 gas and the reaction stirred at 60 ºC under reflux and a stream of H_2 gas for 3 h. The reaction was stopped and the solution filtered through celite. The solvents were removed *in vacuo* and the product freeze-dried from cyclohexane to yield an off white hygroscopic solid (73.8 mg, 87%). R_f [CH_2Cl_2: MeOH: H_2O: 65: 25: 4 v/v] 0.29. FTIR (nujol) νmax: 3673.73, 2360.44, 1943.89, 1918.82, 1889.9, 1793.47, 1698.98, 1558.2, 1340.28, 1068.37, 669.18 (cm^{-1}). HPLC; t_R = 34.22 min, column C-4 peptide, gradient mix: 0.0 min [100% A], 15-25.0 min [100% B], 25.1-45.0 min [100% C], 45.1-55.0 min [100% A]; flow: 1 mL/min. MS (ESI) calculated for $C_{60}H_{113}GdN_8O_9$ *m/z* 1247.79, found 1248.90 $(M + H)^+$.

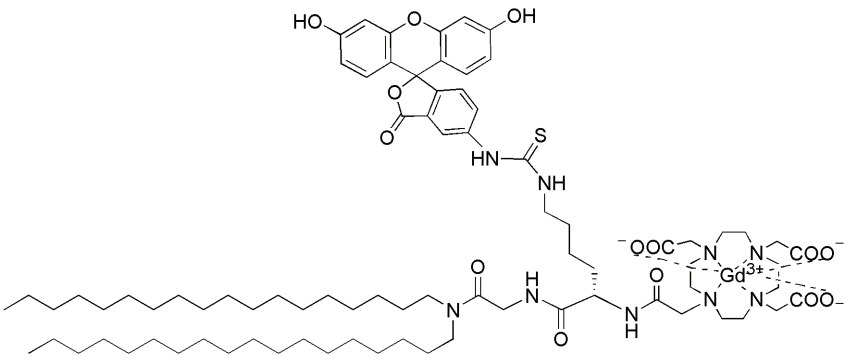
6-Rhodamine-isothiocyanamide-2-(amido-Gd(III) {1,4,7,10-tetra azacyclododec-1-yl}-acetic acid) hexa-amido-*N*,*N*-dioctadecylacetamide, **38**.



Rhodamine B isothiocyanate **37** (11.78 mg, 0.0209 mmol) and the deprotected amine **36** were dissolved in a 1:1 solution of CH_2Cl_2: MeOH (10 mL, v/v). To this was added Et_3N base (8.73 µL, 0.0627 mmol, 3 eq.) slowly and the reaction was stirred at 0 ºC, and allowed to warm to room temperature overnight. The crude mixture was purified by preparative TLC (CH_2Cl_2: MeOH: H_2O: 34.5: 9: 1 v/v), the product isolated and freeze-dried from cyclohexane to yield a bright pink solid (10.4 mg, 29%, decomposition = 269-274 ºC). R_f [CH_2Cl_2: MeOH: H_2O: 34.5: 9: 1, v/v] 0.10. FTIR (nujol) νmax: 3748.94, 2854.13, 2339.23, 1889.9, 1793.47, 1716.34, 1698.98, 1558.20, 1340.28, 1070.30, 1045.23, 669.17 (cm^{-1}). HPLC; t_R = 33.76 min, column C-4 peptide, gradient mix: 0.0 min [100% A], 15-25.0 min [100% B], 25.1-45.0 min

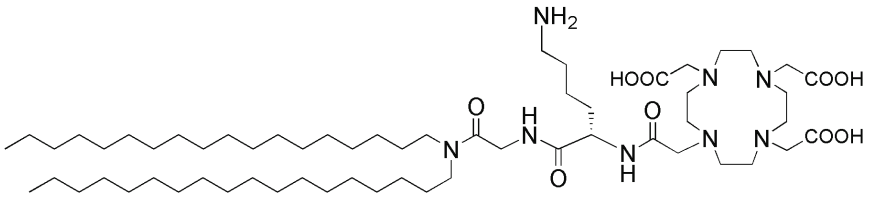
[100% C], 45.1-55.0 [100% A]; flow: 1 mL/min. λ_{ex}: 545 nm and λ_{em}: 565 nm in MeOH MS (ESI+) calculated for $C_{89}H_{143}GdN_{11}O_{12}S^{+}$ *m/z* 1747.99, found 1747.10 (M + H).

6-FITC-isothiocyanamide-2-(amido-Gd(III) {1,4,7,10-tetra azacyclododec-1-yl}-acetic acid) hexa-amido-*N*,*N*-dioctadecylacetamide, **44**.



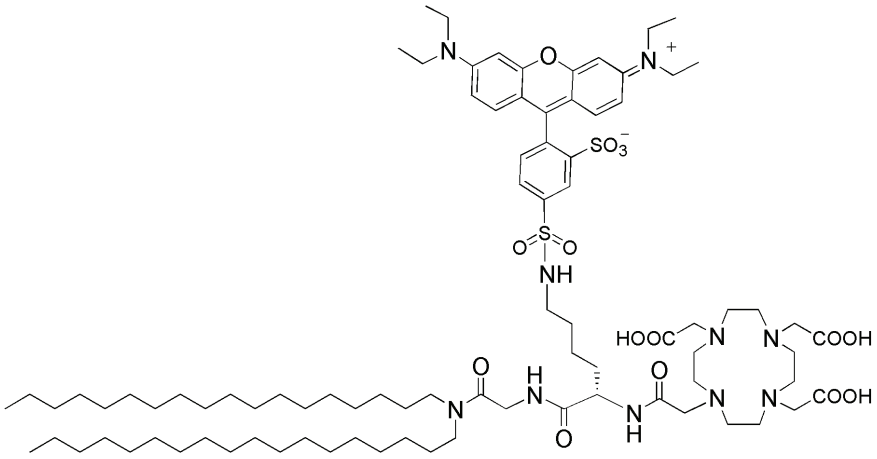
Fluorescein isothiocyanate **43** (27.63 mg, 0.022 mmol) and the deprotected amine **36** were dissolved in anhydrous CH_2Cl_2 (10 mL, v/v). Then Et_3N base (89.20 µL, 0.022 mmol, 3 eq.) was slowly added and the reaction stirred at 0 ºC and allowed to warm to room temperature overnight. The crude mixture was purified by preparative TLC (CH_2Cl_2: MeOH: AcOH: 87: 12: 1 v/v), the product was isolated and freeze-dried from cyclohexane to yield a bright orange solid (10.27 mg, 30%, decomposition = 320-330 ºC). R_f [CH_2Cl_2: MeOH: AcOH: 87: 12: 1, v/v] 0.09. FTIR (nujol) νmax: 2923.56, 2360.44, 1698.98, 1457.92 (cm^{-1}). HPLC; t_R = 33.91 min, column C-4 peptide, gradient mix: 0.0 min [100% A], 15-25.0 min [100% B], 25.1-45.0 min [100% C], 45.1-55.0 min [100% A]; flow 1 mL/min. λ_{ex}: 497 nm and λ_{em}: 535 nm in MeOH. MS (ESI+) calculated for $C_{81}H_{124}GdN_9O_{14}S$ *m/z* 1636.82, found 1659.20 $(M + Na)^{+}$.

6-amino-2-(amido {1,4,7,10-tetra azacyclododec-1-yl}-acetic acid) hexa-amido-*N*,*N*-dioctadecylacetamide, **30**.



The CBz protected lipid **31** (100 mg, 0.0724 mmol) was added to a two necked round-bottom flask equipped with a reflux condenser and stirrer bar. To this was added a 2:1 MeOH: H_2O solution (40 mL, v/v) followed by the addition of 1,4-cyclohexadiene (212.3 µL, 2.27 mmol). The reaction was stirred and 10% Pd-C (10 mg) was added, whilst ensuring the catalyst was fully dispersed in solution. The air was displaced with H_2 gas and the reaction stirred at 60 ºC under reflux and a stream of H_2 gas for 12 h. The reaction was stopped and the solution filtered through celite. The solvents were removed *in vacuo* and the product lyophilised from cyclohexane to yield a white fluffy powder (67.0 mg, 85%). R_f [CH_2Cl_2: MeOH: H_2O: 34.5: 9: 1] 0.12. ^{1}H NMR (400 MHz, $CDCl_3$) δ_H (ppm) 8.3 (s, 2H, 2 x N*H*), 4.55 (s, 1H, C*H*), 4.23 (m, 2H, NCOCH_2NH), 3.44 (m, 6H, 3 x HOOCCH_2N), 3.34 (m, 4H, 2 x NCH_2CH_2), 3.29 (m, 2H, HNCOCH_2N), 3.08 (m, 2H, OOCNHCH_2), 1.80 (s, 2H, CHCH_2), 1.67 (m, 6H, 2 x NCH$_2$CH_2- and OOCNHCH$_2$CH_2), 1.38 (s, 60H, chain CH_2's), 0.87 (t, 6H, 2 x CH_3) (ppm) ^{13}C NMR (400 MHz, $CDCl_3$) δ_C (ppm) 177.0, (*C*OOH), 176.14 (-HN*C*OCH), 173.85 (-CHNH*C*OCH$_2$), 52.0 (DOTA *C*H$_2$'s), 30.22 (-CH*C*H$_2$CH$_2$), 27.94 (chain *C*H$_2$'s), 22.50 (-CHCH$_2$*C*H$_2$), 20.90 ((CH$_3$*C*H$_2$)$_2$),11.73 (*C*H$_3$ x 2) (ppm) FTIR (nujol) νmax: 2360.44, 1698.98, 1650.28, 1558.20, 1540.85 (cm^{-1}). HPLC; t_R = 36.20 min, column C-4 peptide, gradient mix: 0.0 min [100% A], 15-25.0 min [100% B], 25.1-45.0 min [100% C], 45.1-55.00 min [100% A]; flow: 1 mL/min. HRMS (ESI+) calculated for $C_{60}H_{116}N_8O_9$ *m/z* 1092.8865, found 1093.8951 $(M + H)^+$.

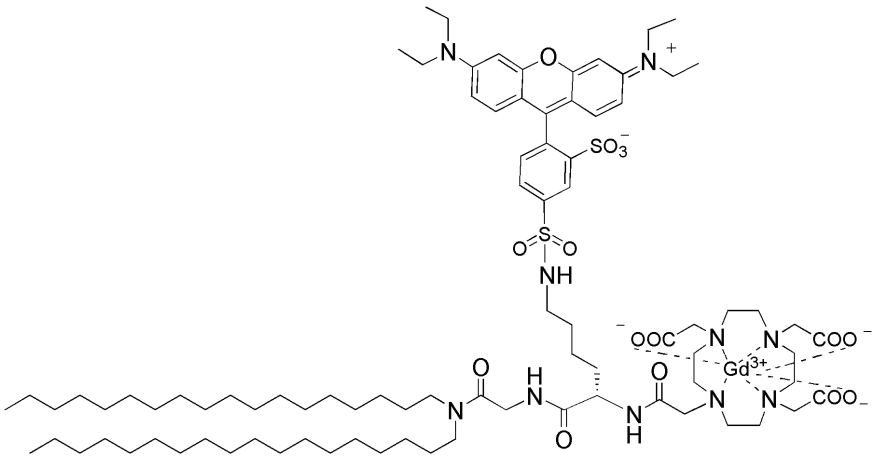
6-Rhodamine-sulfunoamide-2-(amido-{1,4,7,10-tetra azacyclododec-1-yl}-acetic acid) hexa-amido-*N*,*N*-dioctadecylacetamide, **28**.



Amine **30** (143.1 mg, 0.131 mmol) and Lissamine Rhodamine B sulfonyl chloride **47** (75.63 mg, 0.131 mmol) were added to an air evacuated flask to which was added anhydrous CH_2Cl_2 (100 mL). Then Et_3N (1% of solvent, v/v) was added slowly and the reaction stirred under an atmosphere of N_2 at room temperature for 12 h. The solvent was removed *in vacuo* and the crude product purified by flash coloumn chromatography (eluted with (CH_2Cl_2: MeOH: H_2O: 34.5: 9: 1): CH_2Cl_2: 9:1 v/v). The solvents were removed *in vacuo* and the product was freeze-dried from cyclohexane to yield a fluffy purple solid (175.6 mg, 82%, decomposition = 255-260 ºC). R_f [CH_2Cl_2: MeOH: H_2O: 34.5: 9: 1 v/v] 0.31. ^{1}H NMR (400 MHz, MeOD: $CDCl_3$: AcOD: 3: 1: 1) δ_H (ppm) 9.10 (s, 1H, -NCOCH$_2$N*H*COCH), 8.50 (d, 1H, -CHN*H*CO), 8.13 (s, 1H, -N*H*SO$_2$), 7.85 (d, 1H, aromatic), 7.74 (d, 1H, *J* 17.6, aromatic), 7.58 (dd, 1H, *J* 29.2, aromatic), 7.42 (s, 1H, aromatic), 7.34 (t, 1H, *J* 17.6, aromatic), 4.06 (d, 1H, -NCOC*H*$_2$NHCO), 3.96 (m, 18H, -C*H*$_2$NCO, 3 x HOOCC*H*$_2$, -HNCOC*H*$_2$N, -C*H*$_2$NHSO$_3$, and 2 x PhNC*H*$_2$CH$_3$), 3.43 (m, 16H, macrocycle C*H*$_2$'s), 1.18 (s, 36H, chain C*H*$_2$'s, -CHCH$_2$C*H*$_2$, =NC*H*$_2$CH$_3$), 1.10 (s, 6H, 2 x –NCH$_2$C*H*$_3$), 0.71 (t, 6H, chain: 2 x -CH$_2$C*H*$_3$) (ppm). ^{13}C NMR (400 MHz, $CDCl_3$) δ_C (ppm) 174.24 (-*C*OOH), 157.97 (-NH*C*OCH$_2$-), 157.57 (-NH*C*OCH$_2$DOTA), 155.68 (*C*ON(CH$_2$)$_2$-), 144.54 (C=CO*C*=C), 132.62 (*C*H$_2$'s, DOTA), 130.10 (aromatic), 127.31 (aromatic), 125.72 (aromatic), 114.13 (aromatic), 113.56 (aromatic), 95.58 (aromatic), 46.62 (-N(*C*H$_2$CH$_2$)$_2$-), 45.53 (-N*C*H$_2$CH$_3$), 31.70 (-NHCOCH*C*H$_2$-), 29.44 (Chain *C*H$_2$'s), 29.11 (Chain *C*H$_2$'s), 22.39 ($_2$(CH$_3$*C*H$_2$CH$_2$-)), 13.33 (CH$_3$*C*H$_2$N=), 11.74

(CH_3CH_2NC=) (ppm) FTIR (nujol) νmax: 3853.08, 3748.94, 3629.37, 2854.13, 2360.44, 2339.23, 1992.11, 1868.68, 1747.19, 1716.34, 1683.55, 1590.99, 1419.35, 1274.72, 1180.22, 1072.23, 1043.30, 719.32, 669.18 (cm^{-1}). HPLC; t_R = 36.20 min, column C-4 peptide, gradient mix: 0.0 min [100% A], 15-25.0 min [100% B], 25.1-45.0 min [100% C], 45.1-55.00 min [100% A]; flow: 1 mL/min. HRMS (ESI+) calculated for $C_{87}H_{144}N_{10}O_{15}S_2$ *m/z* 1633.0254, found 1634.2624 $(M + H)^+$.

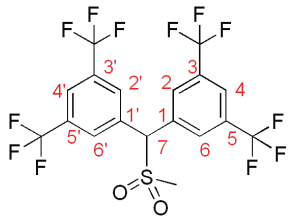
6-Rhodamine-sulfunoamide-2-(amido-Gd(III) {1,4,7,10-tetra azacyclododec-1-yl}-acetic acid) hexa-amido-*N*,*N*-dioctadecylacetamide, **27**.



The fluorescent lipid **28** (20.02 mg, 0.0539 mmol) was added to a round-bottom flask and stirred in pure distilled water (80 mL). To this was added a stoichiometric amount of $Gd.Cl_3.6H_2O$ (88 mg, 0.0539 mmol) and the reaction stirred at 90 ºC for 12 h. The water was freeze-dried to yield a dark purple solid (93 mg, 96%, decomposition. = 327-330 ºC). R_f [CH_2Cl_2: MeOH: H_2O: 34.5: 9: 1 v/v] 0.20. FTIR (nujol) νmax: 3748.94, 3673.73, 2854.13, 2339.23, 1920.75, 1868.68, 1772.26, 1683.55, 1573.63, 1419.35, 1396.21, 1274.72, 1178.29, 1072.23 (cm^{-1}). HPLC; t_R = 34.19 min, column C-4 peptide, gradient mix: 0.0 min [100% A], 15-25.0 min [100% B], 25.1-45.0 min [100% C], 45.1-55.00 min [100% A]; flow 1: mL/min. λ_{ex}: 545 nm and λ_{em}: 568 nm in MeOH MS (ESI+) calculated for $C_{87}H_{141}GdN_{10}O_{15}S_2$ *m/z* 1787.926, found 1809.50 $(M + Na)^+$.

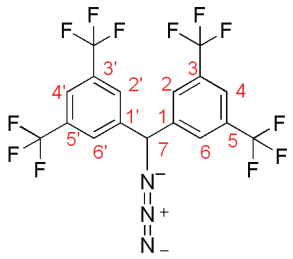
8.1.7 Towards the Synthesis of Trimodal Gadolinium Lipids

Bis(3,5-bis(trifluoromethyl)phenyl)methyl methanesulfonate, **50**.



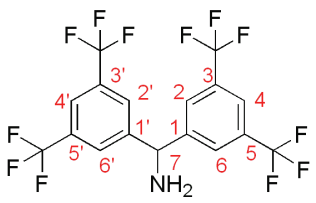
Methanesulfonyl chloride (340 µL, 7.384 mmol) and 3,3',5,5'-tetrakis (trifluoromethyl)benzhydrol **49** (2.0 g, 4.384 mmol) were added to a flask equipped with a stirrer bar. Anhydrous CH_2Cl_2 (24 mL) was also added followed by Et_3N (1.22 mL, 8.768, 2 eq.) and the reaction stirred at room temperature for 12 h. The solvent was removed *in vacuo* and the mixture dissolved in CH_2Cl_2 (20 mL) and then extracted with 0.1M HCl (2 x 10 mL), $NaHCO_3$ (2 x 10 mL) and finally washed with brine (2 x 10 mL). The organic layer was dried over $MgSO_4$, filtered and then reduced *in vacuo* to yield a creamy yellow solid (1.41 g, 60%, mp = 100-106 ºC). R_f [EtOAc: Hexane: 1: 9 v/v] 0.22. ^{1}H NMR (400 MHz, $CDCl_3$) δ_H (ppm) 7.94 (s, 2H, H_4 and $H_{4'}$), 7.90 (s, 1H, H_7), 7.83 (d, 4H, J 9.6, H_1, H_6 and $H_{1'}$, $H_{6'}$), 3.03 (s, 3H, CH_3). ^{13}C NMR (400 MHz, $CDCl_3$) δ_C (ppm) 139.64 (C_1 and $C_{1'}$), 133.16 (C_3, C_5 and $C_{3'}$, $C_{5'}$), 127.79 (C_2, C_6 and $C_{2'}$, $C_{6'}$), 124.74 (CF_3 x 4), 121.47 (C_4 and $C_{4'}$), 80.06 (C_7), 39.48 (-SCH_3) (ppm). FTIR (nujol) νmax: 3743.15, 3066.26, 2856.06, 2356.59, 1830.12, 1697.05, 1635.34, 1517.70, 1280.50, 1143.58, 908.308, 850.454, 790.67, 669.18 (cm^{-1}). HRMS (ESI+) calculated for $C_{18}H_{10}F_{12}O_3S$ *m/z* 518.021, found 553.521 $(M + Cl)^+$.

Bis(3,5-bis(trifluoromethyl)phenyl)methyl azide, **51**.



The mesylated compound **50** (1.53 g, 2.869 mmol) and sodium azide (1.87 g, 28.690 mmol) were added to an oven dried flask and dissolved in DMF (10 mL). The reaction was stirred at 80 ºC for an overnight period. The solvent was removed *in vacuo* and the product purified with flash coloumn chromatography (eluted with EtOAc: Hexane: 1: 19 v/v) to give a yellow oil (681.0 mg, 49%). R_f [EtOAc: Hexane: 1: 9 v/v] 0.45. ^{1}H NMR (400 MHz, $CDCl_3$) δ_H (ppm) 8.27 (s, 1H, H_4 and $H_{4'}$), 8.23 (s, 2H, H_2 and H_6, $H_{2'}$ and $H_{6'}$) (ppm). ^{13}C NMR (400 MHz, $CDCl_3$) δ_C (ppm) 137.63 (-C_1 and –$C_{1'}$), 132.65 (-C_3, -C_5 and –$C_{3'}$, -$C_{5'}$), 129.88 (-C_2, -C_6 and –$C_{2'}$, -$C_{6'}$), 126.92 (4 x -CF_3), 121.29 (-C_4 and –$C_{4'}$) (ppm). FTIR (nujol) νmax: 3741.23, 2856.06, 2360.44, 1876.68, 1857.11, 1837.83, 1731.76, 1687.41, 1548.56, 1280.50, 1135.87, 904.45, 842.74, 757.88, 671.11 (cm^{-1}). HRMS (ESI-) calculated for $C_{17}H_7F_{12}N_3^-$ *m/z* 481.0454, found 504.0378 $(M + Na)^-$.

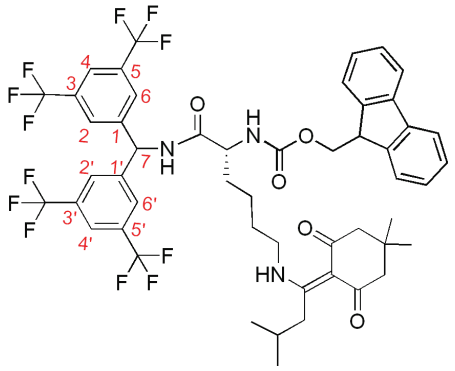
Bis(3,5-bis(trifluoromethyl)phenyl)methyl amine, **52**.



Azide **51** (1.07 g, 2.222 mmol) and triphenylphosphine (1.17 g, 4.444 mmol) were added to a flask followed by DMF (10 mL) and the reaction stirred at room temperature for an hour. Distilled H_2O (6 mL) was then added and the reaction stirred

further for 12 h at 70 ºC. The solvents were then reduced *in vacuo* and the crude mixture purified by flash coloumn chromatography (eluted with EtOAc: Hexane: 1:19 v/v) to give a white solid (400 mg, 40%, mp = 140-143 ºC). R_f [EtOAc: Hexane: 1: 19 v/v] 0.10. ^{1}H NMR (400 MHz, $CDCl_3$) δ_H (ppm) 7.73 (s, 1H, H_4 and $H_{4'}$, *J* 40.0), 7.33 (s, 2H, H_2 and H_6, $H_{2'}$ and $H_{6'}$, *J* 51.2) 2.20 (s, 2H, NH_2) (ppm). ^{13}C NMR (400 MHz, $CDCl_3$) δ_C (ppm) 137.63 (-C_1 and –$C_{1'}$), 132.46 (-C_5, –C_3 and –$C_{5'}$, -$C_{3'}$), 131.14 (-C_2, -C_6 and –$C_{2'}$, -$C_{6'}$), 124.00 (-C_4 and –$C_{4'}$), 62.13 (-C_7) (ppm). FTIR (nujol) νmax: 3741.23, 2857.99, 2360.44, 1876.40, 1857.11, 1731.76, 1702.84, 1650.77, 1548.56, 1525.42, 1513.85, 1378.85, 1058.73 (cm^{-1}). HRMS (ESI+) calculated for $C_{17}H_9F_{12}N$ *m*/*z* 454.0543, found 454.2927 $(M + H)^+$.

9H-fluoren-9-yl-methyl 1-(bis(3,5-bis(trifluoromethyl)phenyl)methylamino)-6-(1-(4,4-dimethyl-2,6-dioxocyclohexylidene)-3-methylbutylamino)-1-oxohexan-2-yl-carbamate **54**.



The primary amine **52** and Fmoc-lys(ivDde)-OH **53** were added to an oven dried flask equipped with a stirrer bar. Anhydrous DMF (10 mL) was also added and the reaction stirred. HBTU and DMAP were added to the reaction and the reaction stirred at 40 ºC for 48 h. The solvent was removed *in vacuo* and the mixture dissolved in CH_2Cl_2 (30 mL) and subjected to firstly, an acidic work up with 7% citric acid (x 2, 20 mL) and then the organic layer was washed with NaHCO3 (x 2, 20 mL) and finally washed with brine (x 2, 20 mL). The organic layer was dried over MgSO4, filtered and purified by flash coloumn chromatography (eluted with EtOAc: Hexane: 1: 4 v/v) and reduced *in vacuo* to yield a bright yellow oil (533.20 mg, 60%). R_f [EtOAc: Hexane: 3: 7 v/v] 0.53. ^{1}H NMR (400 MHz, $CDCl_3$) δ_H (ppm) 7.94 (s, 2H, H_4 and $H_{4'}$), 7.90 (s, 1H, H_7), 7.83 (d, 4H, *J* 9.6, H_1, H_6 and $H_{1'}$, $H_{6'}$), 3.03 (s, 3H, CH_3). ^{13}C NMR (400 MHz, $CDCl_3$)

δ_C (ppm) 139.64 (*C*$_1$ and *C*$_{1'}$), 133.16 (*C*$_3$, *C*$_5$ and *C*$_{3'}$, *C*$_{5'}$), 127.79 (*C*$_2$, *C*$_6$ and *C*$_{2'}$, *C*$_{6'}$), 124.74 (*C*F_3 x 4), 121.47 (*C*$_4$ and *C*$_{4'}$), 80.06 (*C*$_7$), 39.48 (-S*C*H_3) (ppm). FTIR (nujol) νmax: 3741.41, 2857.99, 2360.44, 1876.40, 1733.69, 1700.91, 1689.34, 1650.77, 1548.56, 1525.42, 1056.80 (cm^{-1}). HPLC; t_R = min, column C-4 peptide, gradient mix: 0.0 min [100% A], 15-25.0 min [100% B], 25.1-45.0 min [100% C], 45.1-55.00 min [100% A]; flow: 1 mL/min. HRMS (ESI+) calculated for $C_{51}H_{49}F_{12}N_3O_5$ *m/z* 1011.3481, found 1075.7091 $(M + Zn)^+$.

8.1.8 Xylenol Orange Test

The presence of free gadolinium ions in Gd incorporated compounds was determined by measuring the absorbance at 573 nm of a mixture of xylenol orange solution (990 μL, 0.5 mM in sodium acetate buffer (0.1 M, pH 5.2) and test solution (in 1:1 MeOH: CH_2Cl_2) containing the Gd compound (10 μL). Extinction coefficient ε = 20, 700 L mol^{-1} cm^{-1} whereby [Free Gd] = A573/ε.

8.1.9 Chloroanil Test

To 1-5 mg of resin was added one drop of 2% acetaldehyde in DMF (v/v) followed by one drop of 2% p-chloranil in DMF (w/v). The sample was allowed to stand at room temperature for 5 min. Blue stained beads indicate presence of secondary amines.

8.1.10 MRI Analysis of Gd.DOTA.DSA and Gd.DTPA.BSA

For T_1 analysis, Gd.DOTA.DSA **2**, Gd.DTPA.BSA **19**, and controls of the metal free compound, and Magnevist (Schering AG, Germany) were added to water to give a final concentration of 0.5 mM. The solutions (200 μL) were placed in eppendorf tubes and T_1 relaxation values measured on a 4.7T Varian MR scanner at ambient temperature. For relaxivity measurements; gadolinium liposome formulations were prepared in order to obtain five different gadolinium concentrations between 0.20 to 0.66 μM in 200 μL of distilled water and the molar relaxivity r_1 (mM^{-1} s^{-1}) determined (see **8.1.11** for liposome preparation method). T_1 values were obtained using saturation recovery experiments performed with a standard spin-echo sequence and a 2 mm single slice acquisition (TR = 50, 100, 200, 300, 500, 700, 1200, 3000, 5000, 7000 ms, TE = 15 ms), number of signal averages; 2, FOV; 70 × 70 mm^2, collected into a matrix of 256 × 128.

8.1.11 Liposome Preparations

All lipids were stored as stock solutions in anhydrous organic solvents ($CHCl_3$, MeOH or a mixture of both), at – 20 ºC under argon. Liposomes were made with a range of defined molar ratios of individual lipids to give a predetermined total lipid concentration of 1.2 mg mL^{-1} in water for *in vitro* and 10, 15 or 30 mg mL^{-1} in HEPES (20 mM, NaCl 135 mM, pH 6.5) for *in vivo* experiments. Fluorescent liposomes always contained 0.5 mol% and 1 mol % DOPE-Rhodamine (Avanti Polar Lipids inc. USA) for *in vitro* and *in vivo* experiments respectively (IM injected liposomes contained no fluorescent lipid). Appropriate volumes of each lipid stock were placed in a round bottom flask (typically 5 mL) containing distilled $CHCl_3$ (500 µL) and stirred to ensure thorough mixing of the lipids. The solvent was slowly removed *in vacuo* to ensure production of an even lipid film. The film was re-hydrated with water or buffer at a defined volume. The resulting solution was sonicated for 5-8 min for *in vitro* formulations and 30 min (at 30 ^{o}C) for *in vivo* formulations in order to form gadolinium liposomes of appropriate size. The pH of the liposomal suspension was checked by pH Boy (Camlab Ltd., UK), and if appropriate adjusted to neutral by addition of aqueous solutions of NaOH (0.99 M) and HCl (0.99 M). For each preparation, the size of liposomes was measured by photon correlation spectroscopy (PCS) to ensure a size distribution of on average, below 250 nm for *in vitro* experiments and 100 nm for *in vivo* experiments.

8.1.12 In Vitro Fluorescent Cell Uptake Assay with Gd.DOTA.DSA Liposomes

At 24 h prior to gadolinium liposome uptake experiments, adherent HeLa cells were grown in Dulbecco's-Modified Eagle culture medium (DMEM) with 10% Fetal calf serum (FCS) and 1% penicillin-streptomycin (Sigma-Aldrich), in a 48-well plate (80,000 cells per well, 250 µL of complete medium) and in a wet (37 ºC) 10% CO_2 / 90% air atmosphere. The cells were grown until 80% confluent. The media was then removed and replaced with fresh media (same volume as previous). Bimodal gadolinium liposomes (see **Table 4**) containing 0.5 mol % DOPE-Rhodamine were prepared (see **8.1.11** for preparation method) then added at three different doses (6, 12, and 18 µg) to the wells, swirled to ensure even dispersion and then incubated in a wet (37 ºC) 10 % CO_2 / 90% air atmosphere for either 4, 6, 8 or 10 h. The amount of Gd per liposome sample added to each well was as follows; for the 6 µg gadolinium liposome dose, liposomes **1** and **2** contained; 0.358 µg , liposomes **3** and **4**; 0.449 µg, liposomes **5** and **6**; 0.554 µg and liposomes **7** and **8**; contained 610.32 µg of Gd.

For the 12 µg gadolinium liposome dose, liposomes **1** and **2** contained; 0.716 µg, liposomes **3** and **4**; 0.898 µg, liposomes **5** and **6**; 1.108 mg, liposomes **7** and **8**; 1.220 mg of Gd. Finally, for the 18 µg gadolinium liposome dose, liposomes **1** and **2** contained; 1.074 mg, liposomes **3** and **4**; 1.347 mg, liposomes **5** and **6**; 1.662 mg and liposomes **7** and **8**; 1.831 mg of Gd. After liposome uptake the cells were washed with PBS (2 x 200 µL) and then treated with lysis buffer (100 µL per well). Cell lysate (80 µL) was diluted with MeOH (50 µL) and $CHCl_3$ (300 µL). The resulting solution was vigorously vortexed and then allowed to separate into 2 phases (organic and aqueous). The organic layer was isolated and its fluorescence was recorded on a RF-5301PC Shimadzu spectrofluorophotometer (λ_{ex} 545 nm, λ_{em} 585 nm). As a positive control: control gadolinium liposomes (6, 12 or 18 µg) were added to the lysate of untreated cells, to provide a 100% liposome uptake result. The amount of cellular protein was quantified with a bicinchoninic acid base protein (BCA) assay (Pierce, Rockford, IL, USA).

8.1.13 MTT Cell Viability Assay with Gd.DOTA.DSA Liposomes

Twenty four hours prior to the MTT assay, adherent HeLa cells were grown in DMEM with 10% FCS and 1% penicillin-streptomycin (Sigma-Aldrich), in 48-well (4×10^4 cells per well, 250 µL of complete medium) plates and in a wet (37 ºC) 10% CO_2 / 90% air atmosphere. The cells were grown until 80% confluent and the media was then removed and replaced with fresh media (same volume as previous). Gadolinium liposome formulations **1**, **2** and **7** (see **Table 4**) were added to each well at three doses (6, 12 and 18 µg/well, see **8.1.11** for exact Gd content per liposome dose), and the cells were incubated in a wet (37 ºC) 10 % CO_2 / 90% air atmosphere for either 4, 6, 8, and 10 hours. In addition, at the end of each incubation period the cells were washed with PBS and then incubated for a further 24 h period. A cell proliferation kit (MTT, Roche) assay was used to assess the cells viability post liposome exposure. Briefly, after each uptake period, the media was removed and the cells washed with PBS (1 × 0.5 mL). Then fresh DMEM media (with FCS and streptomycin) was added to the cells (250 µL), followed by addition of the yellow MTT reagent (15 µL) and subsequent incubation for 2 h. The appearance of purple spots and patches was visible at this stage. The media was removed and Formazan solubilising solution was added (~ 100 µL) and the plates were incubated in a wet (37 ºC) 10 % CO_2 / 90% air atmosphere overnight. The lysates were then transferred to 96 welled plates and the absorbance of each well and therefore the amount of purple Formazan was measured at 550 nm with a microplate reader.

8.1.14 Lactate Dehydrogenase Toxicity Assay (LDH) with Gd.DOTA.DSA Liposomes

Twenty four hours prior to the LDH assay, adherent HeLa cells were grown in DMEM with 10% FCS and 1% penicillin-streptomycin (Sigma-Aldrich), in 48-well (4×10^4 cells per well, 250 µL of complete medium) plates and in a wet (37 ºC) 10% CO_2 / 90% air atmosphere. The cells were grown until 80% confluent and the media was then removed and replaced with fresh media (same volume as previous). Gadolinium liposome formulations **1**, **2** and **7** (see **Table 4**) were added to each well at three doses (6, 12 and 18 µg/well, see **8.1.11** for exact Gd content per liposome dose), and the cells were incubated in a wet (37 ºC) 10 % CO_2 / 90% air atmosphere for either 4, 6, 8, and 10 hours. In addition, at the end of each incubation period the cells were washed with PBS and then incubated for a further 24 h period. The LDH assay was carried out using the CytoTox 96® Non-Radioactive Cytotoxicity Assay (Promega, USA). In brief, the supernatant from the cells was transferred to 96-well plates (150 µL) and this was spun down in a centrifuge (2 000 rpm for 10 min), the remaining media was removed from the cells and they were washed with PBS, and lysis buffer was added to the wells, and the plate incubated at 37 ºC for 30 min. The supernatant from the spun cells was transferred to a 96-well plate (50 µL) and cell lysates were also added to the other half of this plate (50 µL). The LDH substrate mix was added to these wells (50 µL) and the plate incubated in darkness for 30 min. The reaction was stopped with the addition of acetic acid (50 µL) and the wells measured for their fluorescence at 490 nm on a microplate reader. The cell death from cytotoxicity of the added gadolinium liposomes was calculated as follows: % cell death from cytotoxicity = (% LDH released from these cells) – (% LDH released from control cells).

8.1.15 MRI Analysis of Cells Labelled with Gd.DOTA.DSA Liposomes

Twenty four hours prior to liposome uptake, adherent HeLa cells were grown in DMEM with 10% FCS and 1% penicillin-streptomycin (Sigma-Aldrich), in a 25 cm^3 culture flask (5×10^5 cells per well, 5 mL of growth medium) and in a wet (37 ºC) 10% CO_2 / 90% air atmosphere. The cells were grown until 80% confluent and the media was then removed and replaced with fresh media. Gadolinium liposomes were prepared (see section **8.1.11**) and then added to each flask, swirled to ensure even dispersion and then incubated in a wet (37 ºC) 10 % CO_2 / 90% air atmosphere for 8 h (125 µL of 1.2 mg mL^{-1} liposome solution containing 8.95 µg Gd (0.057 µM), the optimal dose was scaled up ~ 12.5 fold from the dose used for the *in vitro*

fluorescence assay to label approximately 1 x 10^6 cells in culture, since the HeLa cell population was expected to double over 24 h). After liposome uptake the cells were washed with PBS (2 × 2 mL) and then treated with trypsin-EDTA (500 µL trypsin, 1mM EDTA) for 2 min at 37 ºC. DMEM (complete, 3 mL) was added to neutralise the trypsin. The cells were washed with PBS and then centrifuged in PBS buffer (1 mL), the solution was decanted and the cells reconstituted in PBS by vortexing and spun (1500 rpm for 5 min) into pellets in eppendorf tubes filled with 200 µL PBS. The tubes were imaged whilst placed in a plastic sample holder, and T_1 values were measured on a 4.7T Varian MR Scanner. T_1 values were obtained from saturation recovery experiments performed with a standard spin-echo sequence and a 10 mm single slice acquisition in the sagittal plane (TR = 50, 100, 200, 300, 500, 700, 1200, 3000, 5000, 7000 ms, TE = 15 ms), 4 signal averages, FOV; 100 × 100 mm^2, collected into a matrix of 256 × 128. As negative controls; cells treated with liposomes containing no Gd (substituted for by using the Gd free lipid DOTA.DSA), untreated cells and an eppendorf containing PBS buffer were also imaged.

8.1.16 Fluorescence Microscopy of Cells Labelled with Gd.DOTA.DSA Liposomes

Twenty four hours prior to gadolinium liposome uptake, adherent HeLa cells were grown in DMEM with 10% FCS and 1% penicillin-streptomycin (Sigma-Aldrich), in a 6-well plate (1.25 x 10^5 cells per well, 3 mL of complete medium) fitted with plastic microscopy slides, in a wet (37 ºC) 10% CO_2 / 90% air atmosphere. The cells were grown until 80% confluent and the media was then removed and replaced with fresh media (same volume as previous). Fluorescent gadolinium liposomes (formulation **1**, **Table 4**, prepared as described in **8.1.11**), 37.5 µg per well, were then added to appropriate wells, swirled to ensure even dispersion and then incubated in a wet (37 ºC) 10 % CO_2 / 90% air atmosphere for 8 h (31.25 µL of 1.2 mg mL^{-1} liposomes containing 2.24 µg of Gd (0.014 µmol) was added, based on scaling up of the optimal dose from the *in vitro* fluorescence assay, although this dose was doubled in order to account for the doubling HeLa cell population within 24 h). After liposome uptake the media was removed and the cells were washed with PBS (× 2), heparin (× 1 (20 mg/mL), in order to remove unbound liposomes from cell surface), PBS (× 2), paraformaldehyde (PFA, × 1 (20 min at 37 °C)), PBS (× 2), glycine (× 1 (20 mM, 20 min at 37 °C)), and finally PBS (× 2). The slides were removed from the wells and fixed. Microscopy images were obtained on an Olympus 251 scope, and confocal images were obtained using an upright Leica instrument.

8.1.17 Plasmid DNA Transfection with Gadolinium Lipoplexes formed with Gd.DOTA.DSA

Gadolinium lipoplexes were prepared as per the Trojene® transfection protocol (Avanti Polar Lipids Inc. USA). At 24 h prior to transfection, adherent HeLa cells were grown in DMEM media supplemented with 10% FCS and 1% penicillin-streptomycin (Sigma-Aldrich), in 24-well (6 x 10^4 cells per well, 300 µL of complete medium) plates and in a wet (37 ºC) 10% CO_2 / 90% air atmosphere. The cells were grown until 80% confluent. The media was then removed and replaced with fresh media. Gadolinium lipoplexes, Gd Free lipoplexes (made using the DOTA.DSA lipid), and the Trojene lipoplex mixtures were made by the addition of a 12:1 liposome: DNA w/w ratio of DNA to the preformed liposomes made as described previously (see **8.1.11**, liposome concentration; 1.2 mg mL^{-1}, dose; 12:1 µg of liposome to DNA), and were added to each well, swirled to ensure even distribution, and then incubated in a wet (37 ºC) 10 % CO_2 / 90% air atmosphere for 4 h. The media was removed, and the cells washed with PBS and then fresh media was added (300 µL). The cells were then incubated for a further 24 h. Before the luciferase assay was carried out, the cells were washed with PBS and harvested with lysis buffer (100 µL).

Luciferase Reporter Assay

Luciferase gene expression was measured with the Luciferase Assay System purchased from Promega. Light output readings were done on a Berthold Lumal LB 9507 luminometer. Transfection efficiency, measured in relative light units (RLU) was normalised to the total mass of cellular protein using a bicinchoninic acid base protein (BCA) assay (Pierce, Rockford, IL, USA).

8.1.18 Inductively Coupled Plasma – Atomic Emission Spectrometry Analysis of Cell Lysates Post-incubation with Gd.DOTA.DSA Liposomes

At 24 h prior to gadolinium liposome uptake experiments, adherent HeLa cells were grown in DMEM with 10% FCS and 1% penicillin-streptomycin (Sigma-Aldrich), in a 48-well plate (80,000 cells per well, 250 µL of complete medium) and in a wet (37 ºC) 10% CO_2 / 90% air atmosphere. The cells were grown until 80% confluent. The media was then removed and replaced with fresh media (same volume as previous). Gadolinium liposome **1** (see **Table 4**) was then added at the optimised dose of 12µg to each well, swirled to ensure even dispersion and then incubated in a wet (37 ºC) 10 % CO_2 / 90% air atmosphere for 8 h. After liposome uptake the cells were washed

with PBS (2 x 200 µL) and then treated with lysis buffer (200 µL per well). Samples containing 100% of the gadolinium liposome dose (diluted in water to a total volume of 200 µL) and the cell lysates (200 µL) were submitted for ICP-AES measurements of ^{157}Gd content. Briefly; 150 µL of each sample was pipetted and diluted to 3.75 ml with 2% nitric acid to give a total dilution of 1 in 25 and then analysed on a Varian VIST PRO instrument. All data were corrected for these dilutions and the values; a blank 2% nitric acid sample was also analysed.

8.1.19 Preliminary Intramuscular Injections of Gd.DOTA.DSA Liposomes

High concentration DOTAP and Gd.DOTA.DSA liposomes (50: 50 mol %, 10 mg mL^{-1}) were prepared (see **8.1.11** for preparation method) in HEPES buffer (20 mM, NaCl 135 mM, pH 6.5). Control liposomes were also prepared in a similar manner, with the Gd free DOTA.DSA lipid. Each sample (30 µL) was then injected into the hind leg muscle of C57BL/6 mice previously anaesthetised with an isoflurane/O_2 mix. The mice were then imaged at 5 min, 24 h and 7 days post injection at 4.7 T in the axial plane (spin echo sequence: TR = 400 ms, TE = 30 ms, FOV = 45 x 45 cm^2, averages: 4, matrix size: 256 x 128, slice thickness: 2.0 mm, and 4 slices). T_1 measurements of the injected dose were carried out by imaging eppendorfs containing the gadolinium liposomes and the control Gd free liposomes at 4.7 T in the coronal plane (spin-echo sequence: TR = 50, 100, 200, 300, 500, 700, 1200, 3000, 5000, 7000 ms, TE = 15 ms), 4 signal averages, FOV; 100 × 100 mm^2, collected into a matrix of 256 × 128, slice thickness: 10.0 mm, and 1 slice).

8.1.20 Serum Aggregation Analysis of PEGylated Gadolinium Liposomes Formulated with Gd.DOTA.DSA

Liposomes were prepared as previously described (see section **8.1.11** and **Table 6** for formulations) and added (50 µL) to a 1:1 mixture of FCS/HEPES (20 mM, NaCl, 135 mM, pH 6.5) buffer (total volume: 200 µL). Their initial size prior to incubation was measured using photon correlation spectroscopy. The liposomes were then incubated at 37 °C and their size and poly dispersity index measured every 60 min over 10 h. Control liposomes contained the DOTA.DSA lipid in place of Gd.DOTA.DSA (see **Table 7**).

8.1.21 Zeta Potential Measurements of PEGylated Gadolinium Liposomes Formulated with Gd.DOTA.DSA

PEGylated gadolinium liposome formulation **10** prepared as per section **8.1.11**, was added to a plastic electrode cuvette (1 mL, total liposome concentration: 1.2 mg mL^{-1}) and the electrophoretic mobility was calculated. The electrophoretic mobility is obtained by performing an electrophoresis experiment on the sample and measuring the velocity of the particles using Laser Doppler velocimetry (measurements carried out at 25 °C, on a Zetasizer Nanoseries, Nano-ZS).

8.1.22 Cryo-TEM of PEGylated Gd.DOTA.DSA Liposomes

Gadolinium liposome formulation **10** was prepared as per section **8.1.11** in water (total lipid concentration of 1.2 mg mL^{-1}) and sonicated for 30 min to ensure a size distribution of ~ 100 nm. The liposomes were then dropped onto the surface of copper grids, and excess liquid was blotted using filter paper in an environment chamber with a relative humidity of 100% at 297K. The liposomes were frozen in liquid ethane and the vitrified specimens were stored under liquid nitrogen and placed in the TEM (temperature was maintained at -184 ºC). Images were obtained using a Philips CM200 microscope operating at 200 kV.

8.1.23 Relaxivity Measurement of PEGylated Gd.DOTA.DSA Liposomes

PEGylated gadolinium liposomes were prepared as previously described (see section **8.1.11** and **Table 8** for formulations, at a total liposome concentration of 3 mg mL^{-1}) in HEPES (20 mM, NaCl, 135 mM, pH 6.5) buffer. These liposomes were prepared in order to obtain five different gadolinium concentrations ranging between 0.089 to 0.384 µmol. The liposome solutions were placed in small eppendorf tubes (200 µL), imaged at 4.7 T in the coronal plane, T_1 values obtained, and the molar relaxivity r_1 ($mM^{-1}\ s^{-1}$) determined. T_1 values were acquired using saturation recovery experiments performed with a standard spin-echo sequence and a 2 mm single slice acquisition (TR = 50, 100, 200, 300, 500, 700, 1200, 3000, 5000, 7000 ms, TE = 15 ms), number of signal averages; 2, FOV; 70 × 70 mm^2, collected into a matrix of 256 × 128.

8.1.24 Mouse Tumour Model

IGROV-1 cells (5 x 10^6 /1 mL PBS) were implanted into the flanks of 6-8 weeks old Balb/c nude mice for generation of subcutaneous tumours. After ~2 weeks (estimated tumor weights 40-50 mg) the mice were anaesthetized with an isoflurane/O_2 mix and placed into a quadrature ^{1}H volume coil and positioned into the magnet. Baseline scans were obtained and then the mice were injected intravenously via lateral tail vein with either a 200 µL liposome solution (HEPES (20 mM, NaCl 135 mM, pH 6.5)) and imaged at 4.7 T (spin echo sequence: TR = 400-2800 ms, TE = 10 ms, FOV = 45 x 45 cm^2, averages: 1, matrix size: 256 × 128 thickness: 2.0 mm, and 20 slices). Liposomes were prepared containing a total of 9.87 µM of Gd for the PEGylated liposome formulation **10**, and 4.84 µM of Gd for the folate targeted PEGylated liposome formulation **11**. The total amount of Gd concentration in PEGylated liposome formulation **13** was 2.44 µM. The injected mice were imaged at 3, 16 and 24 h post injection when liposome formulation **10** was injected; they were imaged at 2, 16 and 24 h post injection when liposome formulation **11** was injected and finally 2, 14 and 24 h post injection when liposome formulation **13** was used.
All procedures on animals were conducted in accordance with UK Home Office regulations and the Guidance for the Operation of Animals (Scientific Procedures) Act (1986).

8.1.25 Laser Ablation – Inductively Coupled Mass Spectrometry (LA-ICP MS) of Tumour Sections Post-administration of Gd.DOTA.DSA Liposomes

Tumour sections were mounted on glass slides and no additional sample preparation was carried out. A 266nm Nd:YAG laser system (NewWave, Cambridgeshire) was used in conjunction with an ICP-MS (HP4500, Agilent Technologies, UK) for the analysis of all tissue samples. A 20um laser beam diameter was utilised with a scan speed of 25 um/s.

8.1.26 Immunohistochemistry and FACS Analysis of Folate Receptor Expression

Microscopy immunohistochemistry of folate receptor expression
At 24 h prior to microscopy experiment, adherent IGROV-1, OVCAR-3 and LS174T cells were grown on cover slips in folic-acid free RPMI media with 10% FCS and 1%

penicillin-streptomycin (Sigma-Aldrich), in a 6-well plates (125, 000 cells per well, 3 mL of complete medium) and in a wet (37 ºC) 10% CO_2 / 90% air atmosphere. The cells were grown until 80% confluent. The media was then removed and the cells washed with PBS. Non-specific cell binding was blocked by incubating the cells in 8% BSA/PBS (1 mL) for 1 h at 4 ºC. The primary antibody (MAb Mov18/ZEL, Axxora, UK) selective for the α-FR was then added to each well (5 µg/mL in 3% BSA/PBS (total volume 1 mL)) and the cells incubated at 4 °C for 1 h (for each cell line one well contained no antibody). The cells were washed with PBS (2 x 1 mL), and the 2° antibody (Goat anti-body IgG, FITC conjugated, Santa Cruz Biotechnology, USA) was then added to the cells (1: 1000 dilution, in 3% BSA/PBS (total volume 1 mL)) and the cells were incubated at 4 °C for a further hour. The wells were then washed with PBS (3 x 1 mL) and the slides fixed using an anti-fade mounting medium (Promega).

FACS analysis of folate receptor expression

At 48 h prior to FACS experiment, adherent IGROV-1, OVCAR-3, HeLa and SKBR-3 cells were grown in RPMI media (folic-acid free) with 10% FCS and 1% penicillin-streptomycin (Sigma-Aldrich). Cells were grown in 25 cm^3 culture flasks (5 x 10^5 cells per well, 5 mL of growth medium) and in a wet (37 ºC) 10% CO_2 / 90% air atmosphere. The cells were grown until 80% confluent. The media was then removed and the cells washed with PBS. The cells were then treated with trypsin-EDTA (500 µL trypsin, 1mM EDTA) for 2 min at 37 ºC, then transferred to 25 mL falcon tubes and centrifuged (1500 rpm for 5 min). The PBS was removed and the cells were washed furthermore with PBS and centrifuged (1500 rpm for 5 min). The cells were then incubated in 10% FCS, 1% NaN_3 solution (1 mL) for 1 h at 4 ºC. The cells were spun down (1500 rpm for 5 min) and washed with PBS (1 mL) and this was repeated twice more. The primary antibody (MAb Mov18/ZEL) selective for the α-FR was then added to each falcon (5 µg/mL in 3% BSA/PBS (total volume 1 mL)) and the cells incubated at 4 °C for 1 h (for each cell line one well contained no antibody). The cells were centrifuged (1500 rpm for 5 min) and washed with PBS (3 x 1 mL, followed by centrifugation), and the 2° antibody (Goat anti-body IgG, FITC conjugated) was then added to the cells (1: 1000 dilution, in 3% BSA/PBS (total volume 1 mL)) and the cells were incubated at 4 °C for a further hour. The wells were then washed with PBS (3 x 1 mL) and centrifuged (400 rpm for 5 min). The cells were then diluted in 10% FCS/PBS 1% NaN_3 (1 mL) and analysed for their FITC fluorescence on a flow cytometer.

8.1.27 MRI Analysis of Gd.DOTA.Rhoda.DSA

For T_1 analysis, Gd.DOTA.Rhoda.DSA **27**, DOTA.Rhoda.DSA **28** and Gd.DOTA were added to water to give a final concentration of 0.5 mM. The solutions (200 μL) were placed in eppendorf tubes and T_1 relaxation values measured on a 4.7T Varian MR scanner at ambient temperature. For relaxivity measurements; gadolinium liposome formulations were prepared in order to obtain five different gadolinium concentrations between 0.285 and 0.084 μM in 200 μL of distilled water and the molar relaxivity r_1 (mM^{-1} s^{-1}) determined (see **8.1.11** for liposome preparation method). T_1 values were obtained using saturation recovery experiments performed with a standard spin-echo sequence and a 2 mm single slice acquisition (TR = 50, 100, 200, 300, 500, 700, 1200, 3000, 5000, 7000 ms, TE = 15 ms), number of signal averages; 2, FOV; 70 × 70 mm^2, collected into a matrix of 256 × 128.

8.1.28 IGROV-1 Cell Labelling with Gd.DOTA.Rhoda.DSA Liposomes

Cationic liposomes were formulated in water as per the liposome preparation method described in **8.1.11** using CDAN/DOPE/Gd.DOTA.Rhoda.DSA: 50/45/5 mol% (total lipid concentration of 1.2 mg mL^{-1}). The pH of these liposomes was adjusted to ~ 7 and their size assessed using PCS and was found to be on average ~ 250 nm.
At 24 h prior to cell labelling experiments, adherent IGROV-1 cells (5 x 10^5 in 6-welled plate) were grown on cover slips in DMEM media supplemented with 10% FCS and 1% penicillin-streptomycin (Sigma-Aldrich). Cells were grown until 80% confluent. The media was then removed and the cells washed with PBS. Gadolinium liposome formulation **12** was then added to the cells (150 μL, at 1.976 μM of Gd/well) and allowed to incubate with the cells for 8 h. Post uptake the cells were washed with PBS and fixed as described in **8.1.16**.

8.1.29 MRI Visualisation of IGROV-1 Cells Labelled with Gd.DOTA.Rhoda.DSA Liposome Formulation 12

Twenty four hours prior to liposome uptake, adherent IGROV-1 cells were grown in DMEM with 10% FCS and 1% penicillin-streptomycin (Sigma-Aldrich), in a 25 cm^3 culture flask (5 x 10^5 cells per well, 5 mL of growth medium) and in a wet (37 ºC) 10% CO_2 / 90% air atmosphere. The cells were grown until 80% confluent and the media was then removed and replaced with fresh media. Gadolinium liposomes were prepared (see section **8.1.11**) and then added to each flask, swirled to ensure even

dispersion and incubated in a wet (37 ºC) 10 % CO_2 / 90% air atmosphere for 8 h (150 µL, at 1.976 µmol of Gd/well). After liposome uptake the cells were washed with PBS (2 × 2 mL) and then treated with trypsin-EDTA (500 µL trypsin, 1mM EDTA) for 2 min at 37 ºC. DMEM (complete, 3 mL) was added to neutralise the trypsin. The cells were washed with PBS and then centrifuged in PBS buffer (1 mL), the solution was decanted and the cells reconstituted in PBS by vortexing and spun (1500 rpm for 5 min) into pellets in eppendorf tubes filled with 200 µL PBS. The tubes were imaged whilst placed in a plastic sample holder, and T_1 values were measured on a 4.7T Varian MR Scanner. T_1 values were obtained from saturation recovery experiments performed with a standard spin-echo sequence and a 10 mm single slice acquisition in the sagittal plane (TR = 50, 100, ms, TE = 15 ms), 4 signal averages, FOV; 100 × 100 mm^2, collected into a matrix of 256 × 128.

8.1.30 Histology Experiments

Following MRI, the animals were sacrificed and the tumours, livers and kidneys were excised, frozen in liquid nitrogen, embedded in OCT (VWR) embedding fluid and either 10 or 7 µm thick sections cut, mounted on slides and studied for fluorescence microscopy.

9 . References

(1) Piwinica-Worms, D. R. *Journal of Americal College of Radiology* **2004**, *1(suppl)*, 2-3.

(2) Rome, C.; Couillaud, F.; Moonen, C. T. *European Radiology* **2007**, *17*, 305-319.

(3) Blasberg, R. G. a. G., J. *Molecular Imaging* **2002**, *1*, 280-300.

(4) Stegman, L. D.; Rehemtulla, A.; Beattie, B.; Kievit, E.; Lawrence, T. S.; Blasberg, R. G.; Tjuvajev, J. G.; Ross, B. D. *Proceedings- National Academy of Sciences USA* **1999**, *96*, 9821-9826.

(5) Hogemann, D.; Josephson, L.; Weissleder, R.; Basilion, J. P. *Bioconjugate Chemistry* **2000**, *11*, 941-946.

(6) Yang, M.; Baranov, E.; Moossa, A. R.; Penman, S.; Hoffman, R. M. In *Colloquium on auditory neuroscience: development, transduction and integration*; National Academy of Sciences of the United States of America: Irvine, CA, 2000, p 12278.

(7) Nichol, C.; Kim, E. E. *Journal of Nuclear Medicine* **2001**, *42*, 1368-1374.

(8) Shah, K.; Jacobs, A.; Breakefield, X. O.; Weissleder, R. *Gene Therapy* **2004**, *11*, 1175-1187.

(9) Sadelain, M.; Blasberg, R. G. *Journal of Clinical Pharmacology* **1999**, *39*, 34S-39S.

(10) Bogdanov, A.; Tung, C. H.; Bredow, S.; Weissleder, R. *Gene Therapy* **2001**, *8*, 515-522.

(11) Su, W.; Mishra, R.; Pfeuffer, J.; Wiesmuller, K. H.; Ugurbil, K.; Engelmann, J. *Contrast Media and Molecular Imaging* **2007**, *2*, 42-49.

(12) Wunderbaldinger, P.; Bogdanov Jr, A.; Weissleder, R. *European Journal of Radiology* **2000**, *34*, 156 - 165.

(13) Morin, K. W.; Atrazheva, E. D.; Knaus, E. E.; Wiebe, L. I. *Journal of Medicinal Chemistry* **1997**, *40*, 2184-2190.

(14) Schellingerhout, D.; Bogdanov, A.; Marecos, E.; Spear, M.; Breakefield, X.; Weissleder, R. *Human Gene Therapy* **1998**, *9*, 1543-1549.

(15) Bogdanov, A.; Weissleder, R. *Trends in Biotechnology* **1998**, *16*, 5-10.

(16) Jacobs, A. *Lancet* **2001**, 727-728.

(17) Ghambir, S. S. *Nat. Rev. Cancer* **2002**, *2*, 683-693.

(18) Kramm, C. M.; Senaesteves, M.; Barnett, F. H.; Rainov, N. G.; Schuback, D. E.; Yu, J. S.; Pechan, P. A.; Paulus, W.; Chiocca, E. A.; Breakefield, X. O. *Brain Pathology* **1995**, *5*, 345-381.

(19) Tjuvajev, J. G.; Shu Hsia, C.; Joshi, A.; Joshi, R.; Zong Sheng, G.; Balatoni, J.; Ballon, D.; Koutcher, J.; Finn, R.; Woo, S. L. *Cancer Research* **1999**, *59*, 5186-5193.

(20) Moore, A.; Basilion, J. P.; Chiocca, E. A.; Weissleder, R. *Biochimica Et Biophysica Acta* **1998**, *1402*, 239-249.

(21) Weissleder, R.; Moore, A.; Mahmood, U.; Bhorade, R.; Benveniste, H.; Chiocca, E. A.; Basilion, J. P. *Nature Medicine* **2000**, *6*, 351-354.

(22) Bogdanov Jr, A.; Weissleder, R. *Trends in Biotechnology* **2002**, *20*, S11-S18.

(23) Moats, R. A.; Fraser, S. E.; Meade, T. J. *Angewandte Chemie* **1997**, *36*, 726-728.

(24) Louie, A. Y.; Huber, M. M.; Ahrens, E. T.; Rothbacher, U.; Moats, R.; Jacobs, R. E.; Fraser, S. E.; Meade, T. J. *Nature Biotechnology* **2000**, *18*, 321.

(25) Gambhir, S. S.; Barrio, J. R.; Herschman, H. R.; Phelps, M. E. *Nuclear Medicine and Biology* **1999**, *26*, 481-490.

(26) Weissleder, R.; Simonova, M.; Bogdanova, A.; Bredow, S.; Scott Enochs, W.; Bogdanov, A. *Radiology* **1997**, *204*, 425-430.

(27) Kang, H. W.; Josephson, L.; Petrovsky, A.; Weissleder, R.; Bogdanov, A. *Bioconjugate Chemistry* **2002**, *13*, 122-127.

(28) Mountz, J. D.; Hsu, H. C.; Wu, Q.; Liu, H. G.; Zhang, H. G.; Mountz, J. M. *Journal of Cellular Biochemistry* **2002**, *39*, 162-171.

(29) Doubrovin, M.; Serganova, I.; Mayer-Kuckuk, P.; Ponomarev, V.; Blasberg, R. G. *Bioconjugate Chemistry* **2004**, *15*, 1376-1388.

(30) Wu, J. C.; Yla-Herttuala, S. *European Journal of Nuclear Medicine and Molecular Imaging* **2005**, *32*, S346-S357.

(31) Poduslo, J. F.; Curran, G. L.; Peterson, J. A.; McCormick, D. J.; Fauq, A. H.; Khan, M. A.; Wengenack, T. M. *Biochemistry* **2004**, *43*, 6064-6075.

(32) Narula, J.; Kietselaer, B.; Hofstra, L. *Journal of Nuclear Cardiology* **2004**, *11*, 349-357.

(33) Yang, D. J.; Azhdarinia, A.; Wu, P.; Yu, D. F.; Tansey, W.; Kalimi, S. K.; Kim, E. E.; Podoloff, D. A. *Cancer Biotherapy and Radiopharmaceuticals* **2001**, *16*, 73-84.

(34) Murakami, Y.; Takamatsu, H.; Taki, J.; Tatsumi, M.; Noda, A.; Ichise, R.; Tait, J. F.; Nishimura, S. *European Journal of Nuclear Medicine and Molecular Imaging* **2004**, *31*, 469-474.

(35) Russell, J.; O Donoghue, J. A.; Finn, R.; Koziorowski, J.; Ruan, S.; Humm, J. L.; Ling, C. C. *Journal of Nuclear Medicine* **2002**, *43*, 671-677.

(36) Curtet, C.; Maton, F.; Havet, T.; Slinkin, M.; Mishra, A.; Chatal, J. F.; Muller, R. N. *Investigative Radiology* **1998**, *33*, 752-761.

(37) Torigian, D. A.; Huang, S. S.; Houseni, M.; Alavi, A. *Ca* **2007**, *57*, 206-224.

(38) Hylton, N. *Journal of Clinical Oncology* **2006**, *24*, 3293-3298.

(39) Mukherji, S. K.; Chenevert, T. L.; Castillo, M. *Journal of Neuroophthalmology* **2002**, *22*, 118-122.

(40) Haubner, R.; Wester, H. J.; Burkhart, F.; Senekowitsch-Schmidtke, R.; Weber, W.; Goodman, S. L.; Kessler, H.; Schwaiger, M. *Journal of Nuclear Medicine* **2001**, *42*, 326-336.

(41) Glunde, K.; Pathak, A. P.; Bhujwalla, Z. M. *Trends in Molecular Medicine* **2007**, *13*, 287-297.

(42) Beckmann, N.; Kneuer, R.; Gremlich, H. U.; Karmouty-Quintana, H.; Ble, F. X.; Muller, M. *NMR in Biomedicine* **2007**, *20*, 154-185.

(43) Rudin, M.; Weissleder, R. *Nature Reviews Drug Discovery* **2003**, *2*, 123-131.

(44) Britz-Cunningham, S. H.; Adelstein, S. J. *Journal of Nuclear Medicine* **2003**, *44*, 1945-1961.

(45) Bhatnagar, A.; Hustinx, R.; Alavi, A. *Advanced Drug Delivery Reviews* **2000**, *41*, 41-54.

(46) Frank, R.; Hargreaves, R. *Nature Reviews Drug Discovery* **2003**, *2*, 566-577.

(47) Choudhury, R. P.; Fuster, V.; Badimon, J. J.; Fisher, E. A.; Fayad, Z. A. *Arteriosclerosis Thrombosis and Vascular Biology* **2002**, *22*, 1065-1074.

(48) Fox, N. C.; Cousens, S.; Scahill, R.; Harvey, R. J.; Rossor, M. N. *Journal- American Medical Association South East Asia* **2000**, *16*, 27-31.

(49) Silverman, D. H. S.; Small, G. W.; Chang, C. Y.; Lu, C. S.; de Aburto, M. A. K.; Chen, W.; Czernin, J.; Rapoport, S. I.; Pietrini, P.; Alexander, G. E. *Journal- American Medical Association* **2001**, *286*, 2120-2127.

(50) Modo, M. M. J. a. B., J.W.M *Molecular and Cellular MR Imaging*; 1 ed.; CRC Press, 2007.

(51) Modo, M.; Hoehn, M.; Bulte, J. W. M. *Molecular Imaging* **2005**, *4*, 143-164.

(52) Caravan, P.; Ellison, J. J.; McMurry, T. J.; Lauffer, R. B. *Chemical Reviews* **1999**, *99*, 2293-2352.

(53) Frangioni, J. V.; Hajjar, R. J. *Circulation* **2004**, *110*, 3378-3384.

(54) Rogers, W. J.; Meyer, C. H.; Kramer, C. M. *Nature Clinical Practice Cardiovascular Medicine* **2006**, *3*, 554-562.

(55) Mukherjee, S.; Ghosh, R. N.; Maxfield, F. R. *Physiological Reviews* **1997**, *77*, 759-804.

(56) Sun, R.; Dittrich, J.; Le-Huu, M.; Mueller, M. M.; Bedke, J.; Kartenbeck, J.; Lehmann, W. D.; Krueger, R.; Bock, M.; Huss, R. *Investigative Radiology* **2005**, 504-513.

(57) Harisinghani, M. G.; Saini, S.; Weissleder, R.; et al. *American Journal of Roentgenology* **1999**, *172*, 1347-1351.

(58) Weissleder, R. *Radiology* **1994**, *193*, 593.

(59) Corot, C.; Petry, K. G.; Trivedi, R.; Saleh, A.; Jonkmanns, C.; Le Bas, J. F.; Blezer, E.; Rausch, M.; Brochet, B.; Foster-Gareau, P. *Investigative Radiology* **2004**, *39*, 619-624.

(60) Muller, K.; Skepper, J. N.; Posfai, M.; Trivedi, R.; Howarth, S.; Corot, C.; Lancelot, E.; Thompson, P. W.; Brown, A. P.; Gillard, J. H. *Biomaterials* **2007**, *28*, 1629-1642.

(61) Rad, A. M.; Arbab, A. S.; Iskander, A. S.; Jiang, Q.; Soltanian-Zadeh, H. *Journal of Magnetic Resonance Imaging* **2007**, *26*, 366-374.

(62) Fleige, G.; Seeberger, F.; Laux, D.; Kresse, M.; Taupitz, M.; Pilgrimm, H.; Zimmer, C. *Investigative Radiology* **2002**, *37*, 482-488.

(63) Bulte, J. W. M.; Arbab, A. S.; Douglas, T.; Frank, J. A. *Methods in Enzymology* **2004**, 275-302.

(64) Lewin, M.; Carlesso, N.; Tung, C. H.; Tang, X. W.; Cory, D.; Scadden, D. T.; Weissleder, R. *Nature Biotechnology* **2000**, *18*, 410-414.

(65) Gupta, A. K.; Curtis, A. S. *Biomaterials* **2004**, *25*, 3029-3040.

(66) Qian, Z. M.; Li, H.; Sun, H.; Ho, K. *Pharmacological Reviews* **2002**, *54*, 561-588.

(67) Suzuki, Y.; Zhang, S.; Kundu, P.; Yeung, A. C.; Robbins, R. C.; Yang, P. C. *Magnetic Resonance in Medicine* **2007**, *57*, 1173-1179.

(68) Arbab, A. S.; Yocum, G. T.; Rad, A. M.; Khakoo, A. Y.; Fellowes, V.; Read, E. J.; Frank, J. A. *NMR in Biomedicine* **2005**, *18*, 553-559.

(69) Zhang, Z.; Bos, E. J.; Wielopolski, P. A.; Jong-Popijus, M. d.; Bernsen, M. R.; Duncker, D. J.; Krestin, G. P. *Magma* **2005**, *18*, 175-185.

(70) Shapiro, E. M.; Sharer, K.; Skrtic, S.; Koretsky, A. P. *Magnetic Resonance in Medicine* **2006**, *55*, 242-249.

(71) Bulte, J. W. M.; Duncan, I. D.; Frank, J. A. *Journal of Cerebral Blood Flow and Metabolism* **2002**, *22*, 899-907.

(72) Gilad, A. A.; Winnard, P. T.; van Zijl, P. C.; Bulte, J. W. *NMR in Biomedicine* **2007**, *20*, 275-290.

(73) Voisin, P.; Ribot, E. J.; Miraux, S.; Bouzier-Sore, A. K.; Lahitte, J. F.; Bouchaud, V.; Mornet, S.; Thiaudiere, E.; Franconi, J. M.; Raison, L. *Bioconjugate Chemistry* **2007**, *18*, 1053-1063.

(74) Sitharaman, B.; Tran, L. A.; Pham, Q. P.; Bolskar, R. D.; Muthupillai, R.; Flamm, S. D.; Mikos, A. G.; Wilson, L. J. *Contrast Media and Molecular Imaging* **2007**, *2*, 139-146.

(75) Granot, D.; Kunz-Schughart, L. A.; Neeman, M. *Magnetic Resonance in Medicine* **2005**, *54*, 789-797.

(76) Oliver, M.; Ahmad, A.; Kamaly, N.; Perouzel, E.; Caussin, A.; Keller, M.; Herlihy, A.; Bell, J.; Miller, A. D.; Jorgensen, M. R. *Organic and Biomolecular Chemistry* **2006**, *4*, 3489-3497.

(77) Ahrens, E. T.; Flores, R.; Xu, H.; Morel, P. A. *Nature Biotechnology* **2005**, *23*, 983-987.

(78) Srinivas, M., Morel, A., Ernst, L.A., Laidlaw, D.H. and Ahrens, E.T. *Magnetic Resonance Imaging* **2007**, *58*, 725-734.

(79) Klomp, D.; van Laarhoven, H.; Scheenen, T.; Kamm, Y.; Heerschap, A. *NMR in Biomedicine* **2007**, *20*, 485-492.

(80) Caruthers, S. D.; Neubauer, A. M.; Hockett, F. D.; Lamerichs, R.; Winter, P. M.; Scott, M. J.; Gaffney, P. J.; Wickline, S. A.; Lanza, G. M. *Investigative Radiology* **2006**, *41*, 305-312.

(81) Higuchi, M.; Iwata, N.; Matsuba, Y.; Sato, K.; Sasamoto, K.; Saido, T. C. *Nature Neuroscience* **2005**, *8*, 527-533.

(82) Strijkers, G. J.; Mulder, W. J. M.; van Tilborg, G. A. F.; Nicolay, K. *Anticancer Agents in Medicinal Chemistry* **2007**, *7*, 291-306.

(83) Skjold, A.; Kristoffersen, A.; Vangberg, T. R.; Haraldseth, O.; Jynge, P.; Larsson, H. B. *Journal of Magnetic Resonance Imaging* **2006**, *24*, 1047-1055.

(84) Aoki, I.; Takahashi, Y.; Chuang, K. H.; Silva, A. C.; Igarashi, T.; Tanaka, C.; Childs, R. W.; Koretsky, A. P. *Nmr in Biomedicine* **2006**, *19*, 50-59.

(85) Van Meir, V.; Pavlova, D.; Verhoye, M.; Pinxten, R.; Balthazart, J.; Eens, M.; Van der Linden, A. *Neuroimage* **2006**, *31*, 981-992.

(86) Van Der Linden, A.; Meir, V. V.; Tindemans, I.; Verhoye, M.; Balthazart, J. *NMR in Biomedicine* **2004**, *17*, 602-612.

(87) Kraitchman, D. L.; Heldman, A. W.; Atalar, E.; Amado, L. C.; Martin, B. J.; Pittenger, M. F.; Hare, J. M.; Bulte, J. W. M. *Circulation* **2003**, *107*, 2290-2293.

(88) Mayer-Kuckuk, P.; Gade, T. P.; M. Buchanan, I.; Doubrovin, M.; Ageyeva, L.; Bertino, J. R.; Boskey, A. L.; Blasberg, R. G.; Koutcher, J. A.; Banerjee, D. *Molecular Therapy* **2005**, *12*, 33-41.

(89) Hinds, K. A.; Hill, J. M.; Shapiro, E. M.; Laukkanen, M. O.; Silva, A. C.; Combs, C. A.; Varney, T. R.; Balaban, R. S.; Koretsky, A. P.; Dunbar, C. E. *Blood* **2003**, *102*, 867-872.

(90) Jendelova, P.; Herynek, V.; DeCroos, J.; Glogarova, K.; Andersson, B.; Hajek, M.; Sykova, E. *Magnetic Resonance in Medicine* **2003**, *50*, 767-776.

(91) Bulte, J. W. M.; Douglas, T.; Witwer, B.; Zhang, S. C.; Strable, E.; Lewis, B. K.; Zywicke, H.; Miller, B.; van Gelderen, P.; Moskowitz, B. M. *Nature Biotechnology* **2001**, *19*, 1141-1147.

(92) Jacobs, R. E.; Fraser, S. E. *Science* **1994**, 681.

(93) Daldrup-Link, H. E.; Rudelius, M.; Oostendorp, R. A. J.; Settles, M.; Piontek, G.; Metz, S.; Rosenbrock, H.; Keller, U.; Heinzmann, U.; Rummeny, E. J. *Radiology* **2003**, *228*, 760-767.

(94) Frank, J. A.; Miller, B. R.; Arbab, A. S.; Zywicke, H. A.; Jordan, E. K.; Lewis, B. K.; Bryant, L. H.; Bulte, J. W. M. *Radiology* **2003**, *228*, 480-487.

(95) Horak, D.; Babic, M.; Jendelova, P.; Herynek, V.; Trchova, M.; Pientka, Z.; Pollert, E.; Hajek, M.; Sykova, E. *Bioconjugate Chemistry* **2007**, *18*, 635-644.

(96) Modo, M.; Mellodew, K.; Cash, D.; Fraser, S. E.; Meade, T. J.; Price, J.; Williams, S. C. *Neuroimage* **2004**, *21*, 311-317.

(97) Rudelius, M.; Daldrup-Link, H. E.; Heinzmann, U.; Piontek, G.; Settles, M.; Link, T. M.; Schlegel, J. *European Journal of Nuclear Medicine and Molecular Imaging* **2003**, *30*, 1038-1044.

(98) Bulte, J. W.; Zhang, S. C.; van Gelderen, P.; Herynek, V.; Jordan, E. K.; Duncan, I. D.; Frank, J. A. *Proceedings- National Academy of Sciences USA* **1999**, *96*, 15256-15261.

(99) Bulte, J. W., Zhang,S.C., Van Gelderen, P. Herynek, V., Jordan, E.K., Duncan, I.D. and Frank, J.A. *PNAS* **1999**, *96*, 15256-15261.

(100) Modo, M.; Cash, D.; Mellodew, K.; Williams, S. C. R.; Fraser, S. E.; Meade, T. J.; Price, J.; Hodges, H. *Neuroimage* **2002**, *17*, 803-811.

(101) Bos, C.; Delmas, Y.; Desmouliere, A.; Solanilla, A.; Hauger, O.; Grosset, C.; Dubus, I.; Ivanovic, Z.; Rosenbaum, J.; Charbord, P. *Radiology* **2004**, *233*, 781-789.

(102) Hsiao, J. K., Tai., M.F., Chu, H.H., Chen, S.T., Li, H., Lai, D.M., Hsieh, S.T., Wang, J.L. and Liu, H.M. *Magnetic Resonance Imaging* **2007**, *58*, 717-727.

(103) Adonai, N.; Nguyen, K. N.; Walsh, J.; Iyer, M.; Toyokuni, T.; Phelps, M. E.; McCarthy, T.; McCarthy, D. W.; Gambhir, S. S. *Proceedings-National Academy of Sciences USA* **2002**, *99*, 3030-3035.

(104) Hardy, J.; Edinger, M.; Bachmann, M. H.; Negrin, R. S.; Fathman, C. G.; Contag, C. H. *Experimental Hematology* **2001**, *29*, 1353-1360.

(105) de Vries, I. J. M.; Lesterhuis, W. J.; Barentsz, J. O.; Verdijk, P.; van Krieken, J. H.; Boerman, O. C.; Oyen, W. J. G.; Bonenkamp, J. J.; Boezeman, J. B.; Adema, G. J. *Nature Biotechnology* **2005**, *23*, 1407-1413.

(106) Lyons, S. K. *Journal of Pathology* **2005**, *205*, 194-205.

(107) Eskens, F. A.; Verweij, J. *European Journal of Cancer* **2006**, *42*, 3127-3139.

(108) Neeman, M.; Gilad, A. A.; Dafni, H.; Cohen, B. *Journal of Magnetic Resonance Imaging* **2007**, *25*, 1-12.

(109) Mulder, W. J. M.; Strijkers, G. J.; Habets, J. W.; Bleeker, E. J. W.; van der Schaft, D. W. J.; Storm, G.; Koning, G. A.; Griffioen, A. W.; Nicolay, K. *Faseb Journal* **2005**, *19*, 2008-2010.

(110) Raatschen, H. J.; Swain, R.; Shames, D. M.; Fu, Y.; Boyd, Z.; Zierhut, M. L.; Wendland, M. F.; Misselwitz, B.; Weinmann, H. J.; Wolf, K. J. *Contrast Media and Molecular Imaging* **2006**, *1*, 113-120.

(111) Miller, J. C. a. T., J.H. *Journal of Americal College of Radiology* **2004**, *1*, 4-23.

(112) Chen, X.; Tohme, M.; Park, R.; Hou, Y.; Bading, J. R.; Conti, P. S. *Molecular Imaging* **2004**, *3*, 96-104.

(113) Schmieder, A. H.; Winter, P. M.; Caruthers, S. D.; Harris, T. D.; Williams, T. A.; Allen, J. S.; Lacy, E. K.; Zhang, H.; Scott, M. J.; Hu, G. *Magnetic Resonance in Medicine* **2005**, *53*, 621-627.

(114) Sipkins, D. A.; Cheresh, D. A.; Kazemi, M. R.; Nevin, L. M.; Bednarski, M. D.; Li, K. C. P. *Nature Medicine* **1998**, *4*, 623-626.

(115) Janssen, M. L.; Oyen, W. J.; Dijkgraaf, I.; Massuger, L. F.; Frielink, C.; Edwards, D. S.; Rajopadhye, M.; Boonstra, H.; Corstens, F. H.; Boerman, O. C. *Cancer Research* **2002**, *62*, 6146-6151.

(116) Medarova, Z.; Pham, W.; Farrar, C.; Petkova, V.; Moore, A. *Nature Medicine* **2007**, *13*, 372-377.

(117) So, M. K.; Xu, C.; Loening, A. M.; Gambhir, S. S.; Rao, J. *Nature Biotechnology* **2006**, *24*, 339-343.

(118) Sengupta, S., Evarone D., Zhao, G., Watson, N., Kiziltepe, T and Sasisekharan R. *Nanotechnology in cancer* **2007**, *436*, 26-30.

(119) Torchilin, V. P. *The AAPS Journal* **2007**, *9*, E128-E147.

(120) Cassidy, P. J. a. R., G.K. *Journal of The Royal Society Interface* **2005**, 1-11.

(121) Weissleder, R.; Mahmood, U. *Radiology* **2001**, *219*, 316-333.

(122) Min, J. J.; Gambhir, S. S. *Gene Therapy* **2004**, *11*, 115-125.

(123) Levin, C. S. *European Journal of Nuclear Medicine and Molecular Imaging* **2005**, *32*, S325-S345.

(124) Weissleder, R. *Nature Reviews Cancer* **2002**, *2*, 11-18.

(125) Pomper, M. G. *Academic Radiology* **2001**, *8*, 1141-1153.

(126) Wiest, P. W.; Locken, J. A.; Heintz, P. H.; Mettler, F. A. *Seminars in Ultrasound Ct and Mri* **2002**, *23*, 402-410.

(127) Phelps, M. E. *Proceedings- National Academy of Sciences USA* **2000**, *97*, 9226-9339.

(128) Phelps, M. E. *Journal of Nuclear Medicine* **2000**, *41*, 661-681.

(129) Meikle, S. R.; Kench, P.; Kassiou, M.; Banati, R. B. *Physics in Medicine and Biology* **2005**, *50*, R45-R61.

(130) Hustinx, R.; Benard, F.; Alavi, A. *Seminars in Nuclear Medicine* **2002**, *32*, 35-46.

(131) Contag, P. R.; Olomu, I. N.; Stevenson, D. K.; Contag, C. H. *Nature Medicine* **1998**, *4*, 245-247.

(132) Lanza, G. M.; Winter, P. M.; Caruthers, S. D.; Morawski, A. M.; Schmieder, A. H.; Crowder, K. C.; Wickline, S. A. *Journal of Nuclear Cardiology* **2004**, *11*, 733-743.

(133) Lauterbur, P. C. *Nature* **1973**, *262*, 190-191.

(134) Van Geuns, R. J. M.; Wielopolski, P. A.; De Bruin, H. G.; Rensing, B. J.; Van Ooijen, P. M. A.; Hulshoff, M.; Oudkerk, M.; De Feyter, P. J. *Progress in Cardiovascular Diseases* **1999**, *42*, 149-156.

(135) Parac-Vogt, T. N.; Kimpe, K.; Laurent, S.; Pierart, C.; Elst, L. V.; Muller, R. N.; Binnemans, K. *European Journal of Inorganic Chemistry* **2004**, 3538-3543.

(136) Weinmann, H. J.; Ebert, W.; Misselwitz, B.; Schmitt-Willich, H. *European Journal of Radiology* **2003**, *46*, 33-44.

(137) Bellin, M. F. *European Journal of Radiology* **2006**, *60*, 314-323.

(138) Bottrill, M.; Kwok, L.; Long, N. J. *Chemical Society Reviews* **2006**, *35*, 557-571.

(139) Fatin-Rouge, N.; Toth, E.; Meuli, R.; Bunzli, J. C. *Journal of Alloys and Compounds* **2004**, *374*, 298-302.

(140) Lin, S. P.; Brown, J. J. *Journal of Magnetic Resonance Imaging* **2007**, *25*, 884-899.

(141) Moreau, J.; Guillon, E.; Pierrard, J. C.; Rimbault, J.; Port, M.; Aplincourt, M. *Chemistry* **2004**, *10*, 5218-5232.

(142) Caravan, P. *Chemical Society Reviews* **2006**, *35*, 512-523.

(143) Ratovo, G.; Souchard, J. P.; Urizzi, P.; Coulais, Y.; Nepveu, F.; Hollande, E. *Applied Organometallic Chemistry* **2004**, *18*, 1-8.

(144) Heppeler, A.; Froidevaux, S.; Maecke, H. R.; Jermann, E.; Behe, M.; Powell, P.; Hennig, M. *Chemistry* **1999**, *5*, 1974-1981.

(145) Kumar, K.; Allen Chang, C.; Francesconi, L. C.; Dischim, D. D. *Inorganic Chemistry* **1994**, *33*, 3567.

(146) Feng, J.; Sun, G.; Pei, F.; Liu, M. *Bioorganic and Medicinal Chemistry* **2003**, *11*, 3359-3366.

(147) Sawant, R. M.; Hurley, J. P.; Salmaso, S.; Kale, A.; Tolcheva, E.; Levchenko, T. S.; Torchilin, V. P. *Bioconjugate Chemistry* **2006**, *17*, 943-949.

(148) Aime, S.; Fedeli, F.; Sanino, A.; Terreno, E. *Journal- American Chemical Society* **2006**, *128*, 11326-11327.

(149) Hovland, R.; Glogard, C.; Aasen, A. J.; Klaveness, J. *Perkin 2* **2001**, 929-933.

(150) Storr, T.; Thompson, K. H.; Orvig, C. *Chemical Society Reviews* **2006**, *35*, 534-544.

(151) Langereis, S.; Kooistra, H. A. T.; van Genderen, M. H. P.; Meijer, E. W. *Organic and Biomolecular Chemistry* **2004**, *2*, 1271-1273.

(152) Xu, J.; Churchill, D. G.; Botta, M.; Raymond, K. N. *Inorganic Chemistry* **2004**, *43*, 5492-5494.

(153) Frullano, L.; Rohovec, J.; Aime, S.; Maschmeyer, T.; Prata, M. I.; de Lima, J. J. P.; Geraldes, C. F. G. C.; Peters, J. A. *Chemistry* **2004**, *10*, 5205-5217.

(154) Aime, S.; Cravotto, G.; Crich, S. G.; Giovenzana, G. B.; Ferrari, M.; Palmisano, G.; Sisti, M. *Tetrahedron Letters* **2002**, *43*, 783-786.

(155) Gunanathan. C., P., A., Furman-Haran, E., Seger, D., Eyal, E., Mukhapadhyay, S., Ben-David,Y., Leitus, G., Cohen, H., Vilan, A., Degani, H. and Milstein, D. *Bioconjugate Chemistry* **2007**, *18*, 1361-1365.

(156) Ranganathan, R. S.; Fernandez, M. E.; Kang, S. I.; Nunn, A. D.; Ratsep, P. C.; Radmakrishna Pillai, K. M.; Zhang, X.; Tweedle, M. F. *Investigative Radiology* **1998**, *33*, 779-797.

(157) Anelli, P. L.; Beltrami, A.; Franzini, M.; Paoli, P.; Rossi, P.; Uggeri, F.; Virtuani, M. *Inorganica Chimica Acta* **2001**, *317*, 218 - 229.

(158) Toth, E.; Helm, L.; Kellar, K. E.; Merbach, A. E. *Chemistry* **1999**, *5*, 1202-1211.

(159) Bryant, L. H.; Jordan, E. K.; Bulte, J. W. M.; Herynek, V.; Frank, J. A. *Academic Radiology* **2002**, *9*, S29-S33.

(160) Lutz, J. F.; Stiller, S.; Hoth, A.; Kaufner, L.; Pison, U.; Cartier, R. *Biomacromolecules* **2006**, *7*, 3132-3138.

(161) Lee, H. Y.; Jee, H. W.; Seo, S. M.; Kwak, B. K.; Khang, G.; Cho, S. H. *Bioconjugate Chemistry* **2006**, *17*, 700-706.

(162) Mohs, A. M.; Wang, X.; Goodrich, K. C.; Zong, Y.; Parker, D. L.; Lu, Z. R. *Bioconjugate Chemistry* **2004**, *15*, 1424-1430.

(163) Kobayashi, H.; Kawamoto, S.; Saga, T.; Sato, N.; Hiraga, A.; Ishimori, T.; Konishi, J.; Togashi, K.; Brechbiel, M. W. *Magnetic Resonance in Medicine* **2001**, *46*, 781-788.

(164) Doble, D. M. J.; Botta, M.; Wang, J.; Aime, S.; Barge, A.; Raymond, K. N. *Journal- American Chemical Society* **2001**, *123*, 10758-10759.

(165) Margerum, L. D.; Campion, B. K.; Koo, M.; Shargill, N. In *Rare earth research*; Morss, L. R., Ed.; Elsevier Sequoia: Duluth; MN, 1996, p 185-190.

(166) Chaubet, F.; Bertholon, I.; Serfaty, J. M.; Bazeli, R.; Alsaid, H.; Jandrot-Perrus, M.; Zahir, C.; Even, P.; Bachelet, L.; Touat, Z. *Contrast Media and Molecular Imaging* **2007**, *2*, 178-188.

(167) Aime, S.; Gianolio, E.; Uggeri, F.; Tagliapietra, S.; Barge, A.; Cravotto, G. In *International conference on biological inorganic chemistry*; Dawson, J. H., Ed.; Elsevier: Ann Arbor, MI, 2005, p 931-938.

(168) Mehvar, R. *Journal of Controlled Release* **2000**, *69*, 1-25.

(169) Bogdanov Jr, A., Matuszewski, L., Bremer, C., Petrovsky, A. and Weissleder, R. *Molecular Imaging* **2002**, *1*, 16-23.

(170) Helms, B.; Meijer, E. W. *Science* **2006**, *313*, 929.

(171) Kobayashi, H.; Kawamoto, S.; Jo, S. K.; Bryant, H. L.; Brechbiel, M. W.; Star, R. A. *Bioconjugate Chemistry* **2003**, *14*, 388-394.

(172) Weinmann, H. J.; Bauer, H.; Griesinger, C.; Ebert, W.; Misselwitz, B.; Muhler, A.; Schmitt-Willich, H. *Academic Radiology* **2002**, *9*, S412-S416.

(173) Ladd, D. L.; Hollister, R.; Peng, X.; Wei, D.; Wu, G.; Delecki, D.; Snow, R. A.; Toner, J. L.; Kellar, K.; Eck, J. *Bioconjugate Chemistry* **1999**, *10*, 361-370.

(174) Bullok, K. E.; Gammon, S. T.; Violini, S.; Prantner, A. M.; Villalobos, V. M.; Sharma, V.; Piwnica-Worms, D. *Molecular Imaging* **2006**, *5*, 1-15.

(175) Bull, S. R.; Guler, M. O.; Bras, R. E.; Meade, T. J.; Stupp, S. I. *Nano Letters* **2005**, *5*, 1-4.

(176) Prantner, A. M.; Sharma, V.; Garbow, J. R.; Piwnica-Worms, D. *Molecular Imaging* **2003**, *2*, 333-341.

(177) Kayyem, J. F., Kumar, R., Fraser, S.E. and Meade, T.J. *Chemistry & Biology* **1995**, *2*, 615-620.

(178) Kobayashi, H.; Sato, N.; Kawamoto, S.; Saga, T.; Hiraga, A.; Haque, T. L.; Ishimori, T.; Konishi, J.; Togashi, K.; Brechbiel, M. W. *Bioconjugate Chemistry* **2001**, *12*, 100-107.

(179) Forsen, S. a. R. A. H. *J. Chem. Phys.* **1963**, *39*, 2892-2901.

(180) Aime, S.; Castelli, D. D.; Terreno, E. *Angewandte Chemie* **2005**, *44*, 5513-5515.

(181) Gimbi, B. *Proceedings of the IEEE* **2005**, *93*, 784-99.

(182) Wang, Y. X. J.; Hussain, S. M.; Krestin, G. P. *European Radiology* **2001**, *11*, 2319-2331.

(183) Moffat, B. A.; Reddy, G. R.; McConville, P.; Hall, D. E.; Chenevert, T. L.; Kopelman, R. R.; Philbert, M.; Weissleder, R.; Rehemtulla, A.; Ross, B. D. *Molecular Imaging* **2003**, *2*, 324-332.

(184) Lauffer, R. B.; Parmelee, D. J.; Dunham, S. U.; Ouellet, H. S.; Dolan, R. P.; Witte, S.; McMurry, T. J.; Walovitch, R. C. *Radiology* **1998**, *207*, 529-538.

(185) Davis, S. S. *Advanced Drug Delivery Reviews* **2004**, *56*, 1241-1242.

(186) Lian, T.; Ho, R. J. Y. *Journal of Pharmaceutical Sciences* **2001**, *90*, 667-680.

(187) Lopes de Menezes, D. E.; Pilarski, L. M.; Belch, A. R.; Allen, T. M. *Biochimica Et Biophysica Acta* **2000**, *1466*, 205-220.

(188) Kostarelos, K.; Miller, A. D. *Chemical Society Reviews* **2005**, *34*, 970-994.

(189) Stewart, L.; Manvell, M.; Hillery, E.; Etheridge, C. J.; Cooper, R. G.; Stark, H.; van-Heel, M.; Preuss, M.; Alton, E. W. F. W.; Miller, A. D. *Perkin 2* **2001**, 624-632.

(190) Tagawa, T.; Manvell, M.; Brown, N.; Keller, M.; Perouzel, E.; Murray, K. D.; Harbottle, R. P.; Tecle, M.; Booy, F.; Brahimi-Horn, M. C. *Gene Therapy* **2002**, *9*, 564-576.

(191) Spagnou, S.; Miller, A. D.; Keller, M. *Biochemistry* **2004**, *43*, 13348-13356.

(192) Bulte, J. W. M.; De Cuyper, M. *Methods in Enzymology* **2003**, 175-197.

(193) Lee, Y.; Koo, H.; Lim, Y. b.; Mo, H.; Sang Park, J. *Bioorganic and Medicinal Chemistry Letters* **2004**, *14*, 2637-2641.

(194) Kim, H. S.; Moon, J.; Kim, K. S.; Choi, M. M.; Lee, J. E.; Heo, Y.; Cho, D. H.; Jang, D. O.; Park, Y. S. *Bioconjugate Chemistry* **2004**, *15*, 1095-1101.

(195) Zhang, S.; Xu, Y.; Wang, B.; Qiao, W.; Liu, D.; Li, Z. *Journal of Controlled Release* **2004**, *100*, 165-180.

(196) Bertini, I.; Bianchini, F.; Calorini, L.; Colagrande, S.; Fragai, M.; Franchi, A.; Gallo, O.; Gavazzi, C.; Luchinat, C. *Magnetic Resonance in Medicine* **2004**, *52*, 669-672.

(197) Krause, W.; Klopp, R.; Leike, J.; Sachse, A. *Journal of Liposome Research* **1995**, *5*, 1.

(198) Tilcock, C., Unger, E., Cullis, P. and MacDougall, P. *Radiology* **1989**, *171*.

(199) Unger, E., Tilcock, C., Ahkong, Q.F. and Fritz, T. *Investigative Radiology* **1990**, *25*, S65-S66.

(200) Kabalka, G. W., Davis, M.A., Holmberg, E., Maruyama, K. and Huang, L. *Magnetic Resonance Imaging* **1991**, *9*, 373-377.

(201) Vuu, K.; Xie, J.; McDonald, M. A.; Bernardo, M.; Hunter, F.; Zhang, Y.; Li, K.; Bednarski, M.; Guccione, S. *Bioconjugate Chemistry* **2005**, *16*, 995-999.

(202) Gruender, W.; Biesold, M.; Wagner, M.; Werner, A. *Investigative Radiology* **1998**, *33*, 193-202.

(203) Port, R. E.; Schuster, C.; Port, C. R.; Bachert, P. *Cancer Chemotherapy and Pharmacology* **2006**, *58*, 607-617.

(204) Ayyagari, A. L.; Zhang, X.; Ghaghada, K. B.; Annapragada, A.; Hu, X.; Bellamkonda, R. V. *Magnetic Resonance in Medicine* **2006**, *55*, 1023-1029.

(205) Erdogan, S.; Roby, A.; Sawant, R.; Hurley, J.; Torchilin, V. P. *Journal of Liposome Research* **2006**, *16*, 45-55.

(206) Saito, R.; Krauze, M. T.; Bringas, J. R.; Noble, C.; McKnight, T. R.; Jackson, P.; Wendland, M. F.; Mamot, C.; Drummond, D. C.; Kirpotin, D. B. *Experimental Neurology* **2005**, *196*, 381-389.

(207) Heverhagen, J. T.; Graser, A.; Fahr, A.; Muller, R.; Alfke, H. *Magnetic Resonance Imaging* **2004**, *22*, 483-487.

(208) De Cuyper, M. a. J., M. *European Biophysics Journal* **1988**, *15*, 311-319.

(209) Plassat, V.; Martina, M. S.; Barratt, G.; Menager, C.; Lesieur, S. *International Journal of Pharmaceutics* **2007**, *344*, 118-127.

(210) Martina, M. S.; Fortin, J. P.; Menager, C.; Clement, O.; Barratt, G.; Grabielle-Madelmont, C.; Gazeau, F.; Cabuil, V.; Lesieur, S. *Journal-American Chemical Society* **2005**, *127*, 10676-10685.

(211) Bulte, J. W. M.; De Cuyper, M.; Despres, D.; Frank, J. A. In *Scientific and clinical applications of magnetic carriers*; Hafeli, U., Zborowski, M., Eds.; North Holland: Cleveland; OH, 1998, p 204-209.

(212) Menager, C.; Cabuil, V. *Journal of Colloid and Interface Science* **1995**, *169*, 251.

(213) Bulte, J. W. M.; Ma, L. D.; Magin, R. L.; Kamman, R. L. *Magnetic Resonance in Medicine* **1993**, *29*, 32.

(214) Unger, E., Shen, D.K., Wu, G. and Fritz, T *Magnetic Resonance in Medicine*, *33*, 304-308.

(215) Unger, E. C., Winokur, T., MacDougall, P., Rosenblum, J., Clair, M., Gatenby, R., and Tilock, C. *Radiology* **1989**, *171*.

(216) Kabalka, G. W., Buonocore, E., Hubner, K., Davis, M.A. and Huang, L. *Magnetic Resonance Imaging* **1988**, *8*.

(217) Brandwijk, R. J. M. G. E.; Mulder, W. J. M.; Nicolay, K.; Mayo, K. H.; Thijssen, V. L. J. L.; Griffioen, A. W. *Bioconjugate Chemistry* **2007**, *18*, 785-790.

(218) Mulder, W. J. M.; Strijkers, G. J.; Griffioen, A. W.; van Bloois, L.; Molema, G.; Storm, G.; Koning, G. A.; Nicolay, K. *Bioconjugate Chemistry* **2004**, *15*, 799-806.

(219) Reulen, S. W. A.; Brusselaars, W. W. T.; Langereis, S.; Mulder, W. J. M.; Breuken, M.; Merkx, M. *Bioconjugate Chemistry* **2007**, *18*, 590-596.

(220) van Tilborg, G. A. F.; Mulder, W. J. M.; Deckers, N.; Storm, G.; Reutelingsperger, C. P. M.; Strijkers, G. J.; Nicolay, K. *Bioconjugate Chemistry* **2006**, *17*, 741-749.

(221) van Tilborg, G. A. F.; Mulder, W. J. M.; Chin, P. T. K.; Storm, G.; Reutelingsperger, C. P.; Nicolay, K.; Strijkers, G. J. *Bioconjugate Chemistry* **2006**, *17*, 865-868.

(222) Lindner, L. H.; Reinl, H. M.; Schlemmer, M.; Stahl, R.; Peller, M. *International Journal of Hyperthermia* **2005**, *21*, 575-588.

(223) Lokling, K. E.; Skurtveit, R.; Bjornerud, A.; Fossheim, S. L. *Magnetic Resonance in Medicine* **2004**, *51*, 688-696.

(224) Lokling, K. E.; Fossheim, S. L.; Skurtveit, R.; Bjornerud, A.; Klaveness, J. *Magnetic Resonance Imaging* **2001**, *19*, 731-738.

(225) Mamot, C.; Nguyen, J. B.; Pourdehnad, M.; Hadaczek, P.; Saito, R.; Bringas, J. R.; Drummond, D. C.; Hong, K.; Kirpotin, D. B.; McKnight, T. *Journal of Neurooncology* **2004**, *68*, 1-9.

(226) Saito, R.; Bringas, J. R.; McKnight, T. R.; Wendland, M. F.; Mamot, C.; Drummond, D. C.; Kirpotin, D. B.; Park, J. W.; Berger, M. S.; Bankiewicz, K. S. *Cancer Research* **2004**, *64*, 2572-2579.

(227) Jasanada, F. a. N., F. *Tetrahedron Letters* **1992**, *33*.

(228) Kimpe, K.; Parac-Vogt, T. N.; Laurent, S.; Pierart, C.; Elst, L. V.; Muller, R. N.; Binnemans, K. *European Journal of Inorganic Chemistry* **2003**, 3021-3027.

(229) Storrs, R. W.; Tropper, F. D.; Li, H. Y.; Song, C. K. *Journal- American Chemical Society* **1995**, *117*, 7301.

(230) Urizzi, P.; Souchard, J. P.; Nepveu, F. *Tetrahedron Letters* **1996**, *37*, 4685-4688.

(231) Tournier, H.; Hyacinthe, R.; Schneider, M. *Academic Radiology* **2002**, *9*, S20-S28.

(232) Lattuada, L.; Lux, G. *Tetrahedron Letters* **2003**, *44*, 3893-3895.

(233) Parac-Vogt, T. N.; Kimpe, K.; Laurent, S.; PiÃ©rart, C.; Elst, L. V.; Muller, R. N.; Binnemans, K. *European Biophysics Journal* **2006**, *35*, 136-144.

(234) Anelli, P. L.; Lattuada, L.; Gabellini, M.; Recanati, P. *Bioconjugate Chemistry* **2001**, *12*, 1081-1084.

(235) Leclercq, F.; Cohen-Ohana, M.; Mignet, N.; Sbarbati, A.; Herscovici, J.; Scherman, D.; Byk, G. *Bioconjugate Chemistry* **2003**, *14*, 112-119.

(236) E.C Unger, T. A. F., C. Tilcock, T.E. New *Journal of Magnetic Resonance Imaging* **1991**, *6*, 689-693.

(237) Mier, W.; Hoffend, J.; Kramer, S.; Schuhmacher, J.; Hull, W. E.; Eisenhut, M.; Haberkorn, U. *Bioconjugate Chemistry* **2005**, *16*, 237-240.

(238) Oliver, M.; Jorgensen, M. R.; Miller, A. D. *Synlett* **2004**, 453-456.

(239) Li, C.; Wong, W. T. *Tetrahedron* **2004**, *60*, 5595-5601.

(240) Park, J. G.; Langenwalter, K. J.; Weinbaum, C. A.; Casey, P. J.; Pang, Y. P. *Journal of Combinatorial Chemistry* **2004**, *6*, 407-413.

(241) Jasanada, F.; Nepveu, F. *Tetrahedron Letters* **1992**, *33*, 5745-5748.

(242) Strijkers, G. J.; Mulder, W. J.; van Heeswijk, R. B.; Frederik, P. M.; Bomans, P.; Magusin, P. C.; Nicolay, K. *Magma* **2005**, *18*, 186-192.

(243) Alhaique, F.; Bertini, I.; Fragai, M.; Carafa, M.; Luchinat, C.; Parigi, G. *Inorganica Chimica Acta* **2002**, *331*, 151 - 157.

(244) Mulder, W. J.; Strijkers, G. J.; van Tilborg, G. A.; Griffioen, A. W.; Nicolay, K. *NMR in Biomedicine* **2006**, *19*, 142-164.

(245) Glogard, C.; Stensrud, G.; Hovland, R.; Fossheim, S. L.; Klaveness, J. *International Journal of Pharmaceutics* **2002**, *233*, 131 - 140.

(246) Himmelreich, U.; Aime, S.; Hieronymus, T.; Justicia, C.; Uggeri, F.; Zenke, M.; Hoehn, M. *Neuroimage* **2006**, *32*, 1142-1149.

(247) Miller, C. R.; Bondurant, B.; McLean, S. D.; McGovern, K. A.; O'Brien, D. F. *Biochemistry* **1998**, *37*, 12875-12883.

(248) Keller, M.; Jorgensen, M. R.; Perouzel, E.; Miller, A. D. *Biochemistry* **2003**, *42*, 6067-6077.

(249) www.promega.com

(250) www.avantilipids.com

(251) Bally, M. B.; Harvie, P.; Wong, F. M. P.; Kong, S.; Wasan, E. K.; Reimer, D. L. *Advanced Drug Delivery Reviews* **1999**, *38*, 291-315.

(252) Xu, Y.; Szoka, F. C. *Biochemistry* **1996**, *35*, 5616-5623.

(253) Gabizon, A. A.; Shmeeda, H.; Zalipsky, S. In *International Liposome Society (ILS 2005) Liposome advances: progress in drug and vaccine delivery*; Taylor & Francis: London, 2005, p 175-184.

(254) Maeda, H.; Wu, J.; Sawa, T.; Matsumura, Y.; Hori, K. In *Recent advances in drug delivery systems*; Anderson, J. M., Kim, S. W., Kopecek, J., Robinson, J. R., Eds.; Elsevier: Salt Lake City, UT, 1999, p 271-284.

(255) Iyer, A. K.; Khaled, G.; Fang, J.; Maeda, H. *Drug Discovery Today* **2006**, *11*, 812-818.

(256) Yuan, F.; Dellian, M.; Fukumura, D.; Leunig, M. *Cancer Research* **1995**, *55*, 3752.

(257) Andresen, T. L.; Jensen, S. S.; JÃ¸rgensen, K. *Progress in Lipid Research* **2005**, *44*, 68-97.

(258) Moghimi, S. M.; Szebeni, J. *Progress in Lipid Research* **2003**, *42*, 463-478.

(259) Scherphof, G. L.; Velinova, M.; Kamps, J.; Donga, J. In *Liposome research days: Towards new products for human health*; Hirota, S., Ed.; Elsevier: Shizuoka; Japan, 1996, p 179-192.

(260) Maruyama, K.; Ishida, O.; Takizawa, T.; Moribe, K. *Advanced Drug Delivery Reviews* **1999**, *40*, 89-102.

(261) Allen, T. M.; Brandeis, E.; Hansen, C. B.; Kao, G. Y. *Biochimica Et Biophysica Acta* **1995**, *1237*, 99.

(262) Bhattacharya, S.; Haldar, S. *Biochimica Et Biophysica Acta* **2000**, *1467*, 39-53.

(263) Trubetskoy, V. S.; Cannillo, J. A.; Milshtein, A.; Wolf, G. L. *Magnetic Resonance Imaging* **1995**, *13*, 31.

(264) Evelhoch, J. L.; Gillies, R. J.; Karczmar, G. S.; Koutcher, J. A.; Maxwell, R. J.; Nalcioglu, O.; Raghunand, N.; Ronen, S. M.; Ross, B. D.; Swartz, H. M. *Neoplasia* **2000**, *2*, 152-165.

(265) Gabizon, A.; Horowitz, A. T.; Goren, D.; Tzemach, D.; Shmeeda, H.; Zalipsky, S. *Clinical Cancer Research* **2003**, *9*, 6551-6559.

(266) MÃ¼ller, C.; Schubiger, P. A.; Schibli, R. *European Journal of Nuclear Medicine and Molecular Imaging* **2006**, *33*, 1162-1170.

(267) Langer, O.; Brunner, M.; Zeitlinger, M.; Ziegler, S.; Muller, U.; Dobrozemsky, G.; Lackner, E.; Joukhadar, C.; Mitterhauser, M.; Wadsak, W. *European Journal of Nuclear Medicine and Molecular Imaging* **2005**, *32*, 143-150.

(268) Konda, S. D.; Aref, M.; Wang, S.; Brechbiel, M.; Wiener, E. C. *Magma* **2001**, *12*, 104 - 113.

(269) Oyewumi, M. O.; Yokel, R. A.; Jay, M.; Coakley, T.; Mumper, R. J. *Journal of Controlled Release* **2004**, *95*, 613-626.

(270) Choi, H.; Choi, S. R.; Zhou, R.; Kung, H. F.; Chen, I. W. *Academic Radiology* **2004**, *11*, 996-1004.

(271) Sun, C.; Sze, R.; Zhang, M. *Journal of Biomedical Materials Research Part A* **2006**, *78*, 550-557.

(272) Mastrobattista, E.; Koning, G. A.; Storm, G. *Advanced Drug Delivery Reviews* **1999**, *40*, 103-127.

(273) Reddy, J. A.; Abburi, C.; Hofland, H.; Howard, S. J.; Vlahov, I.; Wils, P.; Leamon, C. P. *Gene Therapy* **2002**, *9*, 1542-1550.

(274) Ghaghada, K. B.; Saul, J.; Natarajan, J. V.; Bellamkonda, R. V.; Annapragada, A. V. *Journal of Controlled Release* **2005**, *104*, 113-128.

(275) Fraser, R.; Dobbs, B. R.; Rogers, G. W. T. *Hepatology* **1995**, *21*, 863.

(276) Hueber, M. M.; Staubli, A. B.; Kustedjo, K.; Gray, M. H. B.; Shih, J.; Fraser, S. E.; Jacobs, R. E.; Meade, T. J. *Bioconjugate Chemistry* **1998**, *9*, 242-249.

(277) Brekke, C.; Morgan, S. C.; Lowe, A. S.; Meade, T. J.; Price, J.; Williams, S. C.; Modo, M. *NMR in Biomedicine* **2007**, *20*, 77-89.

(278) Dirksen, A.; Langereis, S.; de Waal, B. F. M.; van Genderen, M. H. P.; Meijer, E. W.; de Lussanet, Q. G.; Hackeng, T. M. *Organic Letters* **2004**, *6*, 4857-4860.

(279) Maier, O.; Oberle, V.; Hoekstra, D. *Chemistry and Physics of Lipids* **2002**, *116*, 3 - 18.

(280) Li, H.; Gray, B. D.; Corbin, I.; Lebherz, C.; Choi, H.; Lund-Katz, S.; Wilson, J. M.; Glickson, J. D.; Zhou, R. *Academic Radiology* **2004**, *11*, 1251-1259.

(281) Kachel, K.; Asuncion-Punzalan, E.; London, E. *Biochimica Et Biophysica Acta* **1998**, *1374*, 63-76.

(282) Xu, H.; Regino, C. A. S.; Koyama, Y.; Hama, Y.; Gunn, A. J.; Bernardo, M.; Kobayashi, H.; Choyke, P. L.; Brechbiel, M. W. *Bioconjugate Chemistry* **2007**, *18*, 1474-1482.

(283) Achilefu, S.; Srinivasan, A.; Schmidt, M. A.; Jimenez, H. N.; Bugaj, J. E.; Erion, J. L. *Journal of Medicinal Chemistry* **2003**, *46*, 3403-3411.

(284) Giesel, F. L.; Stroick, M.; Griebe, M.; Troster, H.; von der Lieth, C. W.; Requardt, M.; Rius, M.; Essig, M.; Kauczor, H. U.; Hennerici, M. G. *Investigative Radiology* **2006**, *41*, 868-873.

(285) Kimura, A.; Narazaki, M.; Kanazawa, Y.; Fujiwara, H. *Magnetic Resonance Imaging* **2004**, *22*, 855-860.

(286) Oishi, M.; Sumitani, S.; Nagasaki, Y. *Bioconjugate Chemistry* **2007**, *18*, 1379-1382.

(287) Francois, J. a. N., F. *Tetrahedron Letters* **1992**, *33*, 5745-5747.